To the Graduate Council:
I am submitting herewith a dissertation written by Megan Taliaferro Bragg entitled "Structural and spectroscopic studies of transition metal organometallic and coordination complexes with reference to catalysis." I have examined the final electronic copy of this dissertation for form and content and recommend that it be accepted in partial fulfillment of the requirements for the degree of Doctor of Philosophy, with a major in Chemistry.

John F. C. Turner
Major Professor

We have read this dissertation
and recommend its acceptance:

David C. Baker

Engin Serpersu

Ziling Xue

Janice Musfeldt

Acceptance for the Council:

Anne Mayhew
Vice Chancellor and
Dean of Graduate Studies

(Original signatures are on file with official student records.)

Structural and spectroscopic studies of transition metal organometallic and coordination complexes with reference to catalysis

A Dissertation
Presented for the
Doctor of Philosophy
Degree
The University of Tennessee, Knoxville

Megan Taliaferro Bragg
December 2005

Dedication

This dissertation is dedicated to my wonderful husband, Nathan Edward Bragg.

Acknowledgements

I would like to extend my thanks to the many people who have contributed their professional and personal support to my work and have made this research possible. I would like to thank my committee members: Dr. John Turner, Dr. David C. Baker, Dr. Engin Serpersu, Dr. Ziling Xue, and Dr. Janice Musfeldt for their professional contributions and revisions.

Special thanks to Dr. John Turner for sharing his knowledge and expertise in both the theoretical and technical arts of chemistry as well as for the advice and direction he has provided over the last several years. I also would like to thank Dr. David C. Baker who collaborated with Dr. John Turner concerning two projects included in this dissertation, and for providing access to lab resources.

Without the technical assistance of Dr. Hongjun Pan with NMR spectroscopy, I would not have been able to finish my work. Special thanks also to two people who taught me the basics of 2D NMR on different systems: Laurel Morton on the 400 Avance Bruker NMR and Karen Welch on the 600 MHz Inova NMR. Karen also obtained the 600 MHz Inova NMR data for **10**$^{+}$. Cara Nygren is acknowledged and thanked for contributing to verification of several solid-state conformations by collecting and solving single crystal x-ray diffraction data on several compounds.[1-3] Density functional theory calculations were performed by Mr. Richard Lonsdale and Prof. Jennifer C. Green (University of Oxford)[4] whom I would also like to acknowledge.

All research conducted for this dissertation has been funded by Dr. John Turner's NSF grant and start-up funds for which I am very grateful. I would like to thank the University of Tennessee for providing monatary support, which made my work possible. Various conference presentations were made possible with support awarded provided by GSS, ACGS, the dean of arts and sciences, and the department of chemistry.

I would like to acknowledge and Andrew Colvin, for synthesizing large quantities of **10**, **10**$^{+}$**, 10**$^{+2}$**,** and **11**. I also want to acknowledge and Riyam Kafri who synthesized both forms of the sultam in this work as well as initial quantities of catalyst used in the catalytic cycle work. I could not have worked on either project without their help and I thank them both.

Several undergraduates were also extremely helpful with respect to synthesis. Brian Harris assisted with synthesizing **10** and **10^+.** Robert Sacci deuterated **7**. Michael Hedge also helped by purifying large quantities of carbazole and carbazole derivatives.

I would like to thank the current members of the lab of Dr. Turner. I appreciate them very much. Michael Blanchard willingly shared pre-dried solvents, glassware, and glovebox space. He and Jamie Molaison were great to work with and a source of encouragement. Jamie Molaison also helped with high vacuum line work and provided feedback concerning NMR interpretation. Andrew Colvin managed to make me laugh with his antics for which I am grateful. Michelle Dolgos was always willing to help me with concepts and was so friendly to everyone. Mustafa Rajabali has a positive attitude that makes the office brighter. I would also like to thank Onome Swader for her kindness and friendship.

I would like to thank Dr. Rose Boll for the rewarding opportunity as a teaching assistant with the EAP program. I have enjoyed learning from her as well as the fact that teaching with her supported me while I was here. Thanks to Amy Bashaam who helped me proof and print this dissertation. I extend thanks as well to the support staff in the Chemistry Department: the stockroom, glass shop, electronic shop, main office, and general chemistry office whose work made my life easier.

Other appreciation goes to past chemistry teachers and professors who inspired me to continue in the field. Mrs. Stinson taught my high school chemistry class magnificently. Dr. Edward Lisic's teaching skills inspired me while I was at TTU. He also gave me the opportunity to participate in undergraduate research and present at a national conference. Dr. Lee Magid's spectroscopy class was phenomenal and encouraged my interest specifically in NMR.

I would also like to thank my close friends. Elizabeth McNelly, my best friend, was always willing to listen and continually encouraged me with her words and friendship throughout the last five years. Melissa Dunn helped me to have fun and shop in spite of my hectic schedule. I also wanted to thank Brian Hollander who listened to my tirades and understood because he has been there.

I want to thank Nancy and Raymond Judy, my grandparents, for showing me they were proud of me and modeling a marriage I would like to have in fifty years. I want to also thank Jane Ann Howerton who steadfastly encouraged my continued education.

I want to thank my parents, Linda and Wayne Taliaferro, whose unbelievable love, understanding, sacrifice, and encouragement have helped shape me into the person I am today. Thanks to my in-laws, Sharon and Warren Bragg, who are second parents to me in the most amazing ways imaginable. Thanks also to David Taliaferro. He is the coolest brother I could have.

Last, but not least, I would like to thank my husband, Nathan Edward Bragg, who completely appreciates me. He has always defended and protected me. I appreciate so much the sacrifices he has made so that I could take this path, and thank him with all my heart for his steadfast encouragement and love through the years.

Abstract

Inorganic chemistry encompasses a variety of topics and in many ways, these advances affect a wider sphere of chemists than purely inorganic and progress in this field is interesting to many scientists. The developments presented in this dissertation are significant as they affect three issues: catalytic reactivity, ligand fluxionality, and catalyst development. Catalysis affects industrial profit, pharmaceutical development, agrochemical synthesis, spectroscopy, enzymatic activity, and polymerization.

Progress in certain areas such as the [Cp*Rh(TsDPEN)] (TsDPEN = *p*-toluenesulfonyldiphenylethylenediamine) has lead to a moiety that is a powerful and efficient catalyst for the reduction of C=N bonds. The precise mechanism of the reaction has been illuminated through a combination of isolation and detection of key intermediates in the catalytic cycle, independent synthesis under non-catalytic conditions, isotopic labeling in combination with in situ 2-dimensional VT NMR. The intermediacy of a fugative Rh-H is strongly supported, and the 16 electron species [Cp*(*p*-toluenesulfonyldiphenylethylenediamido)Rh] also appears to play a role, implying that there is more than one mechanistic cycle that is important. Understanding this catalyst cycle explains and predicts the stereospecific reductive ability of this catalyst.

Improvement upon the understanding of the fluxional structure of polycyclic tetramines in solution allows for a better knowledge of how these species will act as ligands in solution. They are an interesting ligand-type that is likely to bind with unusual properties to a metal center. A series of these molecules were measured and modeled using 1D and 2D VT NMR spectroscopy. Correlations with the electronic structure, using group theoretical methods, supported by density functional calculation, lead to a full picture of the behavior of these proton sponges in solution.

Amido ligands, when complexed to transition metals have been the subject of intense interest in recent years and have been shown to promote new and unusual reactivity. This chemistry is often a result of both σ and π donation to the metal center. In order to understand this bonding scheme and the donation involved, as well as to study the reaction chemistry, several novel amido complexes, containing both π basic and non-basic ligands, have been synthesized. The ligands and their zirconium complexes have

been characterized extensively using both 2D and VT NMR techniques. The synthesis and characterization of a series of metal carbazolyl complexes by X-ray and NMR techniques is reported.

Table of Contents

1 Introduction 1
1.1 History 1
1.1.1 Initial observation 1
1.1.2 Further development 1
1.1.3 First spectrometer compared to current spectrometer 3
1.1.4 Development of solid state NMR 3
1.1.5 Development of biological applications of NMR 5
1.1.6 Development of biological imaging 5
1.2 Nuclear spin 6
1.2.1 Foreword 6
1.2.2 Fundamental particles 6
1.2.3 Neutrons 7
1.2.4 Protons 8
1.2.5 Nuclei 8
1.2.6 Spin-active nuclei 9
1.2.7 Angular momentum 10
1.2.8 Illustrations of nuclear spin states 12
1.2.9 Boltzman distribution 14
1.3 Factors affecting detectability of the nucleus 16
1.3.1 Magnetogyric ratio 16
1.3.2 Natural abundance 17
1.3.3 Resonant frequency 18
1.3.4 Relaxation 18
1.4 Magnetic interactions 19
1.4.1 Magnetic fields 19
1.4.2 Electric-quadrupolar coupling 22
1.4.3 Spin active nuclei interaction: dipole-dipole coupling 22
1.4.4 Spin rotation interaction 23
1.4.5 Electronic interaction: chemical shift anisotropy 24

1.4.6 Electronic interaction: scalar coupling *J* 27
1.5 Relaxation from excitation 36
1.5.1 Manipulation of spin populations 36
1.6 Nuclear relaxation 39
1.6.1 Mechanisms 41
1.7 Pulsing and related effects 46
1.7.1 Decoupling 46
1.8 Spectrometer 48
1.9 Data manipulation 52
1.10 Fourier transforms 54
1.11 One dimensional experiments 56
1.11.1 Basic pulse diagram and experiment 56
1.11.2 Saturation 57
1.11.3 Polarization transfer 58
1.11.4 NOE 61
1.11.5 Thermodynamics 65
1.11.6 Kinetics 66
1.12 The second dimension 67
1.12.1 Two dimensional techniques 68
1.12.2 Bond correlations 69
1.12.3 Direct detection: HETCOR 70
1.12.4 Space correlations and chemical exchange correlations 71
1.12.5 Phase vs. magnitude 73
1.12.6 Inverse detection 75
1.13 Conclusion 78
2 Catalytic cycle 79
2.1 Foreword 79
2.2 Brief historical account of asymmetric catalysis 79
2.3 Basic catalytic premises 80
2.3.1 General homogeneous catalysis 80

2.3.2 Achirality and chirality 81
2.3.3 Reductive enantioselective catalysts 82
2.3.4 General reductive catalysts 82
2.3.5 MLX naming 84
2.4 Catalytic hydrogenation 84
2.4.1 Description of catalyst intermediates 89
2.5 Catalytic mechanisms of rhodium catalyst cycle 96
2.5.1 Spectroscopic interpretations 96
2.6 Experimental 139
3 Spectroscopic studies of tetraamine-compounds 152
3.1 Forward 152
3.2 Introduction 152
3.2.1 Group theoretical considerations 154
3.2.2 Chemical considerations 161
3.3 Stereochemistry of 10^{+} 162
3.3.1 Spectroscopic interpretations 162
3.3.2 The general structure of 10^{+} 164
3.3.3 Conformational structure of 3^{+} 165
3.3.4 Bonding models and theoretical structure 169
3.4 Stereochemistry of 10 169
3.4.1 Low temperature configuration 182
3.4.2 VT data 184
3.4.3 Room temperature configuration of 10 198
3.5 Stereochemistry of 10^{+2} 206
3.5.1 Spectroscopic studies of 11 211
3.6 Experimental 226
4 Synthesis and spectroscopy of zirconium-amido complexes and carbazoyl derivatives 238
4.1 Forward 238
4.2 Carbazole 238

4.3 Catalysts 239
4.4 Carbazole derivatives 239
4.4.1 Synthesized substituted carbazole molecules 240
4.5 Nitrogen complexes 244
4.5.1 Non-innocent complexes 245
4.5.2 Target carbazole ligands 245
4.6 Experimental and NMR data 247
4.6.1 Zirconium connectivity 247
4.6.2 Carbazole NMR spectroscopy of various derivatives 257
4.6.3 Experimental 257
5 Sugar catalyst preparation and spectroscopy 293
5.1.1 Conclusions on the sugar project 293
5.1.2 Synthesis of 30b[160] 293
5.1.3 Synthesis of 31[162] 297
5.1.4 Synthesis of 32[163] 298
5.1.5 Synthesis of 33[164] 298
5.1.6 Synthesis of 34a[165] 299
5.1.7 Synthesis of 34b 299
5.1.8 Synthesis of metal L donor 299
5.1.9 Synthesis of 35 299
5.1.10 Synthesis of 36 300
5.1.11 Synthesis of 37 300
5.1.12 Related spectroscopy and schemes 301
List of References 308
Vita 325

Table of Tables

Table 2.1: Correlations for 6. 100
Table 2.2: Correlations for 1, part I. 113
Table 2.3: Correlations for 1, part II. 114
Table 2.4: NMR correlations for 5a. 128
Table 3.1: Proton affinity, strain energy, and hydrogen bond strength for 2. 154
Table 3.2: Direct product table for C_{2v}. 157
Table 3.3: NMR correlations for 10^{+}. 171
Table 3.4: NMR correlations for 10 at low temperature. 187
Table 3.5: NOESY integral values for 10 at room temperature by EXSYcalc. 197
Table 3.6: NOESY integral values for 10 at low temperature by EXSYcalc. 197
Table 3.7: NMR correlations for 10 at room temperature. 201
Table 3.8: NMR correlations for 10^{+2}. 215
Table 4.1: Correlation NMR data for 12a. 252
Table 4.2: Correlations for 13a. 260

Table of Figures

Figure 1: Example of original beam NMR spectrometer.[6] 4
Figure 2: An example of a current NMR spectrometer.[30, 31] 4
Figure 3: Quark spin combination for a single neutron *(I = ½).* 8
Figure 4: Quark spin combination for a single proton *(I = ½).* 9
Figure 5: Spin orientation for $I = ½$. 13
Figure 6: Spin orientation for $I = 1$. 13
Figure 7: Spin states without and with a magnetic field.[30] 16
Figure 8: Nucleus and electron cloud. 20
Figure 9: Electric-quadrupolar coupling. 20
Figure 10: Dipole-dipole coupling. 20
Figure 11: Chemical shift anisotropy. 21
Figure 12: Scalar coupling. 21
Figure 13: Spin rotation interaction. 21
Figure 14: Nuclear shapes. 23
Figure 15: Electric currents creating magnetic fields. 25
Figure 16: Coupling trees. 28
Figure 17: Pascal's triangle for $I = 1/2$. 29
Figure 18: Pascal's triangle for $I = 1$. 29
Figure 19: Relationship between Pascal's triangle and peak splitting. 29
Figure 20: Roofing effects. 31
Figure 21: Karplus curves for ^3J coupling. 31
Figure 22: Example of a dihedral angle using a Newman projection. 31
Figure 23: Molecules with chemically equivalent protons. 32
Figure 24: Diastereotopic protons. 34
Figure 25: Variable pulses. 37
Figure 26: Combination pulses. 37
Figure 27: Allowed transitions in an AX system. 39
Figure 28: Allowed relaxations in an AX system. 39
Figure 29: Transverse relaxation T_2. 40

Figure 30: Longitudinal relaxation T_1. 40
Figure 31: Pulse sequence for X^{57}. 57
Figure 32: INEPT pulse sequence. 60
Figure 33: DEPT pulse sequence. 60
Figure 34: NOE difference spectroscopy. 63
Figure 35: Effect of a gradient field. 69
Figure 36: Simple COSY pulse sequence. 72
Figure 37: Simple TOCSY pulse sequence. 72
Figure 38: NOESY pulse sequence. 74
Figure 39: ROESY pulse sequence. 74
Figure 40: HMQC pulse sequence. 77
Figure 41: HMBC pulse sequence. 77
Figure 42: Chiral enantiomeric pair. 81
Figure 43: Imine reductive catalysts containing boron. 83
Figure 44: Some well-known organometallic catalysts. 83
Figure 45: Comparison of X_2 and L ligands. 84
Figure 46: Wilkinson's catalytic cycle. 86
Figure 47: Homopolar and heteropolar oxidative addition to a metal center. 86
Figure 48: Putative ionic hydrogenation catalytic cycle. 87
Figure 49: Ionic catalyst studied by Norton *et al*. 87
Figure 50: Comparison of mechanisms. 88
Figure 51: First possible catalyst cycle. 90
Figure 52: Rhodium catalyst, 1. 91
Figure 53: Crystal structure of 1 as determined by the University of Tennessee. 91
Figure 54: Directed syntheses of catalytically relevant species in the catalyst cycle. 93
Figure 55: Second catalytic cycle for 1, using the diamido intermediate. 94
Figure 56: Synthesis of Mashima[99, 100] catalyst and 16 electron species. 95
Figure 57: Reversible reductive carbonylation.[99, 100] 95
Figure 58: Structure of 6 according to NMR data. 99
Figure 59: Carbon and proton spectra of 6. 99

Figure 60: T_1 relaxation of 6. 101
Figure 61: Example T_1 calculation of Cp*. 101
Figure 62: COSY of 6. 102
Figure 63: TOCSY of 6. 103
Figure 64: HSQC of 6. 104
Figure 65: HMBC of 6. 105
Figure 66: NOESY of 6. 106
Figure 67: Comparison of proton spectra of ligand, 6, to catalyst, 1. 108
Figure 68: Synthesis of 1. 108
Figure 69: Structure of catalyst, 1, which is in accord with NMR data. 112
Figure 70: Proton and carbon spectra of 1. 112
Figure 71: T_1 relaxation of 1. 115
Figure 72: Example of T_1 using Cp*. 115
Figure 73: HSQC of 1. 116
Figure 74: COSY of 1. 117
Figure 75: TOCSY of 1. 118
Figure 76: NOESY expansions of 1. 119
Figure 77: Full NOESY of 1. 120
Figure 78: HMBC of 1. 121
Figure 79: HMBC expansion of 1. 122
Figure 80: Proton spectra of 1 compared to 5a. 124
Figure 81: Structure of 5a which is in accord with NMR data. 127
Figure 82: Proton and carbon spectra of 5a. 127
Figure 83: T_1 relaxation of 5a. 129
Figure 84: Graph of T_1 calculation for the Cp* proton peak for example purposes. 129
Figure 85: HMQC of 5a. 130
Figure 86: COSY of 5a. 131
Figure 87: HMBC of 5a. 132
Figure 88: HMBC expansions of 5a. 133
Figure 89: NOESY of 5a. 134

Figure 90: Reaction of 4 compared to 1 and 7 in d_8-THF. 135
Figure 91: Reaction of 4 compared to 1 and 7 in CD_2Cl_2. 136
Figure 92: VT NMR of 4 in d_8-THF. 137
Figure 93: VT NMR of 4. 138
Figure 94: Carbon and proton spectra of 4. 140
Figure 95: COSY of 4. 141
Figure 96: TOCSY of 4. 142
Figure 97: HMBC of 4. 143
Figure 98: HMBC expansion of aromatic region of 4. 144
Figure 99: HMBC expansion of aliphatic region of 4. 144
Figure 100: Decay of hydride peak in 2. 145
Figure 101: Symmetric tetrahedral tricyclic tetramines. 153
Figure 102: Molecule 10. 156
Figure 103: Interconversion of two C_2 isomers. 156
Figure 104: SALCS for C_{2v} and C_2. 157
Figure 105: Density functional calculations of 10. 158
Figure 106: Molecule10^+. 159
Figure 107: Molecule 10^{+2}. 159
Figure 108: Molecule 11. 159
Figure 109: Density Functional calculations of 10^+. 160
Figure 110: Density functional calculations of 11. 160
Figure 111: Synthetic scheme for 10, 10^+, 10^{+2}, and 11. 163
Figure 112: Two possible configurations of the cation. 166
Figure 113: Line-fitting simulation. 167
Figure 114: The structure of 10^+ that is consistent with the NMR data. 170
Figure 115: Crystal structure of 10^+. 170
Figure 116: Proton and carbon spectra of 10^+. 172
Figure 117: T_1 relaxation study for long relaxation of 10^+. 173
Figure 118: Graph of T_1 relaxation of methine proton. 173
Figure 119: Stacked plot of VT NMR for 10^+. 174

Figure 120: Expanded stacked plot of VT NMR for 10^{+}. 175
Figure 121: Stacked plot of ^{13}C VT NMR for 10^{+}. 176
Figure 122: Expanded stacked plot of ^{13}C VT NMR for 10^{+}. 177
Figure 123: COSY NMR of 10^{+}. 178
Figure 124: HSQC NMR of 10^{+}. 179
Figure 125: HMBC NMR of 10^{+}. 180
Figure 126: NOESY NMR of 10^{+}. 181
Figure 127: Eight possible structures for 10 at low temperature. 185
Figure 128: Proton and carbon spectra of 10 at low temperature. 186
Figure 129: Spinworks simulation of 10 at low temperature. 188
Figure 130: T_1 relaxation study of 10 at low temperature. 189
Figure 131: TOCSY NMR of 10 at low temperature. 190
Figure 132: COSY NMR of 10 at low temperature. 191
Figure 133: HMQC NMR of 10 at low temperature 192
Figure 134: NOESY data of 10 at low temperature. 193
Figure 135: Stacked plot of proton VT NMR for 10. 194
Figure 136: Stacked plot of carbon VT NMR for 10. 195
Figure 137: Spinworks 2.4 simulation of region above coalescence point for 10. 196
Figure 138: Structure of 10 that is consistent with NMR data at room temperature. 200
Figure 139: Proton and carbon spectra of 10 at room temperature 200
Figure 140: T_1 relaxation a room temperature of 10 at room temperature. 202
Figure 141: HMQC of 10 at room temperature. 203
Figure 142: TOCSY of 10 at room temperature. 204
Figure 143: NOESY of 10 at room temperature. 205
Figure 144: The structure of 10^{+2} that is consistent with the NMR data. 212
Figure 145: Crystal structure of 10^{+2}. 213
Figure 146: Side view of the crystal structure of 10^{+2}. 213
Figure 147: Carbon and proton spectra of 10^{+2}. 214
Figure 148: T_1 relaxation data of 10^{+2} 217
Figure 149: 400 MHz HMQC of 10^{+2} 218

Figure 150: Expansion of HMQC of 10^{+2} 219
Figure 151: COSY NMR of 10^{+2}. 220
Figure 152: TOCSY NMR of 10^{+2} 221
Figure 153: NOESY NMR of 10^{+2}. 222
Figure 154: NOESY expansions of 10^{+2}. 223
Figure 155: HMBC of 10^{+2}. 224
Figure 156: HMBC expansions of 10^{+2}. 225
Figure 157: The structure of 11 that is consistent with the NMR data. 227
Figure 158: Crystal structure of 11. 228
Figure 159: Sideview of the crystal structure of 11. 228
Figure 160 Carbon and proton spectra of 11. 229
Figure 161: HMQC NMR of 11 230
Figure 162: Steric hindrance generated on a disubstituted carbazole molecule. 240
Figure 163: Mono and di-substituted carbazole 243
Figure 164: Di and tri-substituted tetrahydrocarbazole. 243
Figure 165: Available forms of the hydrochloric salt starting material 2005. 243
Figure 166: Sterically hindered cyclohexanone. 243
Figure 167: Classical noninnocent coordination 246
Figure 168: Classical noninnocent organometallic complex. 246
Figure 169: Illustrations of carbazole indicating two potential bonding schemes 247
Figure 170: Structure of 12a according to NMR. 250
Figure 171: Carbon and proton spectra for 12a. 250
Figure 172: Crystal structure of $ZrCl_2Cb_3THF{\cdot}KTHF$, 12a 251
Figure 173: Crystal structure of $ZrCl_2Cb_3THF{\cdot}Li(THF)_4$, 12b 251
Figure 174: High VT NMR of 12a. 253
Figure 175: Low VT NMR of 12a. 253
Figure 176: COSY of 12a. 254
Figure 177: NOESY of 12a 255
Figure 178: HMQC of 12a. 256
Figure 179: Structure of 13a according to NMR. 258

Figure 180: Carbon and proton spectra of 13a. 258
Figure 181: Crystal structure of 13a. 259
Figure 182: T_1.study of 13a. 261
Figure 183: Expansion VT NMR of 13a. 262
Figure 184: VT of 13a. 262
Figure 185: HMQC of 13a. 263
Figure 186: Fluxionality of dimethyl species. 264
Figure 187: Proton and carbon spectra of 14 in $CDCl_3$. 271
Figure 188: Proton and carbon spectra of 14 in C_6D_6. 272
Figure 189: Proton and carbon spectra of 16 in $CDCl_3$. 273
Figure 190: Proton and carbon spectra of 16 in C_6D_6. 273
Figure 191: Proton and carbon spectra of 18 in $CDCl_3$. 274
Figure 192: Proton and carbon spectra of 20 in $CDCl_3$. 275
Figure 193: Proton and carbon spectra of 20 in C_6D_6. 276
Figure 194: Proton and carbon spectra of 22 in $CDCl_3$. 277
Figure 195: Proton and carbon spectra of 23 in $CDCl_3$. 278
Figure 196: Proton and carbon spectra of 24 in $CDCl_3$. 279
Figure 197: Proton and carbon spectra of 15 in C_6D_6. 280
Figure 198: Proton and carbon spectra of 17 in $CDCl_3$. 281
Figure 199: Proton and carbon spectra of 17 in C_6D_6. 281
Figure 200: Proton and carbon spectra of 21 in $CDCl_3$. 282
Figure 201: Proton and carbon spectra of 21 in C_6D_6. 282
Figure 202: Proton and carbon spectra of 19 in $CDCl_3$. 283
Figure 203: Proton and carbon spectra of 25 in $CDCl_3$. 284
Figure 204: Proton and carbon spectra of 28 in $CDCl_3$. 285
Figure 205: Proton and carbon spectra of 29 in $CDCl_3$. 286
Figure 206: Proton and carbon spectra of 26 in $CDCl_3$. 287
Figure 207: Proton and carbon spectra of 27 in $CDCl_3$. 288
Figure 208: Synthesis of 3,6-dimethyl-1,2,3,4-tetrahydrocarbazole, 18. 289
Figure 209: Synthesis of 3-methyl-5-tert-butyl-1,2,3,4-tetrahydrocarbazole, 20. 289

Figure 210: Synthesis of 6,8-dimethyl-1,2,3,4-tetrahydrocarbazole, 22. 290
Figure 211: Synthesis of 3-tert-6,8-dimethyl-1,2,3,4-tetrahydrocarbazole, 24. 290
Figure 212: Synthesis of 3,6, 8 – trimethyl-1,2,3,4 tetrahydrocarbazole, 23..... 290
Figure 213: Synthesis of 3-methyl-2,3,4, 4a, 9, 9a-hexahydro-1*H*-carbazole, 14..... 291
Figure 214: Synthesis of Synthesis of 3-*tert*-butyl-1,2,3,4-tetrahydrocarbazole, 16..... 291
Figure 215: Alternative synthesis I of disubstituted carbazole..... 292
Figure 216: Alternative synthesis II of disubstituted carbazole, 27..... 292
Figure 217: Fisher-Indole type synthesis..... 292
Figure 218: Sugar catalyst synthetic scheme..... 294
Figure 219: Scheme for synthesis of 35..... 295
Figure 220: Scheme for synthesis of 36..... 295
Figure 221: Scheme for synthesis of 37..... 295
Figure 222: Sodium/ammonia reaction set-up..... 301
Figure 223: Carbon and proton spectra of 30a in $CDCl_3$..... 302
Figure 224: Synthesis of 30b. 303
Figure 225: Carbon and proton spectra NMR of 30b in $CDCl_3$. 303
Figure 226: Synthesis of 31. 304
Figure 227: Carbon and proton of 31 in $CDCl_3$..... 304
Figure 228: Synthesis of 33. 305
Figure 229: Carbon and proton spectra of 33 in $CDCl_3$..... 305
Figure 230: Synthesis of 34b. 306
Figure 231: Carbon and proton spectra of 34b in $CDCl_3$..... 306
Figure 232: Synthesis of 34a..... 307
Figure 233: Carbon and proton spectra of 34a in $CDCl_3$..... 307

List of Acronyms

BIRD	**Bi**linear **R**otation **D**ecoupling
CSA	**C**hemical **S**hift **A**nisotropy
COSY	**Co**rrelation **S**pectroscop**y**
DNMR	**D**ynamic **N**uclear **M**agnetic **R**esonance
DEPT	**D**istortionless **E**nhanced **P**olarization **T**ransfer
EFG	**E**lectric **F**ield **G**radient
EXSY	**Ex**change **S**pectroscop**y**
FID	**F**ree **I**nduction **D**ecay
HSQC	**H**eteronuclear **S**ingle **Q**uantum **C**oherence
HMBC	**H**eteronuclear **M**ultiple **B**ond **C**orrelation
HMQC	**H**eteronuclear **M**ultiple **Q**uantum **C**oherence
HOMO	**H**ighest **O**ccupied **M**olecular **O**rbital
HPLC	**H**igh **P**erformance **L**iquid **C**hromatography
INEPT	**I**nsensitive **N**ucleus **E**nhanced by **P**olarization **T**ransfer
LUMO	**L**owest **U**noccupied **M**olecular **O**rbital
MAS	**M**agic **A**ngle **S**pinning
MestReC	**M**agnetic **R**esonance **C**ompanion
MEXICO	**M**cMaster Program for **Ex**change L**i**neshape **C**alculati**o**ns
NOE	**N**uclear **O**verhauser **E**ffect
NOESY	**N**uclear **O**verhauser **E**ffect **S**pectroscopy
NMR	**N**uclear **M**agnetic **S**pectroscopy
ORTEP	**O**ak **R**idge **T**hermal **E**llipsoid **P**rojection
PFG	**P**ulse **F**ield **G**radient
ROESY	**R**otating **F**rame **O**verhauser **E**ffect **S**pectroscopy
SALC	**S**ymmetry **A**dapted **L**inear **C**ombinations
TOCSY	**To**tal **C**orrelation **S**pectroscop**y**
VT	**V**ariable **T**emperature

List of Symbols

Å	angstrom
B_0	magnetic field strength
B_1	applied magnetic pulse
B_2	decoupling applied magnetic pulse
d	down [quark]
Δ	pulse delay [pulse diagram]
e	electron charge
E	energy
f_2	detected dimension
f_1	artificial dimension
ν	frequency
γ	magnetogyric ratio
h	Plank's constant
ħ	h/2π
I	nuclear spin
I_{rot}	moment of inertia
I(t)	intensity [t_1]
J	angular momentum quantum number
J	scalar coupling
k	exchange rate constant
m_I	magnetic quantum number
m	multiplicity
N	population [Boltzman]
ρ	momentum
R	relaxation
R_f	radiofrequency
SR	spin rotation
T	temperature

T_1	transverse relaxation
T_2	longitudinal relaxation
t	time
t_c	rotational correlation time
t_2	relaxation time [pulse sequence]
t_1	decoupling delay [pulse sequence]
τ	mixing time [pulse sequences]
W_0	zero quantum relaxation [NOE]
W_1	single quantum relaxation [NOE]
W_2	double quantum relaxation [NOE]
θ	Dihedral angle
ϑ	interdipole angle
u	up [quark]

List of Abbreviations

Bz	benzyl
Cb	carbazole
$CbMe_2$	3, 6-dimethylcarbazole
$Cb(Me)_2$'	6, 8-dimethylcarbazole
Cp*	pentamethylcyclopentadienyl
LT	low temperature [spectroscopy]
Me	methyl
Ph	phenyl
CbH_4	tetrahydrocarbazole
$PrMe_4$	tetramethylpropyl
RT	room temperature [spectroscopy]
*t*Bu	*tert*-butyl
Ts	*p*-toluenesulfonyl
TsDPEN	*p*-toluenesulfonyldiphenylethylenediamine
1D	one dimensional [spectroscopy]
2D	two dimensional [spectroscopy]
3D	three dimensional [spectroscopy]

List of Compounds

1	$[Cp^*Rh(TsDPEN)]Cl$
1-d_2	$[Cp^*Rh(d_2\text{-TsDPEN})]Cl$
2	$[Cp^*Rh(TsDPEN)]H$
3	$[Cp^*Rh(TsDPEN)]NR_2L$
4	$[Cp^*Rh(TsDPEN)NHR_2L]^+BF_4^-$
5a	$[Cp^*Rh(TsDPEN)]^+BF_4^-$
5b	$[Cp^*Rh(TsDPEN)S]^+BF_4^-$
6	(1R, 2R) TsDPEN
6-d_3	(1R, 2R) d_3-TsDPEN
7	3-m-Tolyl-2,3-dihydro-benzo[*d*]isothiazole 1,1-dioxide
8	$[N(CH_2)]_4$
9	$[N(CH_2)_2]_4$
10	$[[N(CH_2)_2]_4(CH)_2]$
10^+	$[[N(CH_2)_2]4(CH)C]^+ Br^-$,
10^{+2}	$[[N(CH_2)_2]_4(CH)_2(Bz)_2]^{2+} 2Br^-$
11	$[[N(CH_2)_2]4C_2]$
12a	$K^+ \cdot THF[ZrCl_2Cb_3(THF)]^-$
12b	$Li^+ \cdot (THF)_4[ZrCl_2Cb_3(THF)]^-$
13a	$ZrCl_2(CbMe_2)_2(THF)_2 \cdot 1.5$Benzene
13b	$ZrCl_2(CbMe_2)_2(THF)$
14	CbH_4Me
15	CbMe
16	CbH_4*t*Bu
17	Cb*t*Bu
18	$CbH_4(Me)_2$
19	$Cb(Me)_2$
20	CbH_4*t*BuMe
21	Cb*t*BuMe
22	$CbH_4(Me)_2$’

23 $CbH_4(Me)_3$

24 $CbH_4(Me)_2tBu$

25 BzCb

26 $BzCb(PrMe_4)_2$

27 $Cb(PrMe_4)_2$

28 $BzCb(tBu)_2$

29 $Cb(tBu)_4$

30a 1,2:5,6-di-*O*-isopropylidine-α-D-glucofuranose

30b 1,2:5,6-di-*O*-isopropylidine-α-D-allofuranose

31 1,2-*O*-isopropylidine-α-D-allofuranose

32 1,2-*O*-isopropylidine-α-D-ribo-pentodialdo-1,4-furanose

33 1,2-*O*-isopropylidine-α-D-ribofuranose

34a 1,2-*O*-isopropylidine-3,5-di-*O*-*p*-toluenesulfonyl-β-D-ribofuranose

34b 1,2-*O*-isopropylidine-5-*O*-*p*-toluenesulfonyl-β-D-ribofuranose

35 $PPhCl_2$

36 $PPhMe_2$

37 $Na[PMe_2]$

1 INTRODUCTION

1.1 History

1.1.1 Initial observation

Pauli predicted the existence of certain nuclear spin angular momentum states in 1926.[5] Almost twenty years passed before nuclear spin states were actually observed. At Columbia in 1938, an instrument was developed by Rabi specifically to measure magnetic moments of certain nuclei but did not give further information about the spin states of the nuclei studied which included ^{6}Li, ^{7}Li, and ^{19}F.[6, 7] He later won a physics Nobel prize in 1944 for this invention.[8] Using a similar method in late 1945 and early 1946, two separate papers reported the absorption of different radiofrequencies within a magnetic field due to magnetic resonance. At MIT, Purcell reported resonance from solid Paraffin and linked these to the two nuclear spin states of protons.[9] At Harvard University, Bloch reported the observance of proton resonance from water in a magnetic field and also correlated this observation to proton magnetic moments.[10] Both Purcell and Bloch won the physics Nobel prize in 1952 for these discoveries and further developments in the field.[8]

1.1.2 Further development

After the initial observance of nuclear spin states, progress with respect to several finer details of NMR was made including relaxation factors, chemical shift, and coupling constants. In 1948, a classical study of nuclear magnetic resonance relaxation factors was published by Bloembergen which described both T_1 and T_2 relaxation as contributions to this phenomenon.[11] The fact that a chemical environment appears to influence the chemical shift effect of particular nuclei was observed on nitrogen-14,[12] fluorine-19,[13] and metals: Li, Na, Al, Cu, and Ga when compared to their chloride salt derivatives.[14] Then, published in January 1951, Proctor used a series of isotopes in the solid state to prove that chemical shift is not the only magnetic influence on the atom and what he termed as “an effect similar to paramagnetism” occurred on the observed nucleus

due to the presence of other spin-active nuclei.[15] Today, this effect is currently referred to as spin-spin or scalar coupling. Shortly thereafter, this observation was repeated in liquids.[16, 17] Initially, this "paramagnetic-like" effect was considered unusual because it was not distinguished from dipole-dipole coupling which is cancelled in the liquid state. Purcell gave further explanation of this type of coupling in 1952 explaining that the interaction of electron clouds and their further interaction with the nucleus leads to spin-spin coupling in the liquid state.[18]

The beginning of pulse sequences began in 1950 when Hahn serendipitously discovered that a short radiofrequency pulse could be applied to samples causing a bulk nuclear shift. This makes it possible to pulse over a range of frequencies and detect strong signals, which inductively decay freely. This technique is still used today and known as the Spin Echo Technique.[19] Then, in 1953, the nuclear Overhauser effect was introduced with respect to solid state detection and the use of microwave frequency to saturate the electronic frequencies; which interact with the nucleus and increase the total nuclear populations.[20] In the liquid state, NOE coupling is averaged through rapid molecular tumbling but significantly affects the relaxation processes of the molecule. The principle is a major one and routinely applied in several experiments such as NOE difference and NOESY, which take advantage of the polarization of certain nuclei to transfer magnetization to nuclear spin states will be further discussed later.

In 1952, chemical exchange was studied by Gutowsky *et al*. They studied PH_3, PF_3, $F_2PO(OH)$ and BrF_5, some at variable temperature, which were assumed to have internal exchange processes and thus proven by this paper.[21] The theory of chemical exchange has played an important role in liquid state NMR. In 1954, a degree of decoupling was first observed for $^{19}F\{^{31}P\}$ in the molecule Na_2PO_3F by varying the frequency and amplitude of the phosphorus nucleus independently.[22]

Discoveries, which lead to improved resolution, also were reported. Sample spinning was theoretically investigated by Bloch[23] and experimentally verified using ethanol by Anderson[24] for the liquid state in 1954. They demonstrated that sample spinning was a viable way to improve the resolution of a peak. Later, in 1957, Golay

reported the use of tuned coils wound around a ping-pong ball to improve the homogeneity of the magnetic field thus improving the resolution *via* shimming.[25]

In 1965, Ernst introduced Fourier transform as a method to transform the FID into a frequency domain.[26] Although at the time, it was initially mathematically cumbersome, the progress of computer disk space and processing speed has made this transform practical to all of the NMR spectroscopy used today.

Although Janeer conceptualized the idea, Ernst[27] developed two-dimensional techniques. First reported in 1975, 2D has greatly increased the scope of NMR applications from routine chemical characterization to complex characterization of macromolecules to imaging. Although other potential classes of experiments were mentioned in this paper, the focus was time space experiments, theory, and experimental results for weakly and strongly coupled systems as well as magnetically equivalent spins. After this major development, for which he won a chemistry Nobel prize in 1991[8] biological and imaging techniques were aptly developed.

1.1.3 First spectrometer compared to current spectrometer

Spectrometers have changed greatly over the last sixty years. An example of the type of spectrometer used to detect resonances in paraffin is shown in Figure 1. There are three magnets and the entire apparatus is under vacuum. An example of a modern spectrometer is shown in Figure 2. In this spectrometer, the magnets are superconducting magnets that must be kept at very low temperatures. The shimming coils are wound around the sample.

1.1.4 Development of solid state NMR

Solid state NMR initially developed at the same time as liquid state NMR but faced limitations due to the additional interaction between molecules in the solid state, which are averaged through molecular motion in liquid state NMR. These interactions lead to increased line broadening and in the case of water, the difference between liquid and solid state is an order of six broader.[28] The discovery of magic angle spinning (MAS) changed the field. It was discovered in 1958 when a solid-state sample was rotated at an angle of 54°.[29] When spun at this angle the line width of the sample is

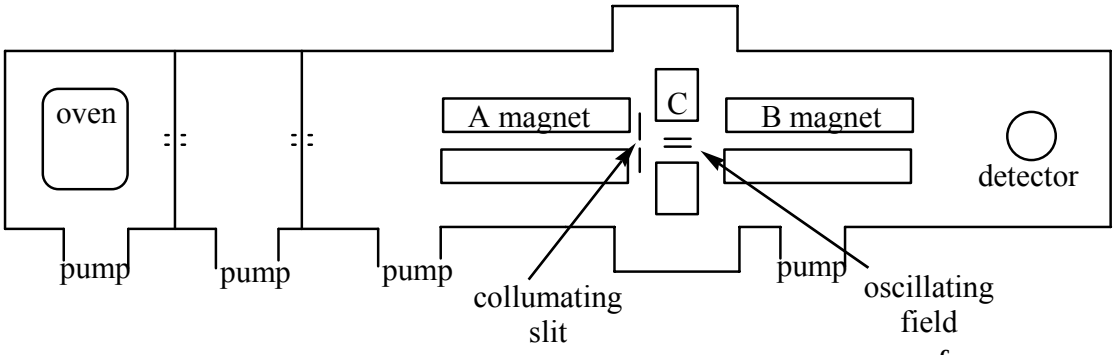


Figure 1: Example of original beam NMR spectrometer.[6]

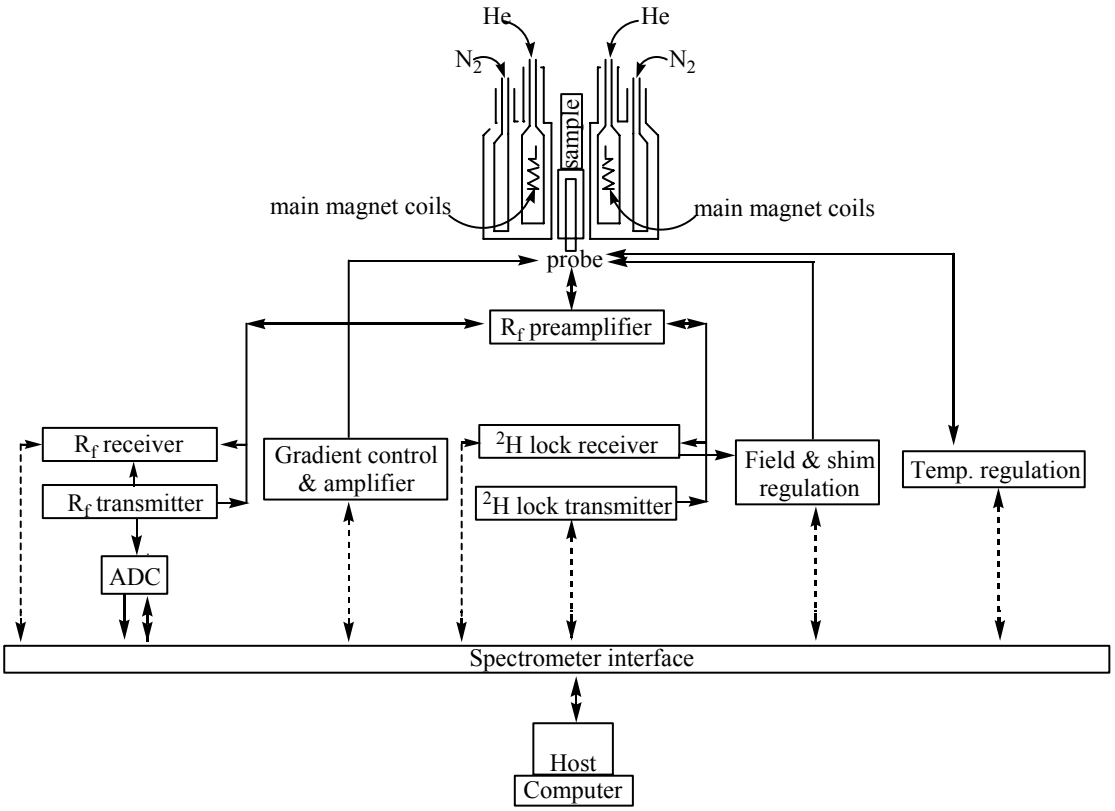


Figure 2: An example of a current NMR spectrometer.[30, 31]

affected as it narrows and spin coupling can be observed.[32] Solid state proton NMR is a technique that compliments X-ray crystallography due to the strong proton detection in the former instrument but extremely weak detection in the later. Solid state NMR is used to study both the interior and surface of many solids.[28]

1.1.5 Development of biological applications of NMR

The early biological development of NMR began in 1957 when the NMR spectrum of ribonuclease was reported.[33] This early spectrum was broadened and could only be separated into four regions. It wasn't until 1967 that a spectrum with much higher resolution than the earlier ribonuclease was reported along with other biological molecules both natural and denatured.[34] In 1973, high resolution ^{31}P NMR of cells was reported. Blood was doped with carbon dioxide, characterized phosphate resonances in the blood and related to pH.[35] Phosphorus is the nucleus of choice when studying cellular activity.

After the development of techniques that suppressed water signals, it was possible to study biological molecules. This area of study was also enhanced with techniques that allowed restraint and perfusion of cells. Two of the major developments were dextran bead[36] and agarose gel.[37] The advance of technology with respect to 2D NMR, and NOE transfer in the 1970's accelerate growth in this field. The first in vivo applications of NMR were published in 1983 by Pyket and Rosen[38]. Additionally in 1983, the first experiment using NOESY and COSY type pulse sequences to identify protons in oligonucleotides[39] was published and lead to increased activity in the field. More recently, Wüthrich developed three dimensional techniques for biological macromolecules[40] for which he received a Nobel prize in 2002.[8]

1.1.6 Development of biological imaging

By 1973, NMR had developed into imaging. Today, the development of NMR into MRS and MRI has increased the scope of NMR with the use of imaging techniques, which take advantage of the fact that different relaxation times penetrate different depths of tissue. The principal founders in this field are Lauterbur[41] and Mansfield[42] who are both medicinal Nobel prize winners in 2003 and 2002 respectively[8]. Imaging has

progressed to the point of being able to recognize cognizant brain responses[43] and is currently used as a means of clinical diagnosis and evaluation.

1.2 Nuclear spin

1.2.1 Foreword

A discussion of nuclear spin, natural abundance, magnetogyric ratio, resonant frequency, relaxation, and other topics with respect to specific fundamental particles, nuclei, atoms, or molecules is relevant because most of the work in this thesis results from measurements and conclusions drawn from nuclear magnetic resonance spectroscopy. An explanation of the basic properties that nuclear and molecular species must exhibit before they can be optimally detected using an NMR instrument is therefore significant for reference within this thesis.

1.2.2 Fundamental particles

Nuclear spin is not a result of motion but is rather an intrinsic property of all subatomic fundamental particles and forces and can be considered an internal dynamical variable of nuclei, electrons, and other subatomic particles. As detailed in section 1.2.7.1, spin is quantized and can take either integer or half-integer values; based on this fundamental division, particles can be divided into two groups; bosons, which possess whole integer spin, and fermions, which possess half-integer spin.[44] The historical significance of the initially empirical allocation of extra internal dynamical variable to the electron,[45-47] and the *a posteriori* theoretical justification by Dirac[48] are discussed in section 1.1.2.

Fermions include protons, neutrons, and electrons. In contrast to the electron, which is considered structureless, protons and neutrons are considered ensembles of other elementary particles known as quarks and leptons. With respect to the intrinsic spin of the nucleus, the quark model of the proton and neutron is successful in describing the observed properties; quarks are heavier particles and posses both spin and fractional electric charge, e, which has a value of 1.62×10^{-19}C.

There are six types of quark: the types are termed flavors and are *up*, *down*, *charm*, *strange*, *top*, and *bottom*. Three flavors have charge values of –e/3 and three have charge values of +2e/3. Combination of different quarks forms subatomic particles in such a way that both the charge and the spin properties of the particle are predictable. In this sense, the fundamental properties of the component nucleons rely on the respective quark structure although there is also dependency upon the gluon interaction, which will be ignored for simplicity.

In an analogous manner; protons and neutrons interact in such a way within the nucleus that the overall charge and spin of the nucleus are predicted, though in a far more complex manner than in the structure of an individual, non-interacting nucleon.

An important principle, which describes the alignment of these subatomic particles when combined and ultimately defines spin, is the Pauli exclusion principle, which states: "The quantum mechanical state of a system containing two identical bosons is invariant under exchange of the two bosons. The quantum mechanical state of a system containing two identical fermions changes sign under exchange of the two fermions".[49]

Nuclear spin is very important with respect to NMR spectroscopy and plays a pivotal role in both conditioning the response of nuclei to magnetic fields as well as influencing the characteristics of the spectra.

1.2.3 Neutrons

The neutron is composed of three quarks, one *up*, and two *down*, forming the combination *udd* and as stated earlier; the spin of these quarks influences the spin of the neutron. The two *d* quarks must align antiparallel due to the Pauli exclusion principle that implies that no two particles can have the same spin quantum numbers. The combination of two antiparallel spins causes cancellation of both spins. The third remaining *u* quark provides the only spin present and the resulting spin of the neutron has a value of ½. The spin arrangement for the neutron is shown in Figure 3. The vertical direction of the arrows in this figure is not intended to reflect the names of the quarks present in these nucleons and should only be perceived as a directional notation used to distinguish parallel or antiparallel alignment.



Figure 3: Quark spin combination for a single neutron *(I = ½)*.
Hashed arrows represent *u* quarks and non-hashed arrows represent *d* quarks.

An interesting feature of the combinations of quarks in nucleons is that with respect to properties other than spin, such as charge, different cancellations occur. As previously stated, the neutron is composed of two *d* quarks and one *u* quark. Each of the two *d* quarks has a charge of –e/3, which cancels the charge of the remaining *u* quark, which has a charge of +2e/3. The resultant value is zero and the neutron has a neutral charge.

1.2.4 Protons

The proton is composed of three quarks, two *u* and one *d*, and as emphasized for neutrons, the combination and cancellation of spin of these quarks influences the spin of the proton. The two *u* quarks must align antiparallel due to the Pauli exclusion principle, causing cancellation of both spins. The third remaining *d* quark provides the only spin present as it is not cancelled by antiparallel alignment. The resultant spin of the proton is ½. An illustration of this phenomenon is shown in Figure 4.

The *uud* arrangement of quarks also predicts the charge on the proton; the resultant charge from two *u* quarks, with a charge of +2e/3 and one *d* quark with a charge of –e/3 leads to a total value of +1 as the charge of the proton.

1.2.5 Nuclei

The presence of protons and neutrons in the nucleus affects the net spin and charge differently. The overall charge of the nucleus is due to the number of protons present in the nucleus. In contrast to the charge of the nucleus, both protons and neutrons influence the total spin of the nucleus. The combination of these spins in the lowest



Figure 4: Quark spin combination for a single proton *(I = ½).*
Hashed arrows represent *up* quarks and non-hashed arrows represent *down* quarks.

energy configuration results in a total nuclear spin known as the ground state nuclear spin and is indicated by the letter, *I*.

An interesting phenomenon arises from the combination of proton and neutron spins. The description of the structure of the nucleus is an excellent example of a strongly coupled, many-body problem and is intractable analytically. Mathematically predicting the spin value of a nucleus based solely on parallel or antiparallel interactions is neither practical nor trivial because the nuclear potential and therefore the structure of the nucleus are poorly understood and will not be detailed further. Moreover, the nuclear potential differs for both neutrons and protons though in both cases, it is not a central force problem; energy level orderings, nuclear orbital angular momentum and degeneracies are anomalous when compared to those that are more familiar in the atom. Therefore, the spin-state of the nucleus is very hard to predict simply by considering the numbers of neutrons and protons. A trend which can loosely generalized when predicting whether an isotope will have whole or half integer ground state spin configuration is that isotopes with even numbers of protons and neutrons typically have either zero or whole integer spin; whereas, isotopes with an odd number of protons and/or neutrons have half integer spin. An extended list of isotopes and their nuclear spin values as well as other nuclear properties is available in the literature.[50]

1.2.6 Spin-active nuclei

Because the number of neutrons in a nucleus does affect the overall spin value of the nucleus, different isotopes of atoms will have different overall spin values. If the spins of protons and neutrons combine in such a way that they completely cancel each other, the value for the spin is zero and they are termed spin-inactive. All other nuclei are

termed spin-active. Clearly, only spin-active nuclei can be observed in a NMR experiment.

The presence of nuclear spin is only detectable in an indirect manner in the absence of a magnetic field. When such a field is present, the energetic degeneracy of the spin states is removed; stimulation and detection of transitions between these states is the basis of NMR spectroscopy.

1.2.7 Angular momentum

1.2.7.1 Schrödinger equation

Nuclear spin obeys the quantum mechanical rules associated with angular momentum. In contrast to classical angular momentum, which may be defined in general for a particle of momentum $\underline{\vec{\mathbf{p}}}$ and position $\underline{\vec{\mathbf{r}}}$ as

$$\vec{\mathbf{l}} = \vec{\mathbf{r}} \times \vec{\mathbf{p}} = \begin{vmatrix} \vec{\mathbf{i}} & \vec{\mathbf{j}} & \vec{\mathbf{k}} \\ r_x & r_y & r_z \\ p_x & p_y & p_z \end{vmatrix} \qquad \mathbf{1.1}$$

and which is continuous in nature for all purposes, the microscopic theory of angular momentum results in quantization of both direction and magnitude. It is necessary to revise the definition of angular momentum on the subatomic scale because classical mechanics do not properly describe properties or motion of quantum particles.

The quantum mechanical description of angular momentum derives from the symmetry properties of rotation. Under these symmetry prescriptions, only one component of the 3-vector, conventionally l_Z and the total magnitude of the 3-vector, l^2 where

$$\vec{\mathbf{l}}^2 = \vec{\mathbf{l}}_x^2 + \vec{\mathbf{l}}_y^2 + \vec{\mathbf{l}}_z^2 \qquad \mathbf{1.2}$$

commute and therefore are observable. The angular momentum is also transferred and manipulated in units of $\hbar$. Other important relationships that hold for any quantum angular momentum, irrespective of the source include:

$$\vec{\mathbf{J}}^2\psi = j(j+1)\hbar \cdot \psi \qquad \mathbf{1.3}$$

$$\vec{\mathbf{J}}_z\psi = m_j\hbar \cdot \psi \quad \textbf{1.4}$$

where $\vec{\mathbf{J}}^2$ represents the total operator for the magnitude of the angular momentum, the *z*-component with *j* and m_j the corresponding eigenvalues.

All quantum particles, whether singly or when in bound states, obey quantum mechanics because of a phenomenon referred to as wave-particle duality. This relationship allows quantum particles to be treated as waves as well as particles; therefore, the field of quantum mechanics assumes that a particle's position is arranged through space in the form of a wave.

The Schrödinger equation can be generally defined as follows:

$$H\Psi = \Psi E \quad \textbf{1.5}$$

where *H* is the Hamiltonian operator and includes both the potential and kinetic energy of the system; likewise, *E* is the energy of the system.[51] When applied to an isotropic rotor, solution of the Schrödinger equation yields:

$$E = \left[J\left(J+1\right)\right] \cdot \frac{\hbar^2}{2I_{\text{rot}}} \quad \textbf{1.6}$$

where $J = 0, 1, 2...n$ where I_{rot} represents the moment of inertia.

In general, these equations can be applied to determine the magnitude of the quantum number *I*, electron spin angular momentum *s*, the total electron orbital angular momentum *L*, and total magnetic quantum number M_L. Since some particles can have more than one type of angular momentum, one or more of these previously mentioned momenta must be summed to determine the total angular momentum generically referred to as *J*. With respect to NMR, the equation

$$J_{tot} = \{J(J+1)\}^{1/2}\hbar \quad \textbf{1.7}$$

is applicable for determining the individual magnitudes of each of the nuclear spin states and is important since the magnitude of the projection influences the transitions as well as relaxations that can occur.

In contrast to orbital angular momentum which only allows $J = 1, 2, 3…n$, spin angular momentum *J* can have values of $J = 1/2, 3/2, 5/2...n$ if the particle is a fermion or $J = 1, 2, 3…n$ if the particle is a boson. The magnetic quantum number m_J is dependent

upon the angular momentum quantum number J and the relationship between J and m_J restricts the values of m_J such that $m_J = J, J\text{-}1, J\text{-}2 \ldots -J$. The magnetic quantum terms will hereafter be referred to as magnetic spin states, which play an essential role in the detection of nuclei *via* NMR.

Magnetic spin states of nuclei are not observable without a magnetic field. In a magnetic field, nuclei with relevant nuclear spin undergo the Zeeman effect and the energy levels become nondegenerate. The amount of energy associated with these states is dependent upon the magnetic field that is applied as well as the type of nuclei involved. Under conditions of thermodynamic equilibrium, the populations of the spin states of the system obey a Boltzman distribution; energy can be applied to the system with a certain frequency to perturb the population of the spin states. Relaxation from this perturbation is detected *via* NMR and further related to the structure of the molecule.[51]

1.2.8 Illustrations of nuclear spin states

To illustrate nondegenerate spin states in a magnetic field further, examples of two types of atoms will be illustrated. The hydrogen atom has the simplest spin configuration to determine of all the elements, due to the presence of only one proton and no neutrons in the nucleus. Because there is only one particle with spin ½, the overall spin of the hydrogen atom is ½; however, several other elements also have this spin configuration of ½. The possible spin states within a magnetic field are either $I = +½$ or $I = -½$. Figure 5 and Figure 6 illustrate the associated spin states for $I = 1$ and $I = ½$.
In the case of the deuterium atom, there is both a proton and a neutron with spins of ½ each. This atom technically has two possible spin configurations, which are separated by a large energy difference of about 10^{11} kJ/mol. If the spins are combined parallel then the nuclear spin is $I = 1$, which is the lowest energy configuration, but if they combine antiparallel, the nuclear spin is $I = 0$. The complexities involved in predicting spins states has already been discussed; however, only one spin state will be the lowest energy configuration. In the case of deuterium, the lowest energy state is $I = 1$. Figure 6 illustrates spin states for an atom with $I = 1$. The representation of arrows in this figure does not indicate coupling to other nuclei but rather parallel or antiparallel spin states

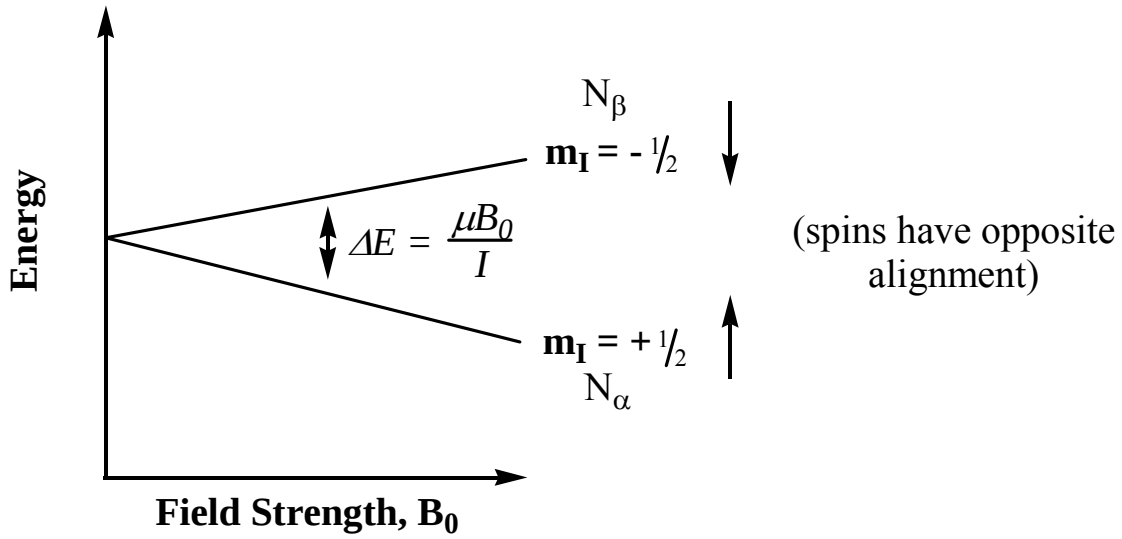


Figure 5: Spin orientation for I = ½.

The β state has higher energy than α state and there are more α spins than β spins when γ *(magnetogyric ratio)* is positive. This is the case for most nuclei.

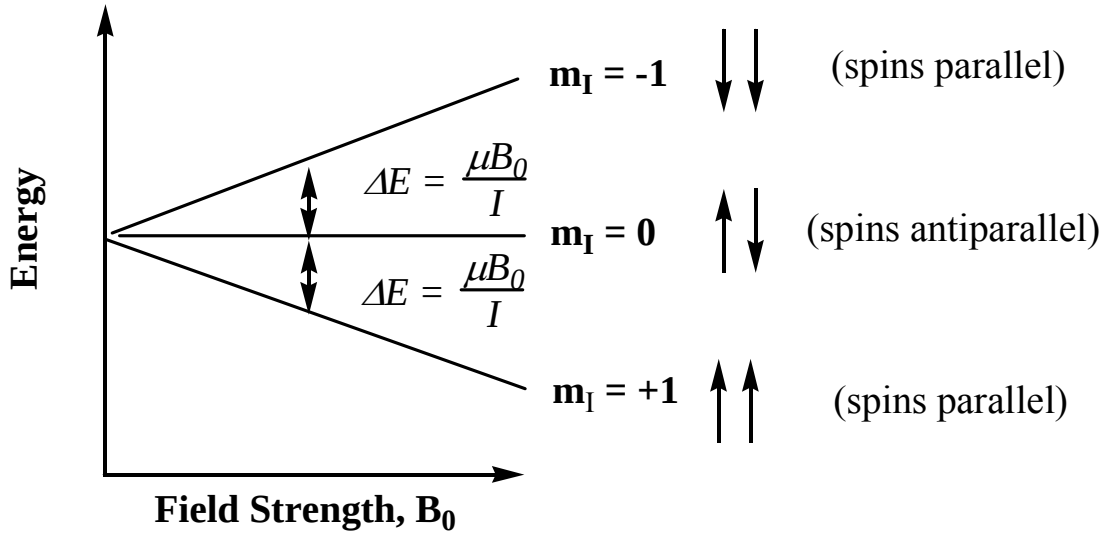


Figure 6: Spin orientation for I = 1.

within the nucleus due to the orientation of the two spins that give the nuclei the spin value of one.

1.2.9 Boltzman distribution

A Boltzman distribution properly describes the population distributions of nuclei in the different spin states m_J that result when spin active nuclei are placed in a magnetic field. Slightly more nuclei will be in the lower energy spin state, which is referred to as the α state except when the magnetogyric ratio for that nucleus is negative.

The generic equation that describes the population difference between these states is therefore:

$$\frac{N_{upper}}{N_{lower}} = e^{-\Delta E/kT}. \qquad \textbf{1.8}$$

The energy difference between the spin states m_J is dependent upon the magnetic field and spin value through the following equation:

$$\Delta E = \frac{\mu}{I} B_0 \qquad \textbf{1.9}$$

where the μ term is known as the nuclear magneton, or nuclear moment. I is the spin of the nucleus and B_0 is the magnetic field strength.

An interesting detail about the population difference is revealed by substituting the energy difference into the Boltzman equation for a nucleus of spin-½. The difference in energy becomes $2\mu B_0$ by substituting $I = ½$ into

$$\Delta E = \frac{\mu}{I} B_0 = 2\mu B_0. \qquad \textbf{1.10}$$

When the previous equation is substituted into Boltzmann equation for ΔE the resultant equation is

$$\frac{N_{upper}}{N_{lower}} = e^{-2\mu B_0/kT}. \qquad \textbf{1.11}$$

When solved, this equation illustrates how similar the populations actually are for hydrogen atoms in a 400 MHz field at 300K. The number of nuclei in the lower state is 150,001 and in the upper state is 150,000.[30] This small population difference is irrelevant

to NMR spectroscopy because this is the equilibrium state and NMR spectroscopy measures energy released from relaxation after states are excited to non-Boltzman distributions.

The energy separations between these spin states can be related to frequency; therefore, if the energy separations between the spin states for each isotope are known, the related resonance frequency of these nuclei can be determined. Because the energy difference is dependent upon the nuclear moment of a specific nucleus, one of the factors used to determine this value is the magnetogyric ratio. Values for this ratio are empirical and tabulated in the literature.[50]

The relationship between frequency, magnetogyric ratio, and field is given by:

$$\nu = \frac{\gamma B_0}{2\pi}, \qquad \textbf{1.12}$$

derived from:

$$\Delta E = \frac{\mu}{I} B_0 \qquad \textbf{1.13}$$

$$\gamma = \left(\frac{1}{\hbar}\right)\frac{\mu}{I} \qquad \textbf{1.14}$$

$$\hbar = \frac{h}{2\pi} \qquad \textbf{1.15}$$

and

$$\Delta E = h\nu\,. \qquad \textbf{1.16}$$

The frequency noted in equation 1.12 is known as the Larmor frequency and is the frequency of the radiation that must be applied to induce a transition and change the population differences of the spin states of nuclei. The Larmor frequency is specific to every isotope and since the magnetogyric ratio is positive for most nuclei, the Larmor frequency is negative and has a clock-wise direction.

Nuclei resonate on a frequency detected by the NMR instrument when non-Boltzman populations of spin states are allowed to relax to thermal Boltzman distributions. Without the presence of a magnetic field, nuclear spin are oriented in all directions with varied origins. When a magnetic field B_0 is applied as illustrated in Figure 7, the possible nuclear spins align only in allowed orientations respective to the

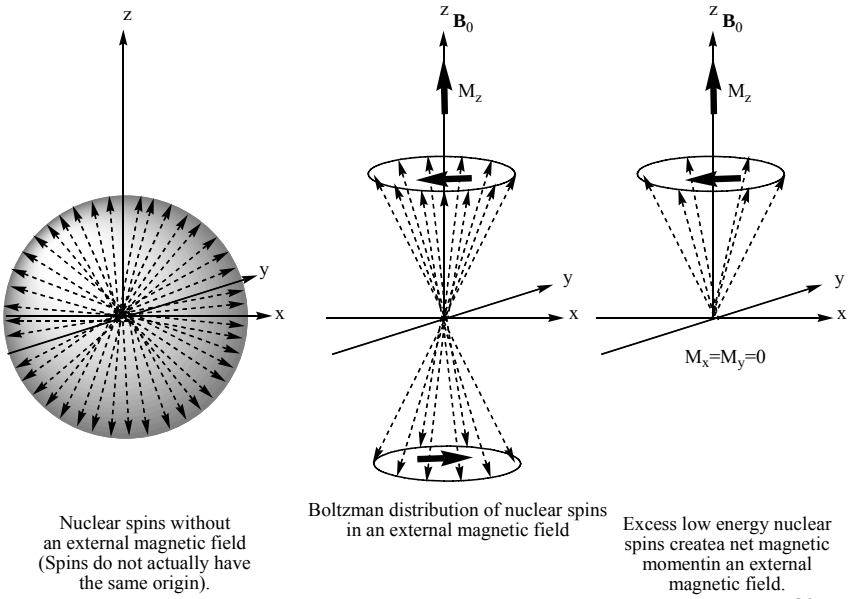


Figure 7: Spin states without and with a magnetic field.[30]

magnetic field due to quantization of space inherent in the quantum description of angular momentum. The lowest energy spin state will have an excess of population of spins and will create a net magnetization vector as they precess.

1.3 Factors affecting detectability of the nucleus

1.3.1 Magnetogyric ratio

Although the spin of the nucleus is one of the most important factors provides the most fundamental factor as to whether the nuclei will be detectable in a magnetic field, another important factor is the magnetogyric ratio of the nucleus. The magnetogyric ratio is a nuclear specific proportionality constant indicating the ratio between the magnetic moment of the nucleus and the angular momentum.

The equation that expresses the ratio of spin and magnetic moment is

$$\gamma = \frac{2\pi}{h}\left(\frac{\mu}{I}\right) = \frac{1}{\hbar}\left(\frac{\mu}{I}\right). \qquad \textbf{1.17}$$

Both the spin I and magnetic moment μ are vectors; therefore, the magnetogyric ratio is positive when the vectors are parallel and negative when they are anti-parallel. Most nuclei have magnetogyric ratio values that are positive. This sign will affect coupling which in turn affects as well as how nuclear spins exchange energy during relaxation. Magnetogyric ratios for spin-active nuclei are often listed with spin values in several reference texts. One of the largest nuclear magnetogyric ratios is that of hydrogen and has a value of $26.7520 \times 10^{7} \text{radT}^{-1}\text{s}^{-1}$.

1.3.2 Natural abundance

Given the isotope dependence of nuclear spin, the natural abundance of the isotope in question plays a major factor in the detectability of the nucleus. Spin-active nuclei that are either monoisotopic or have a predominant single isotope include ^{1}H, ^{19}F, ^{31}P, and ^{103}Rh. However, the natural abundance of an isotope is not the sole governing factor of detectability.

The first nucleus detected *via* NMR was hydrogen. The high natural abundance and magnetogyric ratio in addition to a spin value of $I = ½$ were all factors that allowed this to be the first easily detected nucleus. The natural abundance of the hydrogen atom is 99.99%. Additionally, this nucleus is abundant in organic chemistry and thus had importance as a nucleus in that field.

In contrast to hydrogen, the carbon nucleus has one spin-active isotope, ^{13}C, which has a low natural abundance of 0.011%. As a result, the carbon nucleus is much more difficult to detect than hydrogen and many techniques are currently applied to maximize the signal and circumvent this problem. Although natural abundance was not the only factor limiting this nucleus, it is still a good illustration of the importance of natural abundance.

If there are detectable percentages of several spin active nuclei, the nuclear peaks will integrate to reflect the natural abundances of each spin active isotope. Most of the time, the Larmor frequency difference of the energy of the nuclear states of these isotopes are very different, and the magnet must be tuned to one of the many possible frequencies

for detection; therefore, the observation of both isotopes in the same frequency range is unlikely without an extremely large window.

An important event occurs when the observed nucleus couples to nuclei in which there is more than one abundant spin active isotope. The resultant coupling between multiple isotopes leads to a phenomenon known as satellites. These are small symmetric peaks observed on either side of the signal from the most abundant isotope. Satellites can make spectra appear to be more complicated but rich with information. This case will be discussed more thoroughly in section 1.4.6.6.

1.3.3 Resonant frequency

Another trait of a nucleus that will influence its detectability is the resonant frequency of the nucleus. In some ways, this is an instrumental limitation; nevertheless, it is a factor limiting the detectability of the nucleus. Certain frequencies are too low for observation using current spectrometers without a great deal of extra instrumentation. The energy difference between the different spin states in nuclei varies tremendously depending on the isotope and type of atom. Additionally the difference in these spin states will be related to frequency. When the energy difference between states is very small as is the case for rhodium, the signals from the observed nucleus are easily saturated and, at low frequency, can be complicated by cavity resonance. When the energy difference for a particular nucleus is very similar to the frequency of another nucleus, detectability problems also arise and different probes are used distinguish these isotopes. This commonly occurs for hydrogen and fluorine.

1.3.4 Relaxation

The natural relaxation of the nucleus within a particular environment is the final factor that influences detectability. Quadrupolar, dipole-dipole, as well as CSA relaxation if too fast or too slow can limit detection of an observed nucleus. Relaxation will be discussed later.

1.4 Magnetic interactions

1.4.1 Magnetic fields

When a detectable nucleus is placed in an instrumental magnetic field B_0 the nuclei are affected by that magnetic field so that they split into nondegenerate spin states. Although uniform on the macroscopic scale, each nucleus has uniquely different magnetic environments on the local scale. These unique local environments are due to additional magnetic fields B_X already present around the nucleus. B_X will represent the local magnetic field of the nucleus and does not include B_0, which is the magnetic field due to the magnet and B_1 which is the induced magnetic field caused by an RF current for the purposes of nuclear excitation.

The additional fields can be due to one or a combination of several factors, which include:

- electronic factors,
- spin interactions,
- molecular shape,
- molecular motion.

These interactions cause unique magnetic environments dependent on the molecular configuration as well as the instrumental field, which give rise to different frequencies, or chemical shifts. They are extraordinarily important because they offer a tremendous amount of information about the secondary structure of the molecule. Without these interactions, the fine structure of the molecule would be very difficult to discern. Figure 8 can be used for comparison purposes. Illustrations of each of these types of interactions are shown in Figure 9, Figure 10, Figure 11, Figure 12, and Figure 13. These different interactions are ranked in terms of strength in the following order: quadrupolar coupling > dipole-dipole coupling > chemical shift anisotropy > scalar coupling > spin rotation. The order of appearance is in terms of strength with the exception of spin rotation, which is placed after dipole-dipole coupling due to the length of the two remaining types of electronic interaction.

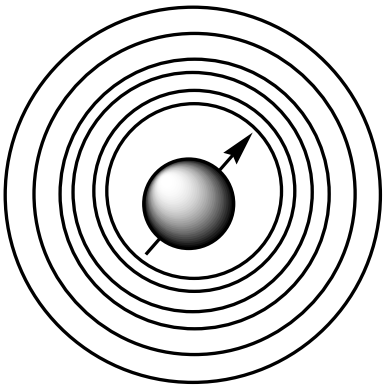


Figure 8: Nucleus and electron cloud.
This figure assumes no interactions and is for comparative purposes.

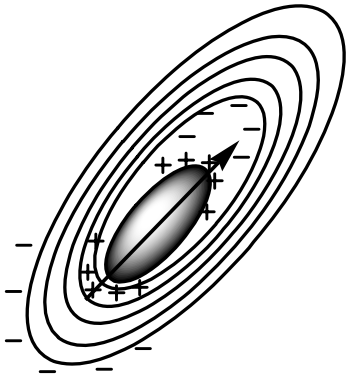


Figure 9: Electric-quadrupolar coupling.
$I > ½$ aspherical nuclear positive charge density interacts with the electron cloud.

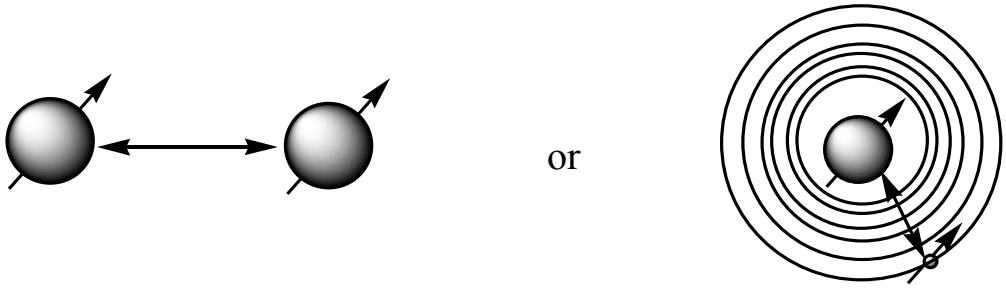


Figure 10: Dipole-dipole coupling.
Nuclei are mutually affected as each nuclear spin interacts with the magnetic moment of the other or a nuclear interacts with an unpaired electron *(paramagnetism)*.

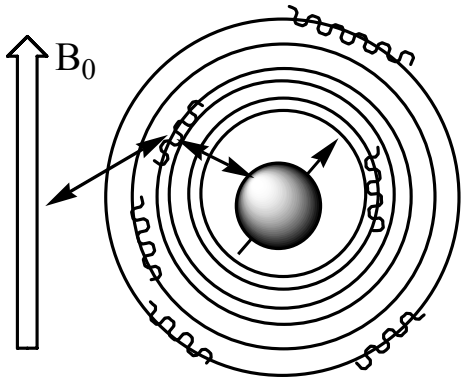


Figure 11: Chemical shift anisotropy.
The magnetic field interacts with the electron cloud, which interacts with the nucleus.

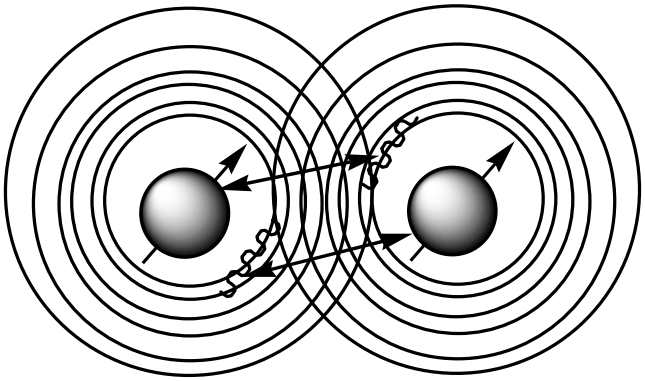


Figure 12: Scalar coupling.
Two electron clouds interact causing indirect interaction with each nucleus.

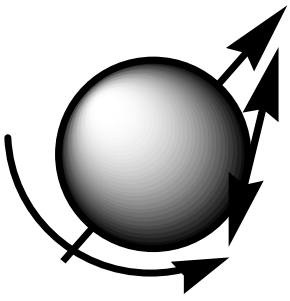


Figure 13: Spin rotation interaction.
Nuclear rotation disturbs molecular bonds. Magnetic field interacts with the nucleus.

1.4.2 Electric-quadrupolar coupling

Electric-quadrupolar coupling only occurs with nuclei that have $I > ½$. Quadrupolar nuclei have aspherical shapes, which can be prolate or oblate. Examples are given in Figure 14. These distorted shapes produce irregular concentrations of positive charge in the nucleus, giving rise to a quadrupole. This deformation of charge interacts with the electric field gradient present in the electron cloud of a low symmetry bond. The coupling occurs due to the magnetic interaction between the aspheric charge density of the nucleus and the electric field gradient or EFG.

In the solid state, both quadrupolar coupling and dipole-dipole coupling generate specific magnetic fields, B_X; however in the liquid state, the magnetic fields average to zero because the orientation of the aspherical nuclear charge density changes as it tumbles in the liquid state. The electric field gradient has the likelihood of having any number of directions or strengths at a certain point in time. The nucleus may experience comparatively strong fields instantaneously; however, the sum interaction over all rotations will be null so that quadrupolar coupling does not affect the nuclear shift at excitation or equilibrium. It does however effect the relaxation of the system. This will be more thoroughly investigated in the relaxation section. This is not to say that these magnetic fields are not important because they can profoundly influence the relaxation of the molecule. In general, the relationship between the spin I_j and quadrupolar frequency, ω_j in isotropic liquids is as follows:

$$\hat{\mathrm{H}}_j^Q \cong \omega_j^Q \left(3\hat{I}_j^2 - \hat{I}_j \cdot \hat{I}_j\right) \qquad \omega_j^Q = 0 \qquad \textbf{1.18}$$

1.4.3 Spin active nuclei interaction: dipole-dipole coupling

Dipole-dipole coupling occurs when the magnetic moment of the nucleus interacts with intra or intermolecular spin active nucleus or an unpaired electron. The substance must be paramagnetic for an interaction with an unpaired electron to be possible. In general, the dependence of the dipolar interaction on the interdipole angle, ϑ, and the distance, r, is:

$$E_{\text{dipole}} \propto \frac{\left(1 - 3\cos^2 \vartheta\right)}{r^3}. \qquad \textbf{1.19}$$

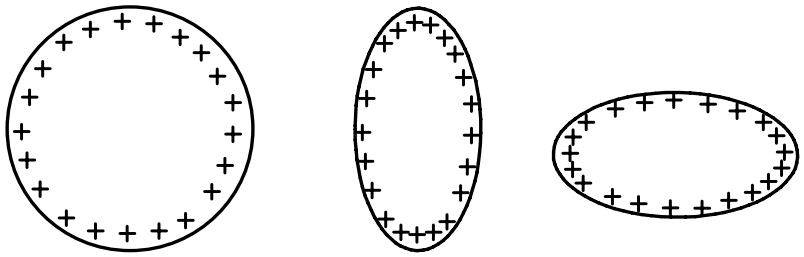


Figure 14: Nuclear shapes.
Spherical ,*left;* prolate ,*middle*; oblate, *right*.
The positive charge is concentrated at the curvatures in nonspherical shapes causing an electric quadrupole.

The induced magnetic field is locally strong but due to rapid molecular motion, these interactions average to zero at equilibrium. In solution, this process does play a major role in relaxation time though it does not contribute to the chemical shift. In solids, where there is no general averaging, the dipole-dipole interaction is significant in both aspects of the spectrum. The effect on relaxation in solution will be described more thoroughly in the relaxation section.

Another version of dipole-dipole coupling occurs in paramagnetic substances, which have an unpaired electron. These unpaired electrons interact with nuclei in a similar manner to another nucleus due to the magnetic moment of the electron. This will be discussed more thoroughly in section 1.6.1.5.

1.4.4 Spin rotation interaction

Each atom and therefore molecule is composed of both positive and negative charges in the bond. In solution, these species rapidly rotate which slightly disturbs the negative electrons in the bonds. An induced magnetic field occurs as they interact with the positively charged nucleus. The induced field interacts with the magnetic moment of the nucleus.

In general, spin rotation also does not affect the chemical shift of the nucleus due to rapid molecular motion, which averages the induced magnetic field to zero as long as the sample is at room temperature. Spin rotation is affected by temperature; therefore, the strength of the induced magnetic field B_X can become a factor at extremely low

temperatures causing a chemical shift change; indeed, the molecular motion slows such that spin rotation is not averaged.

When all other coupling is weak, spin rotation coupling plays a role in the relaxation of spectra for both standard and VT NMR; however, a stronger influence in thermodynamic NMR is the internal motion of the molecule.

1.4.5 Electronic interaction: chemical shift anisotropy

There are several electronic interactions in a magnetic field. The first involves disturbance of electrons by the magnetic field resulting in a change in the effective field at the nucleus and this is termed the chemical shift anisotropy. The second involves disturbance of electrons by electrons of other nearby nuclei resulting in scalar coupling.

Electrons anisotropically circulate around the nuclei that they bind together generating a local unique magnetic field around each nucleus in the molecule. This phenomenon is known as chemical shift anisotropy or *CSA* and allows some nuclei, which have a lot of electron density to be shielded while allowing other nuclei with very little electron density to be deshielded. When compared to a standard value, the degree of shielding or deshielding becomes measure of chemical shift δ. This refers to the central position of the peak due to spin state energy differences. The field created by the electrons influences the frequency of the energy difference between the states of each nucleus in a molecule; therefore, the amount energy released as nuclei relax to Boltzman distribution after excitation is theoretically unique with respect to nuclear environment. This implies that if a molecule contains several atoms of the same isotope but they are in different chemical environments, they should have unique NMR resonances with respect to different environments although there are exceptions to this phenomenon.

Nuclei that are near to electronegative elements either through space or through bonds have a more dramatic chemical shift. Electronegative nuclei, regardless of their spin activity, withdraw electron density from nearby atoms generating a stronger magnetic field around the electronegative nucleus. When this happens in a strong magnetic field, B_0, the increased and decreased magnetic fields, B_X, influence the position of the resonance of the nucleus in question. The electronegative nucleus is typically

shielded by electrons in this field whereas nearby atoms with lower electron density has lowered electronic magnetic fields causing them to be deshielded.

Another related type of shielding and subsequent chemical shift that can occur is when the observed nucleus is near to one or more bonds that contain a greater amount of electron density than a single bond. Double, triple, resonant, and aromatic bonds can have a stronger induced magnetic fields B_X than single bonds within the instrumental magnetic field B_0. These induced magnetic fields directly affect the chemical shift. This is due to electron currents that exist around these bonds. When the effects are due to aromatic molecules such as benzene, it is known as the ring current effect. Figure 15 illustrates some examples of these electronic currents and their subsequent magnetic field effects.

Chemical shift is a function of the strength of the instrumental magnetic field, B_0 and is expressed most often in units of *ppm* or Hz. The use of *ppm* standardizes the chemical shift with respect to any instrumental magnetic field because it is the frequency of the shift with respect to a standard divided by the frequency of the applied magnet. This conversion is valid because the degree of chemical shift is influenced by the strength of the magnetic field and the difference in energy between the states will be directly proportional to the applied magnetic field.

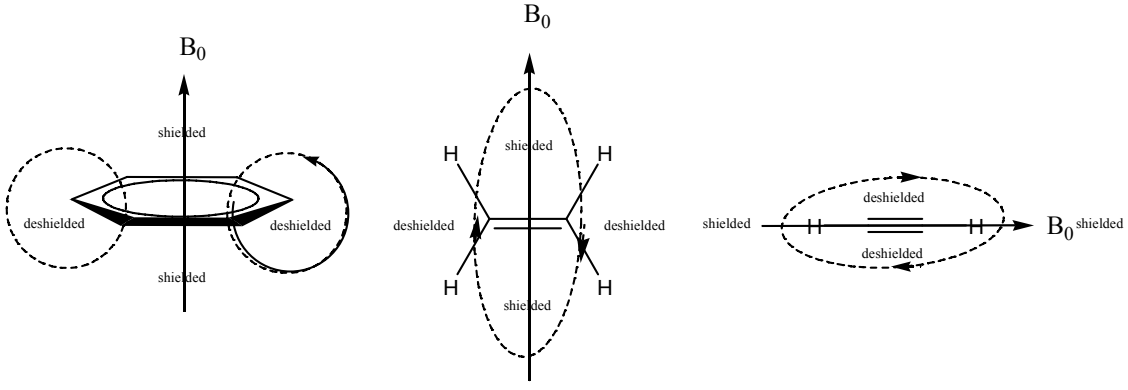


Figure 15: Electric currents creating magnetic fields.
This illustrates shielding and deshielding effects on nuclei.

Additionally, it important to note that the heavier the atom, more electrons are present in the low lying excitable electronic states, therefore, greater effects of CSA are seen for heavy atoms. The heavier atoms will be able to generate a wider range of magnetic fields, which will correspond to a wider range of possible energy differences between each atom of that isotope causing a large range of possible chemical shifts for this type of nucleus. A comparison of hydrogen to carbon illustrates this point. Organic hydrogen atoms typically have a chemical shift range of about δ/ppm 12 whereas carbon atoms typically have a chemical shift range of δ/ppm 200. Some heavy metals have chemical shifts spanning thousands of ppm in range. Several texts are available which indicate appropriate values for particular spin active isotopes in specific environments.

Another factor influencing CSA that is more noticeable in inorganic chemistry is that the oxidation state of the element also greatly affects the shielding or deshielding of the molecule. Organic hydrogen atoms, which have a formal oxidation state of +1, typically have chemical shifts ranging from δ/ppm 0 to 12. Organometallic hydride atoms, which are hydrogen atoms with an oxidation state of -1, and can have a wide range of near zero and negative chemical shifts from approximately δ/ppm 1 to -50 when the metal center has a d^n configuration. The more negative the oxidation state of an atom, the more electron density an atom has. It is most likely, in the cases of negative oxidation state, that the magnetic field due to the electronic current will be able to influence the frequency of the isotope more strongly than for elements with positive oxidation states. The effect does not always increase the shielding of the atom, in some cases other factors such as cone angle will decrease the shielding of the atom

Another related topic to chemical shift is integration. It is mentioned here briefly. When the area under the peak is calculated, it has a specific value that is relative to all the other peaks in the spectra. Integration of peaks corresponds to the number of nuclei in identical and nonidentical environments in the molecular structure. In summarization, the area under the peaks indicate how many observed nuclei give rise to a particular signal. This tool is used to determine how many particular nuclei have the equivalent or accidentally equivalent chemical shifts compared to the other nuclei in the spectrum.

1.4.6 Electronic interaction: scalar coupling *J*

The previously mentioned electronic interaction indicated a relationship between the electronic environments of the observed nucleus and its chemical shift. Additional secondary bond structure can also be obtained from a smaller magnitude scalar interaction between bonding electrons in electron clouds of atoms and bonded nuclei. This indirect perturbation, known as scalar coupling, of the electronic environment rarely changes the central chemical shift of the nucleus but it gives a great deal of information about the surrounding structure.

Scalar coupling depends on: the nature of the bonding in the molecule, the density of electrons in the s orbital which designate this bonding, as well as the magnetic moments of the two nuclei.[30] It is a result of Fermi contact. "Fermi contact interaction is a magnetic hyperfine interaction between a nucleus and an electron that approach each other so closely that they are effectively in contact".[44] This statement does not refer to intra-atomic interaction because an electron in orbit experiences its own nucleus uniformly; however, it does refer intra-molecular interaction because bonding electron will experiences a second nucleus non-uniformly.

Fermi contact is different from paramagnetic dipole-dipole interaction in two manners. First, only *s* orbital electrons, which must be found at the nucleus, can experience Fermi contact. Second, the molecule is typically diamagnetic. The net result of these contacts is an indirect interaction between two closely bonded spin-active nuclei. The Fermi contact principle indicates that although electrons in the outer shells, which are very far from the nucleus, will experience the nuclear magnetic moment as a point dipole, very close *s* orbital electrons will experience a bound nuclear magnetic moment in a non-uniform manner leading to coupling. When electron clouds interact with opposite nuclei, information about the bonding in each nuclei to which the electron clouds belong are transferred to each nucleus mutually *via* electrons.

Scalar coupling is manifested *via* splitting of chemical shifts. Two types of splitting systems can be expressed, either first or second order. Each of these types will be discussed at length in section 1.4.6.1 and 1.4.6.4. .Typically, when electron fields couple *via* scalar coupling, the nuclei within those fields are also coupling with a much

stronger value *via* dipole-dipole coupling, assuming both nuclei are spin active. The dipole-dipole coupling effect is cancelled at equilibrium due to rapid molecular motion whereas scalar coupling is not cancelled. If both nuclei are not spin active, scalar coupling does not occur between electronic clouds.

1.4.6.1 First order systems

Coupling trees are used to describe first order interactions. Examples of these are given in Figure 16. When a first order system is present, the coupling patterns are simple. First order systems are defined as systems in which all the coupling nuclei have chemical shifts differences that are on a much larger order than the coupling values. An example of a first order system is the proton spectrum of ether which has a chemical shift difference on a 300 MHz NMR of 680 Hz (δ/ppm 2.27) and a coupling value of 7 Hz.[52] *AMX* notation indicates these spins are chemically inequivalent and are coupled to one another. First order systems exhibit AMX patterns that follow Pascal's triangles as shown in Figure 17 and Figure 18. Figure 19 shows the relationship between these two concepts and includes a coupling tree for comparison. The leftmost coupling scheme in Figure 16 illustrates the manner in which Pascal's triangles describes the both the number and height of additional peaks that arise when all the coupling constants have values that are approximately equal. These figures indicate both the number of peaks observed as well as their relative intensities. The total number of possible peaks, or multiplicity, *m*, can also be determined using the equation:

$$m = 2nI + 1 \qquad \textbf{1.20}$$

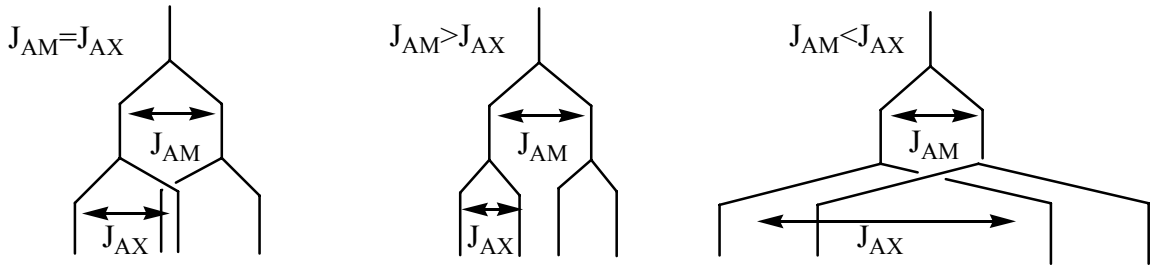


Figure 16: Coupling trees.

N	
0	1
1	1 1
2	1 2 1
3	1 3 3 1
4	1 4 6 4 1

Figure 17: Pascal's triangle for *I* = 1/2.
N represents the number of *I* = ½ spins coupled to observed nucleus with *I* = ½.

N	
0	1
1	1 1 1
2	1 2 3 2 1
3	1 3 6 7 6 3 1
4	1 4 10 16 19 16 10 4 1

Figure 18: Pascal's triangle for *I* = 1.
N represents the number of *I* = 1 spins coupled to observed nucleus with *I* = 1.

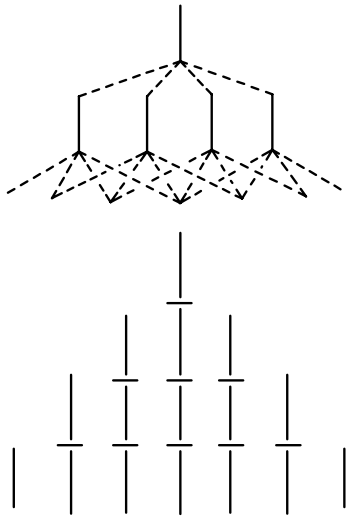


Figure 19: Relationship between Pascal's triangle and peak splitting.
This figure is the splitting pattern of an observed nucleus with *I* = ½ coupling to four other nuclei with *I* = ½.

where *n* equals the number of spin active isotopes with a particular spin value *I*. When more than one nuclear spin is present, the multiplicity due to each coupled spin is determined and then multiplied: for example, a case where two nuclei are coupled with different spin values of $I = 1$ and $I = ½$. Assuming that the quadrupole, $I = 1$ still couples strongly, the applicable equation is:

$$m_T = \left(2nI_{½} + 1\right)\left(2nI_1 + 1\right). \qquad \textbf{1.21}$$

In most first order systems an interesting effect known as roofing occurs when systems couple to one another. Instead of a symmetric splitting height, one side of the multiplet will be higher than the other side and this is called roofing. The higher side is the side nearer to the coupled nucleus. The same effect in reverse is seen in the multiplet of the coupled nucleus, which has spectral peaks which roof toward the first set with the higher side being near the coupled peak. An example of roofing is shown in Figure 20.

1.4.6.2 Karplus relationships

Although it can be very difficult to calculate the coupling constant for a set of coupled nuclei, some general information about the order of the coupling constant and generally approximate values can be discerned by comparing them to similar structures.

Karplus used an observed relationship to predict the magnitude of coupling constants for protons on organic carbon chains over three bonds to include H_a-C-C-H_b. Karplus curves are shown in Figure 21 and depend upon the dihedral angle of the bonds. An illustration of a dihedral angle is given in Figure 22. This relationship is defined as

$$J = J^0 \cos^2 \phi - 0.3 \qquad 0^0 \le \phi \le 90^0 \qquad \textbf{1.22}$$

where a typical value of J^0 is 8.5 Hz and

$$J = J^{180} \cos^2 \phi - 0.3 \qquad 90^0 \le \phi \le 180^0 \qquad \textbf{1.23}$$

where a typical value of J^{180} is 9.5 Hz.[53, 54]

The Karplus curve indicates that both the *eclipsed* and *anti* positions on the Newman projection will have the greatest coupling constant while all angles between these two states will have lower coupling constants, which are minimized at 90º. There is

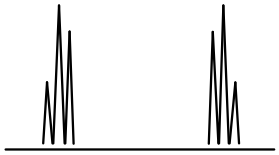


Figure 20: Roofing effects.
Without Roofing, these triplets would have ratios of 1:2:1.

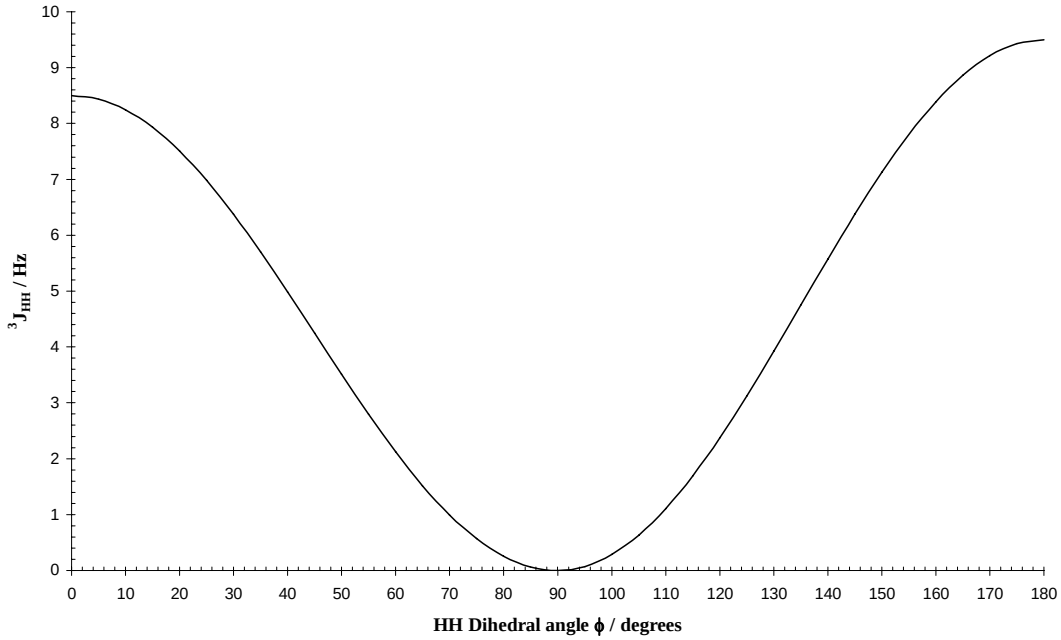


Figure 21: Karplus curves for ^3J coupling.

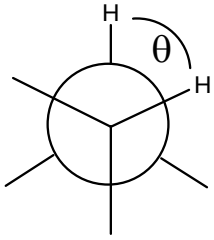


Figure 22: Example of a dihedral angle using a Newman projection.

also a different Karplus curve used to determine the coupling constant of the H_a-N-C-H_b bond of amines based on the dihedral angle also.

1.4.6.3 Equivalence: magnetic vs. chemical

Although there may be several types of nuclear spins in a molecule, not all of these spins will be unique. When nuclei are chemically equivalent, they must be the same isotope and have the same chemical shift. This does not necessarily mean that the spectral peaks for these nuclei will be observed as identical. Chemical shift equivalence indicates the position of the center of the signal, not the coupling patterns. Only when a species is magnetically equivalent will the spectral peaks be observed as identical.

Chemical equivalency is dictated by the symmetry of the molecule in question; when two chemically identical nuclei are related by a symmetry operation, they are chemically equivalent. Examples of two types of species that are chemically equivalent are shown in Figure 23. The first species possesses a mirror plane. Several mirror planes also exists for the second species. It is important to remember that nuclei involved in molecular rotation often have a mirror plane; however, some molecules, which do not have mirror planes, average their positions on a molecular scale through motion.

Magnetic equivalence is a type of chemical equivalence so the conditions for chemical equivalence must be met and additionally these nuclei must have identical coupling constants.

Referring back to Figure 23, if one assumes that *X* is a spin active nucleus, then this species will be magnetically equivalent if both protons couple to each nucleus in the same way with the same value. This would mean that the *trans* coupling between H_a and X_b must be the same value as the *cis* coupling between H_b and X_b. *Trans* and *cis*

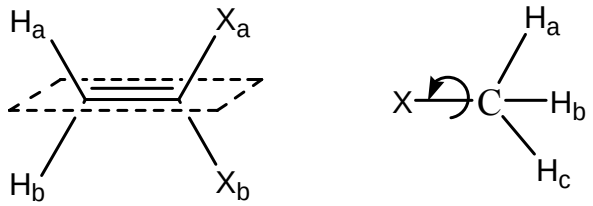


Figure 23: Molecules with chemically equivalent protons.

coupling are rarely identical so the first species in Figure 23 has chemically equivalent protons but magnetically inequivalent protons. Instead of identical peaks, the peaks will have a second order $[AB]_2$ coupling scheme. The second species in Figure 23 is both magnetically equivalent because each proton will couple to the *X* nucleus with the same coupling constant and chemically equivalent due to molecular averaging.

There is a unique short hand notation used to designate coupled systems. If two chemically equivalent but magnetically inequivalent protons bond to two chemically equivalent but magnetically inequivalent nuclei then the notation indicates that only one chemical shift is present by using only one letter but including a subscript of "2." The spin system notation for the species in Figure 23 is therefore $[AB]_2$, which is second order. When species are magnetically equivalent, a subscript after each letter is necessary identifying the number of nuclei that are magnetically equivalent; therefore, the spin notation for the second species is A_3X. When two protons are in different spatial environments so that they are chemically inequivalent but accidentally have the same chemical shift, they would appear to be chemically equivalent. The notation which expresses this type of situation is AA'BB' and it indicates that the nuclei are accidentally equivalent.

1.4.6.4 Second order systems

Second order systems result when the magnitude of coupling is on the same order as the chemical shift difference. These systems exhibit ABC patterns versus AMX patterns and are much more difficult to discern from the spectrum itself. These second order systems are highly dependent upon the magnetic field due to the dependence of chemical shift on this field. At low magnetic field, two spins that have the nearly the same chemical shift with a coupling constant of the same size, appear to be a singlet. At a higher strength magnetic field, the same chemical shift has a different chemical value, which may be slightly larger than the actual coupling constant causing a quartet.

Eventually, with strong enough magnetic field, a doublet of doublets dependent upon the chemical shift difference results when the chemical shift is almost on a different order from the coupling constant. These spectra can therefore be forced towards first

order behavior if placed in a higher magnetic field, which increases the chemical shift difference but does not affect the coupling constant. As an aside, the reason that at low field, a singlet is seen instead of a doublet is that at that field, the center of the doublets never completely coincides but instead overlaps to form a broadened singlet.

1.4.6.5 Diastereotopic nuclei

A unique configuration of species which initially appear as though they should be chemically equivalent but are actually not occur when two apparently chemically equivalent atoms are bound to a chiral nucleus. This is not a form a magnetic equivalence because the nuclei are actually not chemically equivalent. They can have completely different chemical shifts. This occurs due to nearby molecular structure. The structure of the surrounding molecule causes the environments of the nuclei to be different. An example is given in Figure 24

Diastereotopomism is predominantly noticed in organic chemistry with species that are a part of $CH_2R'R''$groups or are CH_2R_2 groups which are bound to a chiral carbon atom. It is most often the result of hindered rotation on the part of the chiral center or the diastereotopomers. The hindered rotation of the chiral center leads to a dominant rotomer, which on average gives each of the diastereotopomers different environments thus causing different chemical shifts. The *tert* butyl group and the phenyl group presumably hinders the rotation of the carbon-carbon bond such that one of the protons H_a mostly has the environment near *X* while the other proton H_b is not influenced by the *X* environment. This causes each proton to be chemically equivalent.

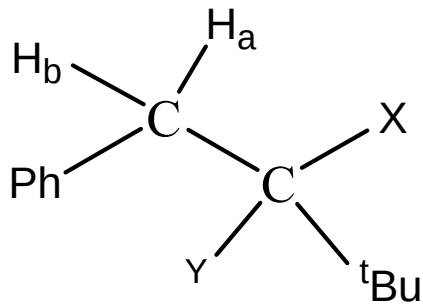


Figure 24: Diastereotopic protons.

1.4.6.6 Satellites

When nuclei couple to other nuclei that have more than one spin active isotope, satellite peaks can appear. Satellite peaks are called satellites because they often involve additional coupling to nuclei with low natural abundance causes them to have a smaller height than the main signal. They are most often symmetrically located on either side of the main signal. Satellites occur more often in organometallic molecules than organic molecules. Even in organic chemistry, satellites in ^{1}H NMR due to coupling between the observed hydrogen nuclei and the 1% abundant ^{13}C nuclei can be observed.

A good example of satellites is presented in the molecule $[PtMe(PMe_2Ph)_3][PF_6]$ which has three distinct proton signals. One is due to the methyl group attached directly to the platinum nuclei, one is due to both of the methyl groups in the PMe_2Ph group *trans* from the methyl groups and the last signal represents the remaining PMe_2Ph groups and is integrated to twice the value of the previous methyl groups. If the coupling from the 100% spin active and abundant ^{31}P nuclei is removed by decoupling, the peaks should appear as singlet peaks. In actuality, doublets that are 1/3 the height of the central signal reside on either side of the singlet peaks due to coupling with the 33% abundant ^{195}Pt nucleus. These doublets are the satellite peaks.

It is important to note that coupling constants do vary depending upon the position of a substituent in certain environments such as a benzene ring. For example, when a two protons couple in a benzene ring, they will couple as doublets; however, the coupling constant of those doublets may be very different due to different scalar coupling values between electron clouds. *Meta* coupling protons will have scalar couple with a value of 1 Hz due to scalar coupling whereas *para* coupling protons have a value of 3 Hz. Ortho coupling protons have values in the range of 6-8 Hz. The difference in these coupling constants is not only related to bond distance but also is related to the electronic current resulting from the planar aromtacity of the ring as shown earlier in Figure 15.

1.5 Relaxation from excitation

1.5.1 Manipulation of spin populations

Bloch diagrams, which illustrate the effect of different degrees and variations of pulses on the net spin magnetization, which will be discussed in this section, are shown in Figure 25 and Figure 26. Nuclei resonate on a frequency detected by the NMR instrument when non-Boltzman populations of spin states are allowed to relax to Boltzman distributions.

To disturb the Boltzman distribution of spin states, a temporary radiofrequency pulse B_1 is applied to the nuclei already aligned in the magnetic field B_0 of the instrument. This radiofrequency current produces an oscillating magnetic field, which is in the range of the difference in energy of nuclear spin states and has an exceedingly smaller magnitude than that of the magnetic field.

In actuality, the energy released from relaxation is rarely a result of a single simple relaxation from a non-Boltzman spin state to a Boltzman spin state. There are two types of relaxation that influence the signal emitted from the nuclei as well as other factors such as internuclear spin-spin coupling which complicate the energy diagrams.

1.5.1.1 Pulse width

Often referred to the as the 90º pulse, the pulse width can also be applied as 180º and 270º pulses which can be applied singly or as a series of pulses. Changing pulse widths is necessary for some 2D NMR techniques; however, in the case of a 90º pulse, the pulse width is the period of time it takes to perturb the spins so that they are changed by 90º from their original orientation in the magnetic field.

The pulse width is short with a wide range of frequencies appropriate for the nuclei being observed. The range is necessary considering that not all of the spin active atoms of the same isotope in the sample will have exactly the same frequency due to bonding and environment. The longer the pulse, the more monochromatic it is. Pulses that are monochromatic are not going to disturb all of the observed isotopes in a sample and may not actually disturb any of them unless that monochromatic frequency happens

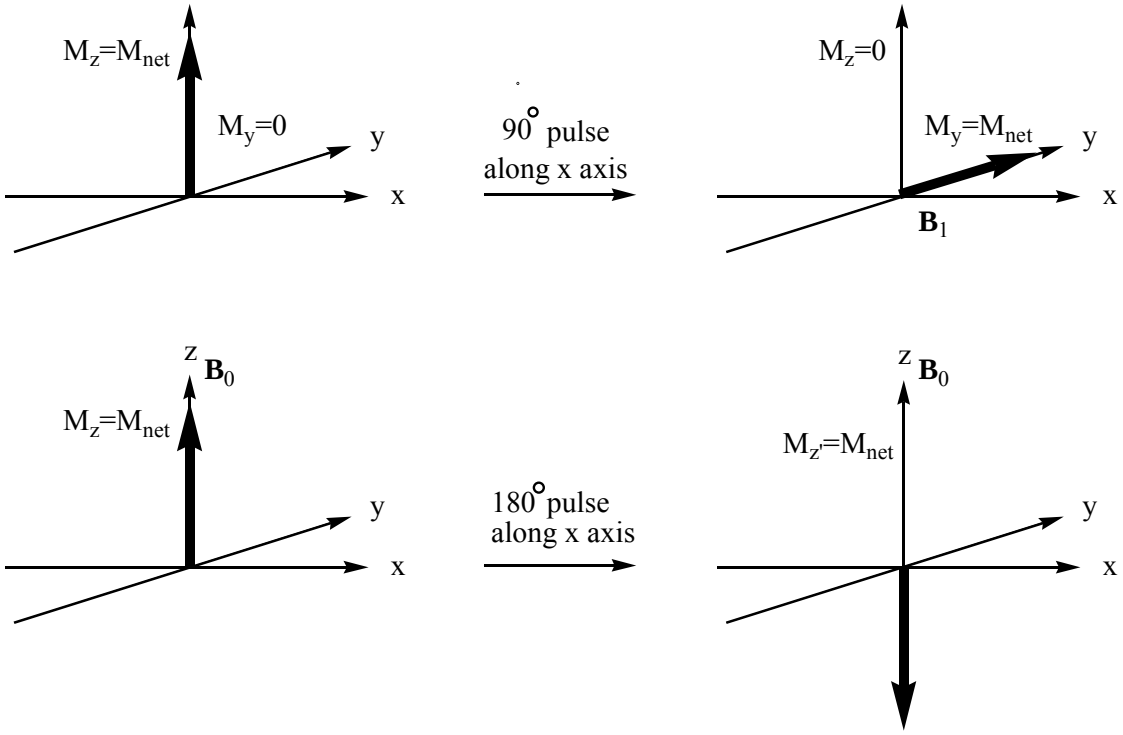


Figure 25: Variable pulses.

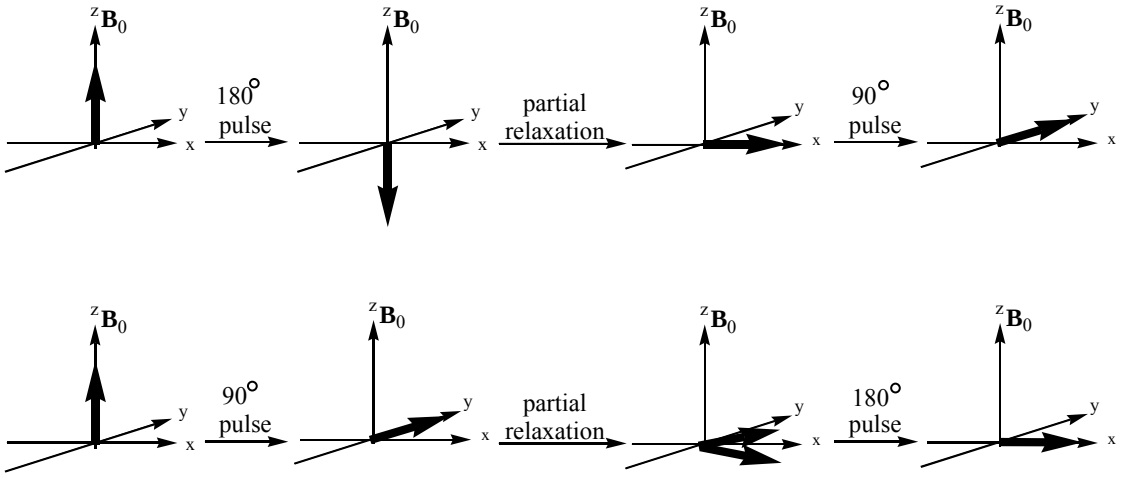


Figure 26: Combination pulses.

to be the same as one of the types of isotopes in a sample; therefore, a short pulse is preferred.

1.5.1.2 Spectral width

The spectral width is the oscillating range of the applied magnetic field B_1. This range should be appropriately large enough to encompass all the spin state energy differences including coupling effects for all the observed nuclei in a molecule. This width is known as the Nyquist limit. When spectral widths are not wide enough, peaks that appear outside of the energy range but that may have been slightly disturbed will be placed within the given window at incorrect positions. This phenomenon is known as folding and can lead to serious interpretation error. It is more practical to use a large spectral width when initially collecting and then minimize it rather than initially to collect data with a very narrow window.

1.5.1.3 Spin transitions

As previously mentioned in section 1.2.9, spin transitions must be induced between nuclear spin states separated by energies governed by the Schrödinger equation. These transitions as well as relaxation must occur for nuclear magnetic resonance detection; hence, both the number of possible states as well as rules governing these transitions must be well understood.

The total number of nondegenerate spin states that a particular ensemble of nuclei project in a magnetic field is equal to 2J+1. This value is based on the previously mentioned equation: $m_J = J, J\text{-}1, J\text{-}2 \ldots n$. Relating this equation specifically to nuclear spin by substituting I for J, results in the total number of spin states:

$$m = 2I + 1 \qquad \textbf{1.24}$$

For example, hydrogen nuclei which have I=½ have a total of 2(½) + 1 = 2 states and these are the +½ and -½ spin states. The previously mentioned equation is not to be confused with equation 1.20 in section 1.4.6.1 which describes multiplicity as: $m = 2nI + 1$. This is a different equation used to describe the total number of peaks that will be observed for coupled nuclei.

It is because these different energy separations exist that electromagnetic radiation of certain frequencies can be used to perturb nuclei thus causing transitions between these states in specific nuclei. Selection rules describing transitions resulting from excitation that accompany these equations can now be outlined. Assuming no spin coupling occurs, the applicable transition rule is that $\Delta m_I = \pm 1$. When spin coupling with other isotopic nuclear spin states occur, the additional transition rule is $\Delta I = 0$, which implies that no transitions are allowed between antiparallel and parallel coupled, spin states. Figure 27 illustrates these transitions and for comparative purposes, Figure 28 illustrates allowed relaxation transitions, which will be discussed shortly.

1.6 Nuclear relaxation

Nuclear relaxation is inversely proportional to time:

$$R = \frac{1}{T} \text{ .} \qquad \textbf{1.25}$$

An excited nucleus can relax two ways and they are compared in Figure 29 and Figure 30. They are important because they both contribute to the overall relaxation of the

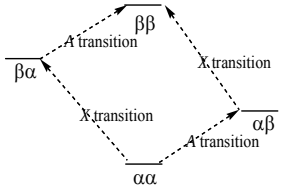


Figure 27: Allowed transitions in an AX system.
The βα and αβ notations are meant to indicate pure states but are combinations of states.

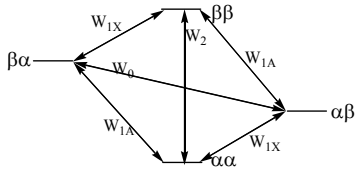
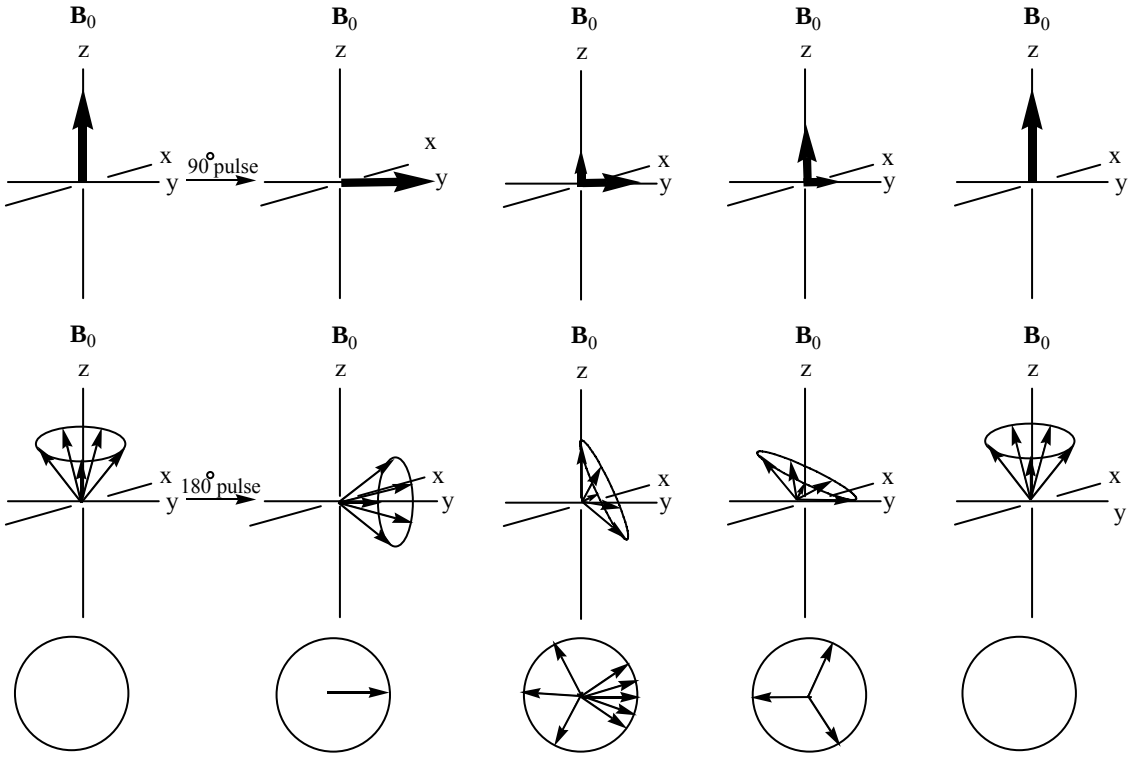


Figure 28: Allowed relaxations in an AX system.
Depending upon the relaxation mechanism, certain transitions will dominate.



(Down z axis view of x,y plane)

Figure 29: Transverse relaxation T_2.
Spins fan in the xy-plane as well as return to the z-axis.

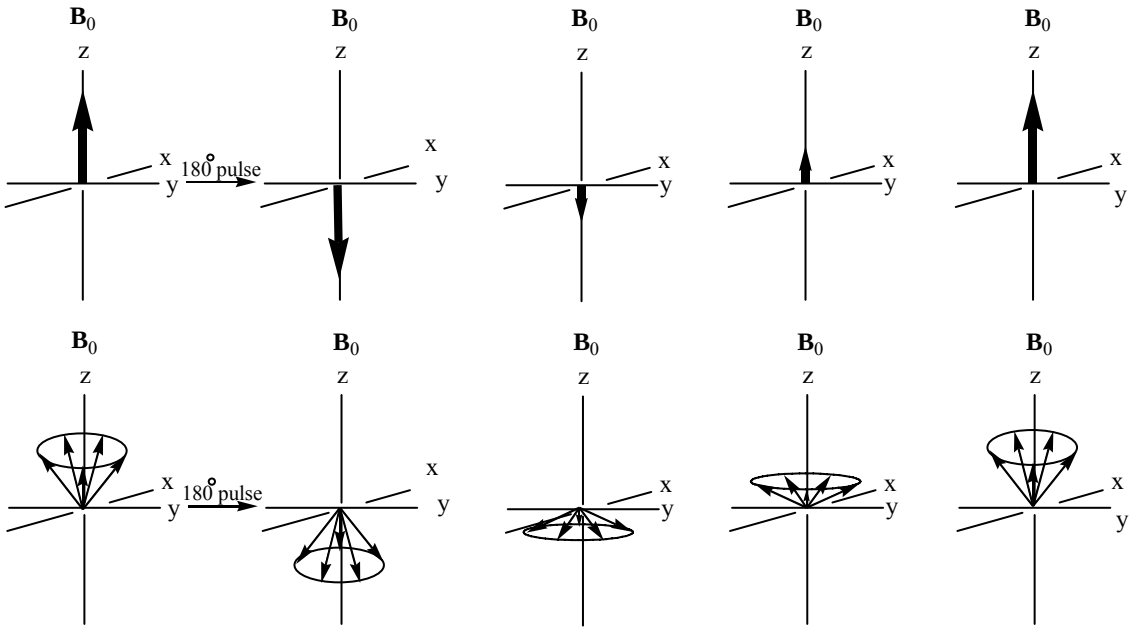


Figure 30: Longitudinal relaxation T_1.

sample. T_1 relaxation, also known as longitudinal relaxation or spin lattice relaxation, occurs as the nuclei are inverted within the M_z axis. Magnetism is generally assumed to be along the *z*-axis although magnetism can be induced in other axes. When the spins realign over a period of time within that single axis, it is known as T_1 or longitudinal relaxation. This type of relaxation would be present after any pulse but another type of relaxation can work in concert with it. This other type of relaxation is T_2 relaxation, also known as transverse or spin-spin relaxation magnetization. T_2 relaxation occurs in the M_{xy}-plane perpendicular to the M_z axis as the spins "fan" and lose coherence in the xy-plane but continue to realign in with the M_z axis due to T_1 relaxation. T_2 cannot be longer than T_1.

1.6.1 Mechanisms

In order of dominance, the four types of mechanisms that influence relaxation are: quadrupole>dipole-dipole>chemical shift anisotropy>spin-rotation. Although scalar coupling can affect relaxation, it usually has a very small effect. Quadrupolar relaxation is only applicable when nuclei have $I > ½$ because the non-spherical shape of the nucleus greatly influence the relaxation of the molecule.

1.6.1.1 Quadrupolar relaxation

Quadrupolar relaxation is a result of electric-quadrupolar coupling and generally increases as *I* increases and affects the longitudinal T_1 relaxation. It is dependent both upon the electric field generated at the nucleus as well as the actual spin value of the nucleus. In most cases, both the electric field and *I* are large enough that the quadrupolar nuclei relax so quickly that most of the coupling information is not observed and a singlet results. In general, fast relaxation leads to very broad peaks due to a short rang of time that corresponds to a large range in energy. Obviously, with larger *I* values, there are more spin states possible which makes transitions between these states more complicated as well as increases the number of possible transitions thus allowing the nuclei to relax more quickly.

The other reason that the nuclei relax so quickly is that the electric field at the nucleus is coupled to the nucleus causing rapid changes in the magnetic moment of the

nucleus as the molecule rotates in solution with respect to the magnetic field. Without excitation, this coupling does not play a role in relaxation because the local magnetic field is averaged through the molecular motion. The spin vector has a fixed relationship with the major axis of charge density, so that physical reorientation of the nucleus due to the EFG also reorients the nuclear spin which causes rapid relaxation. The relaxation arises when the nuclei are excited; the local magnetic field competes with the instrumental magnetic field causing shifting of nuclear spin states. When a local magnetic field competes with the instrumental magnetic fields, the energy difference between these states is in constant fluctuation.

Because quadrupolar nuclei change orientation very quickly, causing a fluctuating magnetic field, the energy applied to induce transition is lost rapidly; and all coupling information is averaged. When both I and the electric field are somewhat small as is the case for deuterium, the relaxation is slow enough to be easily detected but not as slow as for $I = 1/2$ nuclei. A broad peak, which contains some coupling information, is observed for quadrupolar nuclei that relax with neither fast nor short time. As an aside, the speed of relaxation for quadrupolar nuclei is also dependent upon the molecular geometry of that atom.

When other nuclei are coupled to quadrupolar nuclei through dipole-dipole coupling, they are also often broadened because the coupled nuclei cannot couple very well when the nuclear spin states shift quickly.

1.6.1.2 Chemical shift anisotropy relaxation

Chemical Shift Anisotropy is also a type of longitudinal T_1 relaxation and although CSA coupling is averaged to zero in solution, it still plays a role in relaxation. Although there is some CSA relaxation for all types of molecules, except in the cases noted, it typically is not strong enough to compete with the dipole-dipole relaxation. CSA relaxation is only important for nuclei that have many electrons surrounded by a larger electronic field such as in the case of transition metals. The large field leads to a large energy difference between states and thus a large chemical shift range. In these compounds, electronic clouds create a strong local magnetic field, which gives the

molecules other pathways to relax. The electron cloud in these large nuclei has high anisotropy, which means different properties develop depending on the direction.

For example, a molecule containing d_{z^2} orbitals has an anisotropic electronic field because there is a lot of electron density along the z-axis but less along the x and y-axis. Although CSA in this type of molecule is a less dominate effect than quadrupolar relaxation, the relaxation principles are similar. The electric field around each nucleus creates local magnetic fields, which are strong enough to compete with the magnetic field of the instrument. These fields affect the relaxation of the molecule but only play a significant role when quadrupolar relaxation is not present and when electron dense nuclei are observed. The magnetic field fluctuations also increase the relaxation of the molecule. This relaxation does depend on the instrumental magnetic field. Since it is dependent upon the instrument's magnetic field, it becomes more important with high field magnets. CSA relaxation is considered an advantage when it increases some of the otherwise long relaxation times of these types of molecules.

1.6.1.3 Spin rotation relaxation

As a molecule rotates in solution, two types of motion can be distinguished: both the orientation of the molecule τ_c as well as the orientation of the angular momentum τ_{SR} of the nucleus. They are related *via* this equation:

$$\tau_c x \tau_{SR} = \frac{I_{rot}}{6kT} \qquad 1.26$$

where I_{rot} is the moment of inertia of the molecule and T is the temperature of the solution. When all other relaxation is low and the molecules spin quickly enough in solution to slightly disturb the bonding mechanisms and create a small magnetic field, this type of coupling competes with the other relaxation pathways of the molecule. This particular mechanism is obviously temperature dependent thus increasing the temperature of the solution increases the strength of the induced magnetic field causing the molecule to relax faster.

1.6.1.4 Diamagnetic dipole-dipole relaxation

Dipole-dipole coupling results from the magnetic moments of two or more nuclear interactions, which typically average to zero at equilibrium; in spite of the fact that at any single moment, an instantaneous chemical shift of up to 150,000 Hz can occur. This effect averages to zero because at any given orientation, any number of spontaneous chemical shifts can occur or not occur.

During dipole-dipole relaxation, the interaction of these spins play a major role in the relaxation of a nuclei; in fact, it is second only to quadrupolar relaxation. Dipole-dipole relaxation is dependent upon nuclear distance as well as the magnetogyric ratio of each of the spins so that spins with large ratios are more strongly correlated than small ones. It also varies with molecular size and there are limits to the relaxation process due to this interaction. The average maximum time it takes for small molecules to rotate 1 radian is about 10^{11} $rads^{-1}$. Larger molecules rotate more slowly than small molecules.

As the nuclei rotate, the positions of the nuclei randomly and spontaneously change. This causes the magnetic moments of the nuclei to interact differently affecting both the longitudinal and transverse relaxation depending upon the orientation of the spin at the time of interaction. This spontaneous though averaged magnetic field increases the relaxation rate in both the T_1 and T_2 directions where T_2 transfers energy to the T_1 relaxation process and is dependent upon it.

A variable known as the t_c is used to describe the rotational correlation time between nuclei. As long as the molecule rotates very quickly, the intensity of the relaxation is proportional to t_c. This is most often the case for low molecular weight, high temperature, and low viscosity systems. This region is known as the extreme narrowing region and within this limit, $T_1 = T_2$. Molecules with molecular weights greater than 1000 Daltons are outside of the extreme narrowing region. Outside of the limit, the relaxation times become longer and more dependent upon T_2. Longitudinal relaxation becomes less intense at higher instrumental frequencies. Transverse relaxation becomes dominate outside of this region because longer periods of nuclear interaction are facilitated with slower motion.

A very good illustration that compares dipole-dipole relaxation within the same molecule is the relaxation of CH_3, CH_2, CH, and quaternary carbon atoms. Dipole-dipole relaxation is evidenced in the shortened time and scans it takes for CH_3 atoms to appear versus quaternary C atoms, which have no dipole-dipole interaction. The magnetic field due to the hydrogen atom is very strong. Tertiary carbon atoms relax much more slowly than primary carbon atoms.

1.6.1.5 Paramagnetic dipole-dipole relaxation

Nuclei undergoing dipole-dipole coupling can be divided into two types: paramagnetic and diamagnetic coupling. In addition to diamagnetic dipole-dipole coupling with other nuclei, paramagnetic nuclei also have an additional efficient dipole-dipole relaxation. Paramagnetism results when not all electrons in a sample are paired. The magnetic susceptibility of paramagnets is stronger and positive while for diamagnetism it is weaker and negative. This means that the paramagnets pull the instrumental magnetic field inward while diamagnets push the field outwards. Diamagnetic substances do not have the additional relaxation factor that paramagnets do.

Paramagnetism is considered similarly to dipole-dipole relaxation instead of CSA relaxation because the manner of interaction is very similar to dipole-dipole relaxation. An unpaired electron has a spin of ½ and a much stronger magnetic moment than a nucleus with the same value. The nucleus and the unpaired electron interact directly. The unpaired electron has an intrinsic magnetic field, which can interact with its own nucleus as well as other close nuclei causing them to relax quickly when T_1 is short, and slowly when T_1 is long. Paramagnetic samples typically have a short relaxation time unless they are extremely large in which case, the increased time the molecule takes to relax results in reduced T_2 also causing wide line widths. This relaxation is typically very efficient.

The short relaxation times of some paramagnets known as Shift reagents have allowed them to be added to solutions that contain other compounds, which have long relaxation times. This is known as paramagnetic doping. The unpaired electron interacts with the observed compound shortening the relaxation time.

1.6.1.6 Scalar coupling relaxation

This type of relaxation only occurs when a large coupling constant exists between coupled quadrupolar nuclei and non-quadrupolar nuclei. It is typically a scalar quantity but can be disturbed if the quadrupolar relaxation with respect to the T_1 relaxation is very fast. The scalar relaxation affects the T_2 contribution and can cause line broadening to the non-quadrupolar nuclei.

1.7 Pulsing and related effects

1.7.1 Decoupling

As was discussed in section 1.4.6, the effect of scalar coupling between two or more nuclei is peak splitting. In the case of a less detectable nucleus, it is often desirable to remove the coupling to that peak to increase the initial signal intensity. This technique has two potential advantages. The first is increased relaxation *via* NOE, which leads to faster detection, and the second is a simplified spectrum. NOE will be discussed in section 1.11.4.

Decoupling occurs when a second magnetic field B_2 is applied to the coupled A nucleus after excitation to the observed X nucleus from the first field B_1. The decoupling power is turned on when the detector begins to detect the relaxation energy from the observed nucleus. For decoupling to work properly, the Lamar frequency of the nucleus to be decoupled must be much greater than the coupling value between the observed and decoupled nuclei.

1.7.1.1 Homonuclear decoupling

Homonuclear decoupling is described for systems in which both observed and decoupled nuclei are the same isotope whereas hetereonuclear decoupling describes systems in which they are different. One or multiple decoupled nuclei are placed in these types of brackets. The main use of homonuclear decoupling is to identify coupled nuclei but 2D experiments such as COSY have replaced the usefulness of homonuclear decoupling.

1.7.1.2 Heteronuclear decoupling

Heteronuclear decoupling is used extensively. At first, a single resonance was applied at a single frequency to decouple a specific nucleus. Usually, the decoupled nucleus *A*, was observed first so that the frequency of the nucleus were known. Then, a single frequency corresponding to nucleus *A* was applied while *X* is observed. This technique is cumbersome because each frequency seen in the spectrum of A nuclei must be applied independently. It allows the relationships between particular coupled nuclei to become obvious.

Broadband decoupling was used instead of single frequency to decouple all unobserved isotopes in a two-isotope system. This type of decoupling uses a series of pulses with different frequencies, which are applied very quickly in a row. This allows all the *A* nuclei to be decoupled instead of a single frequency without adding heat to the sample. Special programs are used to generate these different pulses, two types are WALTZ and GARP and they will be discussed later. Unless otherwise noted, all of the carbon spectra in this document have been broadband decoupled. Notation for observed 13-C nucleus decoupled from 1-H nucleus is $^{13}C\{^{1}H\}$.

Off-frequency decoupling describes when the decoupler emits a pulse that has a large enough frequency to decouple all the protons in a certain range. In practice, this technique requires too much energy to be used regularly. It also inadvertently heats the sample causing more variations in the magnetic field and line broadening.

1.7.1.3 T_1 and T_2 measurements

Decoupling is used to measure both T_1 and T_2 relaxation. Determination of both of these values can be used on their own or for the purposes of application to better 2D spectra. It has already been shown that a 90° pulse flips the spins into the xy-plane and that a 180° pulse flips the spins in the negative z plane. Relaxation of all spin from a 180° pulse can therefore only occur as T_1 relaxation. When a series of experiments are conducted with various delay times between pulses, the intensity of these peaks are plotted versus the delay times to determine the actual T_1 value.

The measurement of T_2 is determined *via* spin echo. A pulse sequence for this is shown in Figure 26. A single 90º pulse is applied so that the nuclei are excited to the xy-plane. Then, when a 180º pulse is applied, the spins stay in the plane but move in the opposite direction with the faster spins reaching the opposite side of the plane first. When a series of refocusing pulses are applied with different delays, the decay of these spins can be measured after each refocusing pulse. When the intensity of these peaks is plotted versus the delay times, the actual T_2 value can be determined.

1.8 Spectrometer

1.8.1.1 Modern magnet

The NMR instrument is able to produce a very strong magnetic field B_0 because it uses a superconducting solenoid magnet. This magnet is cooled by helium, which in turn is cooled in a liquid nitrogen filled glass Dewar. The current produced by these magnets can last up to 10 years before being recharged.

1.8.1.2 Modern spectrometer

Five of the most significant systems in the magnet will be discussed. These include the probe, lock, tuner, transmitter, and the detector.

The sample is inserted into the probe. It contains two types of coils, each of which are capable of applying the excitation pulse, B_1 as well as detecting the emissions from the nucleus. One coil is for ^{1}H observation and the other is for *X* nucleus observation as well as deuterium locking. The *X* nucleus typically represents any non-hydrogen nucleus. When used for direct detection, the ^{1}H coil is the outer coil and when used for indirect detection, the ^{1}H coil is the inner coil. To stabilize the magnetic field, both warm and cool gases can be passed through the probe for temperature stability, so that the temperature of the sample is maintained thus homogenizing the magnetic field applied to the sample. The probe is one of the most easily damaged parts of the magnet because it contains so many glass tubes used to protect the coils. When samples are inserted incorrectly, they can break the glass tubes in the probe. Some X channels cannot

observe all possible non-hydrogen nuclei so different probes will different coils can be inserted into the instrument so probes are also removable which, if done incorrectly, can also cause damage.

The field frequency lock is used to stabilize the magnetic field with respect to the solvent deuterium signal instead of the observed nuclear sample. Between excitation pulses and relaxation collection, the deuterium nuclei in the solvent are excited and detected to moderate field variations. In this manner, field variations can be detected without disturbing the actual detected spectrum. What is known as a magnetic sweep is applied to detect the deuterium nucleus. This deuterium signal also provides a way to locked and shim the sample with respect to its solvent. When the field does not change, the output from the lock signal is zero. When the field does change, the lock has a value. Either the receiver or transmitter can compensate for the field variation depending on whether the value was positive or negative and whether or not the current needs to be increased or decreased to compensate for it. The operator of the instrument does not have to start this operation; it is programmed to occur naturally.

Not all instruments have tune and match rods but they become necessary the higher the field strength of the magnet. It is often necessary to tune and match the resonant frequency of both the proton and *X* nuclei in the sample. The effect of tuning and matching the magnet is fine-tuning the frequency range of applied magnetic current, B_1 or the decoupling current, B_2. Although individual values will vary, the tuner allows for the average of all the protons in the same to be tuned. It is dependent upon the actual sample in the spectrometer and is directly influenced by the solvent.

Transmitters and detectors are both wired to the coils in the probe that produce the B_1 oscillating magnetic field. The transmitter introduces R_F energy to the electric coils in the probe. It supplies current for any process in the program including the deuterium lock program that runs simultaneously with the main program. The transmitter introduces a continuous wave which is then amplified, phase shifted for the program, or shaped as a pulse before they reach the coils in the probe. The length of the pulse is determined by the pulse width or the amount of current it takes for a particular spin to shift to 90º from original alignment.

Detectors obviously detect the signal. When a nuclear frequency is detected, it actually has a value that is much higher than the frequency of the instrumental magnet. This is often too difficult to store so other techniques that are out of scope of this paper are employed to lower the frequency of the nucleus. Detectors often contain a phase corrector and filters to remove low frequency electronic noise or a high frequency nuclear input. The detector outputs a decaying wave known as a free inductive decay or *FID* which will be discussed in section 1.10.

The detectors play an important role in modulating the data. To phase the waves properly, different phase sensitive detectors are employed which are out of phase by 90º. This enables one detector to detect the sine portion of the wave while the other detects the cosine portion of the wave. There are two methods used to distinguish phase both of which rely on this principle, one is known as simultaneous quadrature detection, and the other is known as sequential quadrature detection. In simultaneous quadrature detection, both detector channels are able to store data with cosine and sine portions simultaneously so that Fourier transform can be used on them. In sequential quadrature detection, the data points are incremented by 90º allowing a single detector to be used.

1.8.1.3 Optimization of magnetic field

To achieve the most uniform, or homogeneous, macroscopic magnetic field, three techniques are employed: sample spinning, sample uniformity, and shimming. For liquid state NMR, the sample is rotated on axis at approximately 20Hz; this rotation is perpendicular to the field direction and averages inhomogeneity. For solid state NMR, the sample is rotated at a 54º angle. This technique is known as magic angle spinning and will not be discussed further.

A uniform sample is one that contains no impurities, solids, or dissolved gases. The glass from which the NMR tube is made must be uniform for high quality data. The tube must also be located in the magnet so that the bottom and top of the liquid in the tube do not distort the magnetic field. A measuring gauge, which holds the spinner and the sample, is often used to ensure that the sample will have the correct position once inserted into the magnet. One more point should be mentioned with respect to sample

spinning and two-dimensional NMR. 2D data are rarely collected when the sample is spinning. This procedure minimizes t_1 noise due to tube imperfections or an inconsistent spin over a long period of time.

A homogeneous sample is prepared by filtering the deuterated solution with a glass wool or silica plug in a pipette. Degassing is used to remove dissolved gas from the sample. To degas, the sample is frozen, then the sample is introduced to a vacuum, which is then removed. Finally, the sample is sealed and thawed. This process is repeated twice more to ensure complete degassing. Care should be taken when thawing an NMR tube. The glass is very thin and if allowed to thaw completely, the solvent will expand at a rapid rate at the bottom where the surface area is highest. This will cause the tube to break. If the sample is carefully thawed from the top to the bottom, the tube will not break.

Deuterated solvent is used so that the solvent alone does not over saturate the probe with signal. Since most solvents are organic liquids, they contain a high concentration of protons. These would otherwise appear very large and broad thus obscuring the dissolved sample's spectrum. Residual solvent peaks are due to the small concentration of undeuterated protons still in the solvent. In addition to external solvents, these residual proton peaks are also used to reference within a particular solvent. They rarely interfere with the spectrum except when the peaks fall in the same location as non-solvent peaks. Clever manipulation of solvent type can often fix this problem and introduce desirable properties to the solution such as high boiling point for VT NMR.

Shimming is the final way to produce a uniform macroscopic magnetic field. There are actually two sets of shimming coils but only one set can be modified by the instrumental operator. These coils are outside of the probe and R_F frequency current passes through them. The frequency of these coils can be modified so that any remaining electric field gradients are cancelled. Shimming techniques can be quickly taught but are only learned with experience. These coils are: zero, first, second….nth order. They are used to fine-tune the magnetic field. This technique is one of the most powerful for obtaining good spectra. Often instruments also allow coarse and fine adjustment of these particular coils. Most current instruments also have computer-aided shimming such as

shim mapping. Shimming maximizes the lock signal. Other parameters such as lock field lock gain, and lock phase also help to maximize the shim.

1.9 Data manipulation

1.9.1.1 Noise

Noise results from two types of thermal motion: electron movement in the coils and ion movement in the sample. Noise is a major problem that must be removed for good spectral resolution. To remove noise, narrow spectral windows, multiple scans, and statistical techniques are often all applied.[55] A narrow spectral window minimizes the size of the FID while maximizing the number of data points in the spectrum. Multiple scans add NMR signals to the FID but do not add additional noise do to the positive/negative nature of noise. Statistical methods used to reduce noise will be discussed soon.

Several mathematical techniques can be applied to the FID before transformation to improve line shape. One of the major problems inherent in the decay of a nuclear signal is that the intensity begins much stronger than the noise of the spectrum but as it decays, the signal to noise ratio decreases dramatically. At the end of the FID, mostly noise is present and this often affects the line shape of the sample. Mathematical data manipulation has become a standard tool used to fix this problem

1.9.1.2 Exponential multiplication

The time domain of the FID is the T_2 relaxation. Exponential multiplication digitally multiplies the data by a decaying exponential function k:[30]

$$k = e^{-\frac{t}{T_2}}. \qquad \textbf{1.27}$$

where t is the time for each point in the FID and T_2 is a constant based on the actual value of the T_2 relaxation. This significantly improves the signal to noise ratio but increases the line broadening. It is effective because it increases the shape of the signal that is

decaying but does not increase the shape of the noise due to the fact that it is not decaying thereby decreasing the noise at the end of the signal.[30]

1.9.1.3 Lorentzian-Gaussian correction

Lorentzian correction digitally improves the resolution of the spectra by transforming the naturally Lorentzian line shape to a Gaussian line shape, which sharpens line shape. The transformation is:

$$k = e^{-\frac{t}{T^*_2}} e^{-bt^2} \qquad \textbf{1.28}$$

where t is the time for each point in the FID, T^*_2 is inputted as a negative number, and b is a positive constant. Unfortunately, this transformation can add false peaks to the spectrum if the FID contains wiggles.[30]

1.9.1.4 Zero-filling

Zero filling is a mathematical process that allows NMR experiments to be terminated sooner than the actual time nuclear spins take to decay fully while maintaining resolution by increasing the signal to noise ratio. Zero-filling replaces the numbers as the end of the FID with zeros after the signal to noise ratio decreases to a certain value. This removes noise and improves linewidth.[30] It is advantageous in that it decreases noise and line width but has the disadvantage that when applied incorrectly, it can remove information from the FID.

1.9.1.5 Linear predication

Linear predication is a different mathematical process that like zero-filling removes the noise from a spectrum by cutting the FID when the signal to noise ratio reaches a certain limit. Then, the data are fitted to a linear prediction to modify the noise content of the spectra. It is a better method than zero filling and but is only useful when there is both a high signal to noise ratio as well as many more points than a typically 1D FID will give. It is used more often with 2D and 3D NMR. This type of prediction can also be applied backwards if the detector begins detecting before the last pulse finishes.[30]

1.9.1.6 Sine-bell weighting

The previous two corrections are typical 1D corrections but the sine-bell weighting is used specifically for 2D corrections and can be unshifted, shifted, or squared depending upon the type of experiment and resultant data. Two-dimensional experiments will be discussed in section 1.12. It is used in 2D experiments because the data are often truncated. It is a method used to complete the data set and increase the resolution by multiplying the signal by a sine bell weighting factor.[30]

1.10 Fourier transforms

1.10.1.1 Free induction decay

The information gained from detectors from signal relaxation is known as a FID or free induction decay. The signal will be strongest at the beginning of the FID and mostly white noise by the end. A FID has positive and negative absorptions, which decrease in magnitude. Mathematical transformation of these data are necessary to convert that data from the time domain to the frequency domain.

1.10.1.2 Transform

Although there are many different types of ways to process FIDs, the most widely used is the Fourier transform. The mathematics in this section will not be discussed in detail but some pertinent equations will be included.

The Fourier transform has the following format:

$$A(\omega) = \int_{-\infty}^{+\infty} A(t) e^{-i\omega t}\, dt \qquad \textbf{1.29}$$

where $A(\omega)$ is the intensity of the signal as a function of frequency, $A(t)$ is the intensity of the FID as a function of time and I is $(-1)^{1/2}$.[56] Substitution of the identity of $e^{-i\omega t}$ leads to

$$A(\omega) = \int_{-\infty}^{+\infty} A(t)[\cos(\omega t) - i\sin(\omega t)]dt \qquad \textbf{1.30}$$

Further separation into two integrals leads to:

$$A(\omega) = \int_{-\infty}^{+\infty} A(t)\cos(\omega t)dt - i\int_{-\infty}^{+\infty} A(t)\sin(\omega t)dt \quad \textbf{1.31}$$

where the first part of the equation represents the *real* portion, or absorption curve, of the FID and the second part represents the *imaginary* portion, or dispersion curve, of the FID.[56] In actuality, the *real* portion starts in phase with the detector and this is why the spectra earlier reported to be a summation of the cosine waves. The *imaginary* part of the FID starts 90º out of phase. An interesting feature of this technique is that the solution to the transformation actually appears as two peaks mirrored on either side of zero, or located at the same frequency but at opposite signs.[56] Only one side of the peak is necessary to interpret the spectrum and the other part is not shown.

The transformation assumes that the signal is exactly in or out of phase with the current. The validity of this assumption is difficult to test because there is a delay between the production of the induced magnetic field and the data collection. The two components can be phase corrected by separating the two parts of the spectra. Each peak may contain a mixture of adsorption and dispersion peaks and the correction is carried out point by point through the data. In actuality, this process has been computerized and is quite simple to perform. The computer uses two multiplication equations which assumes that each peak contains both adsorption and dispersion components.

new disp =(old disp) cosθ - (old abs) sinθ. **1.32**

new abs = (old abs) cosθ + (old disp) sinθ[56] **1.33**

All FIDS will contain signals and white noise. Theoretically, white noise should be constant and have both positive and negative components whereas signal absorption will only have positive peaks. Because the noise has positive and negative components, it should therefore average through time to be zero while the positive and negative components of the signal do cancel. This is not completely true in practice. The improvement of signal to noise with increased FID scans is improves as a factor of the square root of the number scans. This is why spectrometer scans typically increase in the form of 2^0, 2^2, $2^4 \ldots 2^{2n}$ where n = 1, 2…n. The use of multiple scans to improve signal to noise ratio is known as time averaging.

Because the Fourier transform is measured in discrete time units, the Fourier integral becomes:

$$x(n) = \frac{1}{N}\sum\left[A(n)\frac{\cos(2\pi kn)}{N} - iA(n)\frac{\sin(2\pi kn)}{N} \right] \quad \textbf{1.34}$$

where N is the number of points, n is the nth point, and 2πk converts the nth point to radians.[56] This equation is obviously simplified for a single nucleus but the principle is still the same for several nuclei. The solution to the equation results in a peak that corresponds to the frequency of the energy difference between the nuclear states of the observed nucleus.

1.11 One dimensional experiments

1.11.1 Basic pulse diagram and experiment

Pictorial diagrams are used to illustrate pulse sequences, an example of which is shown in Figure 31. The 90º and 180º pulses are actually a series of closely spaced radiofrequency pulses. These multiple pulses over a short period time have the same effect as a single pulse of one frequency. A series of pulses has the added advantage that heat and thus magnetic irregularities in not introduced to the sample. This series of pulses is represented with a solid block on the pulse diagram. The width of the block varies dependent upon the relativity to the 90º pulse width. When pulses are not a multiple of 90º, subscripted roman numerals are used to indicate the length of the pulse.[31]

The Δ symbol represents a defined delay time between pulses, the value of which is dependent upon the coupling constant of the nuclei. The length of is less than the length of time it takes for the nucleus to completely relax. Not shown in this figure is the symbol τ, which is used to signify delays that are not related to coupling constants such as mixing times. The t_2 component corresponds to the data acquisition time, which is theoretically the time it takes for the nucleus to relax completely; in practice, current data manipulation allows shorter time periods than full relaxation. In two-dimensional spectroscopy, the t_2 component corresponds to the f_2 dimension. The t_1 component

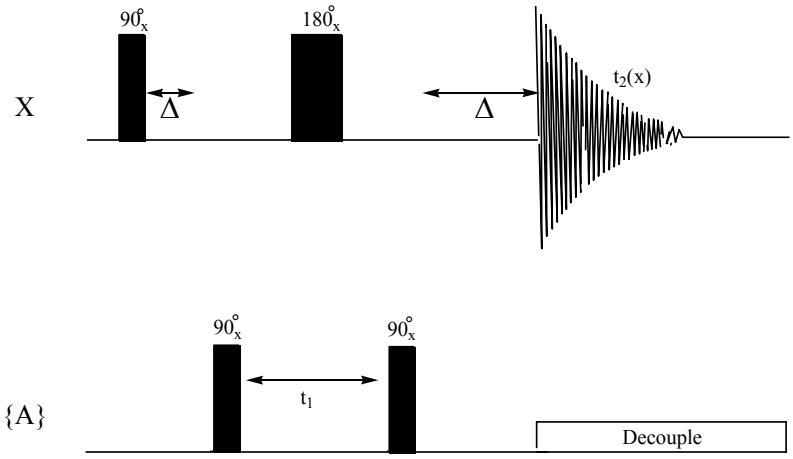


Figure 31: Pulse sequence for X^{57}.

corresponds to a specified length of time between decoupling pulses and corresponds to the f_1 dimension in 2D NMR. Although pulses are applied in a series, decoupling is for the most part applied during the collection of the FID. The basic pulse program involves a pulse intended to excite the nuclei followed by relaxation, sometimes mixing times, a final pulse and data acquisition.[31]

1.11.2 Saturation

Until this point, the use of 90º pulses has been defined as the angle used to move all spins into the y-axis from the z-axis. In actuality, it can be time saving to instead apply a series of lesser degree pulses. The reason this saves time is that the time it takes for the majority of spins to relaxation from the 90º pulse is $5*T_1$. This means that the total time period must pass and data must be collected before another pulse is applied. Smaller angles of

$$\cos\alpha_e = e^{\frac{-t_r}{T_1}} \qquad \textbf{1.35}$$

can be used to flip the pulse. This is because faster pulses than the relaxation time allow the time it takes to obtain a high-resolution spectra as $3*T_2$. Faster pulses mean that the spectrum will contain more noise and thus have broad resonances. This is known as saturation. As an aside, when unwanted signals such as such as water signals are present,

pre-saturation is used to completely broaden and effectively lower the intensity of the signal.

1.11.3 Polarization transfer

Selective polarization, or magnetization, transfer is a technique that can only be used to detect through-bond correlations with a scalar coupling value. This is different from NOE, which takes advantage of through-space dipole-dipole coupling and will be discussed in section 1.11.4.

The net effect of polarization transfer is that spin population difference in one nucleus is transferred to a second nucleus. This means that an excess of spins precessing with a certain nuclear frequency are transferred to a different nucleus and therefore precess at a different frequency thus enhancing the intensity of the new nucleus. For example, in the spin system given in Figure 27, polarization transfer would occur if the populations for $\alpha\alpha$ state were interchanged with the populations of the $\beta\alpha$ state by a weak 180º pulse at the frequency at this transition. This interchange occurs by slightly irradiating the transition frequency of this coupling.

This technique is best employed when one spin has a strong magnetogyric ratio and thus a strong magnetization coupled to a spin with a low magnetogyric ratio and thus a weak magnetization. The net effect causes a transfer of some of the magnetization from the strong to the weak spin thus enhancing the signal of the low signal nucleus. The overall effect of this technique is that in the case of an AX system with weak nucleus *X*, the doublet is for *X* is enhanced but at the expense of an inverted peak. This problem is solved in the INEPT experiment.

1.11.3.1 INEPT

INEPT is an acronym which means Insensitive Nucleus Enhanced by Polarization Transfer. Polarization transfer at a single transition does not give enhancement to all nuclei in the entire spectrum. INEPT was a method developed to increase the sensitivity of non-sensitive nuclei. . This pulse sequence is successful because a 180º pulse is applied to one channel while a 90º pulse is applied to the observed nucleus channel just

before FID collection. An example of this pulse sequence is given in Figure 32 and can be compared to the DEPT pulse sequence in Figure 33.

The final 90º pulse forces the spins that were evolving in the x,y-plane back into the z-axis at opposite angles. It does not change the chemical shift in any way but manipulates the relative populations of the *A* nuclear spin states which interacts with the carbon nuclei. This allows all the coupled protons within that frequency range to transfer their magnetization. The overall effect is that although increased in intensity, the observed nuclei appear with a partially inverted doublet. Asymmetric phase correction, refocusing, and decoupling can all be added to this pulse sequence so that the result is a strong singlet.

1.11.3.2 DEPT

DEPT is an acronym which means Distortionless Enhanced Polarization Transfer. It is similar to the INEPT sequence but there are three main differences, which include an additional *X* nuclear pulse, decoupling, and the angle of the final pulse. Like the INEPT, a pulse is applied to excite the *A* nucleus. A pulse is then applied to the *X* nucleus at the same time as a second pulse applied to the *A* nucleus causing the magnetization to evolve coherently for both spins. After a certain period of time associated with the coupling constant, a θ pulse is applied to the *A* nucleus at the same time as a 180 pulse is applied to the *X* nucleus refocusing the magnetization for the *X* nucleus while transferring coherence or polarization from the *A* nucleus to the *X* nucleus. For simplicity, the decoupler is turned on during acquisition so that instead of multiplets, singlet peaks result. For the purposes of editing, the application of these different pulse angles is independent of coupling values and cover as a range of values. The final proton pulse has an angle such as 45º, 90º, or 135º and it is allowed to evolve before collection. The exact effect is obviously different depending upon the number of coupled nuclei but this pulse sequence has the advantage that depending upon the pulse and number of spins, the resultant peak may appear positive or negative on the spectrum.

The DEPT experiments can be run singly or sequentially to gain information about the molecule. When θ = 135, all CH_3 and CH peaks will be positive but the CH_2

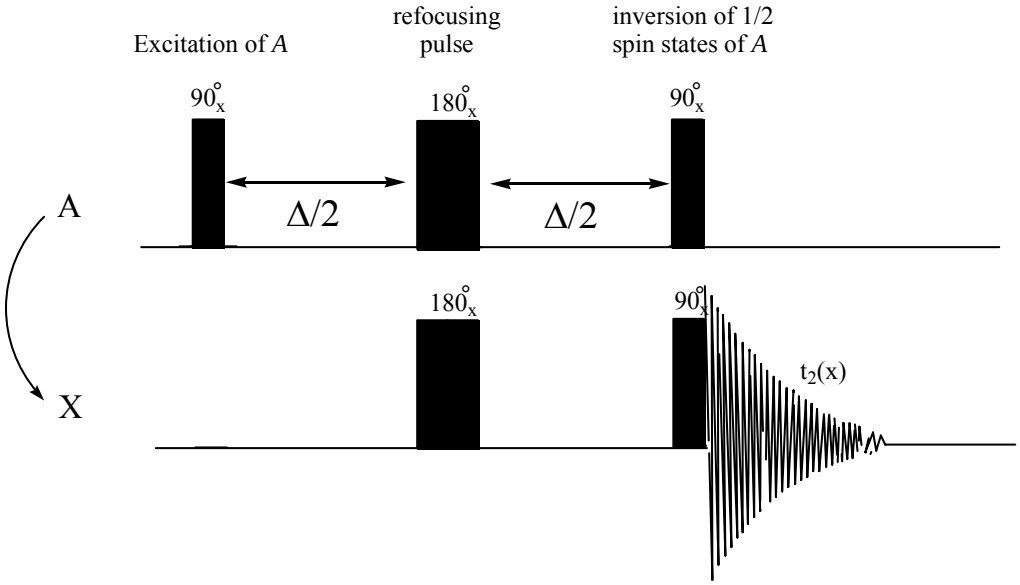


Figure 32: INEPT pulse sequence.

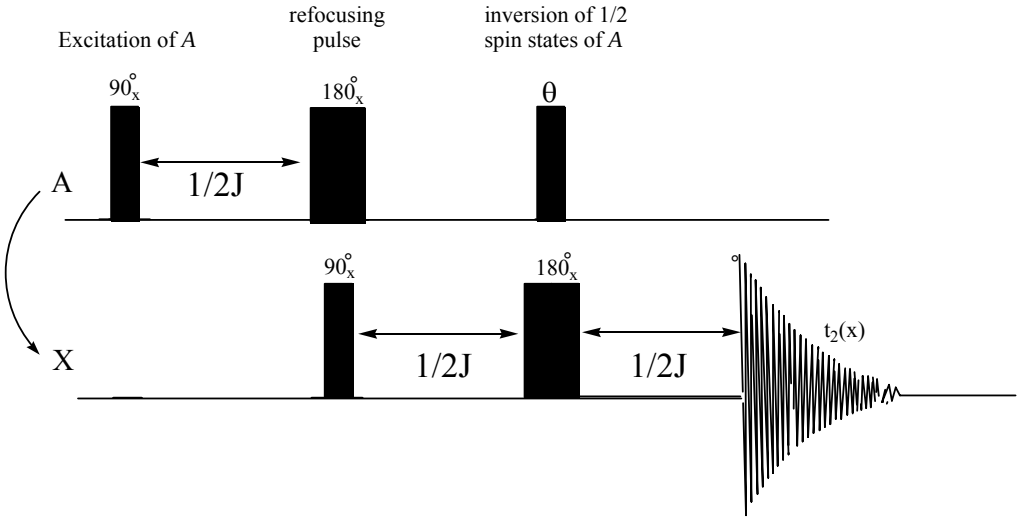


Figure 33: DEPT pulse sequence.

peaks will be negative. When θ = 90, only CH_2 peaks are left and they are positive. When θ = 45, only CH_3 peaks are left and they are positive. This phasing of peaks makes DEPT editing very useful. Often all three experiments are run sequentially, and then the computer edits the data into four separate spectra that each represents a certain type of coupled spins. When this type of editing is often employed, all of the peak intensities are positive. DEPT has the disadvantage that quaternary carbon atoms are not included because there is not polarization to transfer. A pulse sequence that includes these nuclei is known as PENDANT. Further information about this program can be referenced in Claridge[31].

1.11.4 NOE

The nuclear Overhauser effect occurs when one or more nuclei are disturbed so that they have non-Boltzman populations of spin states at equilibrium, which results in a change in the signal intensities for an entire system. This irradiation may occur on the observed nucleus or on the unobserved nucleus during decoupling. The irradiation effectively changes the population densities of each of the spin states for that nucleus which changes the preferred relaxation pathways and either increases or decreases the signal of the observed nucleus. A NOE will occur in two ways: either from equalization of spin states, which is termed *steady state* NOE, or from inversion of spin states, which is termed *transient* NOE. Both of these mechanisms are exploited and in both cases, positive and negative NOE can occur. The increased or decreased intensity of peaks result from unnatural spin state distribution relaxation pathways which are not allowed as they often correlate to a double spin flips where $\Delta I \neq 0$. The simplest case is for a two-spin system *AX* where *A* is observed and *X* is irradiated. When these spins are irradiated a double nuclear flip results in $\Delta I = 2$.

NOE terminology uses *S* to indicate the irradiated spin that is causing spin populations differences for spin *I*, which is the observed nucleus. Although the difference in symbols implies that two completely different isotopes are involved, this is not necessarily the case. NOE not only refers to saturation and transfer between two different isotopes but in fact can be used to describe the effect of NOE from a proton at

one chemical shift value with spin *S* to a proton at a different chemical shift value with spin, *I*.

NOE is dependent upon through-space dipole-dipole coupling which predominantly relies upon the T_1 relaxation mechanism. It is a technique used to measure relative or specific through-space correlations. Steady state NOE is used to measure relative correlations and transient NOE can measure specific magnitudes of correlations. The through-space dependence results because the strength of dipole-dipole coupling decreases as the distance between the spins increases. It is a fortuitous that NOE is not dependent upon through-bond correlations. When employed with other techniques NOE enhances the information gained about the molecule since most other techniques rely upon bonded relationships.

Figure 28 illustrates the relaxation pathways due to NOE. The typical relaxation pathways of this molecule are noted as W_{1C} and W_{1H}. The pathways due to NOE are annotated as W_0 and W_2. When the absorbance effect is negative, the dominant relaxation is zero quantum, W_0, and when positive, the absorbance effect is positive and the dominant relaxation is double quantum, W_2. When rapid molecular tumbling is possible, the W_2 mechanism dominates and when slow molecular tumbling occurs, the W_0 mechanism dominates. If the W_1 pathways contribute to relaxation, the effect of the NOE is lessened and is usually considered leakage pathways. This means that when other processes compete with the dipole-dipole mechanism for relaxation, the NOE is lessened. In the case of proton observance, the other competing mechanism is most often paramagnets in the sample in the form of transition metals or O_2. In relevant nuclei, another competing mechanism is quadrupolar relaxation.

1.11.4.1 Steady-state NOE: difference spectra

When a single peak is irradiated for a certain time period, a change in populations of other nuclei related through-space *via* dipole-dipole coupling occurs, this process is steady state NOE. Under optimum conditions, the NOE generates a theoretical enhancement of 50% for homonuclear and 200% for hetereonuclear coupling. In actual practice, the enhancement is often less than 5% so additional techniques are employed to

improve the sensitivity of this technique. The pulse sequence for a steady state NOE includes irradiating through the decoupling pulse, applying the excitation pulse, and then collecting data. The maximum molecular distance correlated by NOE is 4Å.

In correlation with steady state NOE, difference spectroscopy is also used to clarify the peak enhancements. A simplified illustration of this technique is given in Figure 34. The computer subtracts the non-irradiated spectrum from the irradiated spectrum. Under optimum conditions, the resultant spectrum shows positive signals when nearby nuclear states have been perturbed, no signal when no change has occurred, and a negative signal when irradiation or chemical exchange has occurred. Steady state NOE is used to distinguish stereochemical environments when other techniques cannot such as in the case of sugar conformations. It is often difficult to distinguish all of the stereochemical positions of the nuclei due to the similarity and overlap of coupling constants. In these cases, irradiation at a particular *up* hydrogen will identify other nearby *up* protons in the spectrum.

A problem often associated with steady state NOE can occur when the nucleus that is irradiated has a chemical exchange process with another nucleus causing both

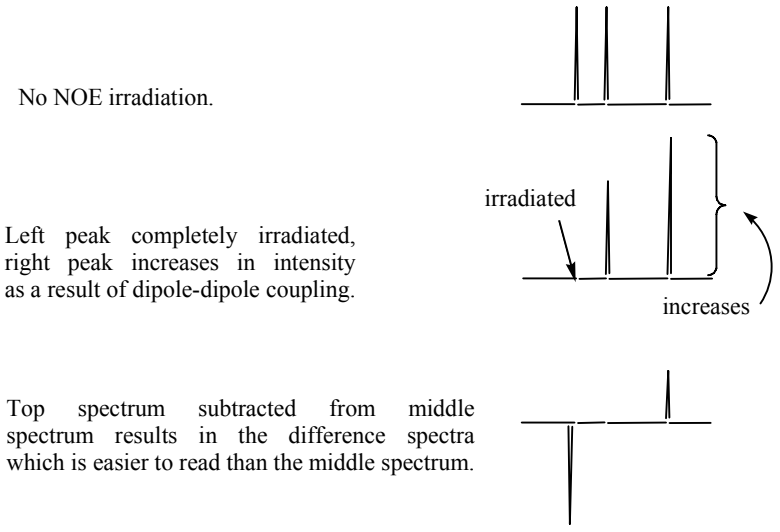


Figure 34: NOE difference spectroscopy.

nuclei to be irradiated. The effect can be such that nuclei with different through-space correlations exchange causing both protons positions to be enhanced regardless of whether both protons are in close proximity to the irradiated peak. If this exchange process is expected, transient NMR should be used instead of steady state NMR.

There are other potential problems with steady state NOE. In the case of two coupled peaks A and B, which are in close proximity, irradiation upon A may have an effect on B which is not of the same magnitude as the effect of the irradiation upon B on nucleus A. This is because each of these nuclei is in different environments and relaxation mechanisms that lower NOE effects are dissimilar. Additionally, if there is a very near neighbor with a similar energy difference, irradiation can be inadvertently transferred to this neighbor causing erroneous results. If the irradiated peak has a lot of scalar coupling, this steady state NOE results can be unreliable because it is difficult to irradiate a series of peaks with the same frequency; however, irradiation can be cycled through the multiplet frequencies if necessary.

1.11.4.2 Transient NOE: NOESY

In transient NMR experiments, not only is the target saturated, the spin states of that target are inverted. After a time period of allowed NOE build up, a 90º pulse is applied and the data are collected.

Although a 1D version of this experiment is known, the most widely used is the 2D version for which close protons show correlations whereas protons that are greater than 4 Å apart do not show correlations. The time it takes for the NOE to build is known as the mixing time. To identify near nuclei, the mixing time should be less similar than T_1.

The biggest problem associated with both types of NOE discussed is in the zero-crossing region, when the molecule has a weight of 1000-2000 Daltons. In this case, the tumbling rate is approximately the same as the observable frequency. Another difficult region for the NOESY is for molecules less than 200 Daltons because NOE in this region are smaller and take longer periods to build up.

1.11.5 Thermodynamics

Both thermodynamic and kinetic motion can be determined from NMR studies. Variation of temperature measures the former and variation of time intervals measures the latter.

Dynamic molecular motion covers a range of motion including intermolecular exchange, intramolecular conversions, intramolecular motion, and isotopic/nuclear exchange. This motion is inherently dependent upon temperature so that generally, faster motion happens at high temperature and slower motion happens at low temperature. When chemical exchange occurs on a fast time-scale, all coupling information is lost and peak positions are averaged. Certain molecular exchange processes occur quickly at room temperature that very low temperatures are required for the individual peaks to be distinguished.

1.11.5.1 Nuclear exchange

Nuclear exchange causes line broadening. It occurs in molecules such as alcohols causing protons attached to oxygen atoms to move from one molecule to another. Peak broadening results due to exchange of protons between systems that have spins that are not completely in the same phase. The difference in phase slightly changes the frequency so that it has slightly different values and becomes broad. When reagents are added to the system to increase the nuclear exchange, the line sharpens because the peaks are averaged. This occurs in the fast exchange region.

Another result of nuclear exchange is the change in chemical shift due to changes in electronic environments. For example, concentrated alcohols have extensive hydrogen bonding whereas diluted alcohols have very little hydrogen bonding. In fast exchange, the average of the signals is only a single visible peak. A fine feature of this result is that this exchange between environments is also dependent upon temperature because it is related to molecular motion. As motion increases, the chemical environments become more similar as the hydrogen bonds are averaged throughout the molecule. The chemical shift is more shielded and as the tumbling slows, due to lower temperature, the

environments become more dissimilar and the averaged chemical shift becomes more deshielded.

Line width in these cases can be used to determine the rate of exchange, k, for a given species. The equation that describes line width is

$$\left(W_{\frac{1}{2}}\right) = \frac{1}{\pi T_2} + \frac{k}{\pi}. \qquad \textbf{1.36}$$

This equation allows for calculation of the exchange rate by plotting the line width at half height versus the inverse of the time. Accurate integration is necessary for this to work. The value of *k* is determined from the y-intercept and it is the rate constant.

The activation energy of a complex can be based on the Eyring theory used

$$\Delta G^{\pm} = RT\left\{23.759 + \ln\left(\frac{k}{T}\right)\right\}. \qquad \textbf{1.37}$$

A plot of ln(k/T) vs. 1/T gives a straight line that can be used to determine the ΔH and ΔS values.

1.11.6 Kinetics

Reactions can be monitored until they finish or slowly reach equilibrium using NMR. In many cases, reaction progress can be effectively charted because many starting materials have different peak positions than the resulting product. The reaction rate must be slow enough at a specific temperature for monitoring. The rate of scrambling can also be determined. Typically, the starting materials for these reactions are placed in an NMR tube, solvent is added, and the tube is placed in the probe with an equilibrated temperature. When a series of reactions are followed at various temperatures, the rate of conversion or exchange can be plotted as a function of time. This process also allows intermediates to be noticed and characterized.

1.11.6.1 Molecular conversion

Interconversion between isomers is a major chemical phenomenon, which is dependent upon temperature. The amount of each isomer present at particular temperature is often important. Polarization transfer can be used to distinguish these

isomers at temperatures above the coalescence temperature. The coalescence temperature is the temperature at which the molecular motion is on the same order as the NMR time scale.

1.12 The second dimension

When discussing Fourier transforms, it was evident that a 1D experiment contained both frequency and intensity information. The dimensionality of an experiment however only refers to the total number of frequency dimensions; therefore, the previously mentioned experiments were one-dimensional. With two frequency dimensions, the experiment is considered two-dimensional, regardless of whether it is homonuclear or hetereonuclear. 2D NMR also contains intensity information; thus, extensive Fourier transforms are necessary to interpret this data. The second dimension inherently increases the number of points in a spectrum and therefore the data size.

Although two dimensions require two frequencies, only one channel collects a FID in these experiments. Information of both dimensions is when a large series of FIDS with evolution times, which are plotted as a contour map. If the evolution time was zero, there would be no time for spin precession and the signal would be zero. On the other hand, if the time were exceedingly long, the signal be zero due to complete decay. There exists a period of time between these two extremes however that the build up and release of spin precession is visible in the form of a sine wave and when plotted together has the scheme of a three dimensional peak which is wide at the bottom and narrow at the top. When applied to a system with several spins in different environments, each particular spin will only appear in small particular ranges of evolution times, which can be correlated to the frequency of the second nucleus.

The real advantage of two-dimensional NMR is that pulse programs incorporate either polarization transfer or NOE into the sequence; therefore, varied t_1 increment allows transfer between two different nuclei; which reveals the coupled, distance, or exchange relationship. These correlations are known as cross-peaks and they indicate a relationship between peaks. In addition to crosspeaks, homonuclear 2D NMR

experiments also contain a series of peaks on a diagonal, which corresponds to the 1D spectrum.

The second domain is artificially generated as a function of intensity since the second nucleus is not directly observed but rather passes information on that is observed in the main nuclear channel; therefore, the series of time increments is important as long as they are in a particular range. More important is that NOE or polarization transfer creates a second dimension that actually corresponds to the frequencies of the other nucleus. The frequency of the t_1 time domain therefore relates to the f_1 domain of the unobserved nucleus.

In homonuclear systems, the terminology "unobserved" is a misnomer because only one nucleus is observed. In this case, one domain is observed and the second is generated; the combination of which allows for correlations between the nuclei.

1.12.1 Two dimensional techniques

1.12.1.1 Spin lock sequences

Spin-lock sequences are used to keep protons from relaxing during precession. A typical spin-lock sequence begins with a 90º pulse followed by a series of 180º pulses with extremely short intervals between them. It is a way to maintain magnetization so that it will travel further distances before relaxation.

1.12.1.2 Phase cycling

Phase cycling is used to improve the quality and continuity of the FID and is used in many NMR experiments. When phase cycling is applied, the R_f signal strength does not change but the phase of the signal is altered for each transient or scan. It has been reported that this improves the data by increasing the coherence of the data so that any unwanted transitions cancel.

1.12.1.3 Pulse field gradients

The Pulse Field Gradients, or PFGs, are imposed magnetic fields that defocuses and then refocuses the net magnetization in the sample. The effect is that like phase

cycling, the unwanted transitions are removed and only good data remains. This was a development in the 1990's which lead to shorter 2D experiment times. It is important because 2D experiments are inherently prone to noise, artifacts, and other problems which dilute an already weak spectrum. This refocusing minimizes the amount it takes to do these experiments and tremendously increases the quality of the data. In pulse sequences, gradient fields are indicated with as a curved shaded block. An illustration of the effect of applying a gradient field to a set of spins is given in Figure 35.

1.12.2 Bond correlations

Certain two-dimensional experiments such as COSY, TOCSY, HSQC, and HMBC are designed so that polarization transfer between coupled nuclei occurs. This may be limited to two or three bond distances or with the addition of mixing times, correlate over longer distances. These techniques elucidate the long-range bond structure and therefore go a long way to finish the correlation.

Polarization transfer affects the observed nucleus. Then, another pulse transfers a portion of its spins to the unobserved nucleus. The remaining spins will precess at a certain t_1 value according to its own frequency which corresponds to its 1D chemical shift

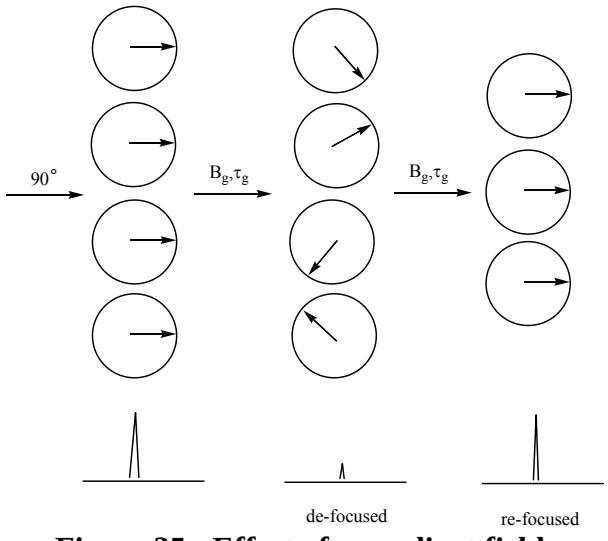


Figure 35: Effect of a gradient field.
Notice that initially after a 90º pulse; application of a gradient field removes nuclei that have been excited through unwanted transitions.

value as well as the ΔE of its nuclear spin states The transferred portion of spins then precess at the frequency of the unobserved nucleus. This new frequency corresponds to the chemical shift of the second nucleus and the ΔE of its nuclear spin states. Because there are two sets of spins precessing at different frequencies, the optimum detection times are different. For each set of spins, the detection is still dependent upon the proper relaxation time for detection. Very short evolution times may allow one frequency to be detectable but it takes longer evolution times for the other frequency to be detected.

The combination of the series of FIDS results in the form of a contour plot indicates two different peaks corresponding to two different frequencies at two different times. One is the diagonal peak and one is the cross-peak. Polarization transfers is inherently more complicated than discussed here and actually involves 13 different components some of which are detectable and some of which are not. It is important to remember that this process can occur for dissimilar isotopes where the ΔE is very different.

1.12.3 Direct detection: HETCOR

The first form of 2D spectroscopy was direct detection. For homonuclear systems, it has no different meaning from indirect detection because in this case, detection still occurs through the H channel.

For hetereonuclear systems, it is very different. Direct detection indicates that the detection occurs through the X channel. This was a time consuming process for nuclei, which have a low magnetogyric ratio considering that it takes at least 128 scans over a wide range of frequencies for a spectrum. This process takes at least 30 minutes per experiment; therefore, running a series of 128 experiments would become time consuming so another process was developed which was time saving.

1.12.3.1 COSY vs. TOCSY

COrrelation SpectroscopY and TOtal Correlation SpectroscopY pulse sequences are applied to elucidate through-bond coupling relationship for protons or other homonuclear species. COSY is used to identify two to three bond coupling and TOCSY

is used to determine greater than three bond coupling. These pulse sequences are compared in Figure 36 and Figure 37.

COSY was the first 2D pulse sequence introduced and is still used extensively today. It has the advantage that it takes low operator skill to start the sequence and it takes a short period to obtain good data. The cross-peaks on these spectra indicate coupling.

Since TOCSY is a correlation over longer bonds, further evolution time is required than in COSY as the coherence is transferred over more bonds and to continue the procession over this longer distance, a pulse lock sequence is used instead of a second 90º pulse. For most spectrometers, this pulse lock sequence is referred to as the mixing time but this terminology can be misleading because it is also used with respect to NOE. For TOCSY, the mixing time is the time it takes to transfer coherence through several bonds. This is accomplished through spin lock sequence. Operators should remember that COSY cross-peaks can breakthrough in TOCSY experiments so these must be compared carefully. Additionally, if very short mixing periods are used, only COSY cross-peaks will appear for TOCSY spectra, Typical TOCSY mixing times range from 30-230ms. The TOCSY experiment itself takes longer than the COSY experiments but it is still a short experiment when compared to other sequences.

1.12.4 Space correlations and chemical exchange correlations

Some two-dimensional experiments have been designed to allow NOE build-up. When NOE correlations occur, they are through-space correlations. Any peak within 4Å is correlated and show NOESY crosspeaks. As already discussed in section 1.11.4.2, NOESY NMR is a type of transient NMR.

1.12.4.1 EXSY

NOE build up can also detect chemical exchange. The 2D program which detects this is EXSY. It is in fact the same pulse sequence as NOESY. There is a limited range of exchange rate that can be used with this experiment. If the exchange is too fast, the resonances will not be resolved and instead of observing two distinct peaks, only a signal

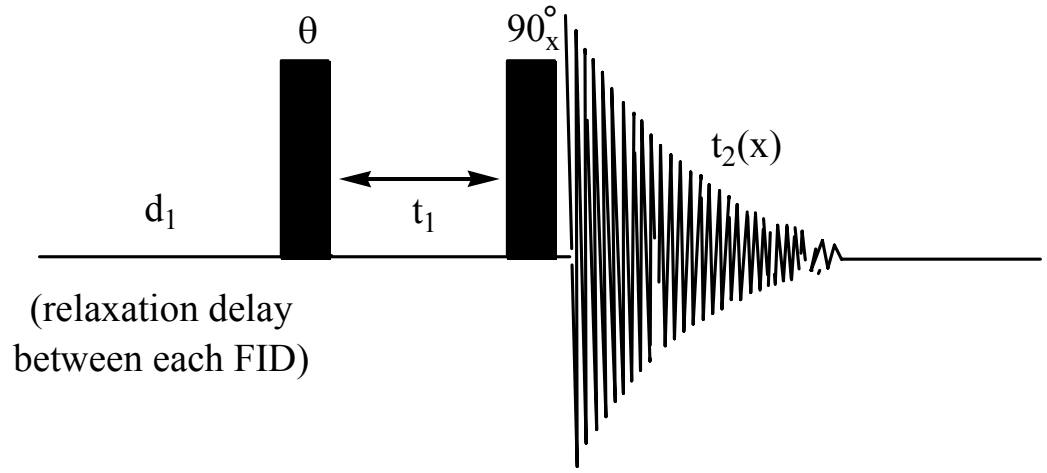


Figure 36: Simple COSY pulse sequence.

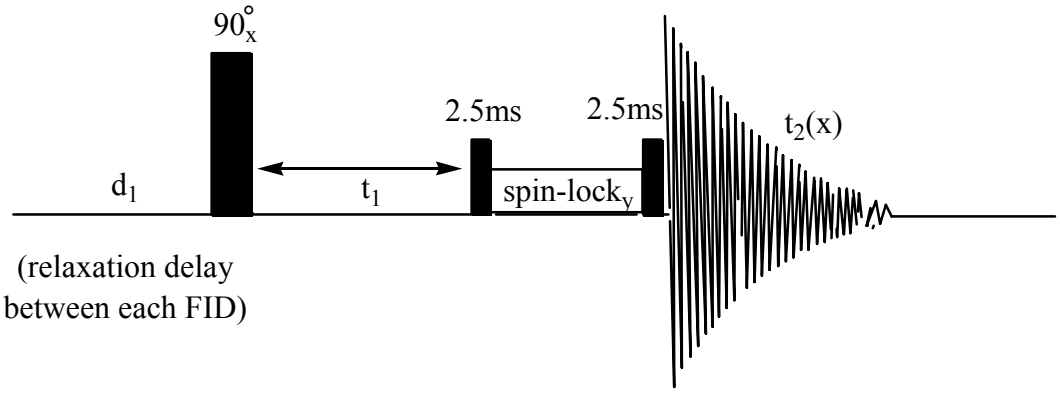


Figure 37: Simple TOCSY pulse sequence.

averaged between these peaks will exist. If the process is too slow, relaxation will dominate and NOE correlations instead of exchange correlations will be detected. The exchange rate must at least be on the same order as the longitudinal relaxation of the molecule.

1.12.4.2 NOESY vs. ROESY

Nuclear Overhauser Enhancement Spectroscopy has already been discussed with respect to the mechanism of spin state inversion. This spin state inversion affects the relaxation rates of neighboring nuclei within 4Å causing correlations between them in the form of cross-peaks. NOESY relies upon the t_c of the molecule and the mechanism decreases as molecular mass increases; therefore, this is not an appropriate experiment for large molecule determinations. A NOESY pulse sequence is shown in Figure 38 and can be compared to the ROESY pulse sequence in Figure 39.

Rotating frame Overhauser Enhancement Spectroscopy can be used instead of NOESY for molecules with molecular weights over 1000 Daltons. A spin-lock sequence increases the frequency so that it is longer than τ_c. This experiment uses positive NOE correlations. Care should be taken when interpreting these experiments because TOCSY signals can break through.

1.12.5 Phase vs. magnitude

1.12.5.1 Phase modulation

Magnitude spectra are also known as absolute value presentation and have the disadvantage that the data gained from these pulse sequences are lower resolution as all the contours are positive. As a result, magnitude spectra cannot be phased but are often very simple to process and this method is still in general use for low resolution spectroscopy. The phases of the frequency waves detected were modulated by adding or subtracting as shown in the Fourier Transform section. When added, signals known as P-type signals are obtained from addition and N-type signals are obtained from subtraction. Addition effectively selects signals with the same precession in t_1 as t_2 whereas subtraction selects signals with opposite precession in t_1 and t_2. Because the information

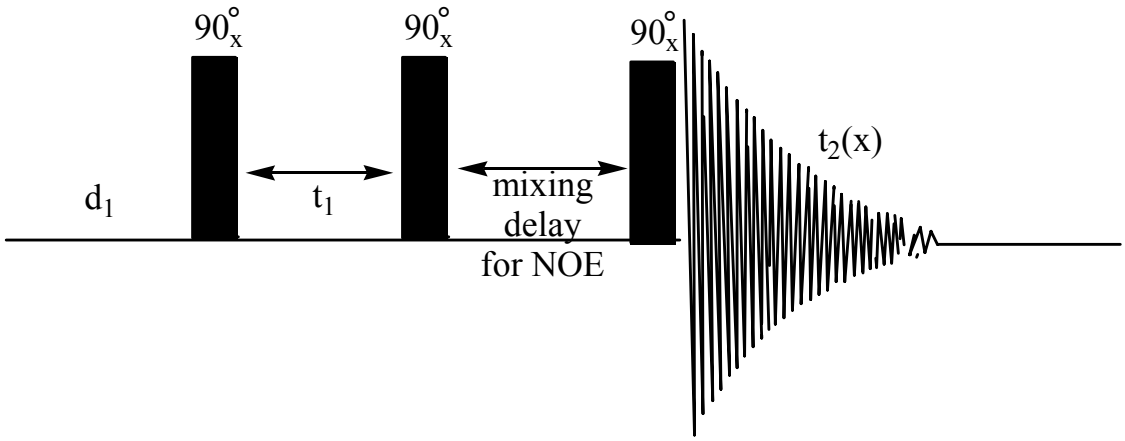


Figure 38: NOESY pulse sequence.

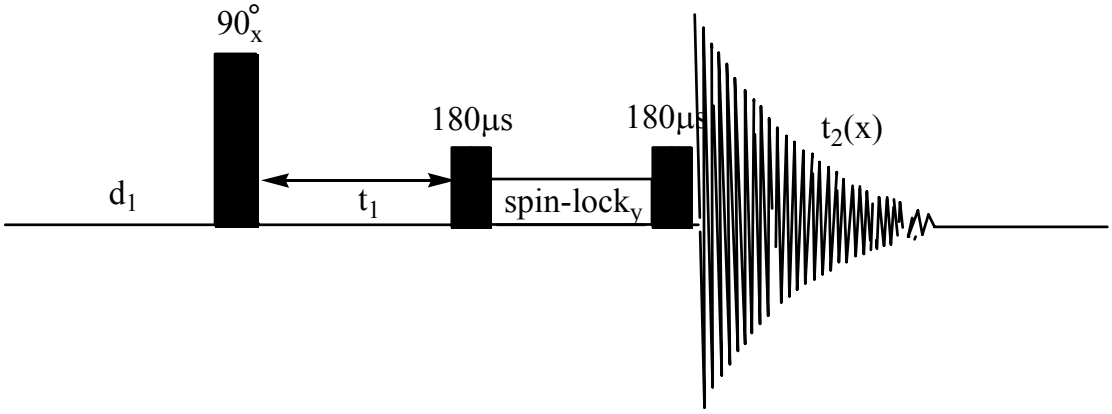


Figure 39: ROESY pulse sequence.

from the P-type or N-type signals is identical but with reversed sign, only one of the two types is displayed.

These data points often need mathematical correction and in the case of COSY experiments, symmetrization is often employed. This method should remove all artificial artifacts but it depends on two stipulations, which are not always true. First, the noise must not accidentally generate symmetrical peaks. Second, the cross peaks must have equal intensity with respect to integration. If this second condition is untrue, it is often the result of shimming error.

1.12.5.2 Amplitude modulation

Amplitude modulation is used for higher resolution spectra and is more commonly employed with 2D pulse sequences. As mentioned when discussing Fourier Transform, the frequency waves must be in phase as a sine wave or out of phase as a cosine wave for data to be detected. In actuality, pulses will contain portions of waves that are dispersive and portions that are absorptive so that the components of the waves must be separated into their sine and cosine counterparts. There are two methods of amplitude modulation dependant on experiment.

To accomplish this in 2D spectroscopy, two sets of data are collected for each t_1 increment. One is the result of a 90º pulse in the y-axis while the other is a result of a 90º pulse in the x-axis. In this way, two sets of information can be gained from the same evolution time and thus properly separated into its sine and cosine components. This is known as the States method.

The other method, known as TPPI, or Time Proportional Phase Incrementation, is used for amplitude modulation is by using twice as many t_1 increments but sampling the data in half the time. The phase for each data points is then modulated by 90º.

1.12.6 Inverse detection

Inverse detection uses the sensitive nuclear channel to detect coupled *X* nuclei. This is distinctly different from the previously described 1D technique such as DEPT or INEPT which are used to detect spin coupling through the *X* channel. The advantage of this procedure is that it increases the sensitivity of the nucleus. Instead of transferring

polarization from the H nucleus to the *X* nucleus, the opposite occurs and these detections are correlated on the H channel.

1.12.6.1 BIRD

Bilinear Rotation Decoupling is an effective way to remove unwanted signal from the sample. Because indirect detection often detects through the proton channel, protons that are coupled to non-spin active forms of the unobserved isotope are removed. This is often necessary because in the case of indirect detection of ^{13}C-^{1}H coupling, additional peaks will show up in the spectra for the majority of protons which couple to the ^{12}C nucleus. Although the coupling is to a non-spin active isotope, which results in a singlet, the singlet due to these protons is still observed unless they are decoupled. The BIRD sequence decouples and effectively suppresses proton signals due to protons attached to ^{12}C. The reason that it works so well is that in the middle of the sequence, a 180º pulse is applied at both the ^{1}H and ^{13}C channels. For ^{13}C-H nuclei, the 180º pulse in the proton channel has no effect but the 180º pulse in the carbon channel switches the transfers the spin states of the protons to opposite carbon spin states. For ^{12}C-^{1}H nuclei, the 180º pulse in the proton channel directs the proton magnetization into the y-axis but the 180º pulse in the carbon channel has no effect. After the final relaxation, the ^{13}C-^{1}H protons rotate back to the +z direction and are detected whereas the ^{12}C-^{1}H protons rotate to the –z direction and are not detected.

1.12.6.2 HMQC vs. HSQC vs. HMBC

A comparison of the HMQC to HMBC pulse sequences is given in Figure 40 and Figure 41. Heteronuclear Multiple Quantum Coherence is an indirect method for determining ^{1}J coupling between two coupled heteronuclear spins. This method greatly increases the sensitivity in comparison to the direct HETCOR method. HMQC is used in correlation with the BIRD sequence to remove unwanted proton signals from the spectrum.

Heteronuclear Multiple Bond Correlation is used to measure ^{2}J - ^{3}J bond distances in molecules. This technique that takes longer than the HMQC experiment. When used

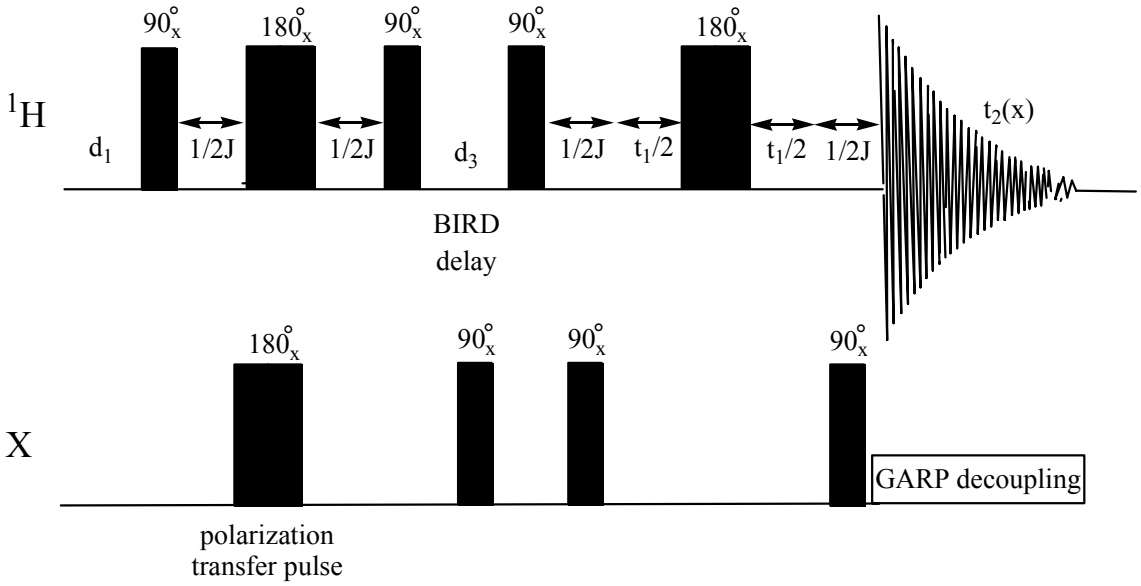


Figure 40: HMQC pulse sequence.

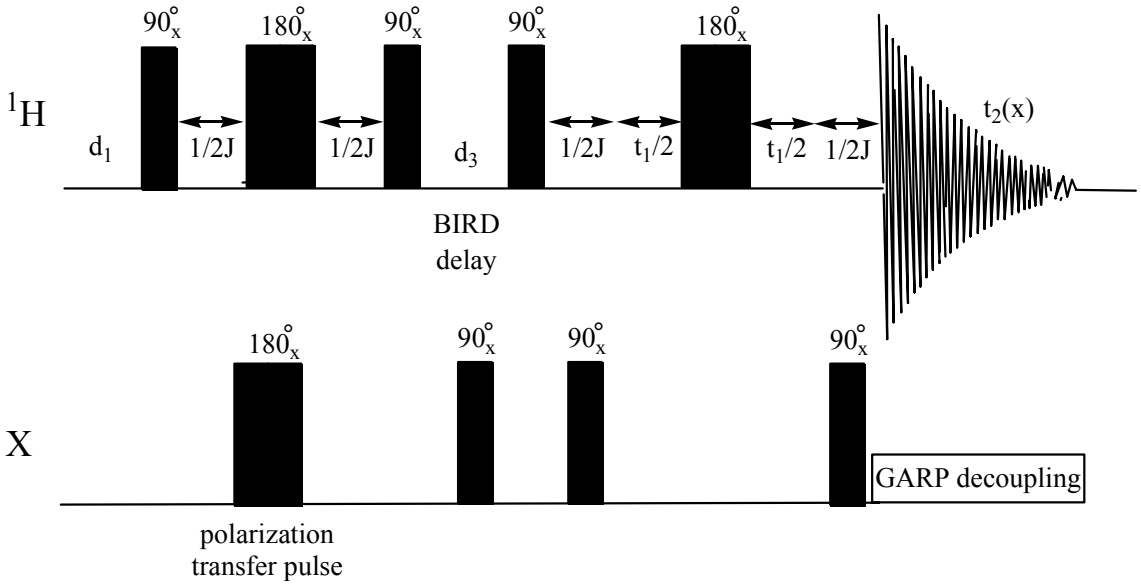


Figure 41: HMBC pulse sequence.

in coordination with the HMQC experiment, it allows for increased structural determination.

Heteronuclear Single Quantum Coherence removes ^{1}H-^{1}H coupling and thus improves the resolution of the spectra. Although more sensitive, it is prone to more operator error if not set up correctly.

While there are many more pulse sequences, these cover the range of sequences used in this paper. A final pulse sequence that is useful is INADEQUATE, which is designed for ^{13}C-^{13}C correlations and allows users to ascertain the carbon skeleton of the organic molecule.

1.13 Conclusion

In conclusion, nuclear magnetic spectroscopy has been treated with respect to nuclear spin, detectability, theory, instrument, mathematical corrections, and pulse sequences. The development of all these methods has advanced the use of NMR in a variety of fields.

2 CATALYTIC CYCLE

2.1 Foreword

A current focus of inorganic chemistry is the synthesis of several classes of highly reactive reductive catalysts. Because of the presence of stereospecific amines in both pharmaceutical as well as agrochemical compounds, the study of catalysts that perform asymmetric reduction of imines is an important area of research. Within the constraints of this research is both the synthesis of novel highly reactive asymmetric catalysts as well as upon understanding the subsequent catalytic cycles associated with the known reactive catalysts that have been reported in this field. Once specific catalyst activity is well understood, characteristics of the cycle can be used to predict reactivity, saving both time and resources.

One such previously uninvestigated catalytic cycle is presented in this work, which demonstrates feasible intermediates. The stability of these intermediates gives credence to the proposed cycle. Interest in this catalytic cycle is a result of the phenomenal theoretical and enantiomeric excess yields of this catalyst with respect to stereospecific reduction of imine bonds. Because the catalyst has been shown to reduce imines bonds specifically to *R* or *S* configurations based on what appears to be steric constraints, it is extremely important to verify and predict what these size constraints are. These predictions can be based upon an accurate catalytic cycle. The cycle that is proposed is unique to this catalyst and appears to follow a previously unreported ionic mechanism quite different from both Noyori's and Mashima's work with similar catalysts.

2.2 Brief historical account of asymmetric catalysis

Both oxidative and reductive catalysis of heterogeneous, multiple phase, as well as homogeneous, single phase, catalysis were seen throughout the beginning of the 20th century. Heterogeneous catalysis was investigated as early as 1903 when Knoevenagel observed reduction using palladium metal.[58] A thorough investigation of heterogeneous

catalysis *via* metal and hydrogen gas was initially led by Braude in 1954. Prior to this work, he had postulated that hydrogen would catalytically transfer from an internal organic molecule under mild conditions[59] but initially was only able to produce these results at low yields after long periods of time.[60-67]

In 1965, Wilkinson published an article[68] which introduced interest in this field with respect to rhodium. He was able to show that certain rhodium(I) catalysts showed high reactivity and used them for homogeneous olefin hydrogenation. In 1976, Schrock *et al*, introduced several catalysts of form $[RhL_2]^+$ which show high reactivity and selectivity under mild conditions.[69-71] These catalysts are used specifically in asymmetric hydrogenation. In recent years, Nobel prizes have been granted to several researchers who have developed the field asymmetric catalysts. These winners include Noyori, Knowles, and Sharpless in 2001 as well as Grubbs, Schrock, and Chauvin in 2005.[8]

2.3 Basic catalytic premises

2.3.1 General homogeneous catalysis

Homogeneous reductive catalysis has some important industrial advantages over heterogeneous catalysts. These advantages include fewer safety concerns due to the lack of pressure and flammability constraints associated with hydrogen donors other than hydrogen gas. Additionally, with homogeneous catalysis, hydrogen donors can be modified so that certain aspects of the reaction can be varied such as temperature, concentration, solvent, and catalyst. This additional system "tweaking" is not available from pure hydrogen gas, as it cannot be modified in the same manner as homogeneous hydrogen donors. The catalyst described in this chapter is a homogeneous catalyst with high reductive yields as well as high enantiomeric excess values. Enantiomers result from mirror images of chiral molecules. The excess of one enantiomer present in solution versus the other is measured *via* the following equation:

$$e.e. = \frac{(major - \min or)}{total} x100\% .^{72} \qquad \textbf{2.1}$$

2.3.2 Achirality and chirality

An object or molecule is chiral if it has a mirror image that cannot be superimposed upon the original image and both images are referred to as enantiomers as shown in Figure 42; however, if the mirror image can be superimposed on the original image, the molecules are the same and are termed achiral. When an object or molecule with unsaturated bonds is achiral but will become chiral after reduction, it is referred to as prochiral.[44]

Reduction of prochiral double bonds lead to two unique products because the alkene has two potential planar reduction faces. Some reductive products give equal proportions of enantiomers while other reductive products give very small proportions of one of the two enantiomers. The physical and chemical properties of enantiomers are unique to each molecule and are not necessarily similar. One enantiomer may therefore have properties that are advantageous for research or industrial use while the other has undesirable side effects. The process of separating enantiomers is often cumbersome and in many cases requires reaction with another chiral substance such as tartaric acid to form diastereomers, which are often more easily separated by physical properties and subsequent recrystallization. Instead of separating enantiomers after they are formed, it is often advantageous in an industrial setting to use a reductive chiral catalyst, which has the effect of only forming the majority or only one of the enantiomers in a pair.

When an achiral catalyst is reacted with prochiral alkenes, two enantiomeric pairs of complexes form at the same rate. If a chiral catalyst is added to a prochiral alkene, two diastereomers will form. The advantage of formation of diastereomers before hydrogenation is that diastereomers generally form at different rates and therefore the ultimate effect is that one diastereomeric complex will preferentially form more easily so that one reduced enantiomer is formed as the major product. This process is known as

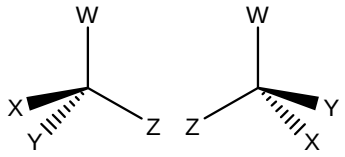


Figure 42: Chiral enantiomeric pair.

asymmetric catalysis and when successful, it is an effective way to eliminate excessive purification steps. An additional advantage is that only a small quantity of chiral catalyst is necessary to yield a large quantity of chiral product.[73]

2.3.3 Reductive enantioselective catalysts

Reductive enantioselective catalysts are necessary due to the plethora of alcohol and amine bonds in agrochemicals, pharmaceuticals, and organic products. Asymmetric catalysts which function to reduce carbonyl and imine bonds are viable in the modern market. It is very important that the asymmetry be retained due to the unique nature of chiral species. Additionally, catalysts which specifically reduce only imine bonds with high enantiomeric excesses are desired.

Baker *et al* has developed[74] and patented (US Pat 6 458 962, 2002) a rhodium catalyst which reduces a variety of imine bonds with high enantiomeric excesses. This catalyst specifically reduces only the imine bond which is advantageous when the molecule also contains alkene bonds which should not be reduced.

The system in this cycle is important for study due to the flexibly and highly reactive nature of this catalyst. Understanding the chemical cycle associated with these processes will have an important bearing on applications of this catalyst to other systems. It is therefore important to prove that the resultant species are stable and observable.

A variety of sultam molecules with specific chirality have been generated from their imine starting material from reaction with catalyst **1**.[75] These sultam molecules have a variety of uses and through modeling have been shown to have characteristics which are necessary for anti-HIV treatment. Specific stereochemistry which result in the presence of this catalyst play a vital role in the predicted reactivity of this species.

2.3.4 General reductive catalysts

Some of the reductive catalysts used specifically for imine reduction use boron with or without a metal centers. Some examples of these are shown in Figure 43. Other varied metals centers have also been used. Catalysis with metals centers are often used for the process of separation. Examples of these are shown in Figure 44. These illustrate

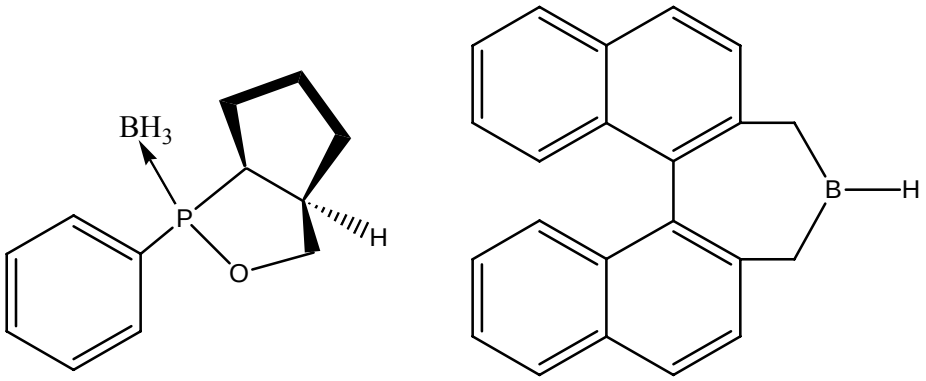


Figure 43: Imine reductive catalysts containing boron.

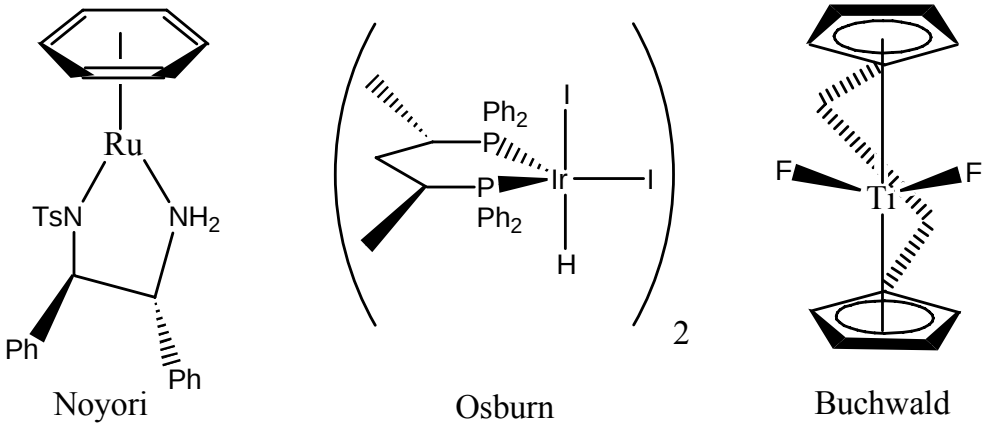


Figure 44: Some well-known organometallic catalysts.

that a wide variety of metal centers have been used as reductive catalysts; however, the majority of them are early transition metals.

2.3.5 MLX naming

Terminology used for ligand to metal bonding in this paper will be described by the neutral MLX naming system whereby both ligands and metal are considered neutral electron donors which contribute separately to the total electron count of the complex. Ligand donors which contribute two electrons are designated as *L* ligands whereas those that contribute one electron are designated as *X* ligands. The additional advantage of this naming system is that the oxidation state of the metal can generally be determined by the number of *X* ligands attached to the metal center. A comparison of these types of ligands is given in Figure 45.

2.4 Catalytic hydrogenation

Catalytic hydrogenation is a fundamental chemical transformation which can employ the simplest molecular reagent and yet remain one of the least understood mechanistic reactions.

Classical inorganic mechanisms for hydrogenation catalysis with late transition metal catalysts follows I-III oxidation addition/reductive elimination cycle that moves between 16 electron and 18 electron intermediates in the majority of cases. In the strictest sense, 1, 3 oxidation addition describes an associative step where both the oxidation state and coordination of the metal as well as the total electron count of the



Figure 45: Comparison of X_2 and L ligands.

system increase by two.[73] A typical cycle for Wilkinson's catalyst[68, 76, 77] is shown in Figure 46.[78]

The cycle in Figure 46 is highly simplified; directly observable species in the catalytic mixture include $RhH_2Cl(PPh_3)_3$, $RhCl(PPh_3)_2$(olefin), $[RhCl(PPh_3)_2]_2$, and $H_2Rh_2C1_2(PPh_3)_4$ which provide external equilibria to the cycle that stabilize the Rh-containing complexes in the absence of substrate. The involvement of the solvent also implies a solvent dependency. Examination of a classic system such as Wilkinson's catalyst using *para*-H_2[79-83] (hereafter *p*-H_2) provides additional evidence of the chemical complexity. The intensity enhancement due to the spin-selected nature of *p*-H_2 allows the direct observation of intermediates such as $H_2Rh(PPh_3)_2(\mu\text{-}Cl)_2Rh(PPh_3)$(olefin), $RhHCl(PPh_3)_2(\mu\text{-}H)_2RhHCl(PPh_3)_2$, $RhH_2Cl(PPh_3)_3$, $RhH_2Cl(PPh_3)_2$(olefin), and $H_2Rh(PPh_3)_2(\mu\text{-}Cl)_2Rh(PPh_3)_2$. There is no reason to believe that there are no other intermediates or associated species present that are still below the detection limit of this technique. Even in such an apparently simple system, there are fundamental questions that still need to be addressed, the answers to which provide methods of optimization of the reaction.

Addition of dihydrogen to a metal center is an example of a homopolar addition and invariably results in *cis* addition to the metal center, whereas heteropolar addition results in either *cis* or *trans* addition, as shown in Figure 47. Catalytic hydrogenation usually conforms to this general scheme.

Recently, *polar* or *ionic* hydrogenation has become the focus of interest, especially for hydrogenation of heteropolar unsaturation.[84-86] The general scheme for this type of reaction is shown in Figure 48.[84, 85, 87] This reaction scheme still relies on using dihydrogen in the laboratory and also implies that the amine formed is sufficiently basic to deprotonate the (η-H_2) metal complex, $L_nM(\eta\text{-}H_2)$. Moreover, if the addition of dihydrogen results not in the formation of $L_nM(\eta\text{-}H_2)$ but of $L_nM(H)_2$, then the catalytic cycle may fail and selectivity may well be lower, as a low-coordinate hydride cation, which is liable be to fluxional, will form in this case.

Work was published by Norton *et al*[88] which proposed an ionic mechanism which relied on dihydrogen. The catalyst studied is shown in Figure 49. Several potential

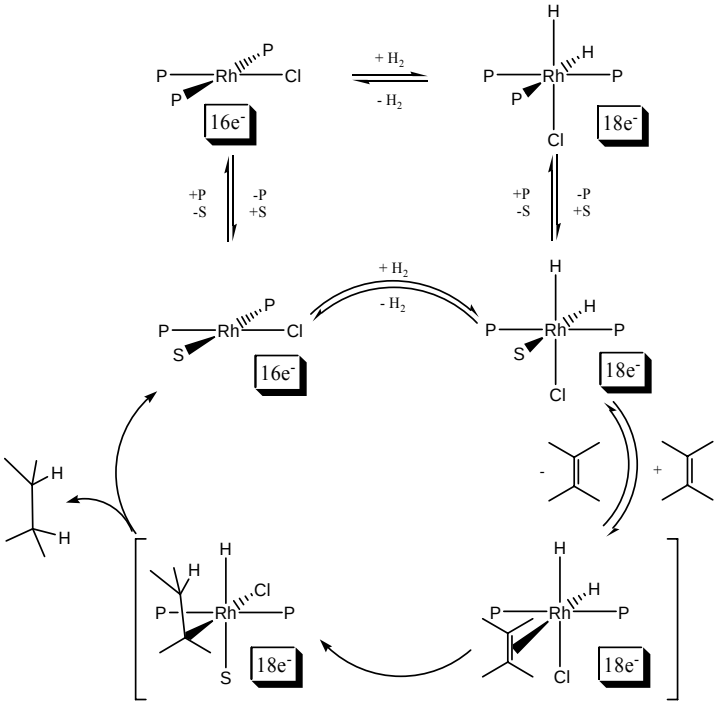


Figure 46: Wilkinson's catalytic cycle.

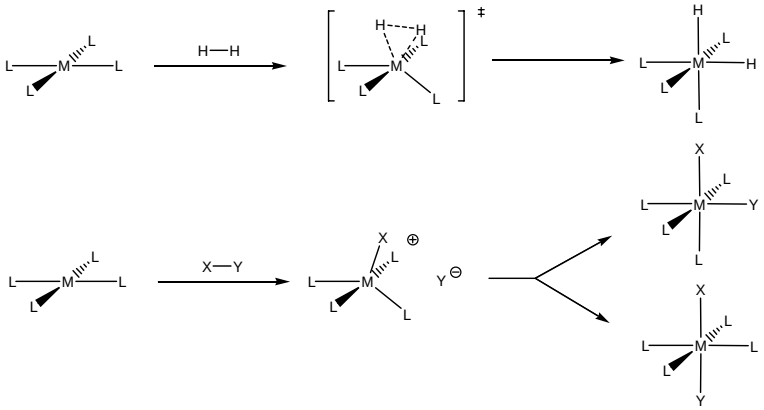


Figure 47: Homopolar and heteropolar oxidative addition to a metal center.

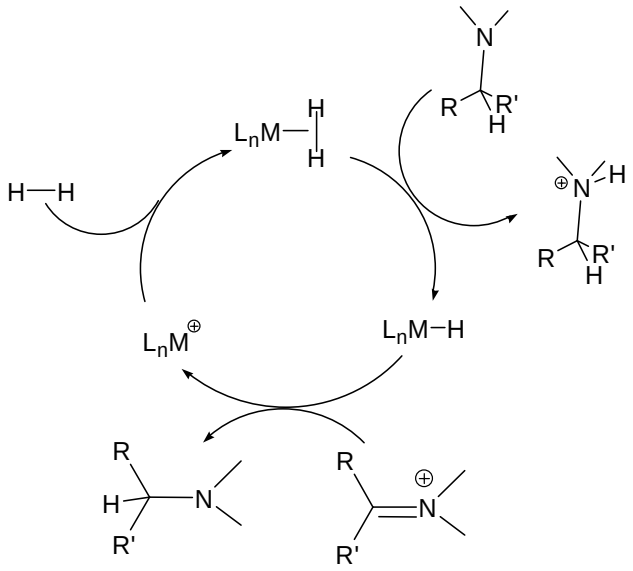


Figure 48: Putative ionic hydrogenation catalytic cycle.
Dihydrogen was used as the {H} source.

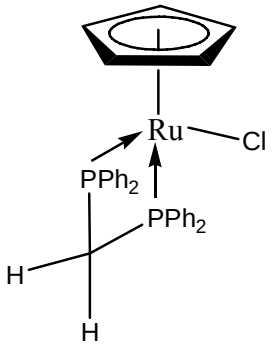


Figure 49: Ionic catalyst studied by Norton *et al*.

reaction intermediates were synthesized to support this work. The source of the ionic hydrogen was H_2 gas which is fundamentally different than the process which is being proposed in this paper. The proposed cycle is very similar to that shown in Figure 48.

The catalyst, **1**,[75, 89] in this chapter has a fundamentally different mechanism. The precatalytic complex is an $18e^-$ rhodium species, Cp*RhCl[(1R,2R)-*p*-$TsN(CHPh)_2NH_2$],[74] the crystal structure has been determined at the University of Tennessee. The general ligand system Cp*MCl[(1R,2R)-*p*-$TsN(CHPh)_2NH_2$] has been applied to transfer hydrogenation by Noyori and co-workers and has also been used with rhodium independently of this work; however, the mechanism of catalysis has only been studied for the ruthenium species.[90-93]

Ionic mechanisms depend upon the external ionic dissociation of hydrogen from a substrate and the subsequent addition of this atom to a metal center. This mechanism has been applied to the catalytic system in this chapter. The mechanism is formally ionic due to the fact that the proton comes from an external soure.

For comparative purposes, another manner in which the typical reaction schemes are classified is shown in Figure 50. These mechanisms include concerted, S_N2, radical, and ionic. With respect to organometallic mechanistic terminology, concerted mechanisms are different from S_N2 mechanisms in that concerted mechanisms involve a

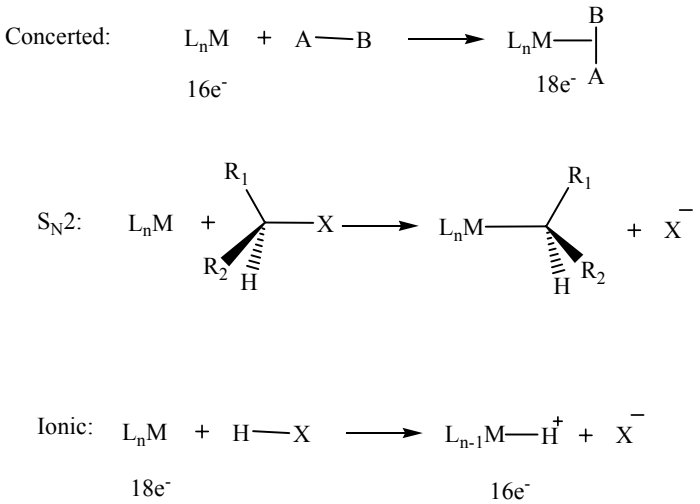


Figure 50: Comparison of mechanisms.

three-centered bond between the metallic electrons and the substrate as shown on the left in Figure 47 whereas S_N2 mechanisms involve the linear attack of metallic electrons on the less polar substrate. The rate of the S_N2 reaction is increased with increased metallic nucleophilicity, leaving group strength, and decreased substrate steric hindrance. Both concerted and S_N2 mechanisms involve a single step that is dependent upon both the substrate and metal for rate.

We have been studying the mechanism of this catalytic reaction intensively, using variable temperature, multidimensional and multinuclear NMR, supplemented by standard organometallic synthesis and characterization.[94] A possible catalytic cycle is shown in Figure 51.

2.4.1 Description of catalyst intermediates

The catalytic reaction is carried out in either CH_2Cl_2 or THF and the H^+/H^- source is Et_3N-HCO_2H, which is held at constant concentration with the azeotropic mixture of Et_3N and HCO_2H. There is an equilibrium between triethylammonium formate and the two neutral species *viz*.

$$Et_3N + HCO_2H \rightleftharpoons [Et_3NH]^+ [HCO_2]^- \qquad \textbf{2.2}$$

which buffers the solution and adds complexity in terms of the species that are present. Macroscopically, CO_2 is generated during the reaction and formic acid is consumed.

The first catalytic cycle begins with the conversion of the chloride precursor **1,** shown in Figure 52 and Figure 53, to a hypothetical and transient formate complex, [Cp*[(1R,2R)-*p*-TsN(CHPh)$_2$NH$_2$]Rh(O$_2$CH)], **1a**, which decomposes with the loss of CO_2 to form the hydride species, Cp*[(1R,2R)-*p*-TsN(CHPh)$_2$NH$_2$]RhH, **2**. Coordination and insertion of the imine into the Rh-H bond results in the formation of the amido-Rh(III) species, Cp*[(1R,2R)-*p*-TsN(CHPh)$_2$NH$_2$]Rh(N(R")CHRR'), **3**. **3** is protonated to form the ammine complex [Cp*[(1R,2R)-*p*-TsNH(CHPh)$_2$NH$_2$]Rh]$^+$, **4**, which may be transient, and on de-coordination of the final reduced amine, yields the cationic species, [Cp*[(1R,2R)-*p*-TsN(CHPh)$_2$NH$_2$]Rh]$^+$, **5**, presumed to be in equilibrium with the solvated form, [Cp*[(1R,2R)-*p*-TsN(CHPh)$_2$NH$_2$]Rh(S)]$^+$, **5a**, where 'S' represents the solvent. There may also be a closed set of coordination equilibria between **4**, **5**, and **5a**.

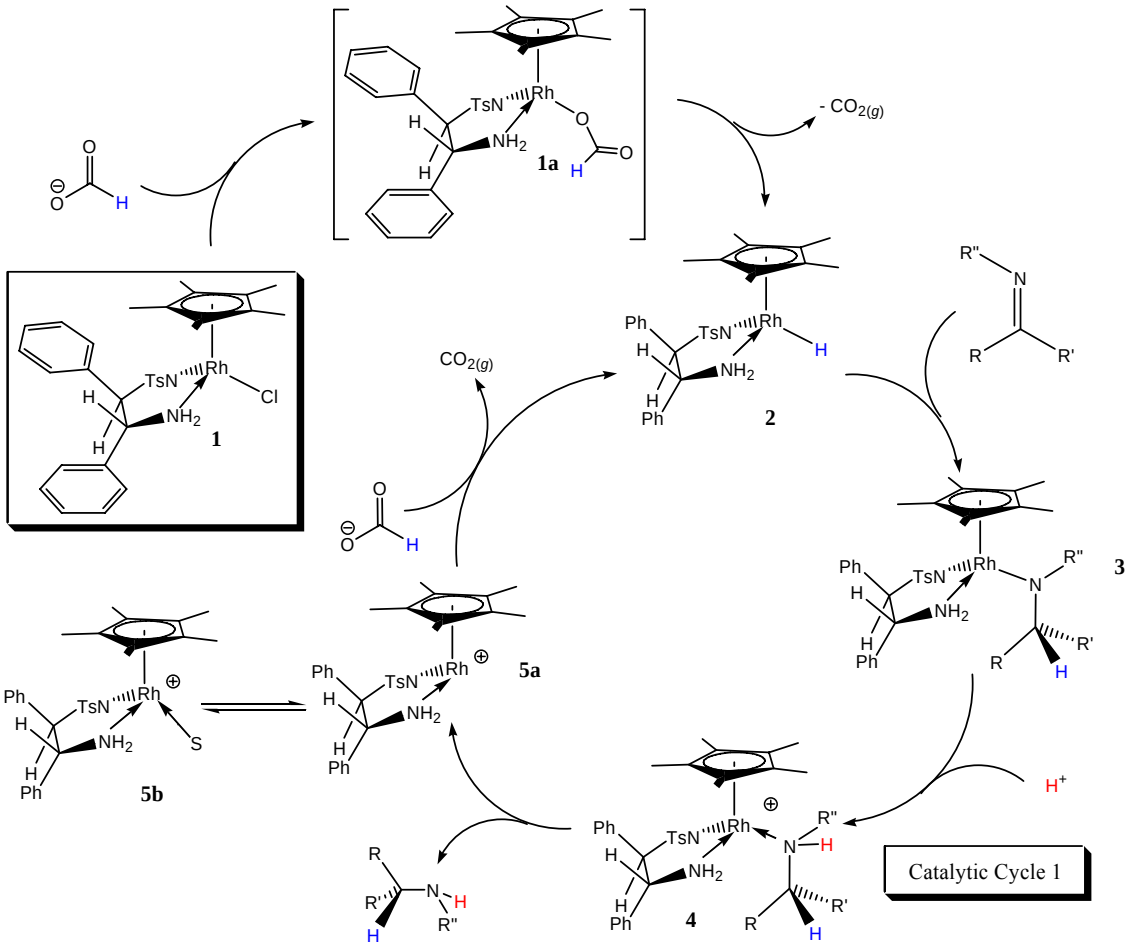


Figure 51: First possible catalyst cycle.

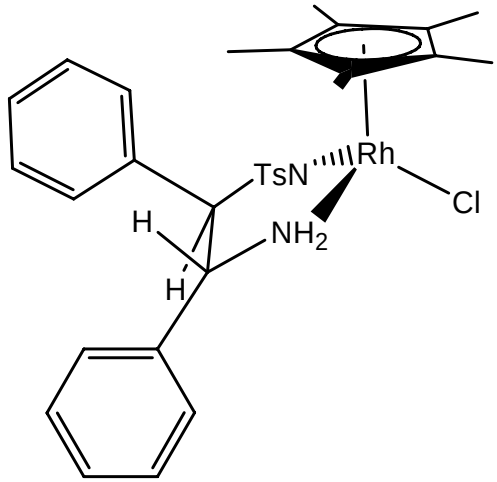


Figure 52: Rhodium catalyst, 1.

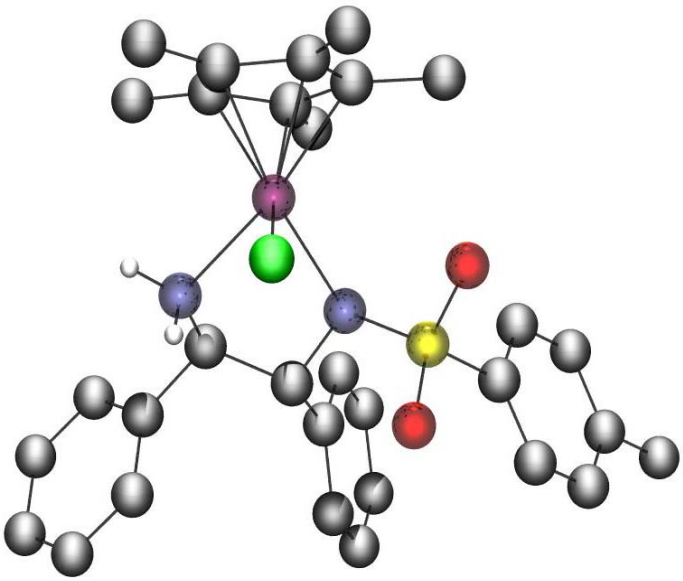


Figure 53: Crystal structure of 1 as determined by the University of Tennessee.

Reaction of this cation with formate ion reforms [Cp*[(1R,2R)-*p*-TsN(CHPh)$_2$NH$_2$]Rh(O$_2$CH)] and the cycle continues.

The instability of the general organometallic species L$_n$M(O$_2$CH) is well known and there are very few terminal organometallic formate molecules known. Rare examples include complexes of Ni, Pd and Pt. [95-98] In this respect, the instability of **1a** is not unusual. Indeed, NMR studies at low temperature show that there is no observable formate species present, and the low temperature NMR spectrum of the reaction shows a smooth replacement of the resonance associated with **1** with the resonances associated with **2**, including a hydride resonance at δ -9.8 (1H, d, $^1J_{HRh}$ = 21.2 Hz). We have also observed a triplet at ~ δ -11 which may be due to either a symmetrical bridging hydride species, or be indicative of an equilibrium between **2** and a dimer, **2**$_2$, which may be tentatively formulated as Cp*[(1R,2R)-*p*-TsN(CHPh)$_2$NH$_2$]Rh(μ-H)$_2$Rh[(1R,2R)-*p*-TsN(CHPh)$_2$NH$_2$]Cp*, although the bonding situation in this system must differ, as it is formally contains two 20e$^-$ species, which are inherently unlikely for Rh.

1, **2**, **4** and **5a/b** have been characterized fully, through a variety of NMR techniques, including low temperature *in situ* 2D-NMR and VT multinuclear NMR on individually prepared compounds *i.e*. directed synthesis of these materials *de novo*, as opposed to studying the full catalytic reaction *in situ*. Syntheses are shown in Figure 54. We are currently in the process of structurally characterizing these materials macroscopically for crystal structure determination.

There is also evidence of a second potential catalytic cycle because within twenty-four hours, the hydride species changes color from red to green. This color change indicates a fundamental change in the complex. Indeed, Mashima's group has studied this the iridium derivative of this same catalyst system[99, 100] and in the case of iridium, they can distinguish two different species as 18 electron and 16 electron systems, respectively. The 16 electron species was reported to be green. They were not able to separate the two rhodium species but also noticed the color change. The second proposed catalytic cycle is shown in Figure 55.

Mashima has studied similar to this one[99, 100] in which an iridium metal center is employed to reduce a carbonyl bond. This system is shown in Figure 56 and Figure 57.

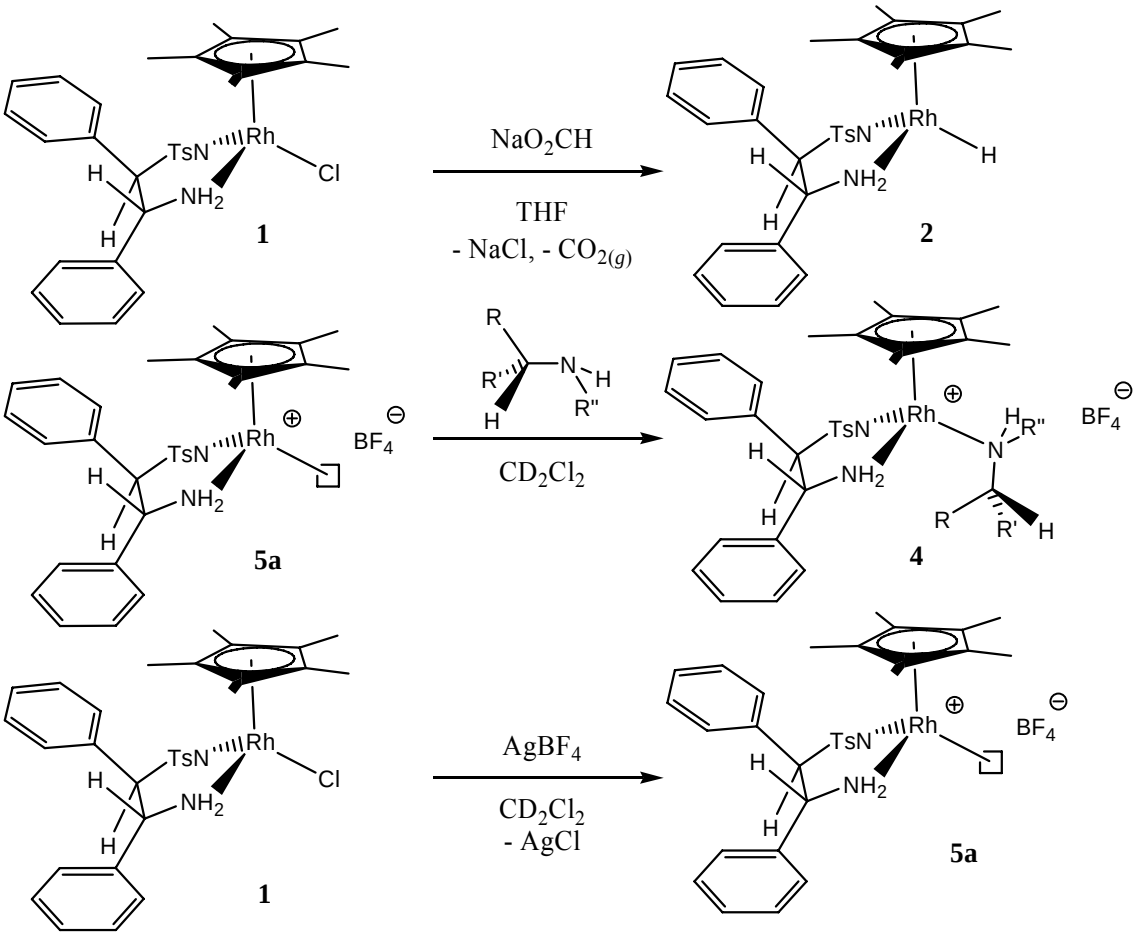


Figure 54: Directed syntheses of catalytically relevant species in the catalyst cycle.

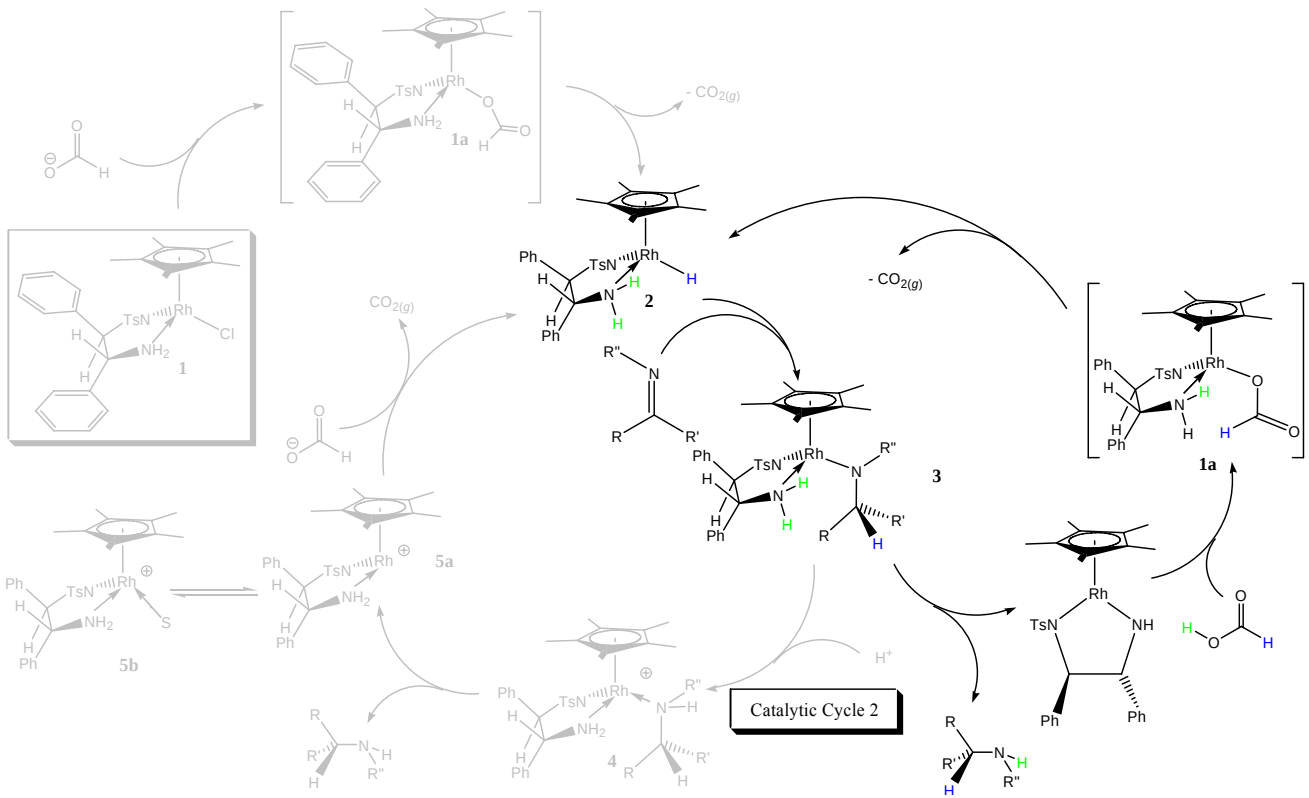


Figure 55: Second catalytic cycle for 1, using the diamido intermediate.

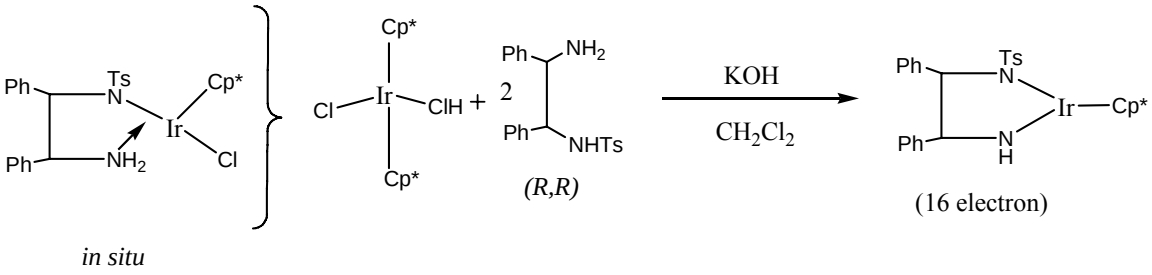


Figure 56: Synthesis of Mashima[99, 100] catalyst and 16 electron species.

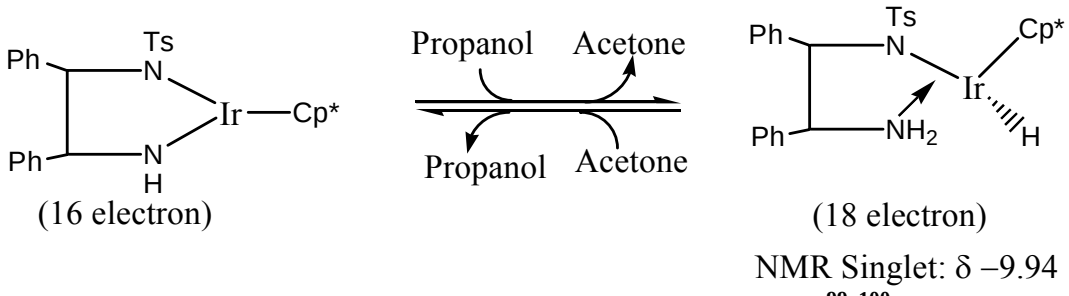


Figure 57: Reversible reductive carbonylation.[99, 100]

The synthesis of the catalyst is different. They are able identify an iridium hydride doublet which is in the same region that this paper identifies a rhodium hydride doublet. Mashima's group did not see the hydride version of the rhodium complex. Mashima indicates that the iridium catalyst is less active than the rhodium catalyst as would be expected He reported that in the case of the iridium derivative, the transformation from the sixteen electron complex and the hydride were reversible and that these two species composed the catalyst cycle.

The cycle proposed for the rhodium species is much more complex and involves more than the sixteen electron complex and hydride proposed by Mashima. Because of it's higher reactivity, the rhodium cycle is more sensitive and some of the intermediates are more difficult to synthesize.

2.5 Catalytic mechanisms of rhodium catalyst cycle

2.5.1 Spectroscopic interpretations

2.5.1.1 Spectroscopy of ligand, (1R, 2R)-TsDPEN, 6

The determination of the stereochemistry of (1R, 2R)-TsDPEN, **6**, from available NMR spectra is not trivial and is certainly not available from a single measurement. Accordingly, this molecule was characterized using one, two-dimensional and variable temperature techniques. 1D and 2D VT techniques were also used to study the fluxionality of this molecule. All studies were conducted using solutions of **6** in d_2-methylene chloride. All spectra were obtained as noted on either a Varian Inova 600 MHz spectrometer or a Bruker Avance 400 MHz spectrometer using a 5 mm broadband probe. Acquisition parameters and other experimental details are given in Section 2.6. For reference purposes, relevant figures, spectra, and tables are placed at the end of this section.

The ^{13}C spectra contain fourteen resonances and ^{1}H data contain eight resonances at room temperature. The COSY data indicate a minimum of two spin system containing one of which contains the tosyl protons and the other contains the backbone CH protons

designated as H_1 and H_2. TOCSY data indicate an extended coupling between the aforementioned systems drawing the backbone H_1 and neighboring phenyl protons into the same system as well as tying the methyl group to the tosyl ring. The backbone H_1 and H_2 coupling is assumed to be between each CH and the nearest ring *ortho* proton because this is a ^3J distance. It is also possible but less likely that the TOCSY coupling occurs between each CH and neighboring *ortho*-protons which is ^4J distances as is *meta*-protons on the same ring.

The HMQC spectrum identifies which carbon atoms to which the backbone protons are attached. The proton attached to C1 (δ/ppm 62.19) has a chemical shift at δ/ppm 4.30 whereas the proton attached to C2 (δ/ppm 65.31) has a chemical shift at δ/ppm 4.12. It is interesting that while H_1 is more deshielded than H_2, C2 is more deshielded than C1. HMQC reaffirms the expected correlation between C3 (δ/ppm 21.27) and H3 (δ/ppm 2.23) which has an integration of three in the proton spectrum as the methyl group on the tosyl group.

The phenyl ring attached to C1 has protons peaks H_{1o} (δ/ppm 7.03), H_{1m} (δ/ppm 7.158), and H_{1p} (δ/ppm 7.152) which correspond respectively to carbon atoms with shifts at δ/ppm 127.43, 128.10, and 128.53. Some of the proton peaks overlap extensively such as H_{1m}, H_{1p}, H_{2m}, and H_{2p}. The positions of these peaks were determined from the center of the HMQC cross-correlation.

The phenyl ring attached to C2 has protons peaks H_{2o} (δ/ppm 7.151), H_{2m} (δ/ppm 7.158), and H_{2p} (δ/ppm 7.098) which correspond respectively to carbon atoms with shifts at δ/ppm 128.36, 128.10, and 127.69. The tosyl ring has protons peaks $H_{Ts\text{-}o}$ (δ/ppm 7.030), $H_{Ts\text{-}m}$ (δ/ppm 7.310) which corresponds respectively to carbon atoms with shifts at δ/ppm 129.57 and 127.52.

HMBC data clarifies the positions of quaternary carbon atoms and reaffirms ring assignments. There is a correlation between H_1 and both C1*o* and C1*i* (δ/ppm 141.14). Additionally, there is a correlation between H_2 and both C2*o* and C2*i* (δ/ppm 142.56). This affirms the label of phenyl ring one and phenyl ring two.

The remaining quaternary carbon atoms are distinguished *via* the tosyl and *ortho* proton. $H_{Ts\text{-}o}$ has correlations with $H_{Ts\text{-}i}$ as well as H_3, and $H_{Ts\text{-}m}$. This must be $H_{Ts\text{-}o}$, as the coupling from $H_{Ts\text{-}m}$ to $H_{Ts\text{-}i}$ would not be expected to appear on this spectrum. $H_{Ts\text{-}m}$ does however have correlations with $H_{Ts\text{-}p}$ as well as $H_{Ts\text{-}o}$. The aromatic section is too complex to identify correlations with many of those protons.

The NOESY data will prove to be extremely important when determining the catalytic mechanisms, as does any exchange data obtained from the NOESY systems. The most interesting correlation is one which is in phase with the diagonal. The means that exchange is taking place. Protons between H_{N1} and H_{N2} are exchanging.

The majority of the aromatic section is too complex to determine many NOESY correlations. H_1 shows correlation with an overlapping multiplet which contains H_{1o} and a tosyl proton. It seems to be very likely that the actual correlation is with H_{1o} since other correlations are observed in this manner and since this peak would be much closer than a tosyl peak. There are also correlations between H_1 and another overlapping region containing H_{1m}, H_{2m}, H_{1p}, and H_{2o}. It seems likely that the peak with closest proximity would be H_{1m} and this is the correlation listed although it could possibly be H_{2o}. H_2 shows correlation with the same region containing H_{1m}, H_{2m}, H_{1p}, and H_{2o}. The assumed peak position is with H_{2o} but there could also be proximity to H_{2m} as well as H_{1m} depending on the orientation of the phenyl ring. Figure 58 shows a proposed structure of the molecule according to NMR. Carbon and proton spectra are shown in Figure 59. Spectral correlations are tabulated in Table 2.1 and relevant 2D spectra are shown in Figure 60 - Figure 66.

2.5.1.2 Evidence of synthesis of 1

Some of the major differences between the spectra of **1** and **6** are obvious and when compared are proof for the existence of a different compound, **1**. The amine hydrogen attached to the same carbon atom as the tosyl-group in the ligand is no longer present. The other amine hydrogen atoms become inequivalent and are deshielded by about δ/ppm 1. Both carbon atom protons become more shielded by δ/ppm 0.5 to 1 and show

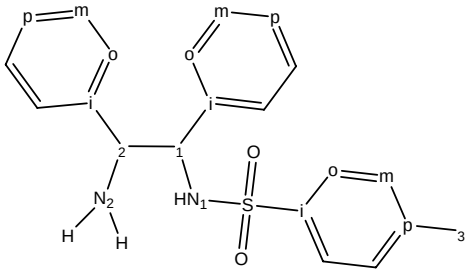


Figure 58: Structure of 6 according to NMR data.

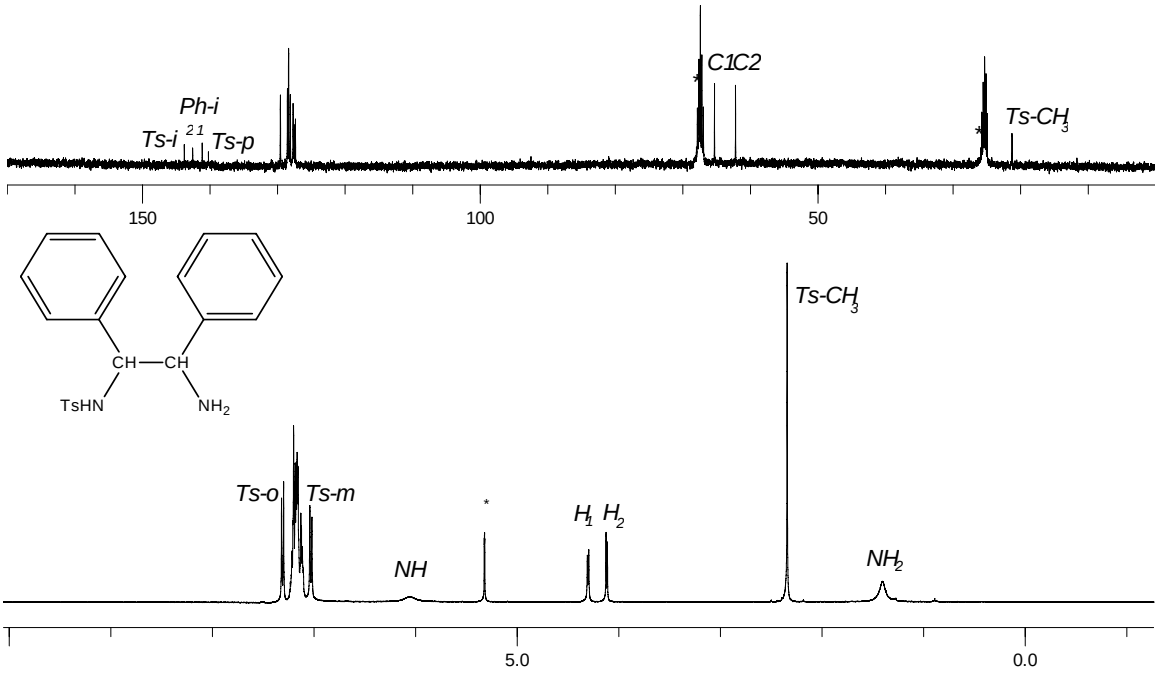


Figure 59: Carbon and proton spectra of 6.

^{1}H-NMR (400 MHz) 7.31 (d, *J* = 8.3 Hz, 2H) 7.17 (m, 10H) 7.03 (d, *J* = 8.5 Hz, 2H) 6.06 (s, 1H, NH) 4.30 (d, *J* = 5.2 Hz, 1H) 4.12 (d, *J* = 5.2 Hz, 1H) 2.34 (s, 3H) 1.40 (s, 2H, NH) ^{13}C-NMR (400 MHz) 143.796 (C), 142.559 (C), 141.144 (C), 140.219 (C), 129.569 (CH), 128.529 (CH), 128.355 (CH), 128.098 (CH), 127.693 (CH), 127.517 (CH), 127.340 (CH), 65.313 (CH), 62.188 (CH), 21.269 (CH_3)

Table 2.1: Correlations for 6.

^{1}H position	^{13}C *(ppm)*	^{1}H *(ppm)*	m	^{2}J *(*Hz*)*	COSY / TOCSY	^{j}HMBC *(C)*	NOESY
N_1	N/A	6.060	s	N/A	-	-	[c]N_1
N_2	N/A	1.400	s	N/A	-	-	[c]N_2
[g]1	65.31	4.300	d	5.2	2, [a]1*o*	1*o*, 1*i*	2, [d]1*o*, [d]1*m*
[g]2	62.19	4.120	d	5.2	1, [b]2*o*	2*o*, 2*i*	1, [d]2*o*
1*i*	141.14	N/A	N/A	N/A	N/A	N/A	N/A
1*o*	127.43	7.030	m	-	-	unclear	[d]1
1*m* & 2*m*	128.10	[f]7.158	m	-	-	unclear	[e]1
[h]1p	128.53	[f]7.152	m	-	-	unclear	Unclear
2*i*	142.56	N/A	N/A	N/A	N/A	N/A	N/A
2*o*	128.36	[f]7.151	m	-	-	unclear	[d]2
[h]2p	127.69	7.098	m	-	-	unclear	Unclear
Ts-*i*	143.80	N/A	N/A	N/A	N/A	N/A	N/A
Ts-*o*	129.57	7.030	d	8.40	Ts-*m*, 3	3, Ts-*i*, Ts-*m*	-
Ts-*m*	127.52	7.310	d	8.40	Ts-*o*, 3	Ts-*p*, Ts-*o*	-
Ts-*p*	140.22	N/A	N/A	N/A	N/A	N/A	N/A
3	21.27	2.340	s	N/A	Ts-*m*, Ts-*o*	Ts-*p*, Ts-*m*	-

Dashes are used to indicate that these data could not be assigned. All spectra were obtained on a Bruker Avance 400 MHz instrument using a 5 mm probe. Unless otherwise noted, all experiments were performed at room temperature. All other symbol explanations follow. [a/b]These correlations are assumed because they are the only proton in a large overlap that results from ^{4}J coupling; other protons would have to be a correlation from ^{5}J or greater coupling and this is not likely in COSY data. [c]Exchange information is indicated. [d/e]These correlations are assumed correct because of proximity to the correlated proton compared to other protons in the overlap. [f]This proton peak position is determined from the central portion of the HMQC correlation. [g]The peak labeled as H_1 could be reversed with the peak labeled as H_2. There are no correlations to distinguish which methine peak is correlated with N_1 vs. N_2. If the labeling were reversed, the phenyl ring labeling would also have to be reversed since there are correlations tying the phenyl rings to particular methine protons. [h]Due to overlap of peaks this value cannot be discerned as specifically belonging to one ring or the other. It is possible that the positions for H_{1p} and H_{2p} are reversed

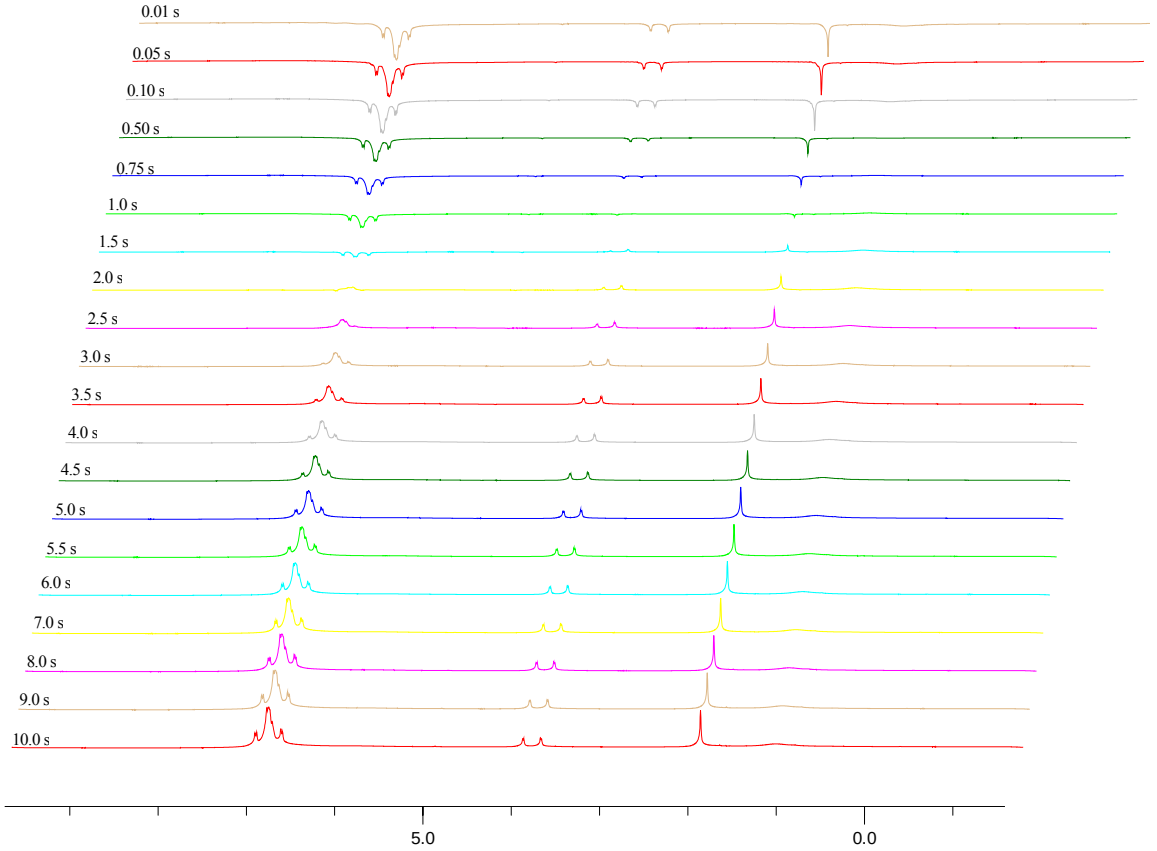


Figure 60: T_1 relaxation of 6.

^{1}H-NMR (400 MHz) 7.31 (3.02 s) 7.17 (2.56 s) 7.03 (2.8 s) 6.06 (5.05 s) 4.30 (1.74 s) 4.12 (1.34 s) 2.34 (1.7 s) 1.40 (0.92 s)

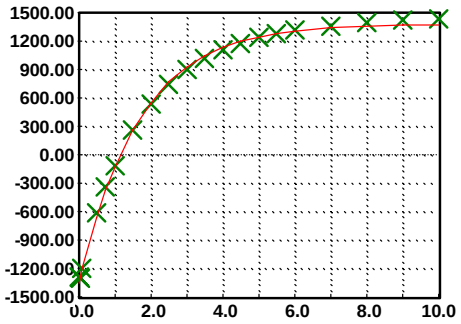


Figure 61: Example T_1 calculation of Cp*.

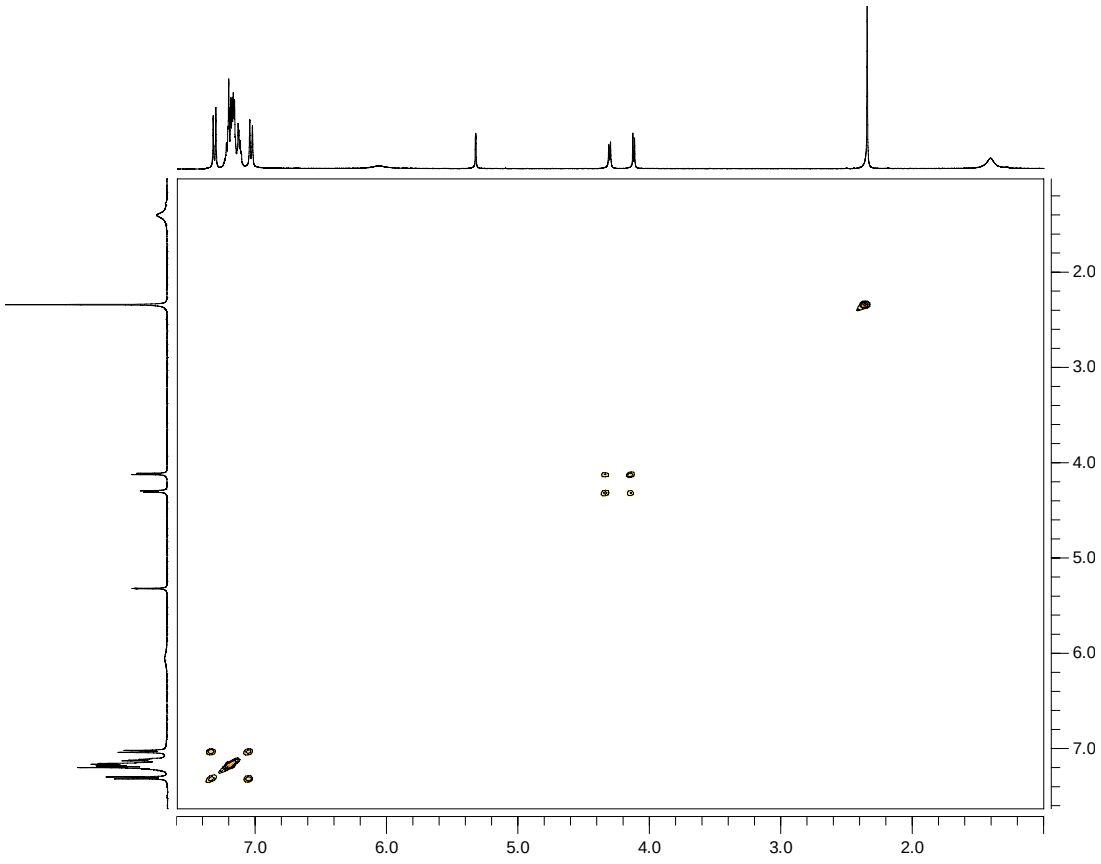


Figure 62: COSY of 6.

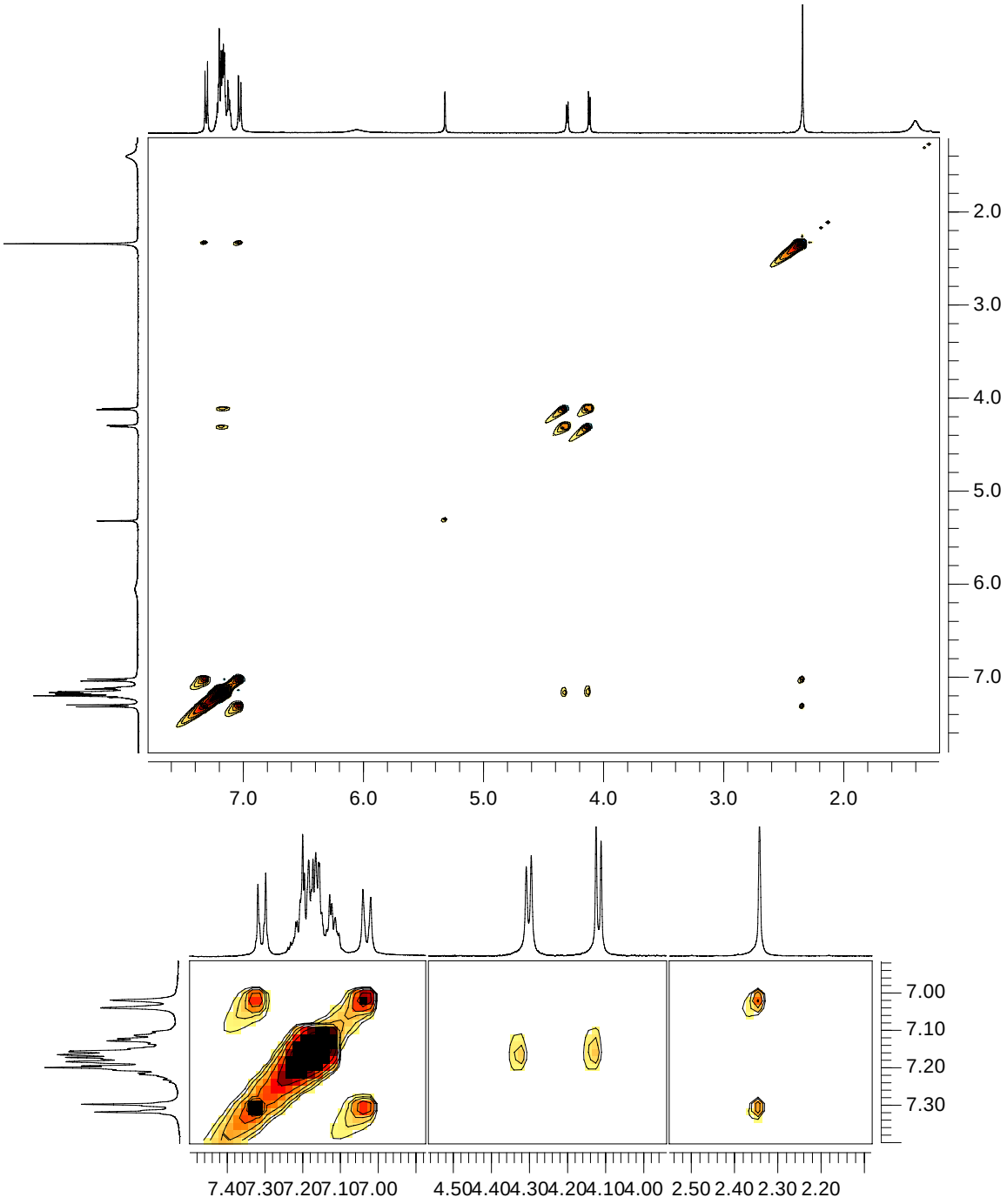


Figure 63: TOCSY of 6.

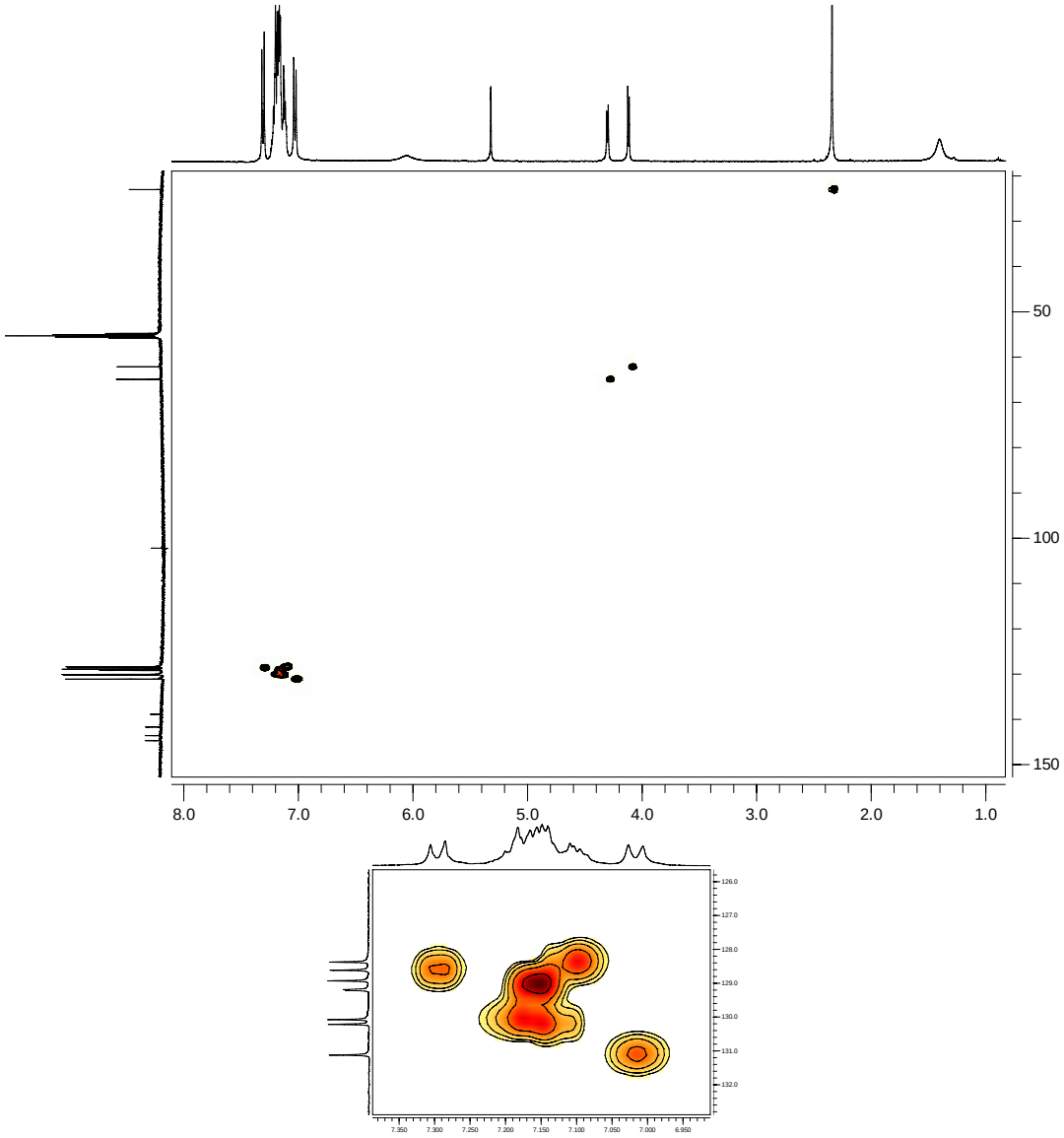


Figure 64: HSQC of 6.

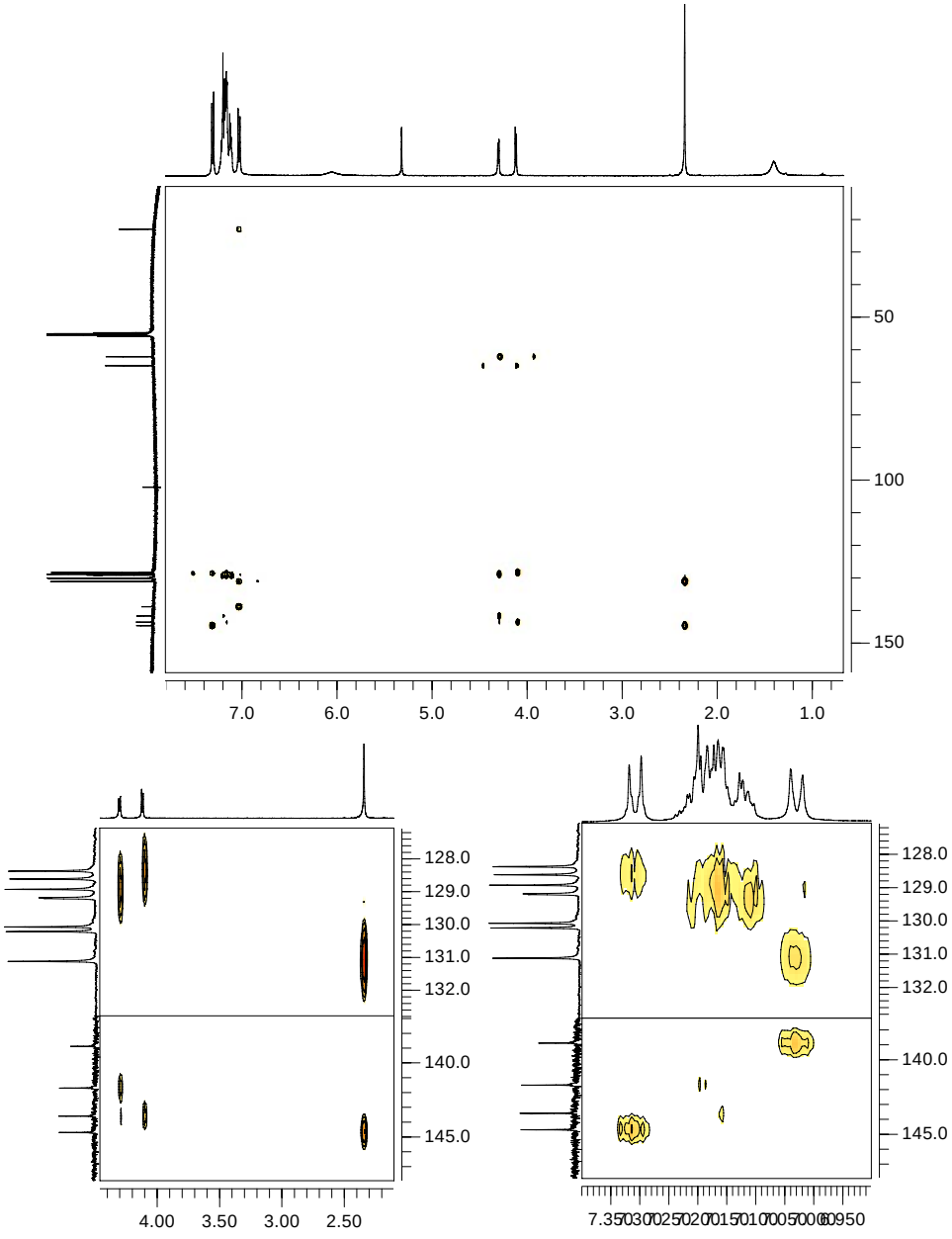


Figure 65: HMBC of 6.

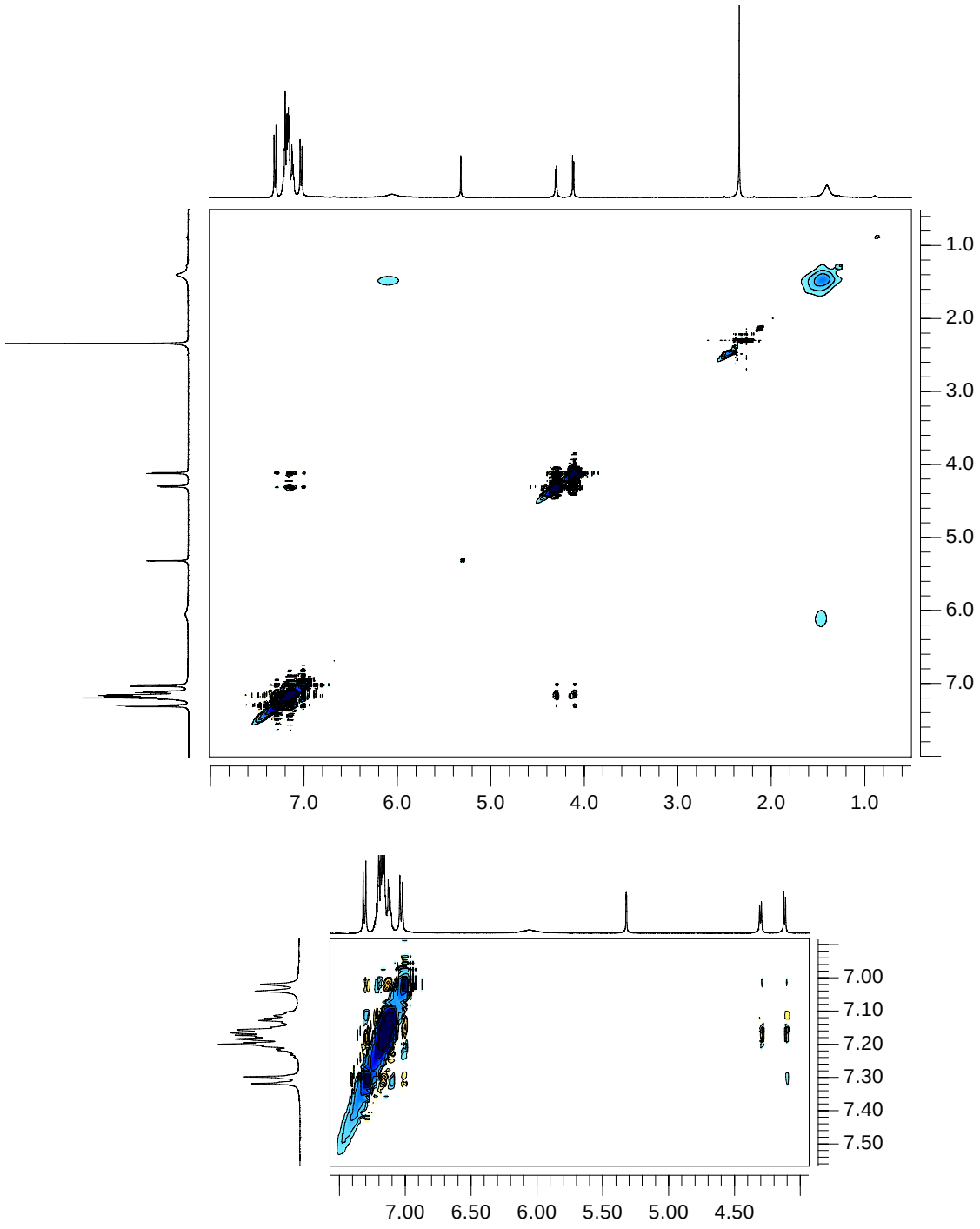


Figure 66: NOESY of 6.

more coupling the ligand. The presence of a Cp* ring is evident and the methyl group becomes more shielded. The aromatic region also changes drastically. These differences indicate the presence of a species different from the starting material. There is a comparison of the proton NMR of the starting material and resultant catalyst product in Figure 67. The reaction scheme for this synthesis is shown in Figure 68.

2.5.1.3 Spectroscopy of catalyst, 1

This molecule was characterized using 1D and two-dimensional NMR. All studies used solutions of the catalyst in d_2-dichloromethane. For reference purposes, the proton NMR, carbon NMR, and a proposed final structure of the molecule is given at the end of this section. A comparison of all spectroscopic data are given in the same section and correlation information follows in a table.

At room temperature, the ^{13}C data contain thirteen resonances, four of which are quaternary and ^{1}H data contain fourteen distinguishable resonances; however, one of the previously mentioned fourteen ^{1}H resonances contains two unique protons identified by HMQC data which lie in nearly the same position so that they appear to be the same resonance; in fact they have different integration values. There is a lot of symmetry in the aromatic portion of the molecule. Although typical carbon spectrum integration should not be used on a regular basis, it can be used in correlation with proton integration to verify the number of protons in a section in a general manner. Only two of the eight aromatic methine protons integrate to one while the rest integrate two. This does make sense considering that there are possible symmetry planes throughout the aromatic rings causing *ortho* and *para* positions to be symmetric and overlap, especially in the carbon spectrum. COSY spectra indicate a minimum of five spin systems. Four of the five spins systems are designated as the tosyl protons (δ/ppm 6.809 and 7.310), phenyl ring one protons (δ/ppm 6.1819 and 7.112), phenyl ring two protons (δ/ppm 6.650, 6.783, 6.750, and 6.848) and the remaining backbone CH protons designated as H_1 (δ/ppm 3.710) and H_2 (δ/ppm 3.970). COSY data also indicate coupling between the two amine protons H_{up} (δ/ppm 3.450) and H_{dn} (δ/ppm 3.890). TOCSY data indicate an extended coupling between the aforementioned systems drawing H_1 and H_2 into the same spin system as H_{up}

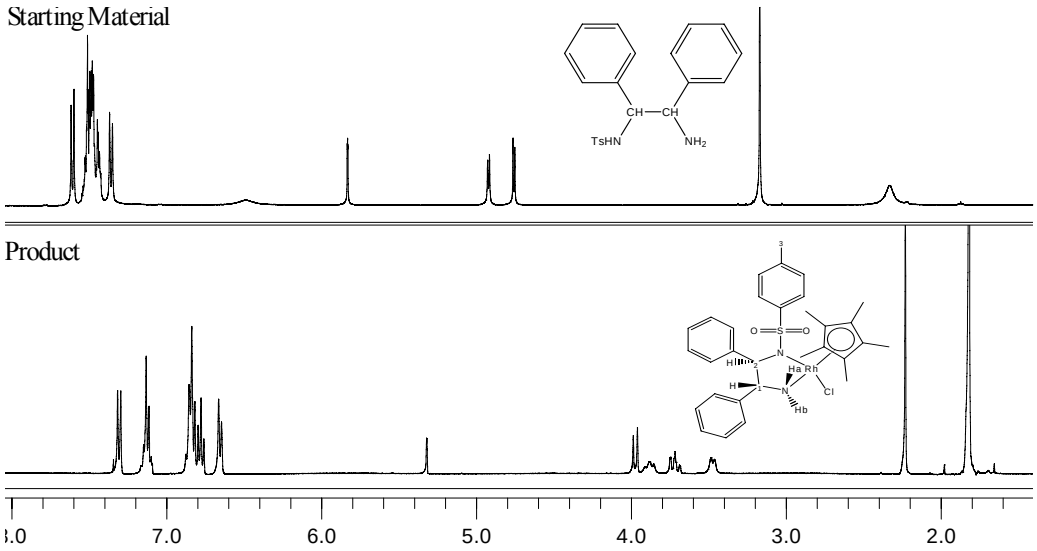


Figure 67: Comparison of proton spectra of ligand, 6, to catalyst, 1.

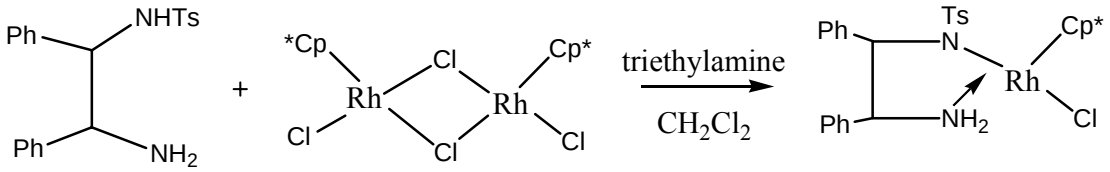


Figure 68: Synthesis of 1.

and H_{dn} which would be expected. Additionally, the methyl group can be correlated with the tosyl ring.

The HMQC spectrum identifies which carbon atoms to which the backbone protons are attached. The proton attached to C1 (δ/ppm 72.13) has a chemical shift at δ/ppm 3.710 whereas the proton attached to C2 (δ/ppm 69.97) is more deshielded with a chemical shift at δ/ppm 3.970. Other important information that the HMQC was able to determine was the presence of two unique proton resonances, $H_{1\text{-}m}$ and $H_{1\text{-}p}$, at δ/ppm 7.112 due to the overlap with two distinct carbon resonances; C1-*p*, which has an integration of one carbon atom (δ/ppm 128.818) and C1-*m*, which has an integration of two carbon atoms (δ/ppm 129.008). This is in accord with the integration of three for the proton region. These are not diastereotopic protons due to the identical chemical shift; instead, they are accidentally equivalent. The identification of the actual position of all of these HMQC correlations is possible with both HMBC and NOESY data. Without the associated data, it is possible to determine that C1-*p* is most likely a *para*-position as is C2-*p* (δ/ppm 126.877) because of the integration of the carbon spectrum compared to the integration of the proton region.

The HMBC spectrum is extremely beneficial in identifying the location and difference between the quaternary carbon atoms as well as which protons in the aromatic rings are *ortho* and *meta* positions. Additionally, it is used to identify which phenyl ring is attached to which backbone carbon, C1 or C2. This subsequently leads to the determination of the location of the remaining ring protons *via* COSY correlations. This experiment obtains information through ^{2}J or ^{3}J coupling; the most common of which is ^{3}J coupling since a value of 8 Hz was used as the long-range coupling constant. It is also possible for HMQC coupling to breakthrough and these can be easily identified by comparison with the HMQC spectrum. This breakthrough will not be mentioned with these correlations, as it gives no further information about the molecule than already determined.

The HMBC is able to identify the quaternary carbon positions using easily identifiable protons. Such is the case when looking for the correlations with H_3 (δ/ppm 2.23) which shows long distance coupling to carbon atoms with resonances of δ/ppm

139.85 and 128.305. These must correspond to CTs-*p* and CTs-*m* carbon atoms respectively because other distances would be too far for HMBC correlations. They can be differentiated because only one of these two carbon atoms has correlations to protons. The appropriate proton correlations can be identified *via* HMQC correlations.

Another important correlation is between H_5 (δ/ppm 1.820) and an unusual carbon atom, C4, which appears as a doublet at δ/ppm 94.56 with a coupling constant of 8.40 Hz with no HMQC correlations. This long distance correlation is to the quaternary carbon atom in the Cp^* ring. It is a doublet due to coupling with the Rhodium nucleus which has a spin of ½.

The phenyl ring systems can be distinguished by correlations with backbone carbon atoms H_1 and H_2. H_1 correlates with C2 and C1-*o*; likewise, $H_{1\text{-}o}$ correlates with C1 and H_2 correlates with C1. H_2 correlates with C1, C2-*i*, and C2-*o*; likewise, $H_{2\text{-}o}$ correlates with C2. COSY data allow for the remainder of the phenyl ring protons to be determined, assigned, and compared. Other ring correlations include $H_{1\text{-}o}$ to C1-*m* as well as C1, $H_{1\text{-}m}$ and $H_{1\text{-}p}$ to C1-*o*. It is not possible to distinguish between $H_{1\text{-}m}$ and $H_{1\text{-}p}$ but both of these correlations are possible. The second phenyl ring correlations include $H_{2\text{-}o}$ to C2-*p* as well as C2.

Although there are no correlations between H_2 and the tosyl ring carbon atoms, $H_{Ts\text{-}m}$ corresponds to CTs-*i* (δ/ppm 142.41). In addition to correlating to C3, $H_{Ts\text{-}o}$ also corresponds to CTs-*p*. The fact that the *meta*-protons are correlating to *ipso*-carbon atoms and *para*-protons correlating to *ortho*-protons instead of the reverse is not concerning because these distances are ^3J for which the value of long range coupling specified in the HMBC experiment is better suited. It is also interesting that H_{Nup} shows a correlation to C2.

The NOESY data will prove to be extremely important when determining the catalytic mechanisms, as does any exchange data obtained from the NOESY systems. When used in accord with previous data, information about the molecular structure can be clearly obtained. The orientation of the amide protons can be determined because there is a correlation between H_{Nup} and H_5 which indicates that this proton is oriented close to the Cp^* ring. Other expected close-proximity correlations with H_{Nup} include

H_{Ndn} and H_1. There is an unusual correlation in phase with the diagonal indicating that exchange is taking place. This is an exchange between H_{Ndn} and H_2.

The orientation of the aliphatic backbone methine protons can also be distinguished with the NOESY data. There is a correlation between H1 and H5 indicating that this proton is close to the Cp* ring. Other expected correlations with H_1 include H_{Nup}, H_{Ndn}, $H_{1\text{-}o}$, and $H_{2\text{-}o}$. These correlations obviously verify the HMBC assignment for the *ortho*-protons in the phenyl rings.

In the case of this spectrum, the NOESY spectra can be compared to the HMQC spectra to verify the exact positions of the protons in the overlapping multiplet which contains $H_{1\text{-}o}$, $H_{2\text{-}m}$, $H_{2\text{-}m'}$, $H_{2\text{-}p}$, and $H_{Ts\text{-}m}$. These correlations made it easier to distinguish the difference between the peaks by spreading their positions over a wider range. A previously undistinguished difference between $H_{2\text{-}m}$ and $H_{2\text{-}m'}$ was also distinguished. It is assumed that these protons are symmetrical with respect to the aromatic ring in which they are contained but that external proximity of one of these protons to the Cp* ring likely slightly varies their chemical shift slightly.

$H_{1\text{-}o}$ as previously mentioned shows correlation to H_1 and unlike $H_{2\text{-}o}$, shows no correlation to the Cp* ring. This would be expected since the H_1 proton is tilted towards the Cp* ring, this phenyl ring would be tilted away from it. $H_{1\text{-}o}$ also has correlations with H_2, $H_{1\text{-}m}$, and possibly $H_{1\text{-}p}$ although these two resonances cannot be distinguished.

$H_{2\text{-}o}$ must be in a position near to the Cp* ring due to correlation to H_5 and in fact this whole ring must be tilted towards the Cp* ring if the H_2 proton is tilted away from it. The H1 proton show correlations to the Cp* ring but the H_2 proton does not. Additionally, $H_{2\text{-}o}$ shows expected proximity to H_1, H_2, and $H_{2m'}$. In the same ring, there are also expected distance correlations between H_{2m} and H_{2p}.

Finally the $H_{Ts\text{-}o}$ has correlations with $H_{Ts\text{-}m}$ and H_5. $H_{Ts\text{-}m}$ has correlations with H_3. These are expected and indicate that the *ortho* protons are tilted toward the Cp* enough to have close proximity to it while the *meta*-protons are near to the methyl group.

Figure 69 shows a proposed structure of the molecule according to NMR. Carbon and proton spectra are shown in Figure 70. Spectral correlations are tabulated in Table 2.2 and Table 2.3. Relevant 2D spectra are shown in Figure 71 - Figure 79.

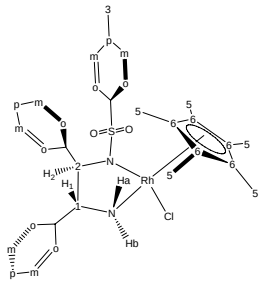


Figure 69: Structure of catalyst, 1, which is in accord with NMR data.

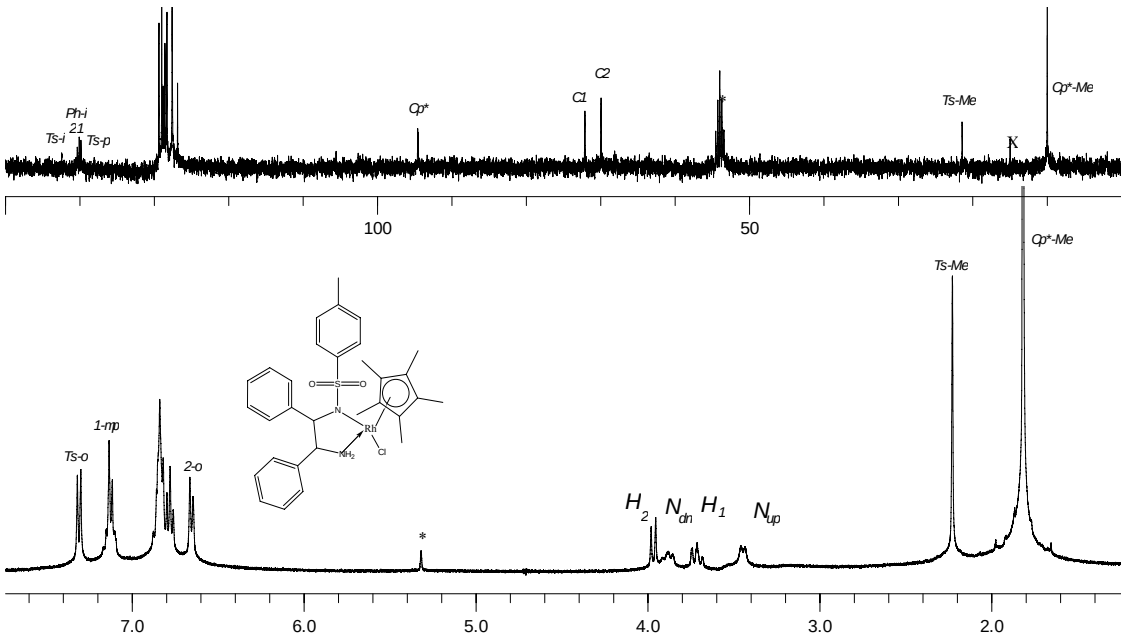


Figure 70: Proton and carbon spectra of 1.

^{1}H-NMR (400 MHz) δ/ppm 7.31 (d, J = 8.1 Hz, 2H) 7.13 (m, 3H) 6.85 (m, 5H) 6.78 (t, J = 7.6 Hz, 2H) 6.65 (d, 1H, J = 7.2 Hz, 2H) 3.97 (d, J = 10.8 Hz, 1H) 3.89 (m, 1H) 3.71 (t, J = 12.4 Hz, 1H) 3.45 (d, J = 9.4 Hz, 1H) 2.23 (s, 3H) 1.82 (s, 15H) ^{13}C-NMR (400 MHz) 142.41 (C) 140.350 (C), 140.094 (C), 139.854 (C), 129.374 (CH), 129.008 (CH), 128.820 (CH), 128.564 (CH), 128.305 (CH), 127.614 (CH), 127.577 (CH), 126.877 (CH), 94.56 (d, CH, J_{RhC} = 8.4 Hz), 72.125 (CH), 69.959 (CH), 21.429 (CH_3), 9.993 (CH_3)

Table 2.2: Correlations for 1, part I.

^{1}H position	^{13}C *(ppm)*	^{1}H *(ppm)*	*int*	m	^{2}J (Hz)
N_{up}	N/A	3.450	1	d	9.1
N_{dn}	N/A	3.890	1	m	-
1	72.13	3.710	1	t	11.1
2	69.96	3.970	1	d	10.8
1-*i*	140.09	N/A	N/A	N/A	N/A
1-*o*	127.614	[a]6.819	2	m	[b]7.8
1-*m*	129.008	7.112	2	m	[b]7.5
1-*p*	128.818	7.112	1	"	"
2-*i*	140.35	N/A	N/A	N/A	N/A
2-*o*	129.374	6.650	2	d	7.2
2-*m*	127.577	[a]6.783	1	t	7.6
2-*m'*	"	[a]6.750	1	t	"
2-*p*	126.877	[a]6.848	1	m	[c]8.1
Ts-*i*	142.41	N/A	N/A	N/A	N/A
Ts-*o*	128.564	7.310	2	d	8.10
Ts-*m*	128.305	[a]6.809	2	m	[c]8.1
Ts-*p*	139.85	N/A	N/A	N/A	N/A
3	21.423	2.23	3	s	N/A
4	94.56	N/A	N/A	d	8.4
5	9.99	1.820	15	s	N/A

Table notes given after Table 2.3.

Table 2.3: Correlations for 1, part II.

^{1}H position	^{13}C *(ppm)*	^{1}H *(ppm)*	COSY	TOCSY	HMBC *(C)*	NOESY
N_{up}	N/A	3.450	N_{dn}	[f]1, [f]2	2	N_{dn}, 1, **5**
N_{dn}	N/A	3.890	N_{up}	1, 2		1*, N_{up}
1	72.13	3.710	2	[f]N_{up}, N_{dn}	2, 1-*o*	N_{up}, N_{dn}*, 1-*o*, **2-*o***, **5**
2	69.96	3.970	1	[f]N_{up}, N_{dn}	1, 2-*i*, 2-*o*	1-*o*, **2-*o***
1-*i*	-	N/A	N/A	N/A	N/A	N/A
1-*o*	127.614	[a]6.819	1-*m*/1-*p*	-	1-*m*, 1	1-*m*/1-*p*, 1, 2
1-*m*	129.008	7.112	[e]1-*o*	-	1-*o*	[d]1-*o*, 1-*p*
1-*p*	128.818	7.112	[e]1-*o*	-	1-*o*	[d]1-o, 1-p
2-*i*	140.35	N/A	N/A	N/A	N/A	N/A
2-*o*	129.374	6.650	2-*m'*	2-*p*	2-*p*, 2	2-*m'*, 1, 2, **5**
2-*m*	127.577	[a]6.783	-	-	2-*i*	2-*o*
2-*m'*	"	[a]6.750	2-*o*, 2-*p*	-	2-*i*	2-*p*
2-*p*	126.877	[a]6.848	2-*m*	2-*o*	-	2-*m*
Ts-*i*	142.41	N/A	N/A	N/A	N/A	N/A
Ts-*o*	128.564	7.310	Ts-*m*	3	Ts-*p*, 3	**5**, Ts-*m*
Ts-*m*	128.305	[a]6.809	Ts-*o*	3	Ts-*i*	3, Ts-*o*
Ts-*p*	139.85	N/A	N/A	N/A	N/A	N/A
3	21.423	2.23	-	Ts-*o*, Ts-*m*	Ts-*m*, Ts-*p*	Ts-*m*
4	94.56	N/A	N/A	N/A	N/A	N/A
5	9.99	1.820	-	-	4	2-*o*, Ts-*o*, 1, N_{up}

Dashes are used to indicate that these data could not be assigned. All spectra were obtained on a Bruker Avance 400 MHz instrument using a 5 mm probe. Unless otherwise noted, all experiments were performed at room temperature. All other symbol explanations follow. [a]Exact peak positions determined from NOESY data. [b]Other coupling constants are present. [c]Coupling constant is part of an overlapping multiplet but this particular value could be determined. [d]This correlation is could be with either 1-m or 1-p, due to the fact that these peaks overlap. [e]This correlation is could be with either 1-m or 1-p, due to the fact that these peaks overlap; however, it is most likely due to 1-m since 1-o is closer to it. [f]These are weak correlations.

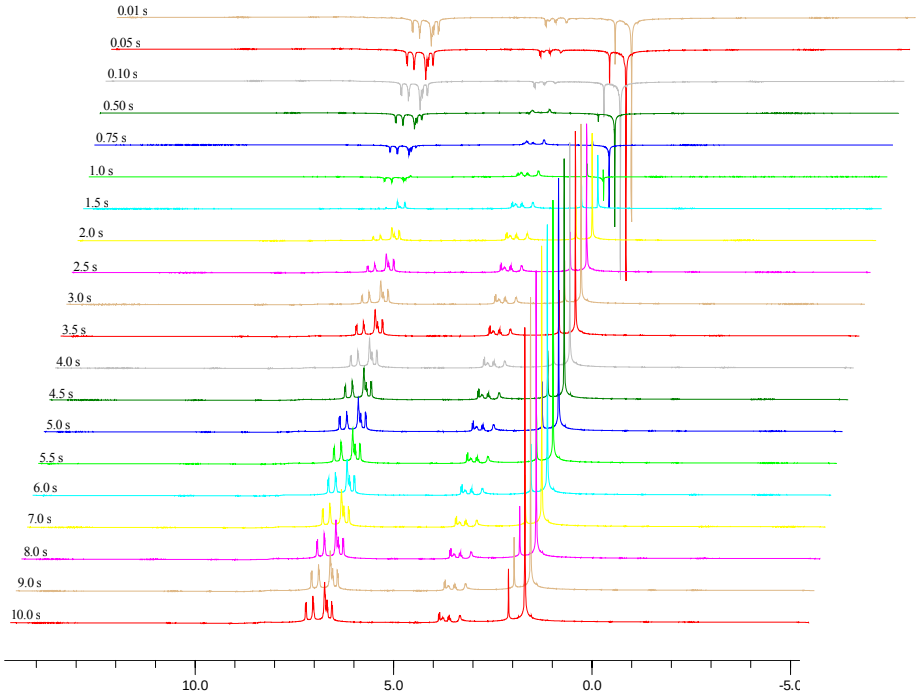


Figure 71: T_1 relaxation of 1.

^{1}H-NMR (400 MHz) δ/ppm 7.31 (2.1 s) 7.13 (2.07) 6.85 (1.7 s) 6.78 (1.8 s) 6.65 (1.33 s) 3.97 (0.8 s) 3.89 (^{a}0.3 s) 3.71 (^{a} 0.72 s) 3.45 (0.25 s) 2.23 (0.97 s) 1.82 (1.6 s) ^{a}From other T_1 data.

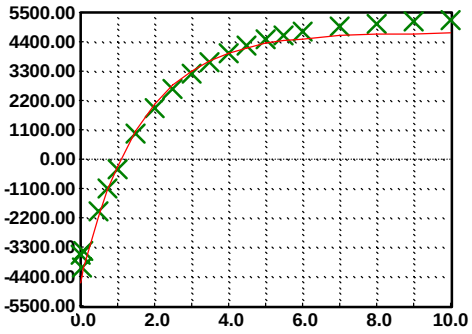


Figure 72: Example of T_1 using Cp*.

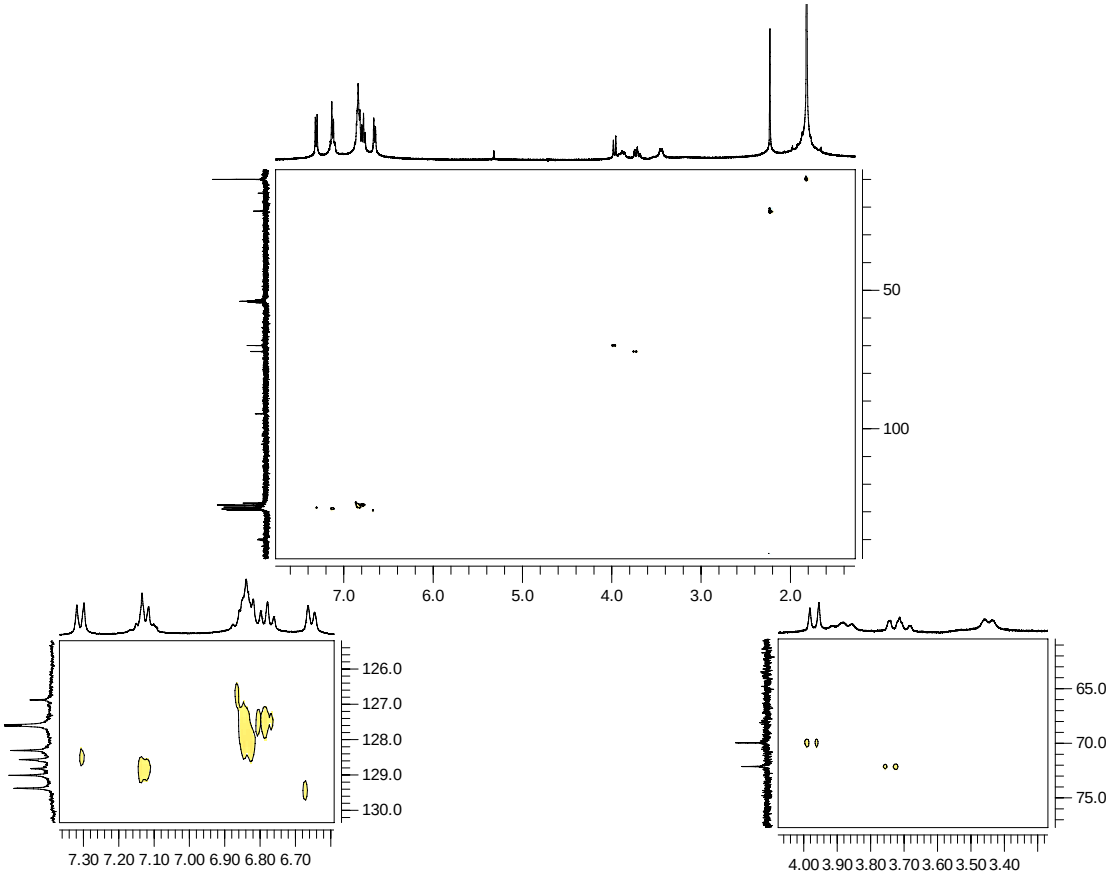


Figure 73: HSQC of 1.

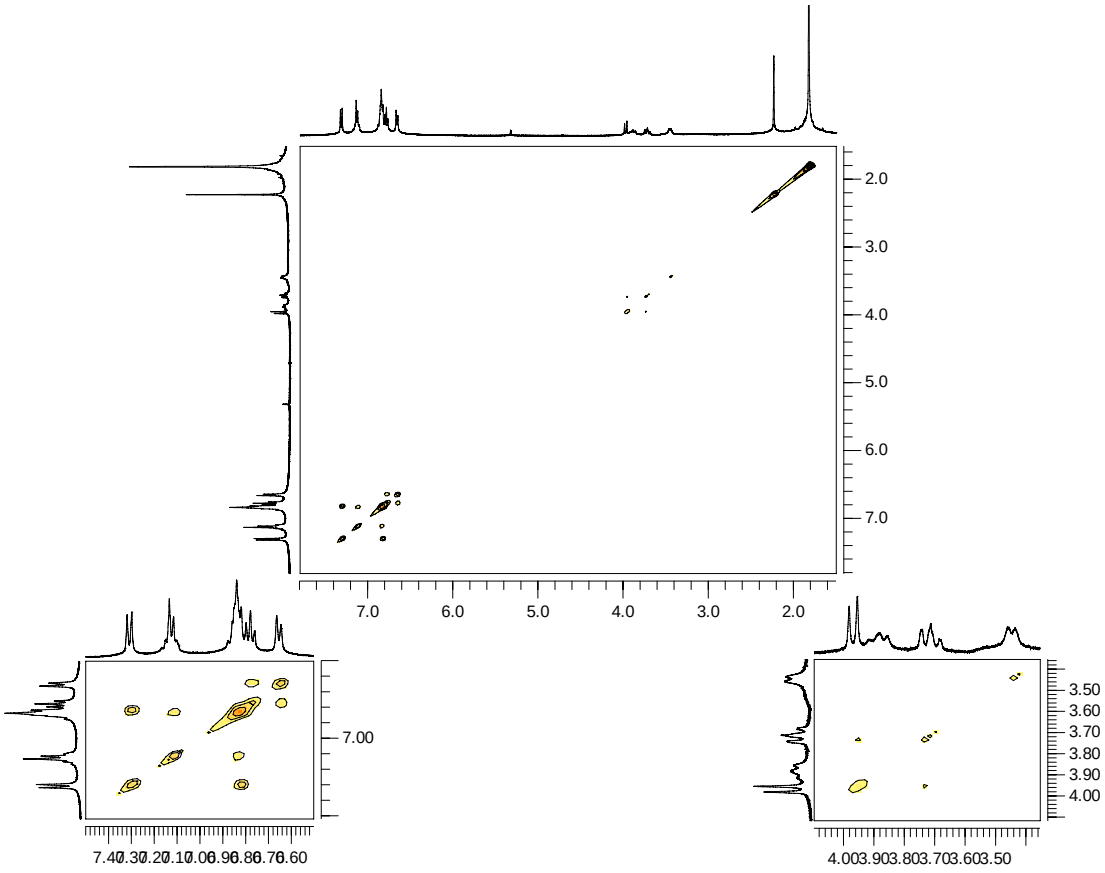


Figure 74: COSY of 1.

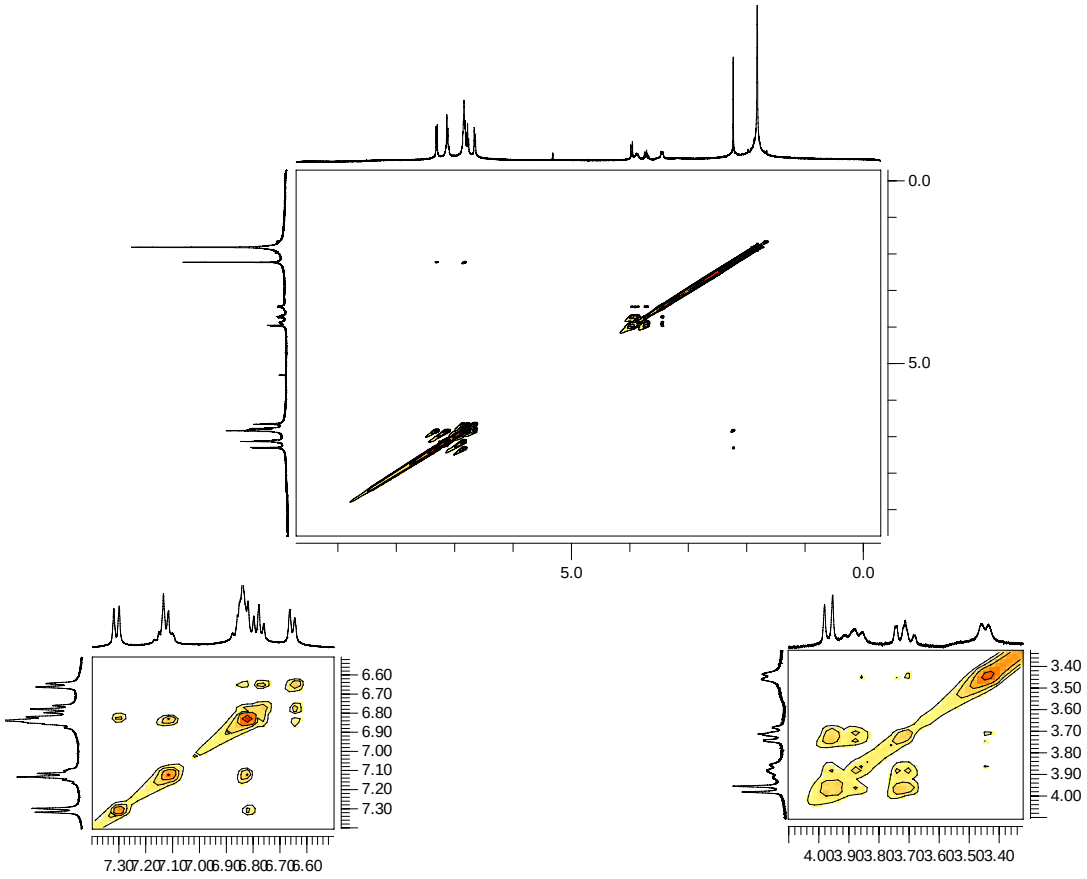


Figure 75: TOCSY of 1.

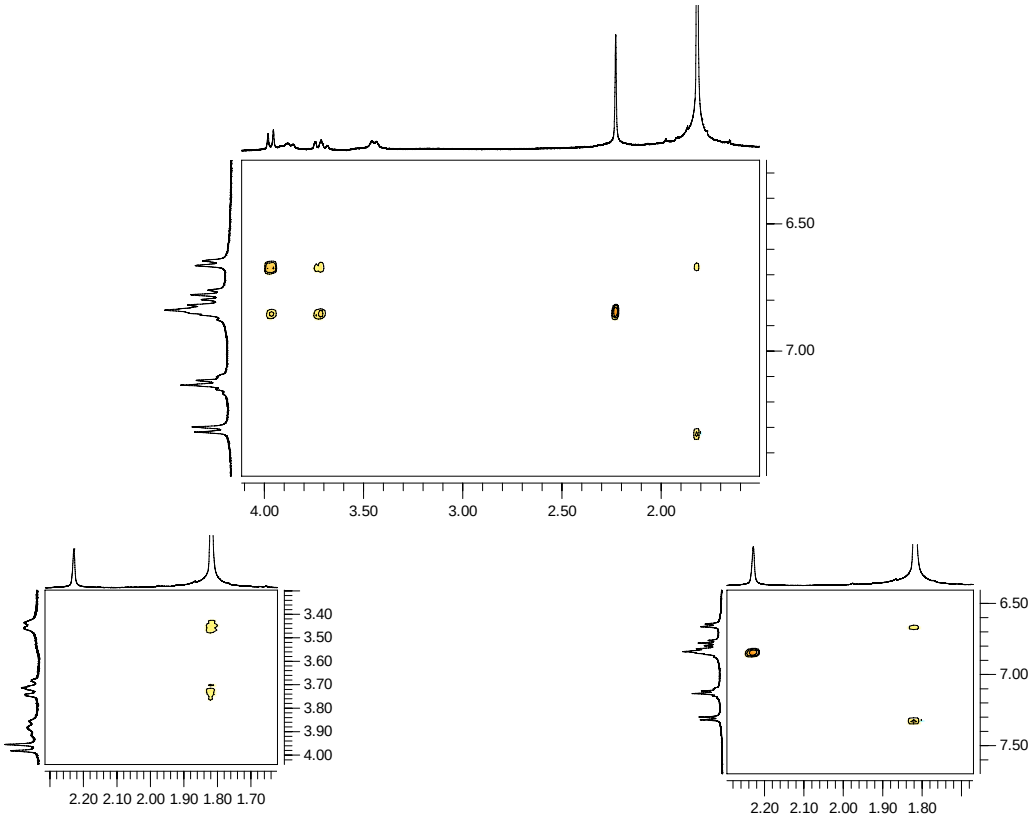


Figure 76: NOESY expansions of 1.

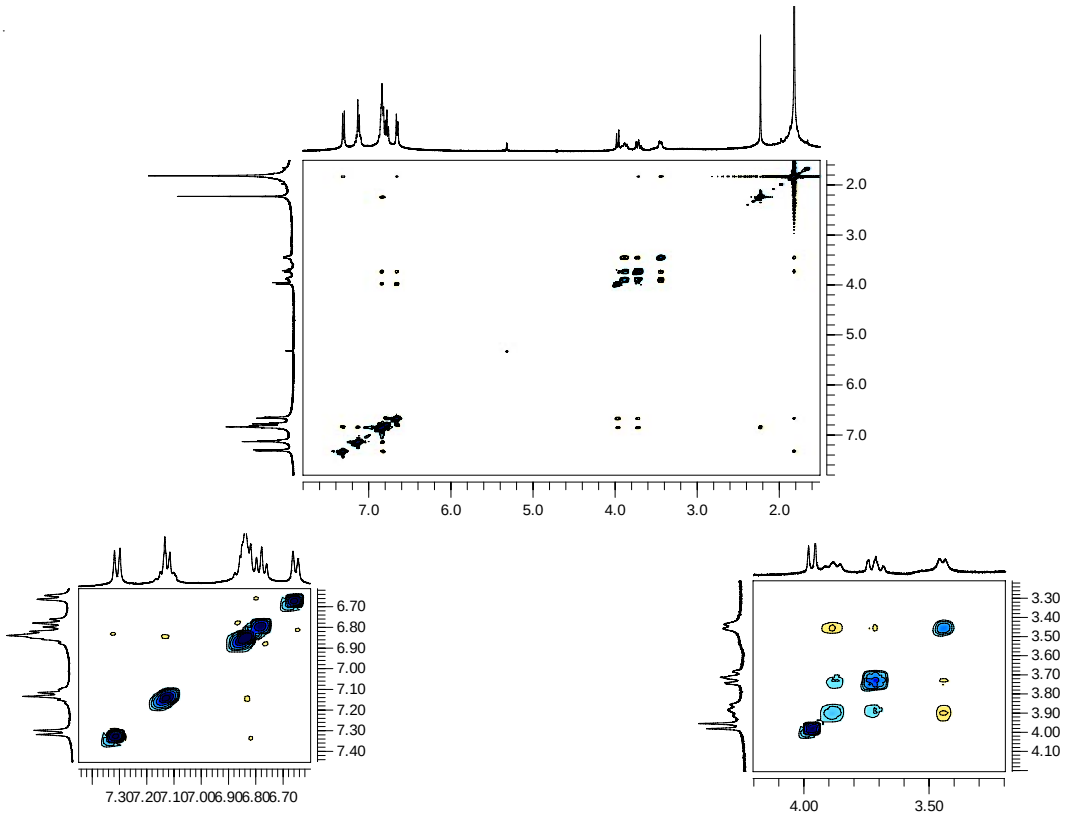


Figure 77: Full NOESY of 1.

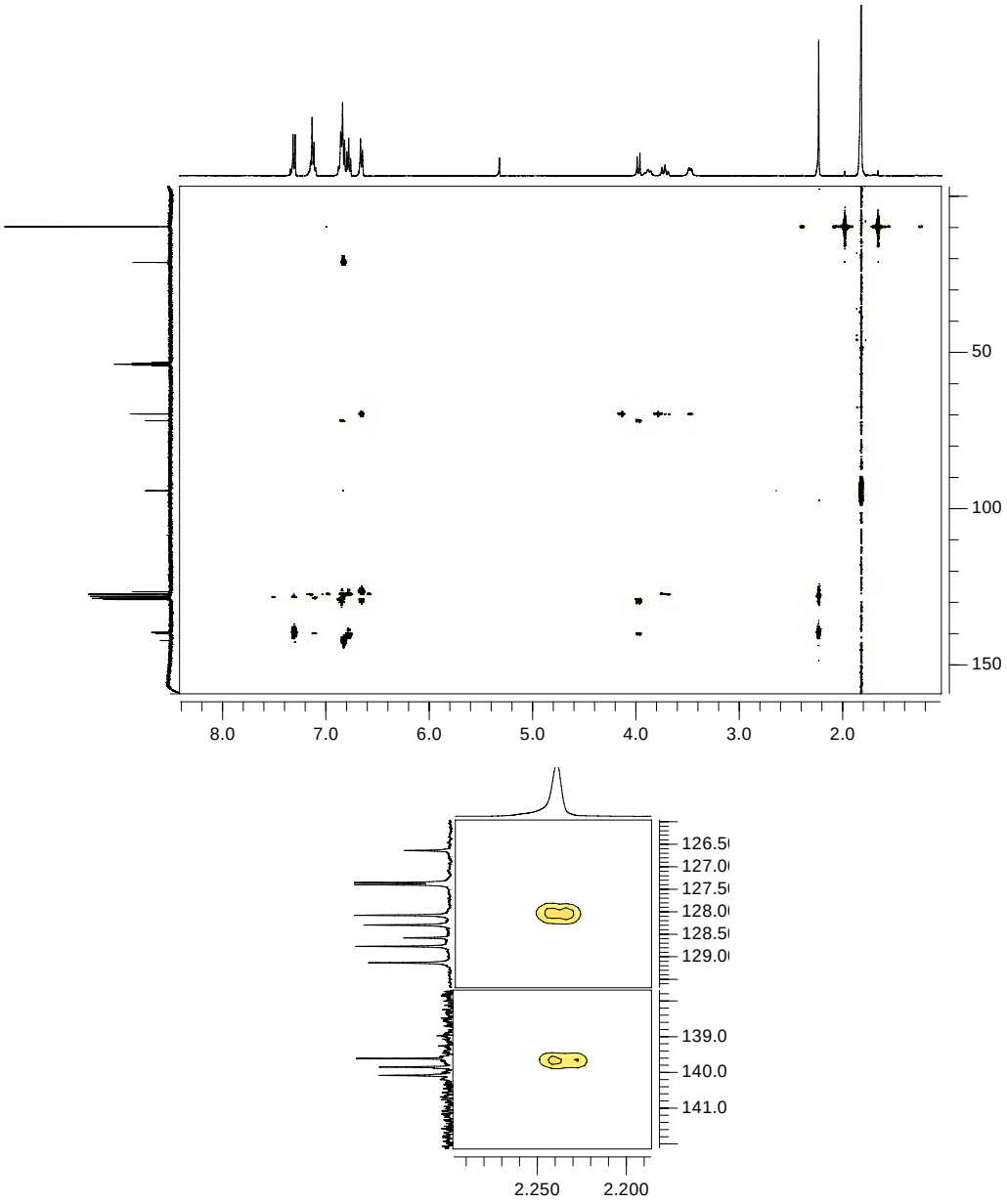


Figure 78: HMBC of 1.

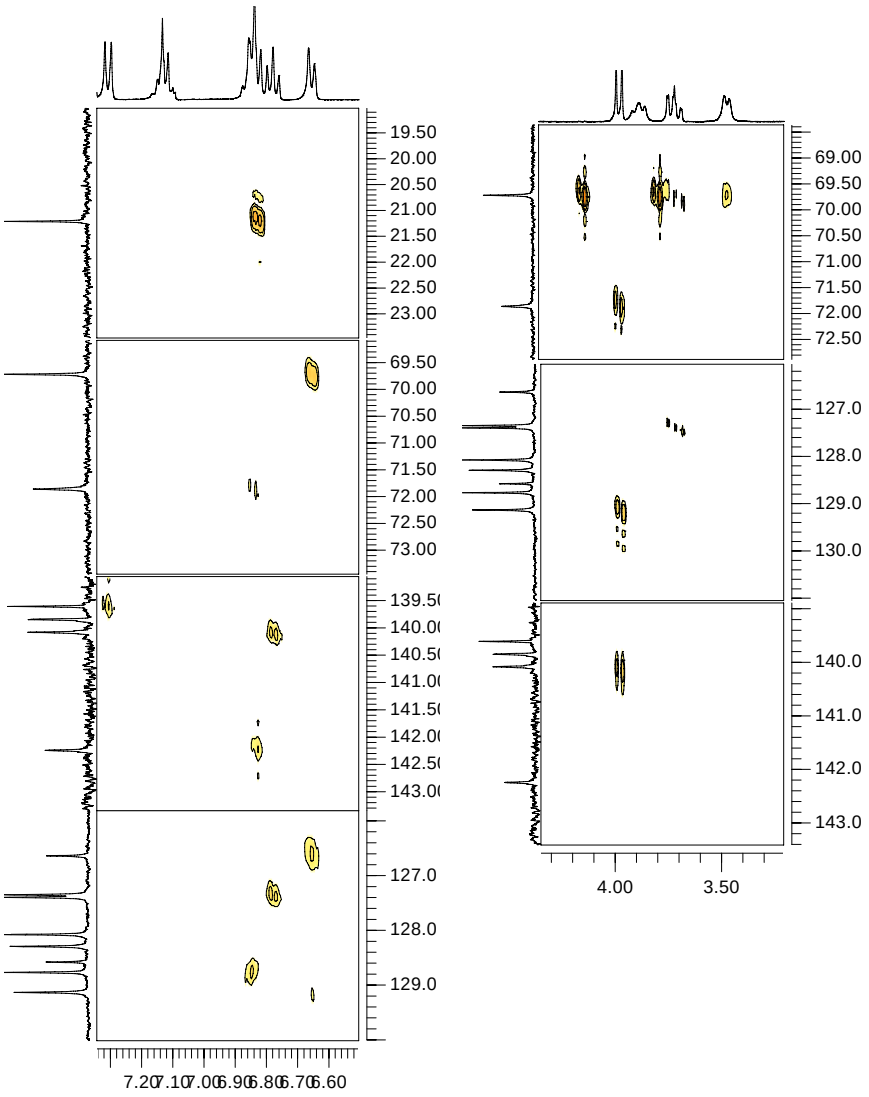


Figure 79: HMBC expansion of 1.

2.5.1.4 Evidence of 5a

The most obvious difference between **1** and **5a** is that the backbone CH and NH region is more deshielded and spread apart by δ/ppm 0.5 to 1. The aromatic region contracts as it becomes slightly more deshielded in some cases and especially more complicated. There is a comparison of the starting material and product in Figure 80. The synthesis was shown in Figure 54. Degradation of the silver chloride salt in solution is obvious by a small broad peak at about δ/ppm 3.5. The presence of the degraded product was inevitable in the long range 2D and the period of time it requires to run these experiments. This degradation did not appear to affect the other portions of the proton or carbon spectra as comparisons were made before and after the degradation peak appeared. As a result, the 2D data are considered valid.

2.5.1.5 Spectral data of 5a

This molecule was characterized using 1D and two-dimensional NMR. All studies used solutions of the catalyst in d_2-dichloromethane. For reference purposes, the proton NMR, carbon NMR, and a proposed final structure of the molecule is given at the end of this section. A comparison of all spectroscopic data are given in the same section and correlation information follows in a table.

At room temperature, the ^{13}C spectrum contains seventeen resonances, two sets of which were distinguished using HMBC data and the ^{1}H spectrum contains fourteen resonances at room temperature. Five of the ^{13}C resonances are quaternary carbon atoms. Although typical carbon spectrum integration should not be used on a regular basis, it can be used in correlation with proton integration to verify the number of protons in a section in a general manner. In this manner and in correlation with HMQC data, two of the overlapping carbon signals can be separated.

COSY spectra indicate a minimum of four spin system which can each be connected to the other systems *via* H_1 (δ/ppm 4.03) or H_2 (δ/ppm 4.39) and that spin system. The spins systems are designated as the tosyl protons (δ/ppm 6.83 and 7.09), phenyl ring one protons (δ/ppm 7.06, 7.17, and 7.23), phenyl ring two protons (δ/ppm

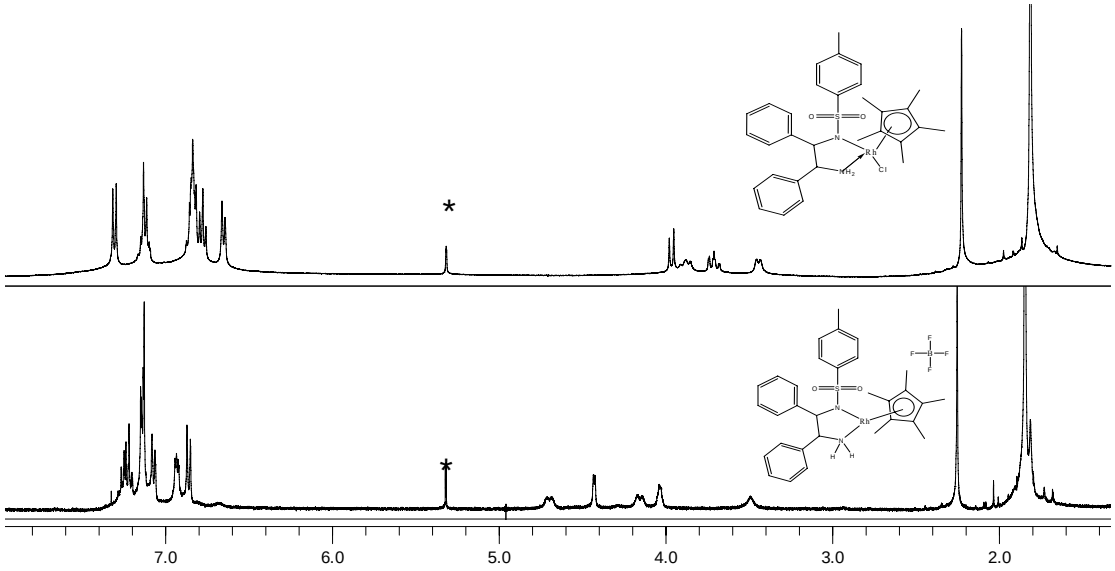


Figure 80: Proton spectra of 1 compared to 5a.

6.94, 7.11, and 7.23) and the remaining backbone system designated as H_1 (δ/ppm 4.03), H_2 (δ/ppm 4.39), NH_{up} (δ/ppm 4.21) and NH_{dn} (δ/ppm 4.97).

COSY data also indicate the connectivity between these systems by correlating H_1 with $H_{1\text{-}o}$, $H_{2\text{-}o}$, and NH_{up}. coupling between the two amine protons H_{up} (δ/ppm 3.450) and N_{dn} (δ/ppm 3.890). Additionally, the methyl group, H_3 (δ/ppm 2.25), also correlates to other tosyl ring proton, $H_{Ts\text{-}p}$. TOCSY data indicate slightly more information in addition to the COSY data.

The HMQC spectrum identifies which carbon atoms to which the backbone protons are attached. This information can be obtained from the table.

The HMBC spectrum does show long range coupling between certain systems and reinforces the assignments already made. H_2 is correlated with C2-*i*, C2-*o*, and C1. This correlations defines which phenyl ring is attached to C1 *vs.* C2. As a result of the C-2 correlations, the C1 atom must be the signal correlated to the remaining phenyl ring. Additionally, $H_{1\text{-}o}$ has correlations with C1, which verifies the assignment.

Phenyl ring 1 is further clarified with correlations between: $H_{1\text{-}o}$ and C1-*p*. This is not unusual considering that this distance covers three bonds rather than the two bonds that do not show an interaction between $H_{1\text{-}m}$ and C1-*p*. In all these cases, this does not mean that correlations are missing, only that the program was not calibrated to calculated coupling constants over these distances. Additionally, $H_{1\text{-}m}$ correlates with C1-*i* and $H_{1\text{-}p}$ correlate with it also.

Phenyl ring 2 is also further clarified with correlations between: $H_{2\text{-}o}$ and C2-*m*. This correlation is also present in reverse where $H_{2\text{-}m}$ correlates with C2-o. Additionally, the tosyl ring is distinguished *via* correlations with $H_{Ts\text{-}o}$ and CTs-*p*. $H_{Ts\text{-}m}$ has correlations with C3, CTs-*o*, and CTs-*i*. All of these correlations make sense.

The NOESY data will prove to be extremely important when determining the solution structure. One of the important correlations is between H_1 and NH_{up}. This indicates that this amido proton is indeed in the same direction as H_1, which from the starting configuration is *up*. Another important correlation is that between NH_{dn} and $H_{1\text{-}o}$. By default NH_{dn} must be *down* if NH_{up} is to be *up*, the correlation between NH_{dn} and $H_{1\text{-}o}$ reinforces that conclusion since phenyl ring 1 must be *down* if H_1 is to be *up*. An

expected correlation is that between NH_{up} and NH_{dn}. H_1 also has the expected correlation with H_2. Additionally both H_1 and H_2 show correlations with $H_{1\text{-}o}$ and $H_{2\text{-}o}$. Neither of these correlations appears to be inconsistent.

NOESY information with respect to the ring systems also is important as it can reinforce other data. $H_{1\text{-}o}$ and $H_{1\text{-}m}$ have correlations. $H_{Ts\text{-}o}$ correlates with both $H_{Ts\text{-}m}$ and C5 which corresponds to the Cp* ring indicating that these aromatic protons must be close to the Cp* ring. $H_{Ts\text{-}m}$ also correlates with $H_{3,\ which}$ is to be expected.

Figure 81 shows a proposed structure of the molecule according to NMR. Carbon and proton spectra are shown in Figure 82. Spectral correlations are tabulated in Table 2.4. Relevant 2D spectra are shown in Figure 83- Figure 89.

2.5.1.6 Evidence of the synthesis of molecule 4

This reaction was performed in two different solvents and both sets of spectra have been included. When the reaction is performed in d_2-methylene chloride, there is a large chemical shift of the sultam amine proton about δ/ppm 1.3. The rest of the spectra appear very much the way it would be expected for an overlap of the two spectra. In the case of d_8-THF, one major difference was the upfield shift of the sultam amine proton about δ/ppm 0.3. Additionally the two NH peaks are almost completely converged. On the 600 MHz instrument, there NH peaks converge completely. There is a comparison of the starting material and product in two different solvent systems in Figure 90 and Figure 91. The synthesis is shown in Figure 54.

2.5.1.7 Spectral data of molecule 4

The VT NMR is very interesting as it shows that the chemical shifts of all three NH protons in the bound species vary extensively depending on temperature. Most importantly, the NH_s peak becomes further deshielded as temperature decreases. Comparisons in two different solvents are shown in Figure 92 and Figure 93.

There are no 2D correlations between either NH_s or CH_s and the rest of the catalytic species. This is not necessarily disturbing considering that the scalar coupling . could be disturbed between the sultam and the metal canter. This is due to the fact that

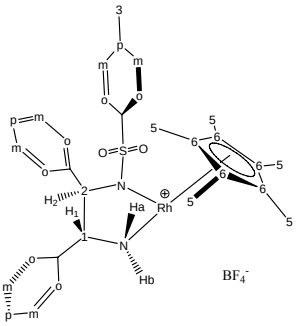


Figure 81: Structure of 5a which is in accord with NMR data.

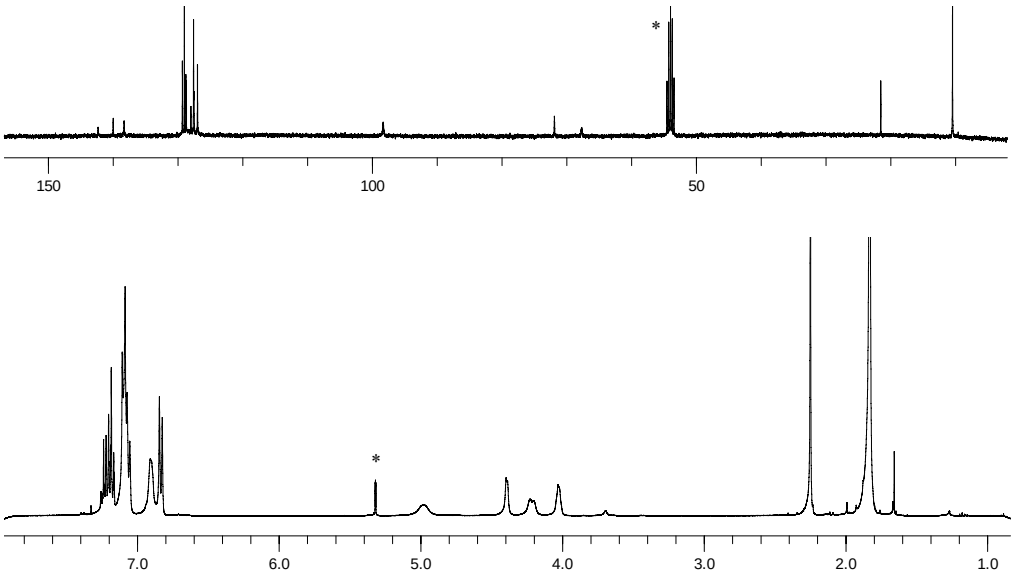


Figure 82: Proton and carbon spectra of 5a.

^{1}H-NMR (400 MHz) δ/ppm 7.21 (m, 3H) 7.09 (m, 7H) 6.90 (d, *J* = 2.9 Hz, 2H) 6.84 (d, *J* = 8.0 Hz, 2H) 4.97 (s, 1H) 4.39 (d, *J* = 4.0 Hz, 1H) 4.21 (m, 1H) 4.03 (d, *J* = 3.8 Hz, 1H) 2.25 (m, 3H) 1.83 (s, 15H) ^{13}C-NMR (400 MHz) 142.324, 139.997, 138.317, 129.322 (2), 129.024 (2), 128.790/128.712 (3), 128.005 (1), 127.598/127.532 (4), 126.989 (2), 98.334, 71.915, 67.720, 21.552, 10.479

Table 2.4: NMR correlations for 5a.

^{1}H position	^{13}C (δ/ppm)	^{1}H (δ/ppm)	m	^{2}J (|J|/Hz)	COSY	HMBC *(C)*	NOESY
N_{up}	N/A	4.21	b	-	N_{dn}, 1	-	N_{dn}, 1
N_{dn}	N/A	4.97	b	-	N_{up}, 1	-	N_{up}, 1-*o*
1	67.72	4.03	d	3.8	1-*o*, 2-*o*, N_{up}	-	2, 1-*o*, 2-*o*, N_{up}
2	71.92	4.39	d	4.0	1	1, 2-*i*, 2-*o*	1, 1-*o*, 2-*o*
1-*i*	140.00	N/A	N/A	N/A	N/A	N/A	N/A
1-*o*	[a]126.99	7.06	m	-	1-*m*, 1-*p*	1, 1-*p*	N_{dn}, 1, 2, 1-*m*
1-*m*	129.02	7.17	m	-	1-*o*	1-*i*	1-*o*
1-*p*	[b]128.71	7.23	m	-	1-*o*	1-*o*	-
2-*i*	138.32	N/A	N/A	N/A	N/A	N/A	N/A
2-*o*	127.60	6.94	d	2.9	2-*m*	2-*m*	1, 2
2-*m*	[b]128.79	7.11	m	-	2-*o*	2-*i*	-
2-*p*	128.01	7.10	m	-	unclear	-	-
Ts-*i*	138.32	N/A	N/A	N/A	N/A	N/A	N/A
Ts-*o*	[a]127.53	7.09	m	-	Ts-*m*	Ts-*p*	5, Ts-*m*
Ts-*m*	129.32	6.83	d	8.0	Ts-*o*	Ts-*o*, Ts-*i*, 3	3, Ts-*o*
Ts-*p*	142.32	N/A	N/A	N/A	N/A	N/A	N/A
3	21.55	2.25	s	-	Ts-*m*	Ts-*m*, Ts-*p*	Ts-*m*
4	98.36	N/A	b	-	N/A	N/A	N/A
5	10.50	1.83	s	-	Ts-*o*	5	Ts-*o*

Dashes are used to indicate that these data could not be assigned. All spectra were obtained on a Bruker Avance 400 MHz instrument using a 5 mm broadband probe. Unless otherwise noted, all experiments were performed at room temperature. All other symbol explanations follow. [a]The center of HMBC crosspeaks is used to distinguish these close carbon atom resonances. [b]Carbon and proton integration are used in correlation to distinguish these peaks. [c]Exchange information is indicated.

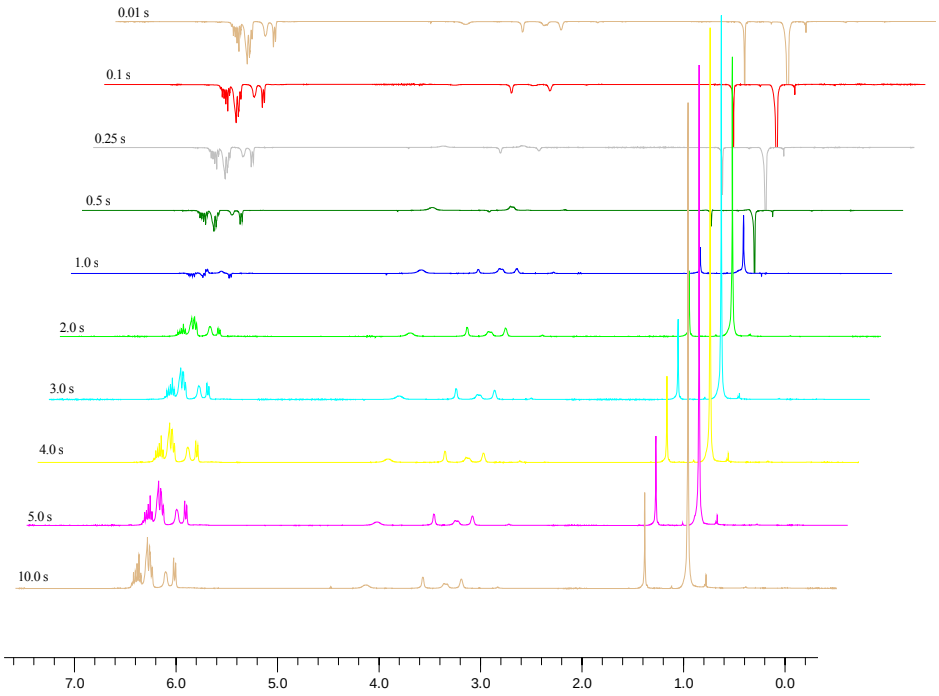


Figure 83: T_1 relaxation of 5a.

Time delays: 10.0 s, 5.0 s, 4.0 s, 3.0 s, 2.0 s, 1.0 s, 0.5 s, 0.25 s, 0.10 s, 0.05 s, 0.01 s.
T_1 results: δ/ppm 7.21 (1.7 s) 7.09 (1.6 s) 6.90 (1.15 s) 6.84 (1.8 s) 4.97 (0.202 s) 4.39 (0.87 s) 4.21 (0.22 s) 4.03 (0.68s) 2.25 (0.96s) 1.83 (1.2s)

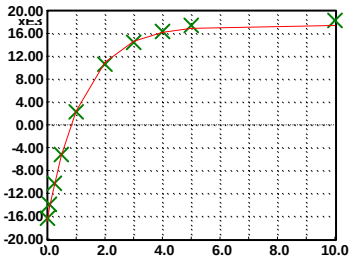


Figure 84: Graph of T_1 calculation for the Cp* proton peak for example purposes.

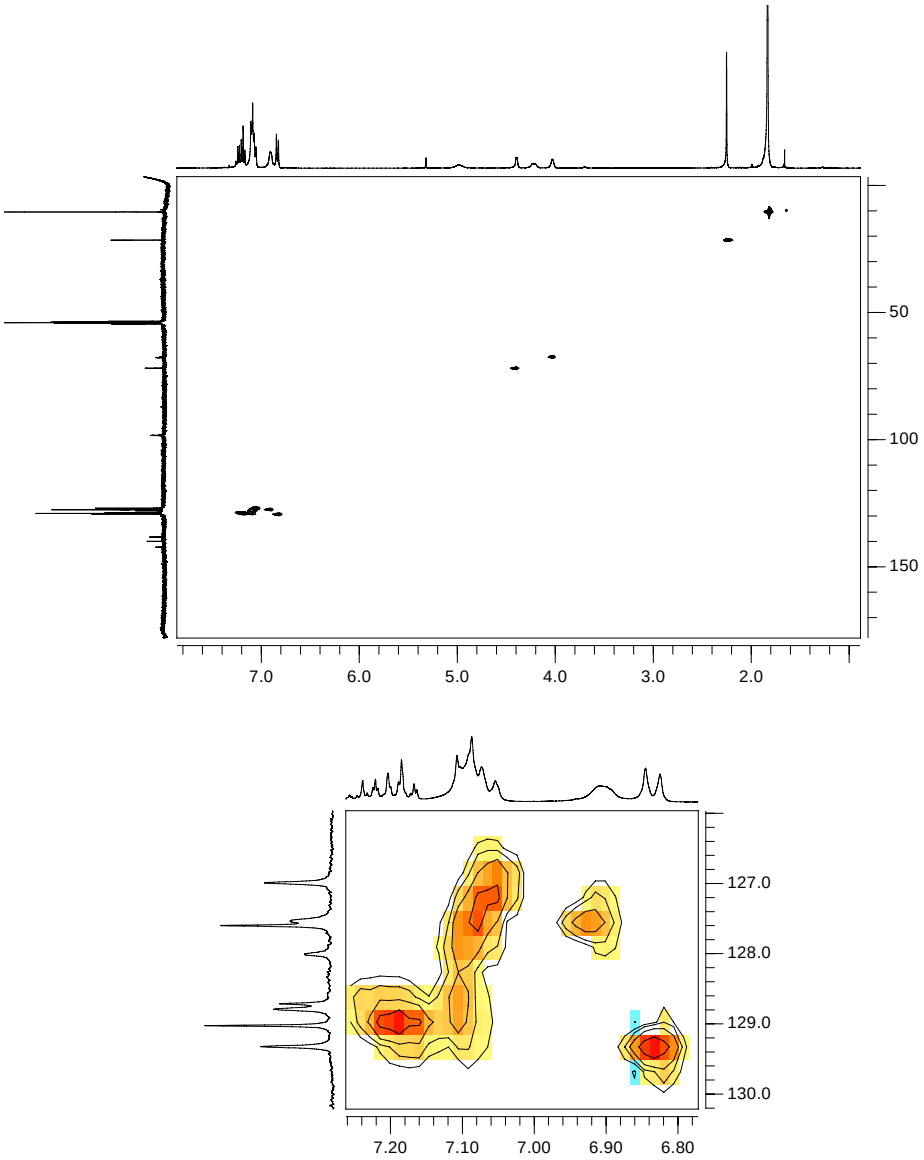


Figure 85: HMQC of 5a.

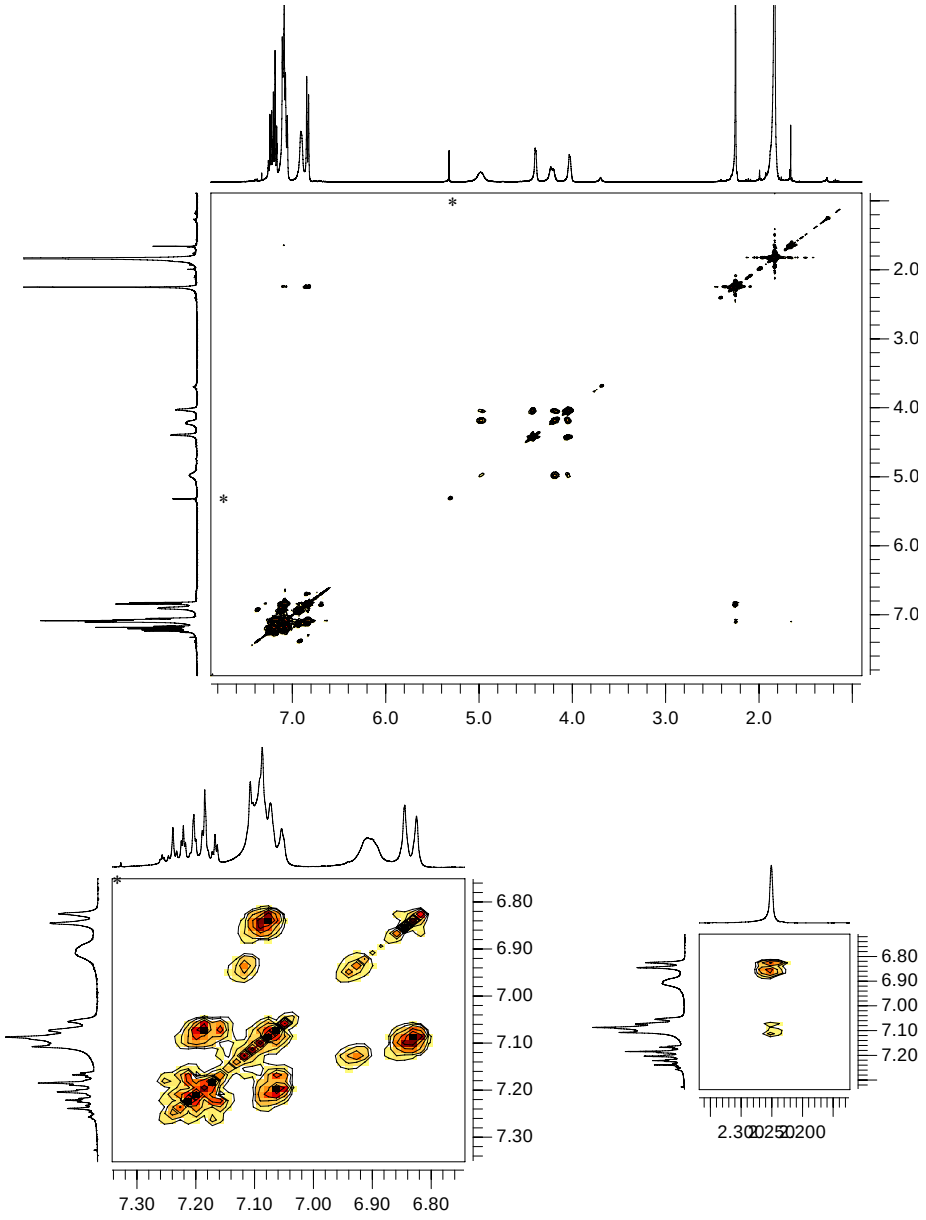


Figure 86: COSY of 5a.

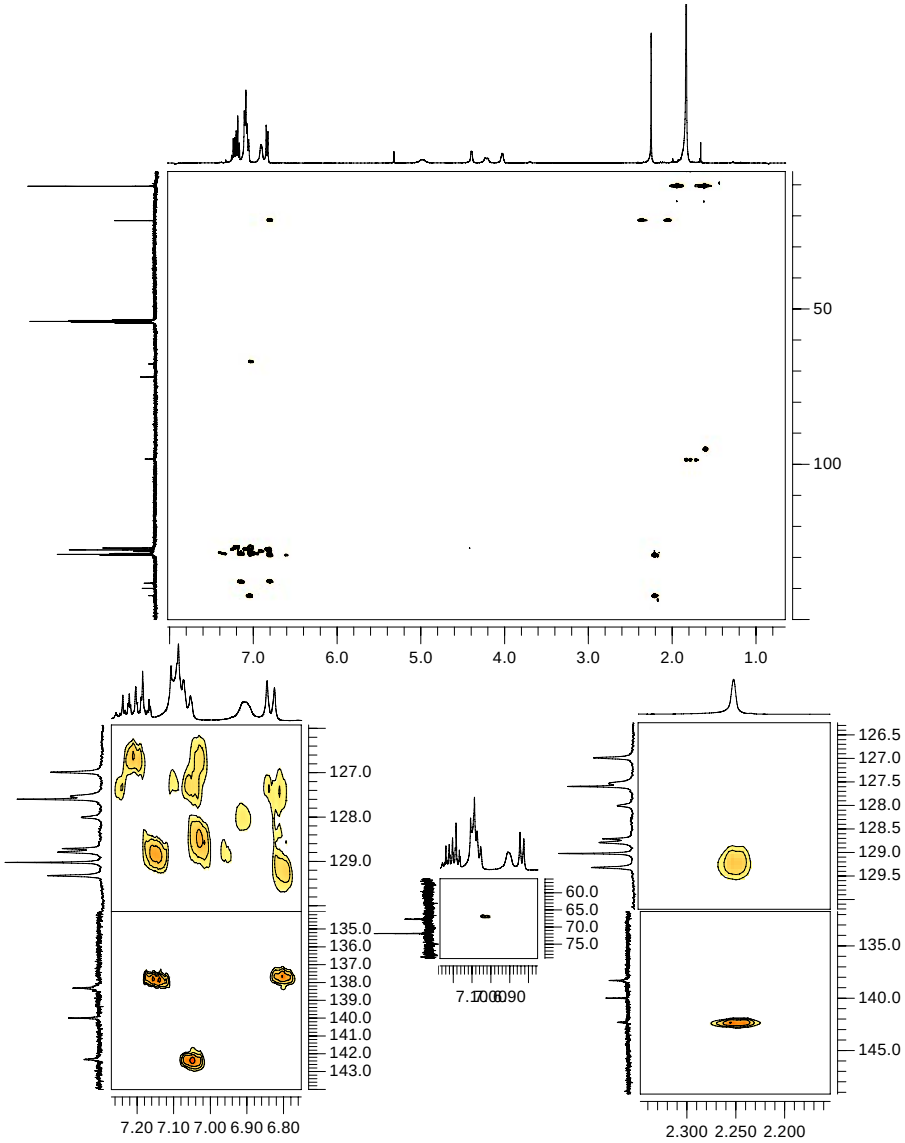


Figure 87: HMBC of 5a.

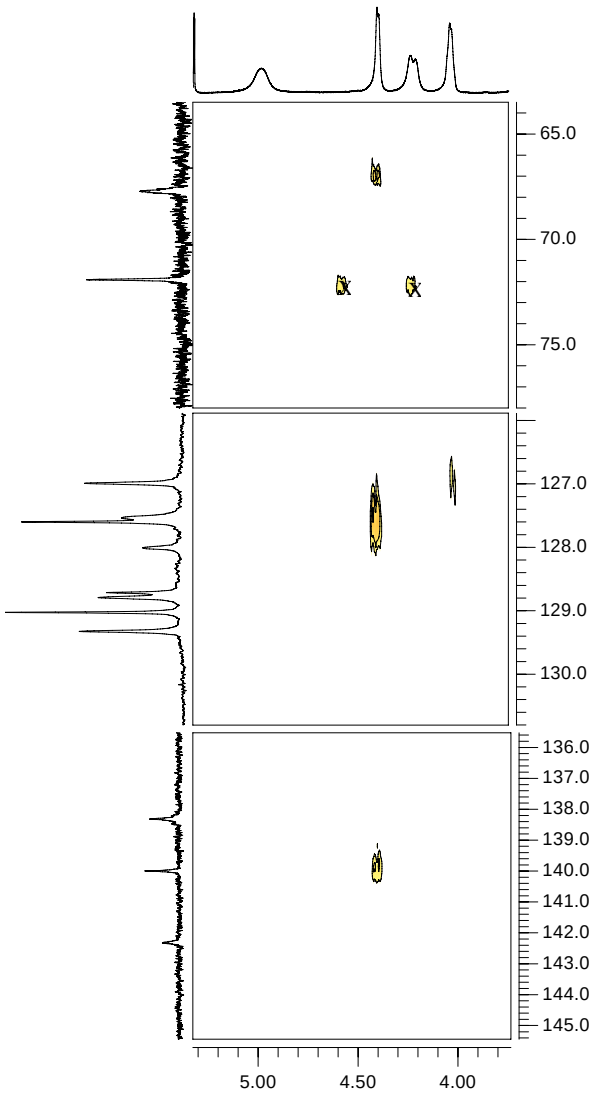


Figure 88: HMBC expansions of 5a.

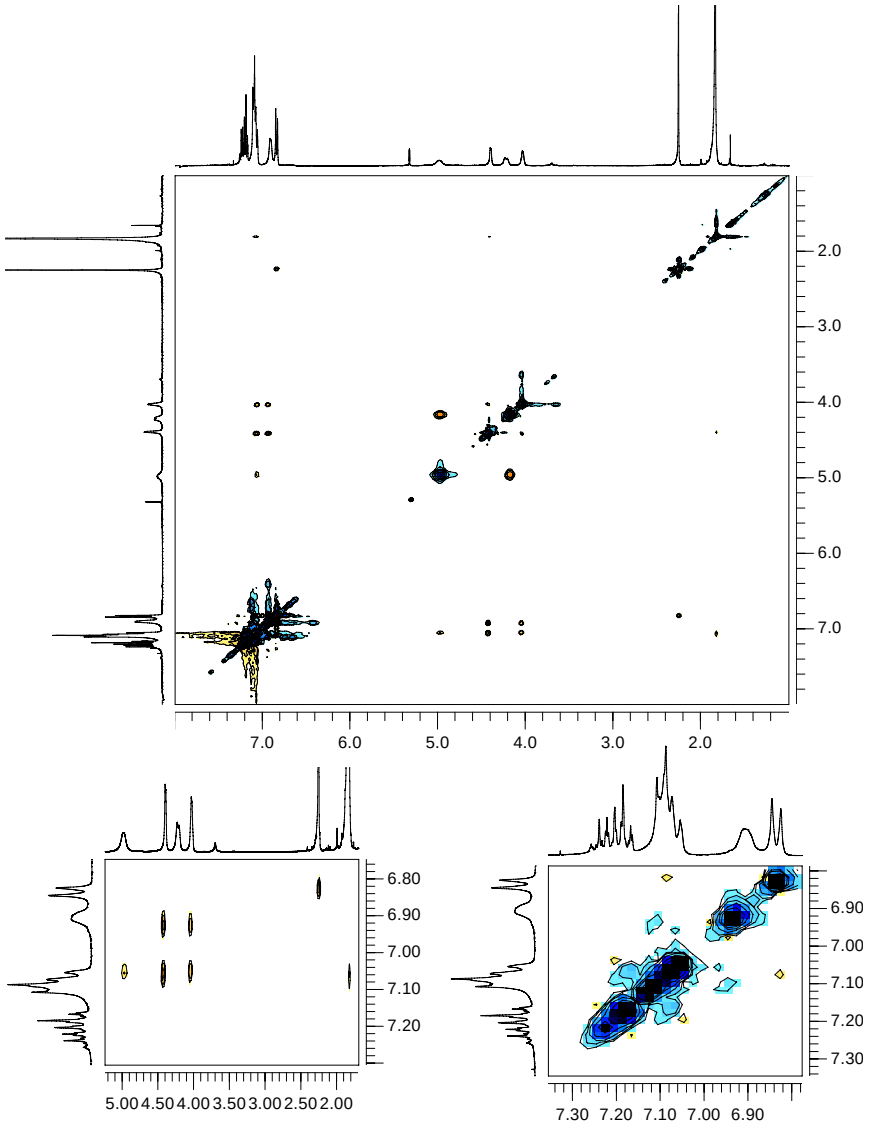


Figure 89: NOESY of 5a.

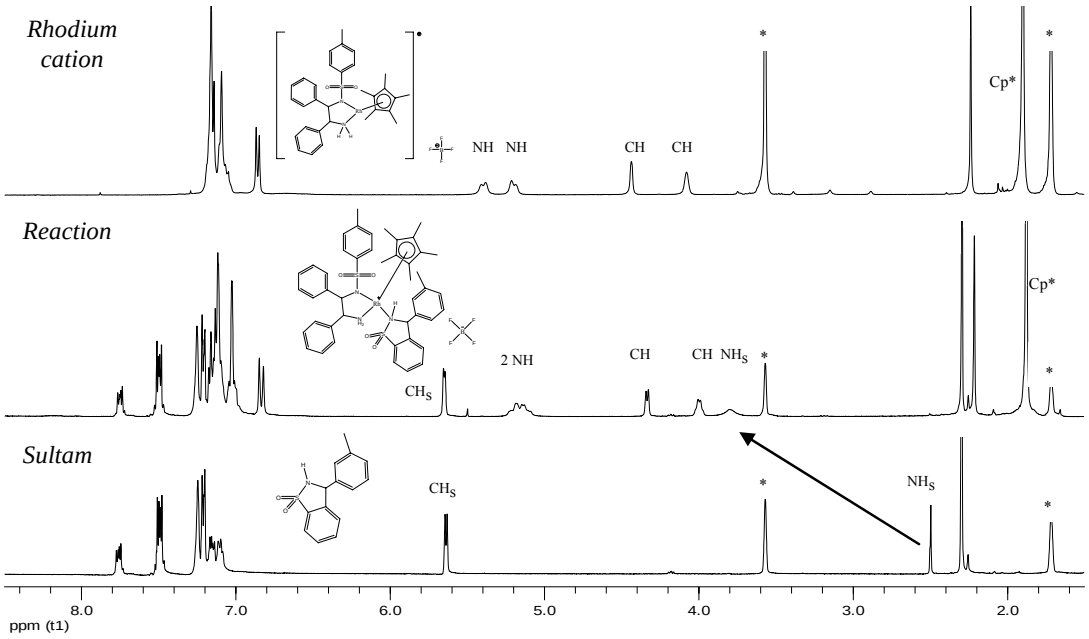


Figure 90: Reaction of 4 compared to 1 and 7 in d_8-THF.
Data obtained on a 400 MHz NMR.

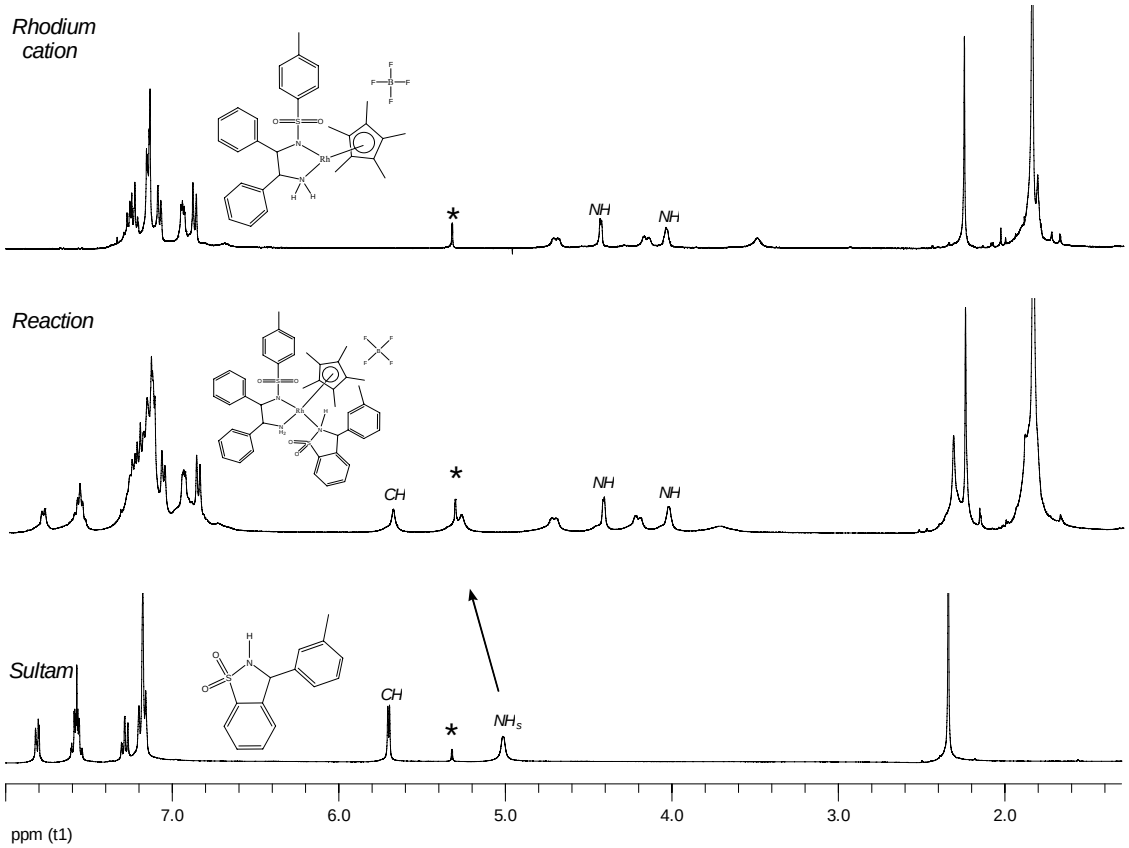


Figure 91: Reaction of 4 compared to 1 and 7 in CD_2Cl_2.
Data obtained on a 400 MHz NMR.

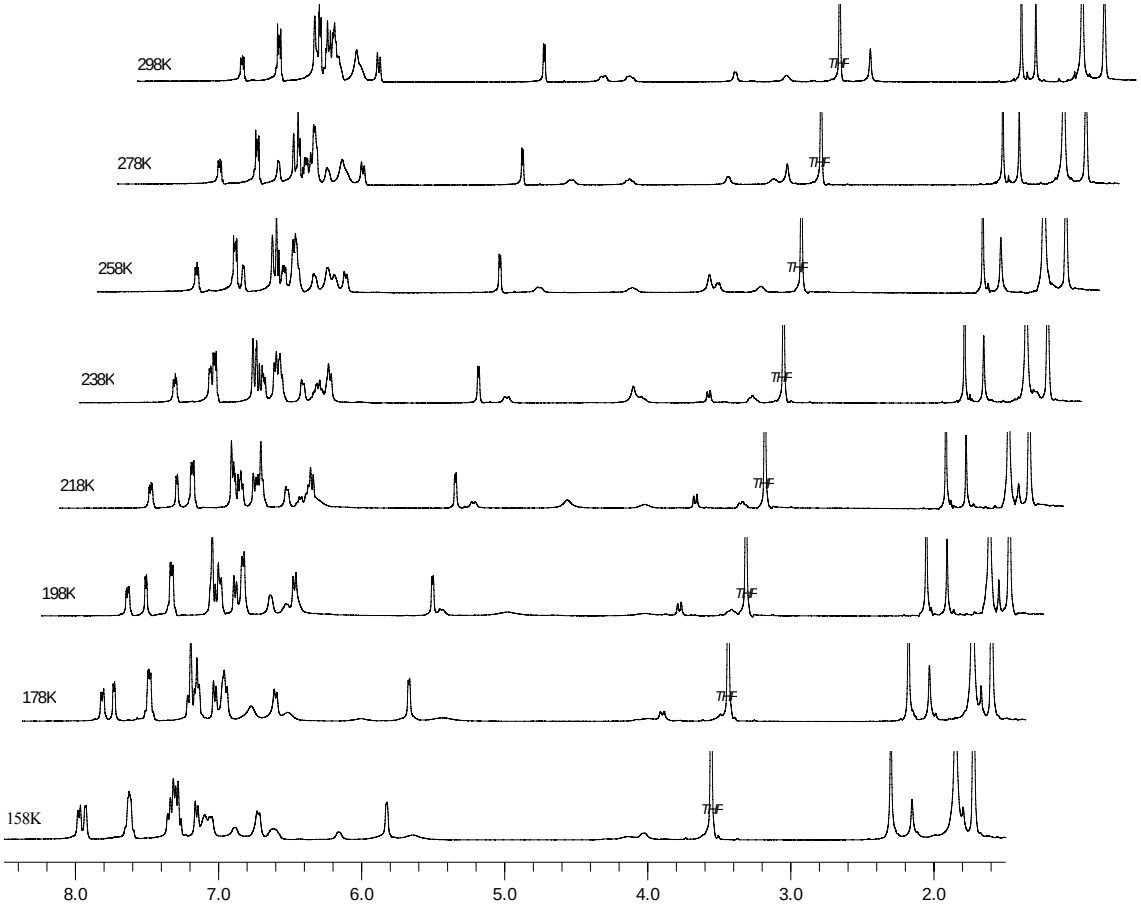


Figure 92: VT NMR of 4 in d_8-THF.

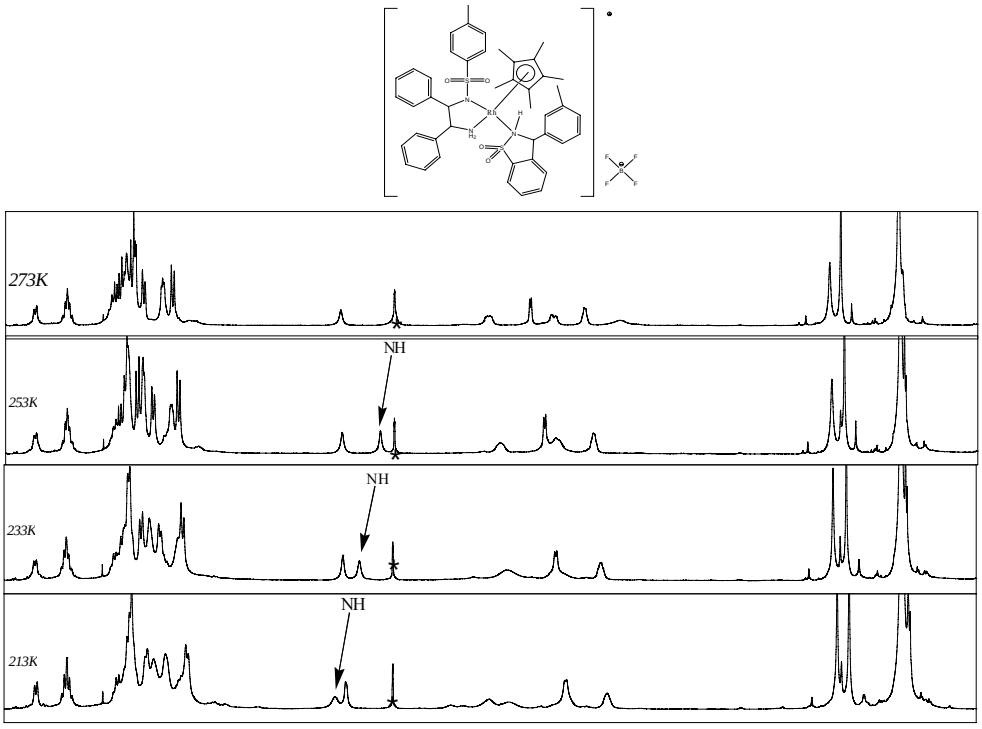


Figure 93: VT NMR of 4.

the d_z^2 metal orbital which contains *s* character is not necessarily strongly involved in the bonding to the sultam.

Typical 2D correlations that have already been investigated do appear to be present within each of the two parts of the molecule: **7** and **5**. Carbon and proton spectra are shown in Figure 94. Relevant 2D spectra are shown in Figure 95 – Figure 99.

2.5.1.8 Data for 2

By NMR a hydride peak developed at δ/ppm -9.22 and J_{RhH} = 21.2 Hz but the species was unstable. As a result, two-dimensional correlations were not possible. A kinetics type of experiment was run to determine the length of time for this peak to decay and a plot is shown in Figure 100.

2.6 Experimental

2.6.1.1 Compound 1

This reaction was initially performed on a small scale in an NMR tube and then repeated on a large scale. In a small round bottom flask, chloroform was added to 1 g (3 mmol) of TsDPEN. In a separate round bottom flask, chloroform was added to 0.843 g (1 mmol) of rhodium chloride dimer. TsDPEN was added to the dimer and then 0.455 mL of pre-dried triethylamine was added at low temperature. This reaction was allowed to stir for an hour and the color changed from orange to red-orange. A small amount of water was added to both quench the reaction and to remove the salt, which did not precipitate from this reaction regardless of the variation of procedure. Part of the difficulty was the fact that the product catalyst was only soluble in polar solvents such as dichloromethane or chloroform. Magnesium sulfate was added and the mother liquor was filtered and dried two more times with magnesium sulfate. The solvent was removed and the product was recrystallized from chloroform/hexanes.

Deuterated catalyst was also synthesized for some reactions. Compound ***d*$_2$-1** was deuterated using a fresh unopened bottle of d_1-methanol, which had been pre-dried over magnesium oxide. The methanol was transferred to a high vacuum ampoule containing **6**

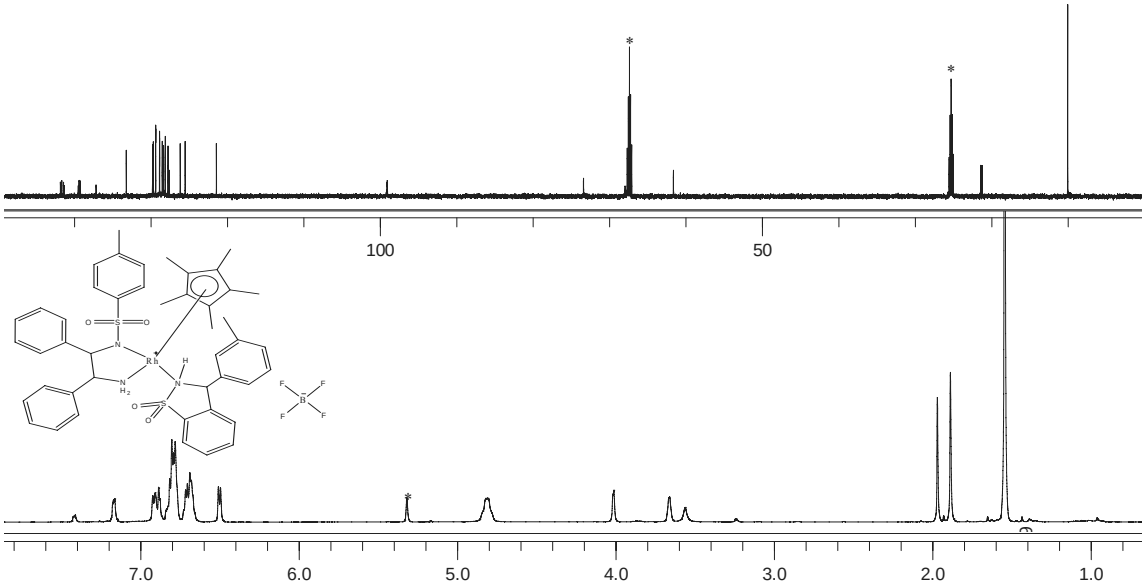


Figure 94: Carbon and proton spectra of 4.

^{1}H-NMR (600 MHz) δ 7.17 (m, 2H) 6.90 (m, 4H) 6.80 (m, 10H) 6.70 (m, 6H) 6.50 (m, 2H) 4.82 (m, 2H) 4.02 (d, 1H, *J* = 3.5 Hz) 3.66 (d, 1H, *J* = 3.3 Hz) 3.56 (s, 1H) 1.97 (s, 3H) 1.89 (s, 3H) 1.55 (s, 15H) ^{13}C-NMR (600 MHz) δ 141.848 (C), 141.670 (C), 141.442 (C), 141.379 (C), 139.511 (C), 139.411 (C), 139.230 (C), 137.182 (C), 133.222 (CH), 129.794 (CH), 129.701 (CH), 129.383 (CH), 129.374 (CH), 128.892 (CH), 128.873 (CH), 128.528 (CH), 128.355 (CH), 128.127 (CH), 127.767 (CH), 127.597 (CH), 126.172 (CH), 125.524 (CH), 121.437 (CH), 99.121 (d, *J* = 7 Hz, CH), 73.411 (CH), 61.649 (CH), 21.420 (CH_3), 21.262 (CH_3), 10.064 (CH_3)

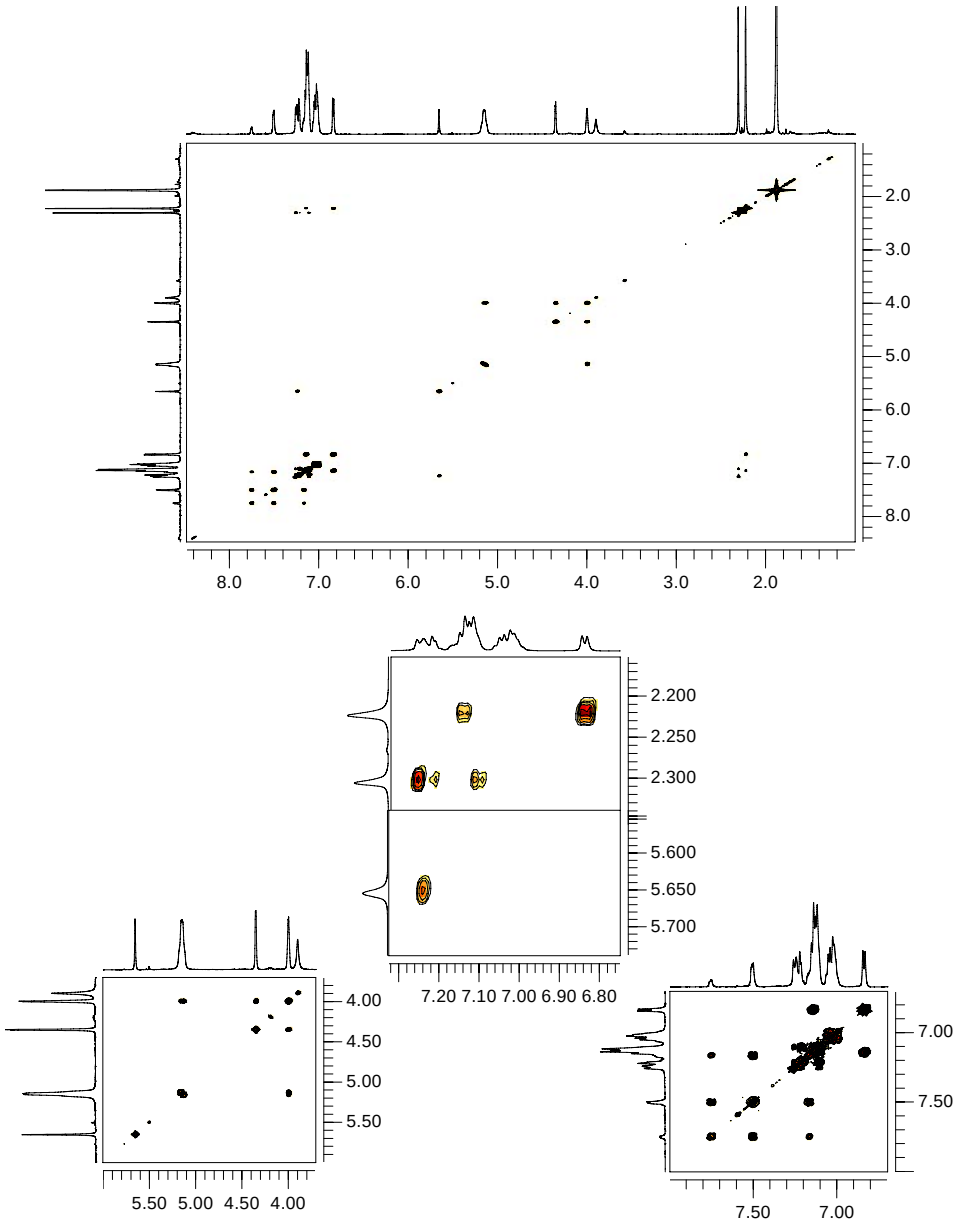


Figure 95: COSY of 4.

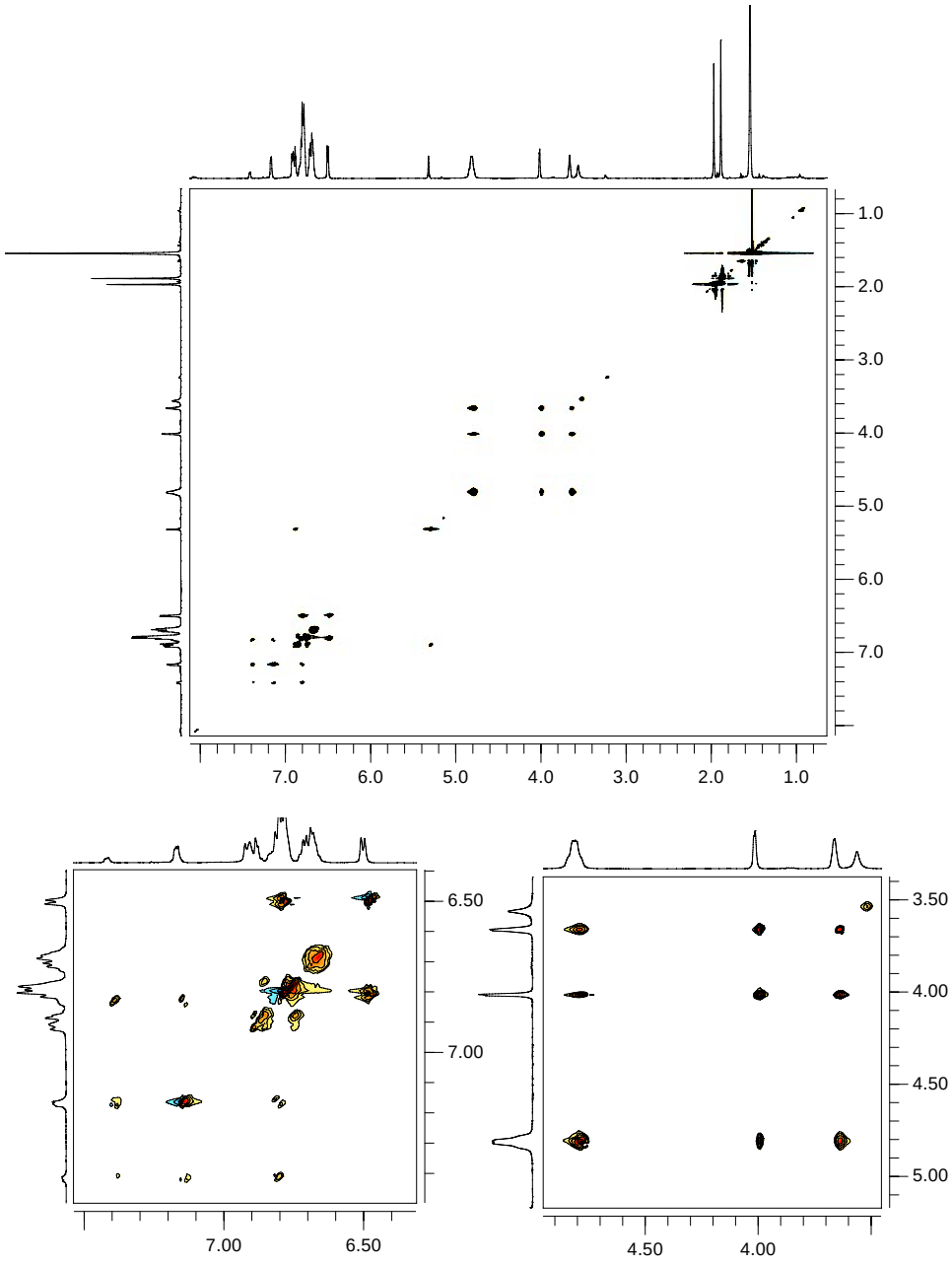


Figure 96: TOCSY of 4.

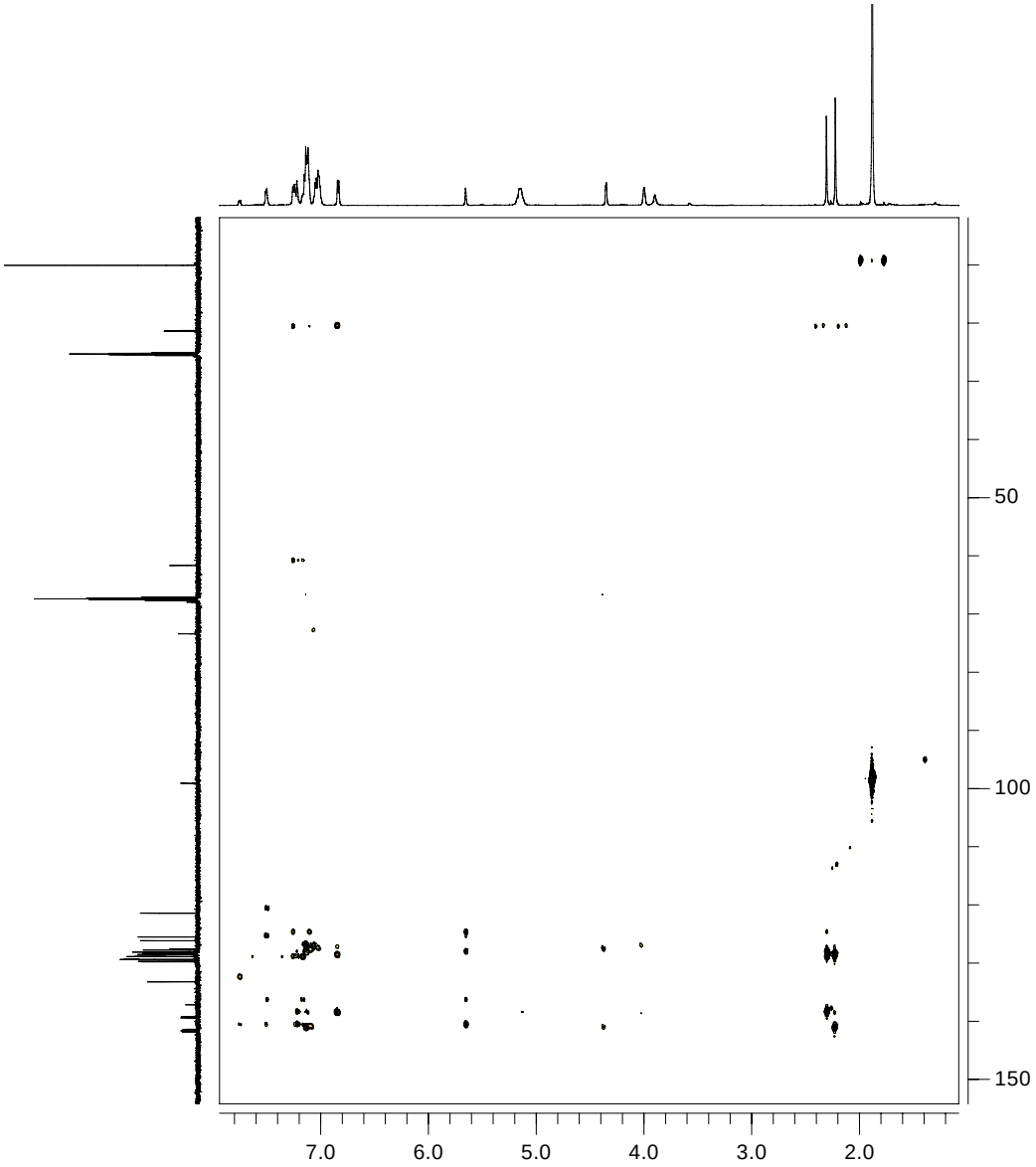


Figure 97: HMBC of 4.

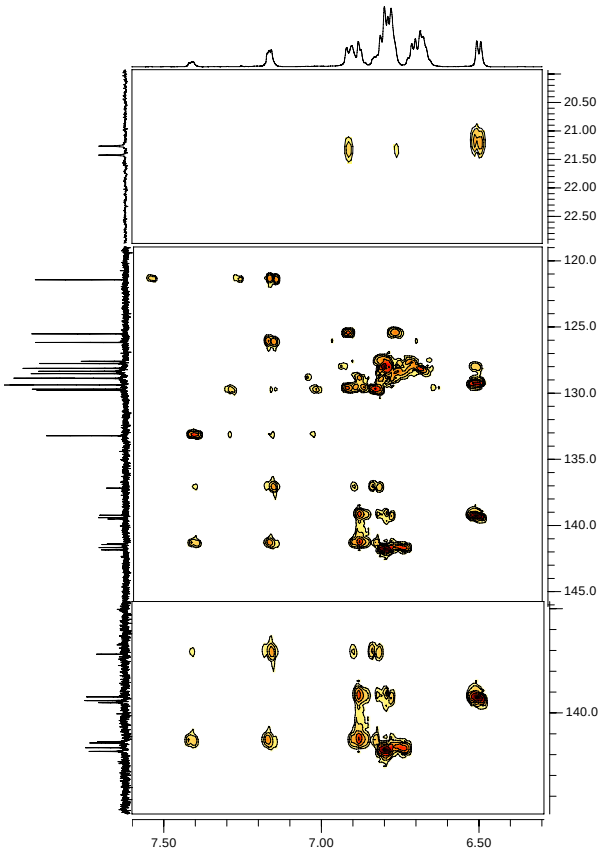


Figure 98: HMBC expansion of aromatic region of 4.

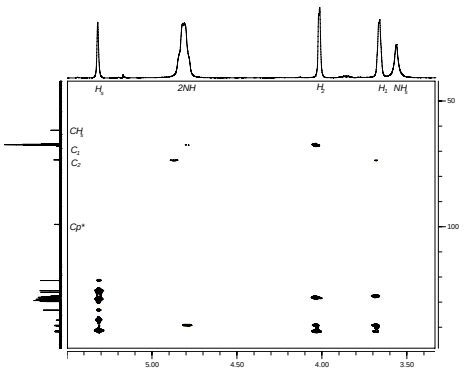


Figure 99: HMBC expansion of aliphatic region of 4.

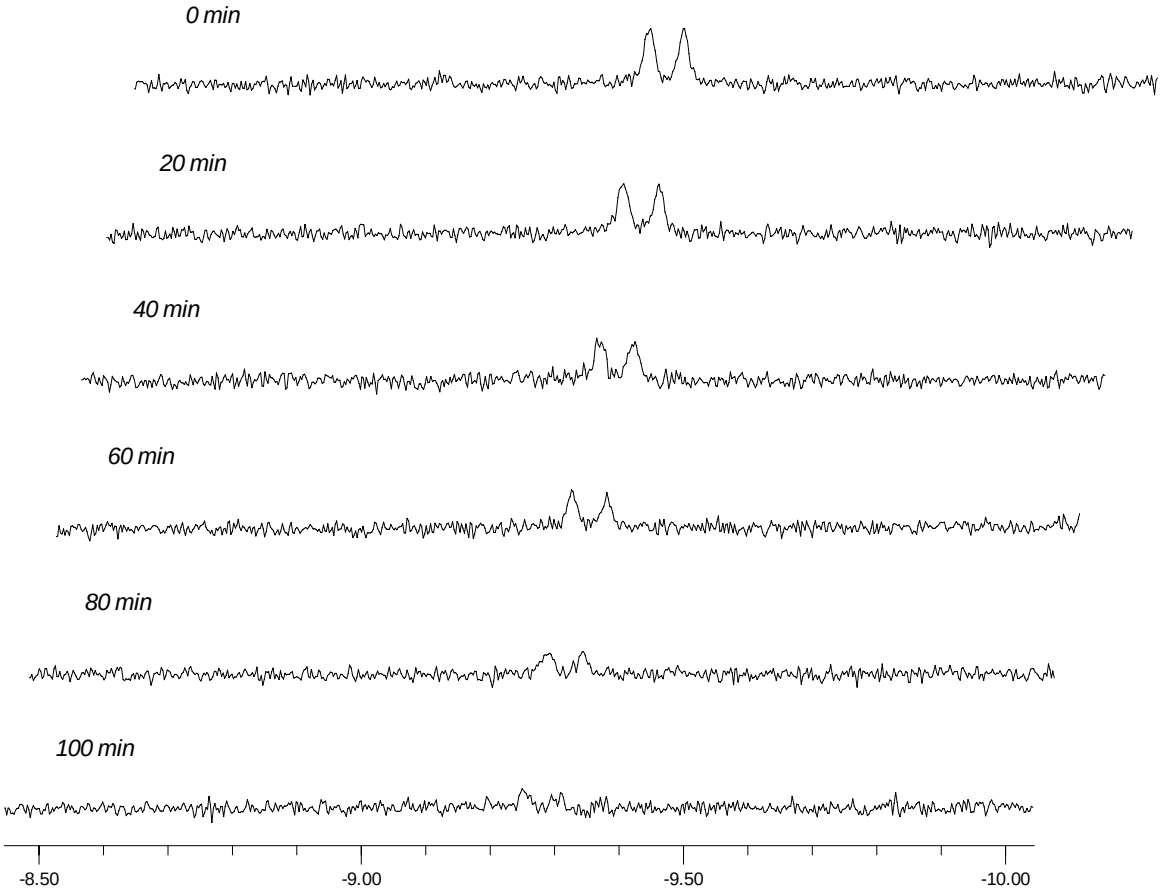


Figure 100: Decay of hydride peak in 2.

Deuterated catalyst was also synthesized for some reactions. Compound ***d*$_2$-1** was deuterated using a fresh unopened bottle of d_1-methanol, which had been pre-dried over magnesium oxide. The methanol was transferred to a high vacuum ampoule containing **6** and allowed to stir for 24 hours. It was then evacuated. This process was repeated three times and yielded product with less than 5% hydrogen *via* NMR integration.

Then 0.5 g (1.5 mmol) of ***d*$_3$-6** and 0.4215 g (0.5 mmol) of rhodium dimer was added to an ampoule. D_2-dichloromethane was vacuum transferred into the flask. Pre-dried triethylamine was also back-transferred so that the ampoule in which it was contained lost 0.17 g (1.6 mmol) of total mass. This reaction was allows to react for one hour. Then, the solvent was removed *via* vacuum, washed three times in a glovebox, and recrystallized from d_1-chloroform/hexanes.

2.6.1.2 Compound 5a

This reaction was initially performed on a small scale in an NMR tube and then repeated on a large scale. In small Schlenk flask, 0.1 g (0.16 mmol) of **1** and 0.34 g of silver(I) fluoroborate were placed. To the flask, THF was added at low temperature. When warmed to approximately 0 °C, the reaction proceeded exceedingly fast as the color changed from red-orange to blood red. The mother liquor was filtered from the salt and the solvent was removed by vacuum. The product was recrystallized from chloroform. This reaction also was performed in dichloromethane with the same product yield. If allowed to remain in solution for more than twenty-four hours, a thin silver mirror plated on the container and the product began to degrade.

The silver fluoroborate was purified by dissolving in benzene. The mother liquor was filtered and placed in a freezer. The resultant crystals were filtered and stored in a dark refrigerator in a glovebox.

2.6.1.3 Compound 4

This reaction was performed on a small scale in an NMR tube. In an NMR tube, 0.015 g (0.02 mmol) of **5a** and 0.006 g (0.02 mmol) of **7** were placed. Pre-dried d_2-dichloromethane was added at low temperature. When the reaction warmed to 0 °C, the color changed from blood red to red.

2.6.1.4 Compound 2

This reaction was performed on a small scale in an NMR tube. In an NMR tube, 0.02 g (0.03 mmol) of **1** and 0.004 g (0.035 mmol) of potassium formate or sodium formate was placed. Pre-dried d_8-THF was added at low temperature. Even at room temperature, very little change could be seen in the color of the reaction.

2.6.1.5 Acquisition and processing parameters for 7

All samples were placed in NMR solvents which were previously dried by reflux over potassium, sodium, or calcium hydride for several days. The molecules were synthesized using Schlenk and vacuum line techniques. The NMR samples were handled in a glovebox and placed in either a Young's NMR tube with a Teflon cap or flame sealed before spectra were obtained. The solvent was transferred to the samples under reduced pressure.

Both of the 1D proton and carbon spectra for **7** were obtained on a Bruker Avance 400 MHz spectrometer at room temperature. The proton spectrum was obtained with the following parameters: pulse sequence, *zg30;* spectral width, 4006 Hz; number of scans, 16; relaxation time, 1.0 s; time domain points, 32768; pulse angle, 90°; multiplied by the exponential function with line broadening 0.3 Hz; and Fourier transformed. The carbon spectrum was obtained with the following parameters: pulse sequence, *zgdc;* spectral width, 17,123 Hz; number of scans, 486; pulse angle, 90°; with proton decoupling using the WALTZ-16 sequence; multiplied by the exponential function with line broadening 1.0 Hz; and Fourier transformed.

The T_1 relaxation study was obtained on a Bruker Avance 400 MHz spectrometer. The pulse sequence used was *tlir* with the following parameters: spectral width, 4006 Hz; number of scans, 8; relaxation times used were : 0.5 s, 1.0 s, 3.0 s, 5.0 s, 6.0 s, 7.0 s, 8.0 s, 9.0 s 10.0 s, 11.0 s, 12.0 s, 13.0 s, 14.0 s, 15.0 s, 17.0 s, 20.0 s; time domain points, 8192; pulse angle, 90°; multiplied by the exponential function with line broadening of 0.5 Hz; and Fourier transformed.

The HSQC spectrum was obtained on a Bruker Avance 400 MHz spectrometer at room temperature using the following parameters: pulse program, *invist*, spectral widths

of 4006 and 68,000 Hz in the ^{1}H and ^{13}C dimensions, respectively; number of scans, 56; 128 FIDS were collected. The resulting data points were zero-filled to 256 points in the t_1 dimension and multiplied by a sine squared window function shifted by $\pi/2$ along both dimensions and double Fourier transformed.

The COSY spectrum was obtained on a Bruker Avance 400 MHz spectrometer at room temperature with the following parameters: pulse program, cosy45, spectral width in both dimensions of 4006 Hz; 256 FIDS collected; number of transients 8; 1.4 s relaxation delay. The resulting data points were multiplied by an exponential function in the t_2 dimensions with 2.0 Hz line broadening and then Fourier transformed. Then, the data points were linear predicted from points 256 to 511 points in the t_1 dimension and multiplied by a sine squared window function shifted by $\pi/2$; Fourier transformed; and symmetrized.

The TOCSY spectrum was obtained on a Bruker Avance 400 MHz spectrometer at room temperature with the following parameters: pulse program, mlevtp, spectral width in both dimensions of 4006 Hz; 256 FIDS collected; number of points, 1000; number of transients, 48; 1.4 s relaxation delay, 0.20 second mixing time. Phase sensitive data points were obtained. The resulting data points were multiplied by an exponential function in the t_2 dimensions with 2.0 Hz line broadening and then Fourier transformed. Then, the data points were linear predicted from points 256 to 511 points in the t_1 dimension and multiplied by a sine squared window function shifted by $\pi/2$; Fourier transformed; and symmetrized.

The NOESY spectrum was obtained on a Bruker Avance 400 MHz spectrometer at room temperature with the following parameters: pulse program, noesytp, spectral width in both dimensions of 4006 Hz; 256 FIDS collected; number of scans 32; 2.2 s relaxation delay, 0.80 second mixing time. Phase sensitive data points were obtained. The resulting data points were multiplied by an exponential function in the t_2 dimensions with 2.0 Hz line broadening and then Fourier transformed. Then, the data points were linear predicted from points 256 to 511 points in the t_1 dimension and multiplied by a sine squared window function shifted by $\pi/2$; Fourier transformed; and symmetrized.

2.6.1.6 Acquisition and processing parameters for 1

Both of the 1D proton and carbon spectra for **1** were obtained on a Bruker Avance 400 MHz spectrometer at room temperature. The proton spectrum was obtained with the following parameters: pulse sequence, *zg30;* spectral width, 4006 Hz; number of scans, 16; relaxation time, 1.0 s; time domain points, 65536; pulse angle, 90°; multiplied by the exponential function with line broadening 0.3 Hz; and Fourier transformed. The carbon spectrum was obtained with the following parameters: pulse sequence, *zgdc;* spectral width, 26,667 Hz; number of scans, 1024; relaxation time, 2.0 s; time domain points, 65536; pulse angle, 90°; with proton decoupling using the WALTZ-16 sequence; multiplied by the exponential function with line broadening 1.0 Hz; and Fourier transformed.

The T_1 relaxation study was obtained on a Bruker Avance 400 MHz spectrometer. The pulse sequence used was *tlir* with the following parameters: spectral width, 4006 Hz; number of scans, 8; relaxation times used were : 10.0 s, 5.0 s, 4.0 s, 3.0 s, 2.0 s, 1.0 s, 0.5 s, 0.25 s, 0.10 s, 0.05 s, 0.01 s; time domain points, 8192; pulse angle, 90°; multiplied by the exponential function with line broadening of 0.5 Hz; and Fourier transformed.

The HSQC spectrum was obtained on a Bruker Avance 400 MHz spectrometer at room temperature using the following parameters: pulse program, *invist*, spectral widths of 4006 and 64,232 Hz in the ^{1}H and ^{13}C dimensions, respectively; relaxation time, 1.4 s; time domain points, 2048; number of scans, 32; 256 FIDS were collected. The resulting data points were zero-filled to 512 points in the t_1 dimension and multiplied by a sine squared window function shifted by $\pi/2$ along both dimensions and double Fourier transformed.

The COSY spectrum was obtained on a Bruker Avance 400 MHz spectrometer at room temperature with the following parameters: pulse program, cosy45, spectral width in both dimensions of 4006 Hz; 256 FIDS collected; number of transients 8; 1.4 s relaxation delay. The resulting data points were multiplied by an exponential function in the t_2 dimensions with 2.0 Hz line broadening and then Fourier transformed. Then, the data points were linear predicted from points 256 to 511 points in the t_1 dimension and

multiplied by a sine squared window function shifted by π/2; Fourier transformed; and symmetrized.

The TOCSY spectrum was obtained on a Bruker Avance 400 MHz spectrometer at room temperature with the following parameters: pulse program, mlevtp, spectral width in both dimensions of 4006 Hz; 256 FIDS collected; number of points, 1000; number of transients, 48; 1.4 s relaxation delay, 0.20 second mixing time. Phase sensitive data points were obtained. The resulting data points were multiplied by an exponential function in the t_2 dimensions with 2.0 Hz line broadening and then Fourier transformed. Then, the data points were linear predicted from points 256 to 511 points in the t_1 dimension and multiplied by a sine squared window function shifted by π/2; Fourier transformed; and symmetrized.

2.6.1.7 Acquisition and processing parameters for 4

The T_1 relaxation and variable temperature studies were obtained on a Bruker Avance 400 MHz spectrometer. The pulse sequence used was *tlir* with the following parameters: spectral width, 4486 Hz; number of scans, 8; relaxation times used were : 0.5 s, 1.0 s, 3.0 s, 5.0 s, 6.0 s, 7.0 s, 8.0 s, 9.0 s 10.0 s, 11.0 s, 12.0 s, 13.0 s, 14.0 s, 15.0 s, 17.0 s, 20.0 s; time domain points, 8192; pulse angle, 90°; multiplied by the exponential function with line broadening of 0.5 Hz; and Fourier transformed.

The COSY spectrum was obtained on a Varian Inova 600 MHz spectrometer at room temperature with the following parameters: pulse program, *gCOSY*, spectral width in both dimensions of 4486 Hz; 600 FIDS collected with 1 transient; 2.0 s relaxation delay. Magnitude data points were obtained. The data points were zero filled to 1024 points in the t_1 dimension. The data points were multiplied by an unshifted sinebell window function in both dimension and double Fourier transformed. The data points were then symmetrized.

The TOCSY spectrum was obtained on a Varian Inova 600 MHz spectrometer at room temperature with the following parameters: pulse program, *TOCSY*, spectral width in both dimensions of 4486 Hz; 1200 FIDS collected with 4 transients; 2.0s relaxation delay, 0.080s spin-lock mixing time. Phase sensitive data points were obtained. The

resulting data points were multiplied by a sinebell window function shifted by $\pi/2$ in the t_2 dimension and Fourier transformed. Then, the data points were linear predicted from points 1200 to 2399 points in the t_1 dimension and multiplied by a sine squared window function shifted by $\pi/2$ in the t_1 dimension; Fourier transformed; and symmetrized.

The NOESY spectrum was obtained on a Varian Inova 600 MHz spectrometer at room temperature with the following parameters: pulse program, *NOESY*, spectral width in both dimensions of 4486 Hz; 800 FIDS collected; 16 transients; 2.0s relaxation delay, 0.5 s mixing time. Phase sensitive data points were obtained. The data points were multiplied by a sinebell window function shifted by $\pi/2$ and Fourier transformed. The data points were predicted linearly predicted from 600 to 1199 points in the t_1 dimension; multiplied by a sine squared window function shifted by $\pi/2$; Fourier transformed; and symmetrized.

The HMBC spectrum was obtained on a Varian Inova 600 MHz spectrometer at room temperature using the following parameters: pulse program, *gHMBC*, spectral widths of 4486 and 36,199 Hz in the ^{1}H and ^{13}C dimensions, respectively; 600 FIDS were collected; 16 transients; 2.0s relaxation delay. Magnitude data points were obtained. A linear prediction was applied in the t_1 dimension from 600 to 1199 points and multiplied by an unshifted sinebell window function in both dimensions and double Fourier transformed.

3 SPECTROSCOPIC STUDIES OF TETRAAMINE-COMPOUNDS

3.1 Forward

Ligands that have several lone pairs available for bonding to metal centers play a vital role in the majority of the catalysts reported today. Tetrahedral tricyclic tetramines contain four closely spaced nitrogen atoms with several lone pairs available for metallic bonding. As a result, they are thought to be potentially good ligands when bound to a catalyst.

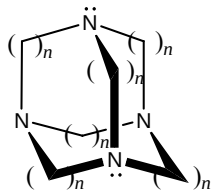
Very few data are currently available in terms of solution structure of these ligands. Although this is a result of their hygroscopic nature, no studies have been previously performed which considers this characteristic. Presented in this chapter for the first time is a description of the solution state structure and fluxionality of a family of tetrahedral tricyclic tetramines based on VT, 2D, and ^{1}H NMR data. This is important because in addition to presenting novel characterization of these compounds, this report also allows for future modeling of the solution state structure of this ligand when bound to a metal center for the purposes of understanding these catalytic systems better.

3.2 Introduction

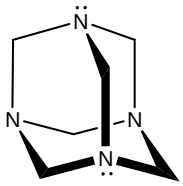
The general structure of the homologous series of *n*-symmetric tetrahedral tricyclic tetramines, or adamanzanes, and the first two members of the family are shown below in Figure 101.

The smallest member of the series, hexamethylenetetramine or urotropine, has long been used pharmacologically,[101] and has been used more recently as a ligand in the synthesis of self-assembled transition metal arrays, amongst other applications.

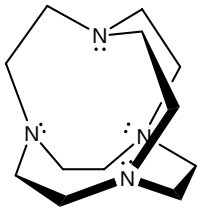
In 1923, the smallest cage-adamanzane became the first organic structure obtained by X-ray diffraction.[102] Large cages and bowls were first synthesized by Schmidtchen[103] in 1980. In 1990, Weisman reported the first synthesis of small bowl-adamanzanes and



The *n*-symmetric tetrahedral
tricyclic tetramine series
1,3,5,7-tetraaza-tricyclo[(2*n*+1).(2*n*+1).*n*.*n*]-anes



1,3,5,7-tetraaza-tricyclo[3.3.1.1^{3,7}]decane
(urotropine, **8**), (*n* = 1)



1,4,7,10-Tetraaza-tricyclo[5.5.2.2^{4,10}]hexadecane, **9**,
(*n* = 2)

Figure 101: Symmetric tetrahedral tricyclic tetramines

indicated their legating properties in his paper.[104] Later, in 1995, medium sized cages were synthesized by Springborg *et al*.[105]

Molecules of this type are also fundamentally interesting, due to the presence of eight non-bonding electrons. By variation of n, the spatial arrangement of the these formal lone pairs can be adjusted; in **8**, the formal lone pairs are *exohedrally* disposed with respect to the cage framework, predicating external coordination to metal centers and the possibility of formation of polymeric, monodentate structures in the solid state. Conversely, **9** is thought to display an *endohedral* arrangement, confining the non-bonding electrons into a small region of space inside the cage, which adds a significant Coulombic contribution to the overall energetics of the molecule. Calculations at various levels of theory support this assertion.[106-109] Interestingly, the nitrogen atoms in **9** are almost planar by calculation[107] in the perendohedral arrangement of lone pairs.

The close proximity of the formal lone pairs in 9 and related species implies that hydrogen bonds formed by these species should be extraordinarily strong and that they should therefore act as 'proton sponges'.[110, 111]. The proton affinity, strain energy and hydrogen bond strength of **9** are tabulated in Table 3.1.[108]

Table 3.1: Proton affinity, strain energy, and hydrogen bond strength for 2.

Calculation Method	Proton affinity / kJmol^{-1}	Strain Energy / kJmol^{-1}	Hydrogen Bond strength / kJmol^{-1}
HF	1091.8	77.2	-83.4
B3-LYP	1062.1	80.9	-88.1

The protonated form of **9**, [**2**H]$^{+}$, has been reported,[112] though the preparation is not repeatable in this laboratory[113] or the laboratory of others.[114] Other pK_A values of some bowl-adamanzanes illustrate their extreme basicity, with values which range from pK_A =11.55 to values greater than 15.[115] Likewise, the tetraprotonated form of these species is extremely acidic.[115]

3.2.1 Group theoretical considerations

Molecular distortions in closed shell systems occur through mixing of the **h**ighest **o**ccupied **m**olecular **o**rbital (HOMO) and the **l**owest **u**noccupied **m**olecular **o**rbital (LUMO); such a mixing is mediated by a normal coordinate, *q*, and is generally described group theoretically by the second order Jahn-Teller distortion.[116-123] The first order Jahn-Teller distortion applies to open shell systems where the unpaired electrons occupy a degenerate state and so does not apply to the molecules in this portion of the thesis.

The requirement for a second order Jahn-Teller distortion is that

$$a_s \in \Gamma_{HOMO} \otimes \Gamma_{LUMO} \otimes \Gamma_q \qquad \textbf{3.1}$$

where a_1 represents the scalar irreducible representation *i.e.* the most symmetrical representation in the group and $\otimes$ represents the direction product. As

$$a_s \in \Gamma_i \otimes \Gamma_i \qquad \textbf{3.2l}$$

then this implies that

$$\Gamma_q = \Gamma_{HOMO} \otimes \Gamma_{LUMO} \qquad \textbf{3.3}$$

It is also important to note that second order Jahn-Teller distortions can give rise to dramatic changes in molecular geometry if *q* is dominated by angular changes; this is a

simple consequence of the difference in the magnitude of displacement between vibrational vs. angular excitations. Small changes in the molecular energy can therefore affect large changes in geometry when q is predominantly a normal coordinate based on angular deformations.

For **10**, decahydro-2a,4a,6a,8a-tetraaza-cyclopentaacenaphthylene, shown in Figure 102, a symmetric rotomer of C_{2v} symmetry is thought of as the transition state for an a_2 symmetry vibrational interconversion of two C_2 isomers as shown in Figure 103.

Within **10,** four formal lone pairs are contained; these orbitals are formally non-bonding in a delocalized, molecular orbital approach. The **s**ymmetry **a**dapted **l**inear **c**ombinations in C_{2v} and C_2 can therefore be written schematically as shown in Figure 104 where '●' represents an endohedral lone pair and '○' represents an exohedral lone pair. Correlations between these configurations can then be constructed:

$$\begin{aligned} a + a' &\rightarrow a_1 \\ a - a' &\rightarrow a_2 \end{aligned} \qquad \textbf{3.4}$$

and

$$\begin{aligned} b + b' &\rightarrow b_2 \\ b - b' &\rightarrow b_1 \end{aligned} \qquad \textbf{3.5}$$

The direct product table for C_{2v} is given in Table 3.2. Considering the putative C_{2v} transition state for the interconversion of the two C_2 isomers, constructed *via* an a_2-symmetry normal coordinate mode, then

$$\Gamma_q = a_2 \qquad \textbf{3.6}$$

therefore,

$$\Gamma_{HOMO} \otimes \Gamma_{LUMO} = a_2 \qquad \textbf{3.7}$$

From the direct product table for C_{2v} only HOMO-LUMO combinations of either (A_1, A_2) or (B_1, B_2) can be vibronically coupled by the a_2-symmetry normal coordinate mode.

No symmetry constraints were imposed on the refinement of Density functional theory calculations and the molecular configuration for the molecule is in Figure 105.

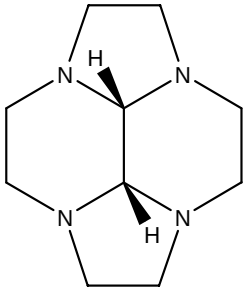


Figure 102: Molecule 10.
Decahydro-2a,4a,6a,8a-tetraaza-cyclopenta[fg]acenaphthylene

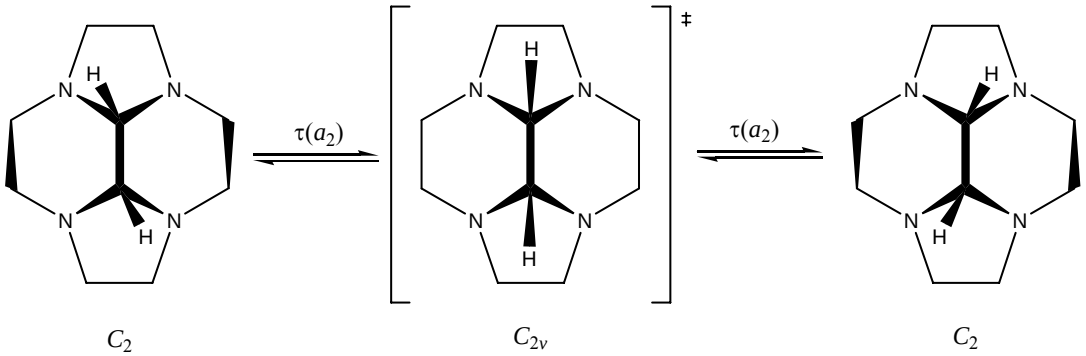
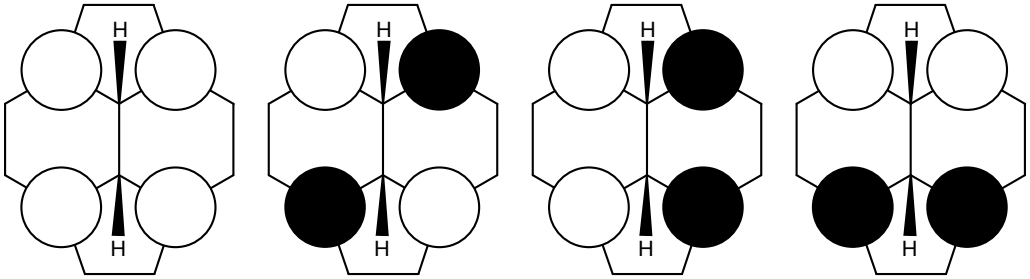


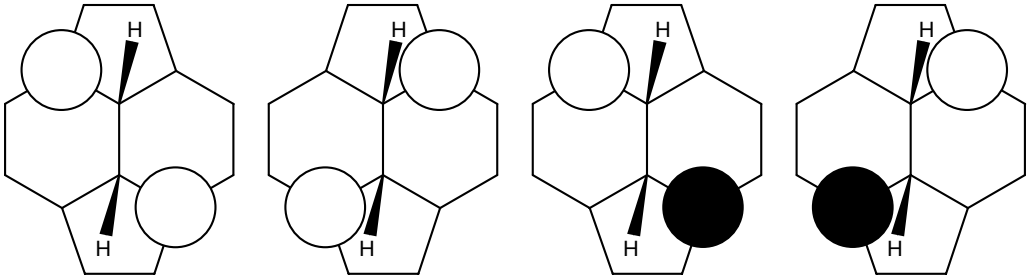
Figure 103: Interconversion of two C_2 isomers.

C_{2v}



a_1 a_2 b_1 b_2

C_2



a a' b b'

Figure 104: SALCS for C_{2v} and C_2.

Table 3.2: Direct product table for C_{2v}.

C_{2v}	***A_1***	***A_2***	***B_1***	***B_2***
A_1	A_1	A_2	B_1	B_2
A_2		A_1	B_2	B_1
B_1			A_1	A_2
B_2				A_1

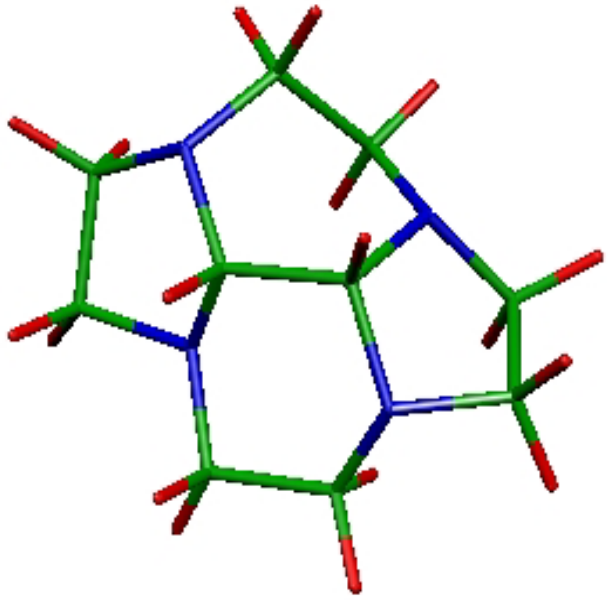


Figure 105: Density functional calculations of 10.

The calculated ground state geometry from these calculations is essentially identical to the idealized $a-a'$ ground state detailed above, implying that a fluxional process - $(a-a') \rightarrow [a_2]^{\ddagger} \rightarrow (a-a')$ is group theoretically allowed under the second order Jahn-Teller theorem.

It is notable that this rearrangement is coupled to a low energy normal coordinate and that the inversion processes that occur at each individual N atom are coupled under this description.

The remaining molecules examined in this chapter are shown in Figure 106, Figure 107, and Figure 108. Density functional calculations were also used to calculate the structures of **10**$^{+}$, shown in Figure 109, and **11,** shown in Figure 110. For **10**$^{+}$, the calculated values are less strained than the crystal structure indicates. The calculated bond length for **11** is longer than the value determined experimentally from the crystal structure.

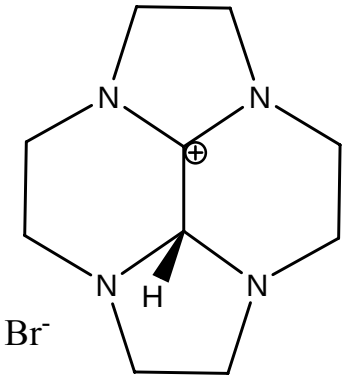


Figure 106: Molecule10^{+}.
1,2,3,4,5,6,7,8,8*c*-otahydro-1*H*-4*a*,6*a*,8*a*-triaza-2*a*-azoniacyclopent[*fg*]acenaphthylene bromide

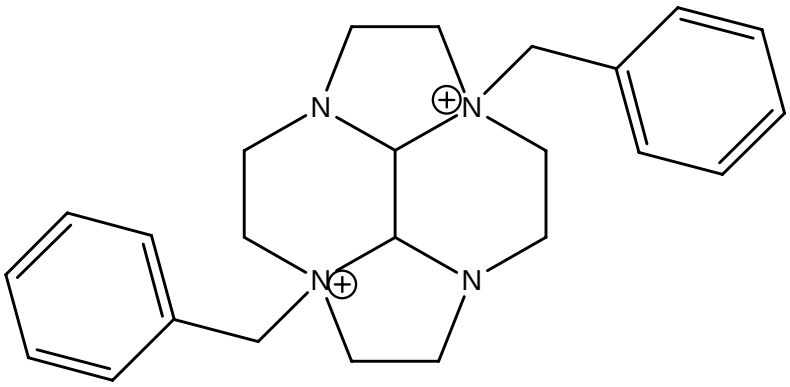


Figure 107: Molecule 10^{+2}.
1,2,3,4,5,6,7,8,8*c*-octahydro-6*a*,8*a*-diaza-2*a*,4*a*,-diazoniacyclopent[*fg*]acenaphthylene bromide

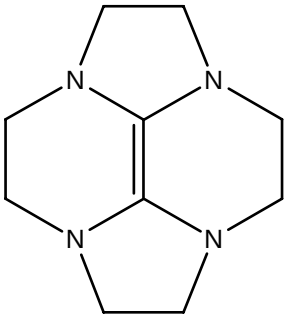


Figure 108: Molecule 11.
1,2,3,4,5,6,7,8-octahydro-2a,4a,6a,8a – tetraazacyclopenta[fg]acenaphthylene

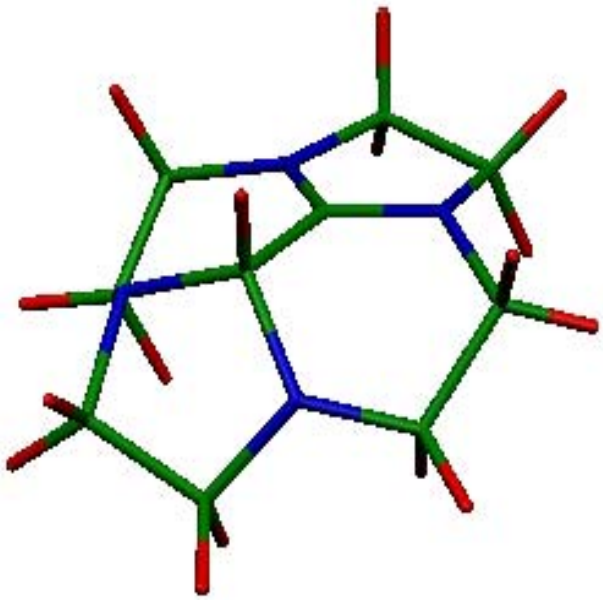


Figure 109: Density Functional calculations of 10^{+}.

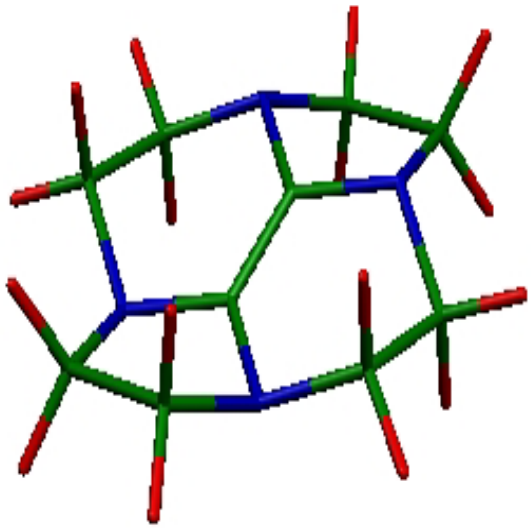


Figure 110: Density functional calculations of 11**.**

3.2.2 Chemical considerations

The electron rich nature and the spatial arrangement of the formal lone pairs ensure that adamanzanes and related species are capable of bonding with early as well as late transition metals. Wong and Weisman *et al* have already shown that some of the members of the polytetraamines bind with gallium, indium,[124] copper, zinc,[125] and cadmium.[126] Other metals to which these bowl species have been bound include lithium, sodium[104], nickel, cobalt, iron, and palladium.[115]

Because of their ligating applications, uses for these complexed species include catalysis, as well as pharmaceutical and radiological applications. One such example, 1,4,8,11-tetraazacyclotetradedane-N,N',N'',N'''-tetraacetic acid, has been reacted with ^{64}Cu and the complex used as a PET imagining agent.[127, 128] Functionalized 1,4,7,10-tetraazacyclotetradedane has applications as a fluorescent probe for Y^{3+} and La^{3+}.[129] Moreover, the ability of these materials to act as 'proton sponges' complicated both the synthesis and spectroscopic analysis of these systems.

As part of the investigation of the chemistry of tetraamines in the group, a series of polytetraamine ligands has been synthesized and investigated *via* 1D and 2D VT NMR. With rigorous synthetic techniques, pure materials can be produced in which the molecular species of interest is not complexed to another species.

Previous attempts to characterize these materials have been fraught with difficulty due to their hygroscopic nature. In the presence of water, the solids become sticky presumably due to the formation of protonated and hydrogen bonded species, causing the spectrum to degrade. Previously reported spectra of these systems have been so unclear that only wide proton ranges are indicated. Due to these broad peaks only carbon NMR data have been used to study fluxionality.[130] The work presented in this chapter therefore presents the first systematic study of the structure and dynamics of these species. ^{1}H NMR is more important for VT studies of this compound rather than ^{13}C NMR because the ^{13}C spectrum is simple; moreover, the processes that are implied in section 3.2.1 only involve staggered *vs.* eclipsed conformations across a CH_2CH_2 unit and are therefore only detectable in the ^{1}H NMR spectrum. The carbon atoms indicate framework connectivity

but give no further information. 2D correlations between the proton atoms is also possible to clarify the shape of the molecule in solution. The synthesis of the species examined in this chapter is shown in Figure 111.

3.3 Stereochemistry of 10^+

The determination of the stereochemistry of 2,3,4,5,6,7,8,8c-octahydro-1H-4a,6a,8a-triaza-2a-azonia-cyclopentaace[*fg*]naphthalene, $\mathbf{10}^+$, from available NMR spectra is not trivial and is certainly not available from a single measurement. Accordingly, this molecule was characterized using one, two-dimensional and VT techniques. One and two dimensional VT techniques were also used to study the fluxionality of this molecule. All studies were conducted using solutions of $\mathbf{10}^+$ in d_3-acetonitrile. All spectra were obtained as noted on either a Varian Inova 600 MHz spectrometer or a Bruker Avance 400 MHz spectrometer using a 5 mm broadband probe. Acquisition parameters and other experimental details are given in Section 3.6. For reference purposes, relevant figures, spectra, and tables are placed at the end of this section.

3.3.1 Spectroscopic interpretations

The spectroscopic investigations presented in this chapter depend critically on the use of NOE-dependent and other correlational spectroscopic techniques. In order to determine the maximum transfer of magnetization, the details of which have been given in the introductory chapter, the relaxation profile of the molecule was determine through inversion-recovery methods. The recorded spectra for this T_1 determination is given with the spectra at the end of the section. Whereas most of the T_1 values are on the order of 2.5 seconds and are normal, an unusually long relaxation time was found for H_1, . For this proton, $T_1^{H_1} = 11.3\text{s}$, determined parametrically using

$$I(t) = I_0 + P\exp\left\{\frac{-t}{T_1}\right\} \qquad \textbf{3.8}$$

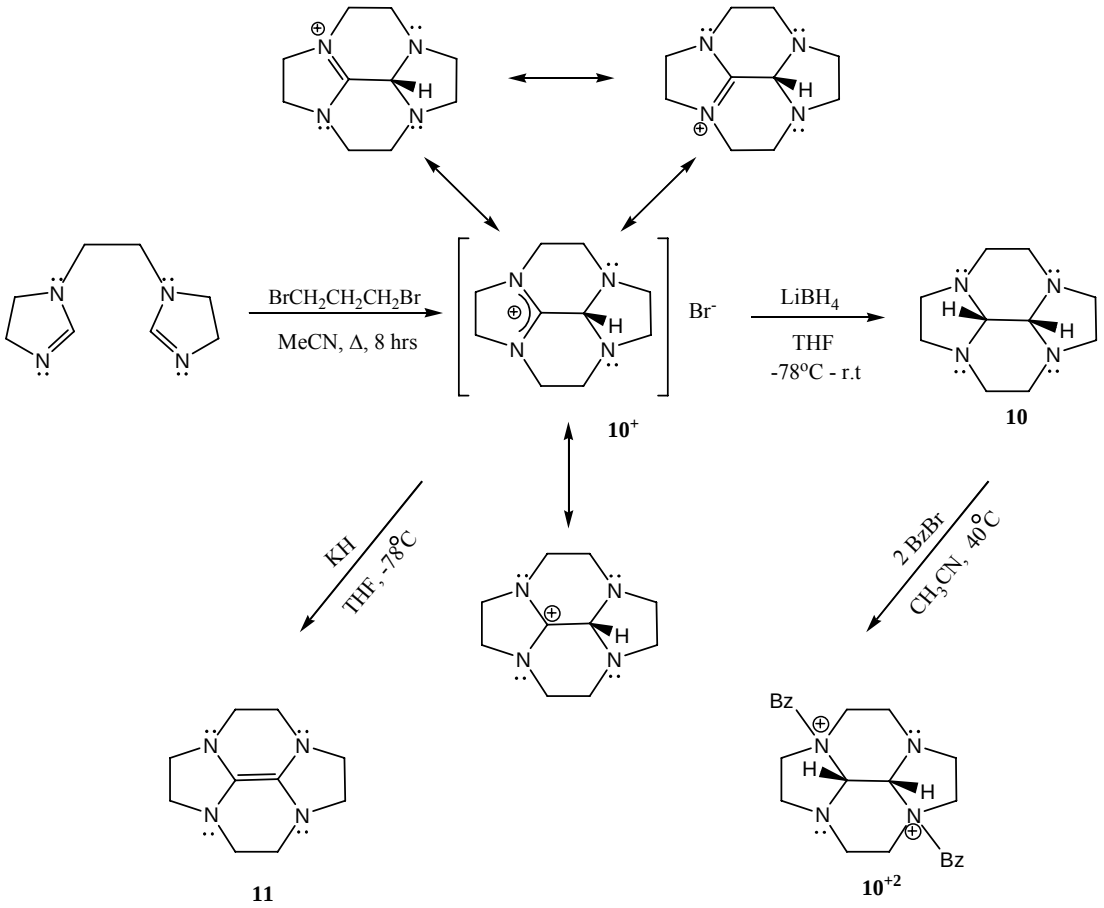


Figure 111: Synthetic scheme for 10, 10^{+}, 10^{+2}, and 11.

This abnormally long relaxation time was taken into account in subsequent data collections.

3.3.2 The general structure of 10^+

The ^{13}C spectra contains six resonances and ^{1}H data contain seven resonances at room and low temperature. The COSY data indicate one distinct spin system containing four proton resonances, those designated as H_{3a}, H_{3e}, H_{4a}, and H_{4e}. Although the lack of evidence of lack of spin-coupling relationships, shown by lack of correlations, should be used cautiously in establishing spatial relationships and atomic connectivity, TOCSY data did not indicate further coupling. It is reasonable to assume that these protons are contained in the same ring system thus implying that this spin-system contains the H atoms in either one of the five or six-membered rings. Due to the fact that these rings are separated by electronegative nitrogen atoms, which are quadrupolar, it is unlikely that the long range couplings will be retained through the nitrogen atom nor that ^4J data result from COSY peaks. Even with TOCSY data, ^4J correlations can be hard to discern since these long rang coupling values would be so small.

HSQC data indicate two resonances consistent with diastereotopic protons that correspond to protons in the same spin system. Protons designated as H_{3a} and H_{3e} are connected to C3 (δ/ppm 43.51) and protons designated as H_{4a} and H_{4e} are connected to C4 (δ/ppm 44.29). HMBC data indicate ^3J correlations between H_3 and C4 as well as H_4 and C3 signifying that these carbon atoms are indeed bonded. These protons must be in the same ring.

The protons in the two five membered rings would be expected to have very different chemical shifts from each other due to the fact that one ring contains a carbocation while the other does not. Placing H_{3a}, H_{3e}, H_{4a}, and H_{4e} in the either equivalent or accidentally equivalent six-membered rings as opposed to the five-membered rings is logical. Additionally, there are seventeen protons in the system, and H_{3a}, H_{3e}, H_{4a}, and H_{4e} each integrates to two when compared to the remaining regions which have integrations of four excluding the H_1 proton which has an integration of one.

This supports the fact that these protons represent accidentally or fully equivalent six membered rings.

DEPT data indicate that there is only one quaternary carbon atom, C2 (δ/ppm 165.76) which corresponds to the carbocation. This is supported by the fact that the resonance intensity is both very low and very deshielded which would be expected for a carbocation. Another observation obtained from DEPT data is that there is only one tertiary carbon atom, C1 (δ/ppm 71.98). HSQC data pairs H_1 with C1. With these important resonances identified, the HMBC spectrum further identifies the proton resonances attached to other carbon atoms which correlate to either carbon atom C1 or C2. H_1 correlates to C5 whereas C1 correlates to H_5. This indicates that the protons at H_5 which integrate to four protons are the protons in the five-membered ring which contains the tertiary carbon atom. In contrast, C2 correlates to H_9 placing the H_9 protons which also integrate to four protons in the same five-membered ring as the carbocation C2. The more deshielded value of H_9 also supports the fact that it is in the same ring as the carbocation because of the inductive effect that stabilizes the carbocation removes electron density from the rest of the ring thus deshielding this proton. The fact that H_1 is also deshielded is a result of the proximity to two nitrogen atoms (^3J) while none of the remaining protons is bound to more than one nitrogen atoms.

3.3.3 Conformational structure of 3^+

Now that the general connectivity of the rings have been discerned, it is important to be able to determine which of the two possible relationships for C3 and C4 exist which implies the presence of absence of a plane of symmetry in the molecule as shown in Figure 112. The major difference is based on HMBC data which indicate that both H_3 protons are correlated to the carbocation C2 whereas both H_4 protons are correlated to C1. This indicates that the leftmost figure in Figure 112 is correct. Additionally, other HMBC data supports this conclusion: H_9 correlates to C3 placing this carbon closer to H_9, H_5 correlates to C4 placing this carbon nearer to H_5 and H_4 correlates to C5 which also places this carbon nearer to H_4. This assignment is further supported by NOESY data which will be discussed.

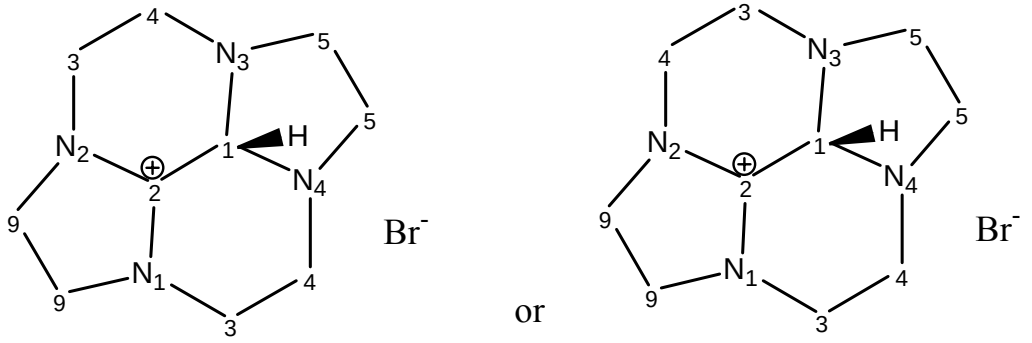


Figure 112: Two possible configurations of the cation.

Axial and equatorial orientations of protons H_{3a}, H_{3e}, H_{4a}, and H_{4e} are very important and indicate a great deal of information about the structure of the molecule. Initial determinations can be based on the dihedral angle and coupling values as related to the Karplus equation and then supported by NOESY data. The coupling constants were analyzed using MestRe-C. One of the four peaks, H_{3e} (δ/ppm 3.30) was first line-fitted and then the line-fitting was imported into the coupling constant analyzer to determine the coupling constants for these peaks. The simulation is shown in Figure 113. MestRe-C uses a Levenberg-Marquardt and Downhill Simplex Method for line fitting.

A total of six coupling constant values were determined to be: 2.0 Hz, 5.4 Hz, 5.4 Hz, 9.8 Hz, 12.2 Hz, and 14 Hz. Due to the number of protons involved, two of these must be a result of one bond (^2J) coupling and three must be a result of two bond (^3J) coupling. Based on the Karplus equation, the values 12.2 Hz and 14 Hz are too large to be considered a result of dihedral coupling. They fall in a range typical of geminal coupling constants which is -8 Hz to -18 Hz[54]. The sign of these coupling constants cannot be determined from 1D NMR but it is reasonable to assume that due to their magnitude, these coupling constants are a result of geminal dihedral coupling which must exist in this system. Furthermore, the only coupling constants that each set of diastereotopic protons has in common is this set and a coupling of 5.4 Hz. As will be shown later, the 5.4 Hz coupling is a result of a dihedral coupling. In conclusion, H_{3a} and

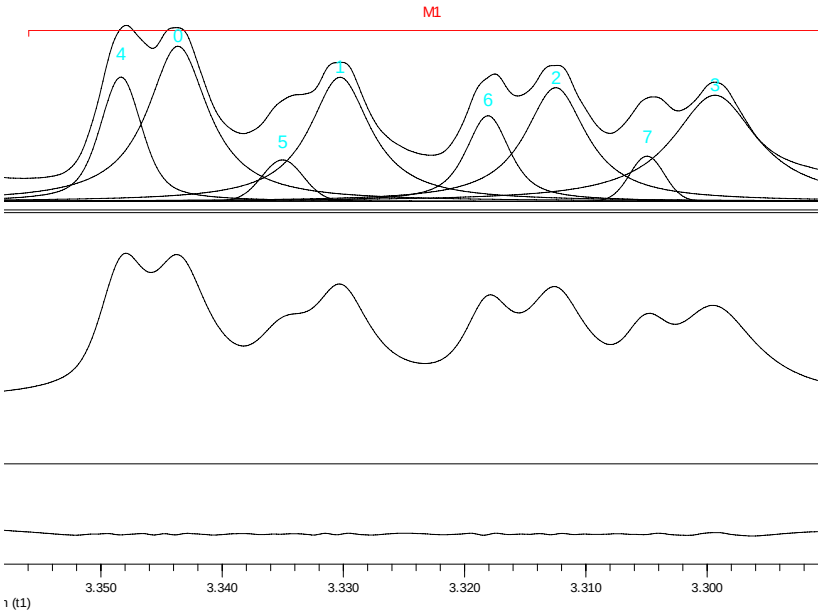


Figure 113: Line-fitting simulation.
Top spectrum indicates original spectrum with line-fitting applied. Middle spectrum is simulated from best line-fit. Bottom spectrum indicates the difference between the original and the simulated spectrum.

H_{3e} have a coupling constant of 12.2 Hz and H_{4a} and H_{4e} have a coupling constant of 14 Hz.

The remaining coupling constants: 2.0 Hz, 5.4 Hz, 5.4 Hz, and 9.8 Hz are shared between one proton in one set of diastereotopic protons and a different proton in the other diastereotopic set. Each value corresponds to only one possible interaction between sets of protons. The largest value of 9.8 Hz indicates that the coupling is at an extreme angle such as 180 ° or 0 . In fact, a slightly larger than standard value for J^0 must be used with the equation to determine this. In any case, this is either an axial-axial interaction or an extremely unusual equatorial-equatorial interaction. Based on this information alone, the interaction between H_{3a} and H_{4a} is most likely axial-axial; there is also only one remaining type of interaction further supported by NOESY data.

Simple deduction allows one to calculate that the remaining H_{3a} coupling values must be a result of an axial-equatorial interaction between H_{3a} and H_{4e}; likewise, the remaining H_{4a} coupling value must also be a result of an axial-equatorial interaction

between H_{4a} and H_{3e}. Since the angle between H_{3a} and H_{4a} is 180°, the fact that these angles are approximately the same and would therefore produce similar coupling constants, is reasonable. An angle of 61° is calculated as a result of a coupling constant value of 5.4 Hz and the assumption that J^0 = 9.5 Hz. Finally, the remaining interaction must be an equatorial-equatorial interaction between H_{4e} and H_{3e}. The angle associated with a coupling constant value of 2.0 Hz is 37° and was calculated using the Karplus equation and the assumption that J^0 = 9.5 Hz.

NOESY correlations support the previous conclusions on coupling constants as well as help to determine whether H_{4a} or H_{3a} is *up*. All NOESY spectra in this chapter follow the convention that diagonal peaks are negative. The distance correlations are therefore positive while any exchange correlations remain in phase with the negative diagonal peaks. The positive peaks are denoted with warm colors and negative peaks are denoted with cool colors.

A very important correlation that can be obtained from the NOESY data is that between H_1 and H_{4a}. This indicates that H_{4a} is *up* and by default, H_{3a} is *down*. Further structural information can be obtained from correlations between H_9 and both H_{3a} and H_{3e}. It is reasonable to assume that the five-membered ring containing H_9 is very nearly planar due to the carbocation C2. This allows for the fact that at least one of the two protons on each of the C9 carbon atoms will be in close proximity to both the *down* axial proton H_{3a} and the *up* equatorial proton H_{3e}. An interaction which initially seems unusual is also present between H_5 and both H_{4e} and H_{3a}. This interaction can be explained by assuming that the five-membered ring containing H_5 is tilted slightly underneath the molecule possibly as a result of the proton H_1. This would account for the fact that at least one of the two protons on each of the C5 atoms would be in close proximity to both the *down* axial proton H_{3a} and the *down* equatorial proton H_{4e}.

All of the information is with respect to solution structure but also has correlations to the crystal structure of this molecule which has also been determined.[131] VT NMR was also used to determine the fluxionality of this species in solution. Very little fluxional behavior changed. The signals corresponding to 4a and 3e only slightly increased in intensity.

3.3.4 Bonding models and theoretical structure

Although the symmetry of $\mathbf{10}^+$ is low and contains a plane of symmetry as the only symmetry element beyond the identity element, the system is not subject to the second order Jahn-Teller distortion, whereas **10**, is heavily distorted using this mechanism.

In general, radial interactions, dictated by the Coulombic interactions between atoms, are much stronger than an angular interaction. Intuitively, angular potentials are shallow and often contain several local minima, the barriers between which are usually low. For $\mathbf{10}^+$ to undergo such a distortion would require a change in the orbital arrangement in the conjugation-stabilized carbocation; by undergoing torsion along the C1-C2 vector, the stabilization of the carbocation will be strongly reduced. This raises the energy of the *pseudo*-a_2 normal coordinate that is required to interconvert the two asymmetric isomers and as a consequence, thermal population of this mode is not possible at the temperatures of measurement. It is also of note that there is no exchange of H_1 between C1 and C2 in either an intra- or intermolecular mechanism.

Figure 114 shows a proposed structure of the molecule according to NMR. A crystal structure is shown in Figure 115. A correlational table of the 2D data is given in Table 3.3. The carbon and proton spectra are shown in Figure 116. T_1 relaxation data as well as related graphs are shown in Figure 117 and Figure 118. VT data for this molecule is in Figure 119 - Figure 122. Relevant 2D spectra are shown in Figure 123 - Figure 126.

3.4 Stereochemistry of 10

The determination of the stereochemistry of decahydro-2a, 4a, 6a, 8a-tetraaza-cyclopenta[fg]acenaphthalene, **10**, as derived from available NMR spectra is not trivial. This molecule was characterized using 1D, and 2D NMR. Both 1D and 2D VT techniques were used to study the fluxionality of this molecule. All studies used solutions of **10** in d_8-toluene. Acquisition parameters and other experimental details are given in Section 3.6.1.3. For reference purposes, relevant figures, spectra, and tables are placed at the end of this section.

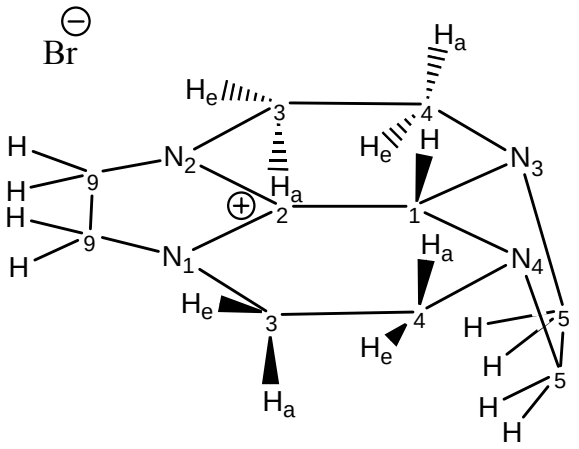


Figure 114: The structure of 10^+ that is consistent with the NMR data.

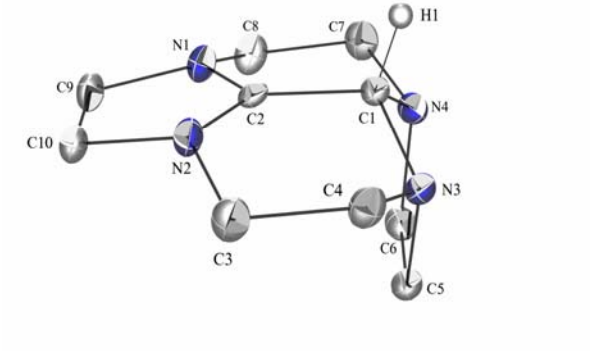


Figure 115: Crystal structure of 10^+.

Table 3.3: NMR correlations for 10^+.

^{1}H position	^{13}C δ/ppm	^{1}H δ/ppm HSQC	^2J (|J|/Hz)	^3J (|J|/Hz)	COSY&TOCSY	HMBC *(C)*	NOESY *(H)*
1	71.98	4.42	--	--	--	**5**	**4_a**
2	165.76	--	--	--	--	--	--
$3_{e\ up}$	43.51	3.31	3_a (*12.2*)	4_e *(2.0ee)* 4_a *(5.4ae)*	3_a, 4_e, 4_a	4, **2**	3_a, 4_e, 4_a, **9**
$3_{a\ dn}$		3.55	3_e (*12.2*)	4_e *(5.4ae)* 4_a *(9.8aa)*	3_e, 4_e, 4_a	4, **9**, **2**	3_e, 4_e, 4_a, **5, 9**
$4_{e\ dn}$	44.29	3.19	4_a (*14*)	3_e *(2.0ee)* 3_a *(5.4ae)*	3_a, 3_e, 4_a	3, **5**, **1**	3_a, 3_a, 4_a, **5**
$4_{a\ up}$		3.4	4_e (*14*)	3_e *(5.4ae)* 3_a *(9.8aa)*	3_a, 3_e, 4_e	3, **5**, **1**	3_e, 3_a, 4_e, **1**
5	48.19	3.03	m	m	--	**4**, **1**	**4_e, 3_a**
9	51.04	3.9	m	m	--	**2**, **3**^{a}	**3_e, 3_a**

Numbers in bold indicate that this atom is in a different spin system than the atom to which it is correlating. ^{a}Peak is visible when spectrum intensity is increased.

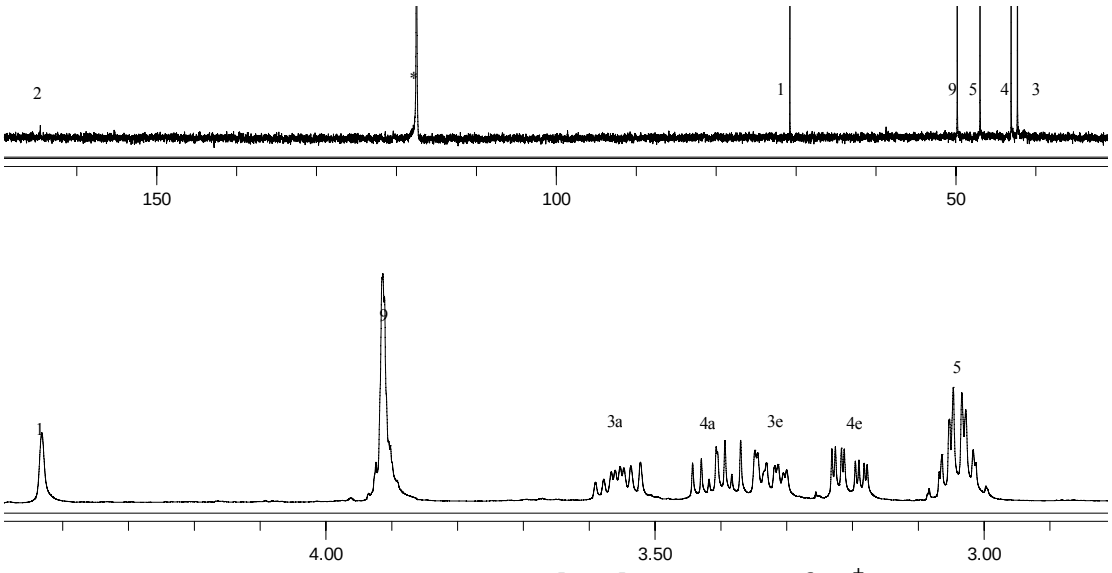


Figure 116: Proton and carbon spectra of 10^+.

^{1}H-NMR (400 MHz) δ/ppm 4.42 (s, 1H) 3.9 (m, 4H) 3.55 (ddd, 2H, *J* = 5.4 Hz, *J* = 9.9 Hz, *J* = 12.4 Hz) 3.40 (ddd, 2H, *J* = 5.3 Hz, *J* = 9.7 Hz, *J* =14.0 Hz) 3.31 (ddd, 2H, *J* = 2.0 Hz, *J* = 5.5 Hz, *J* = 12.1 Hz) 3.19 (ddd, 2H, *J* = 2.0 Hz, *J* = 5.4 Hz, *J* = 13.9 Hz) 3.03 (m, 4H) ^{13}C-NMR (400 MHz) δ/ppm 165.76 (C), 71.98 (CH), 51.04 (CH_2), 48.18 (CH_2), 44.29 (CH_2), 43.51 (CH_2).

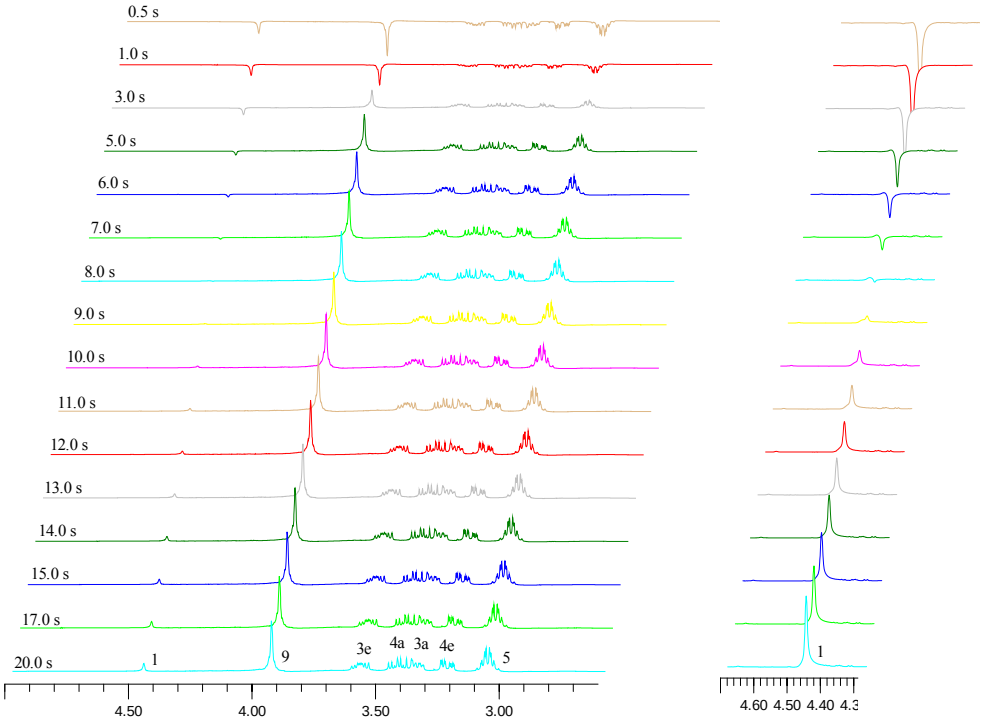


Figure 117: T_1 relaxation study for long relaxation of 10^+.

Relaxation times: 0.5 s, 1.0 s, 3.0 s, 5.0 s, 6.0 s, 7.0 s, 8.0 s, 9.0 s 10.0 s, 11.0 s, 12.0 s, 13.0 s, 14.0 s, 15.0 s, 17.0 s, 20.0 s. ^{1}H-NMR (400 MHz) δ/ppm 4.42 (11.9 s)

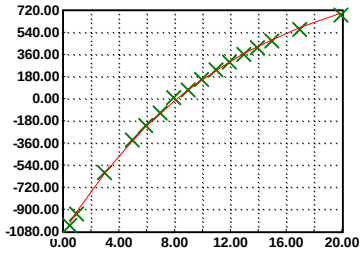


Figure 118: Graph of T_1 relaxation of methine proton.

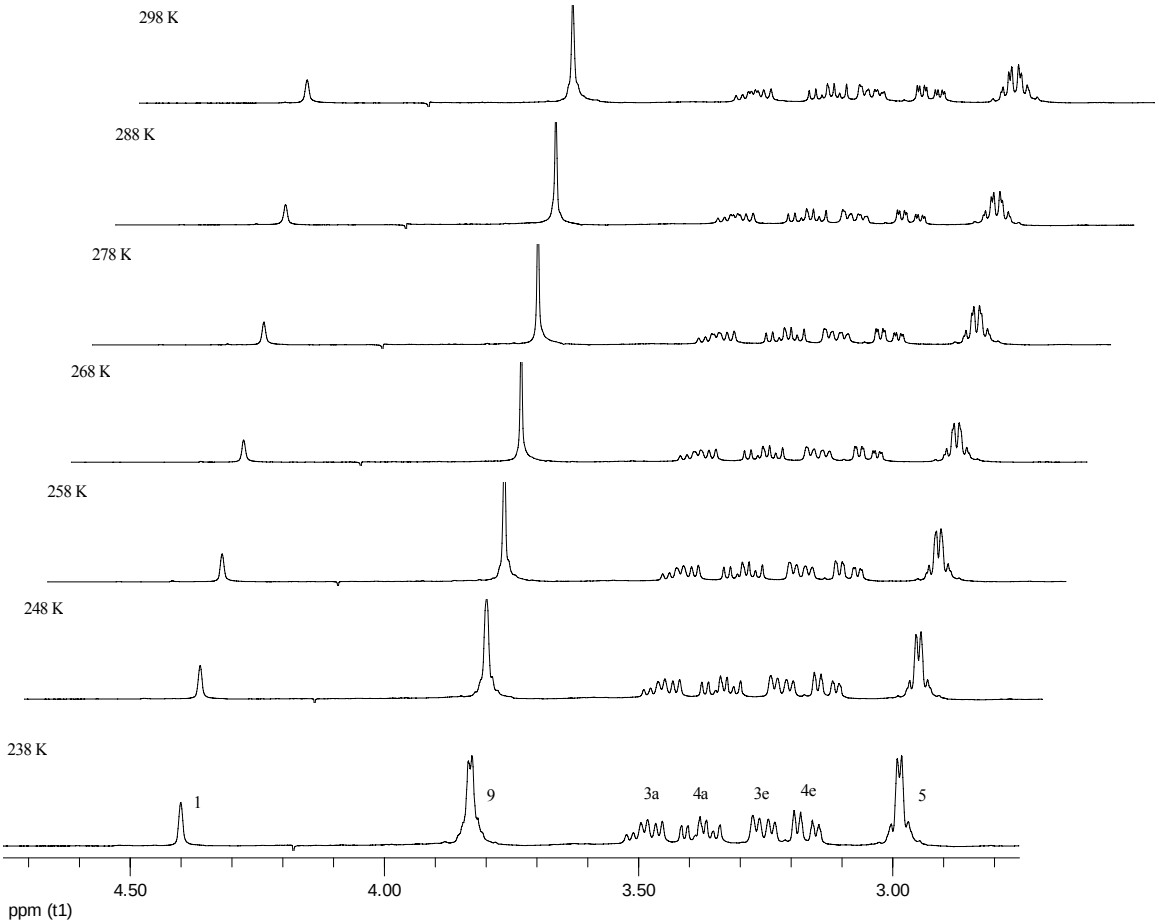


Figure 119: Stacked plot of VT NMR for 10^{+}.

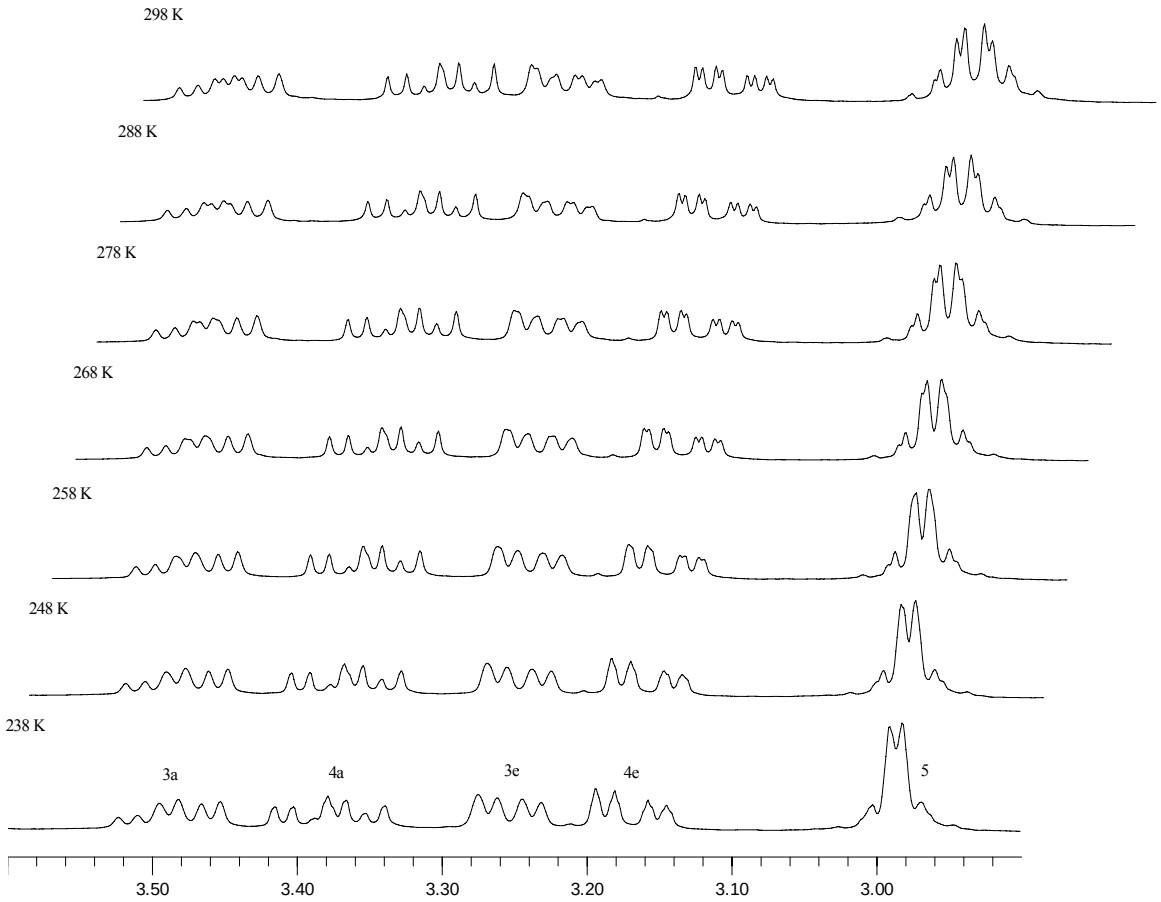


Figure 120: Expanded stacked plot of VT NMR for 10^{+}.

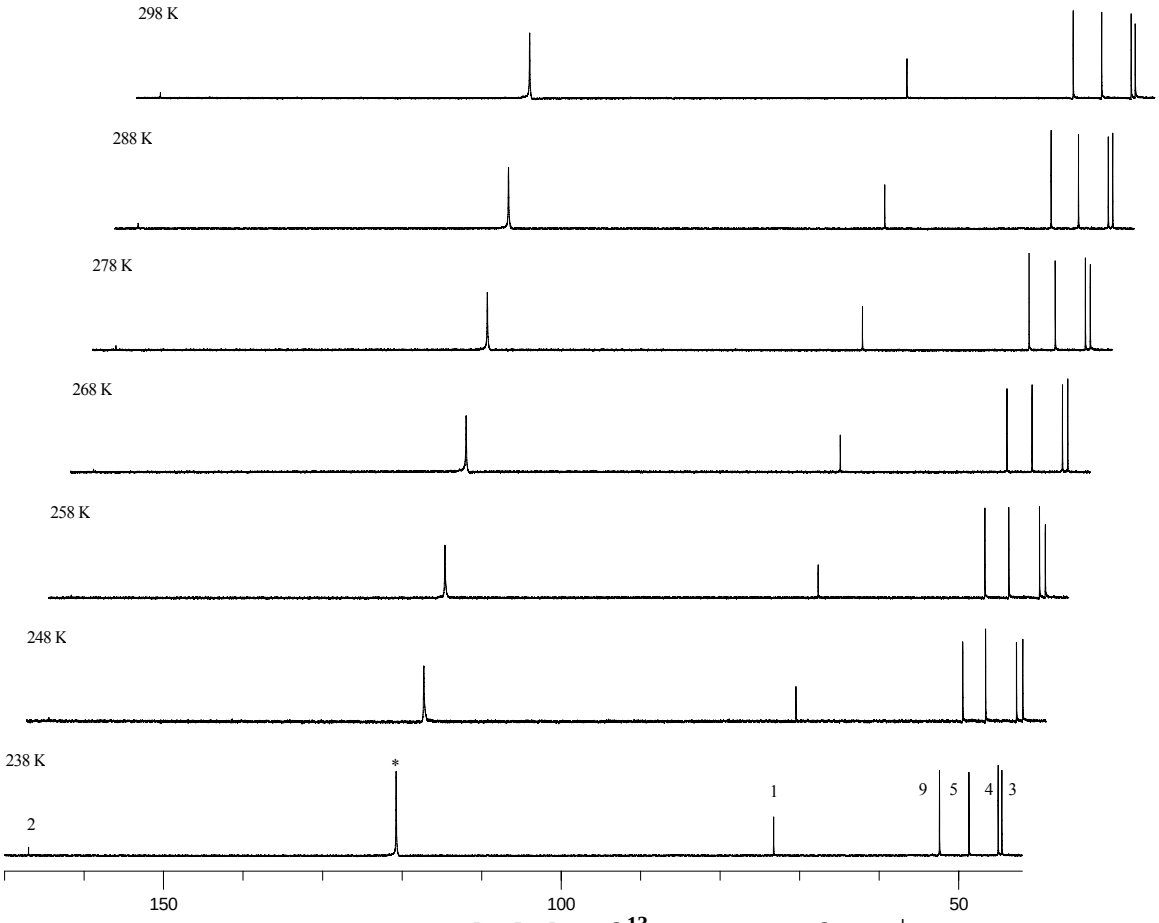


Figure 121: Stacked plot of ^{13}C VT NMR for 10^{+}.

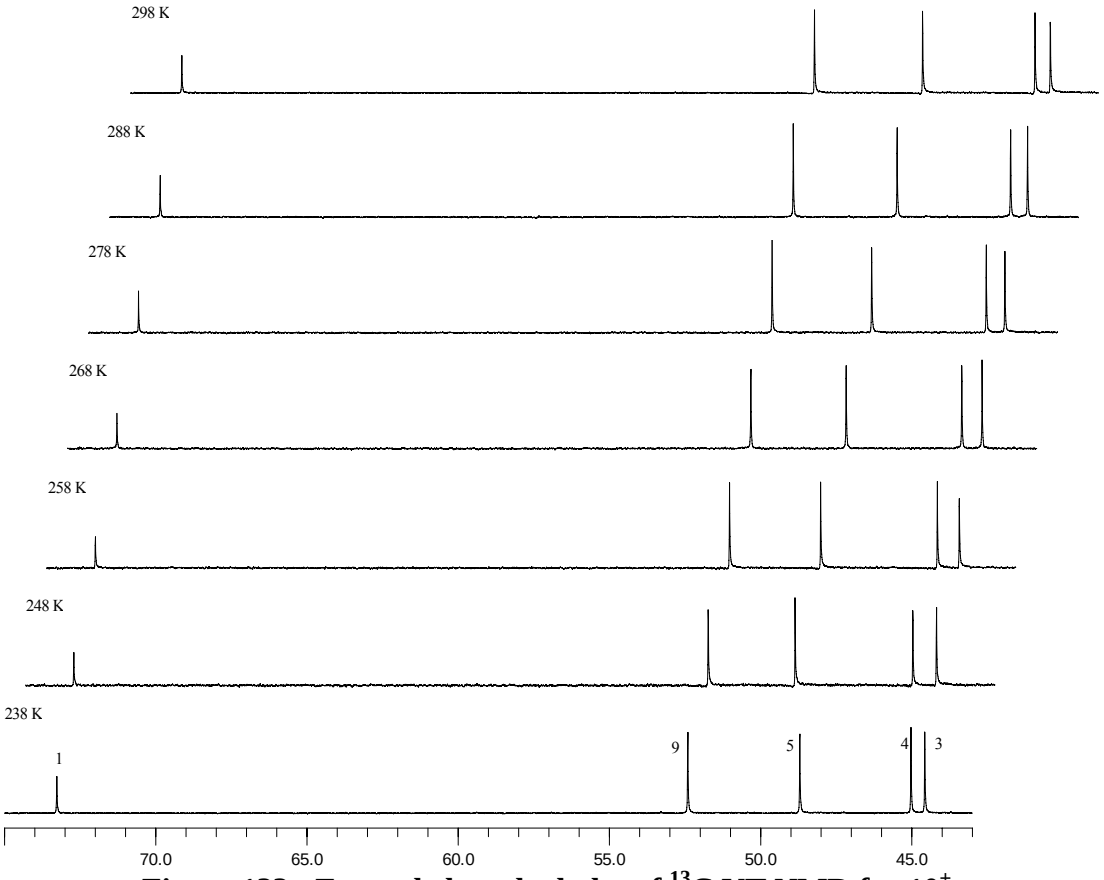


Figure 122: Expanded stacked plot of ^{13}C VT NMR for 10^{+}.

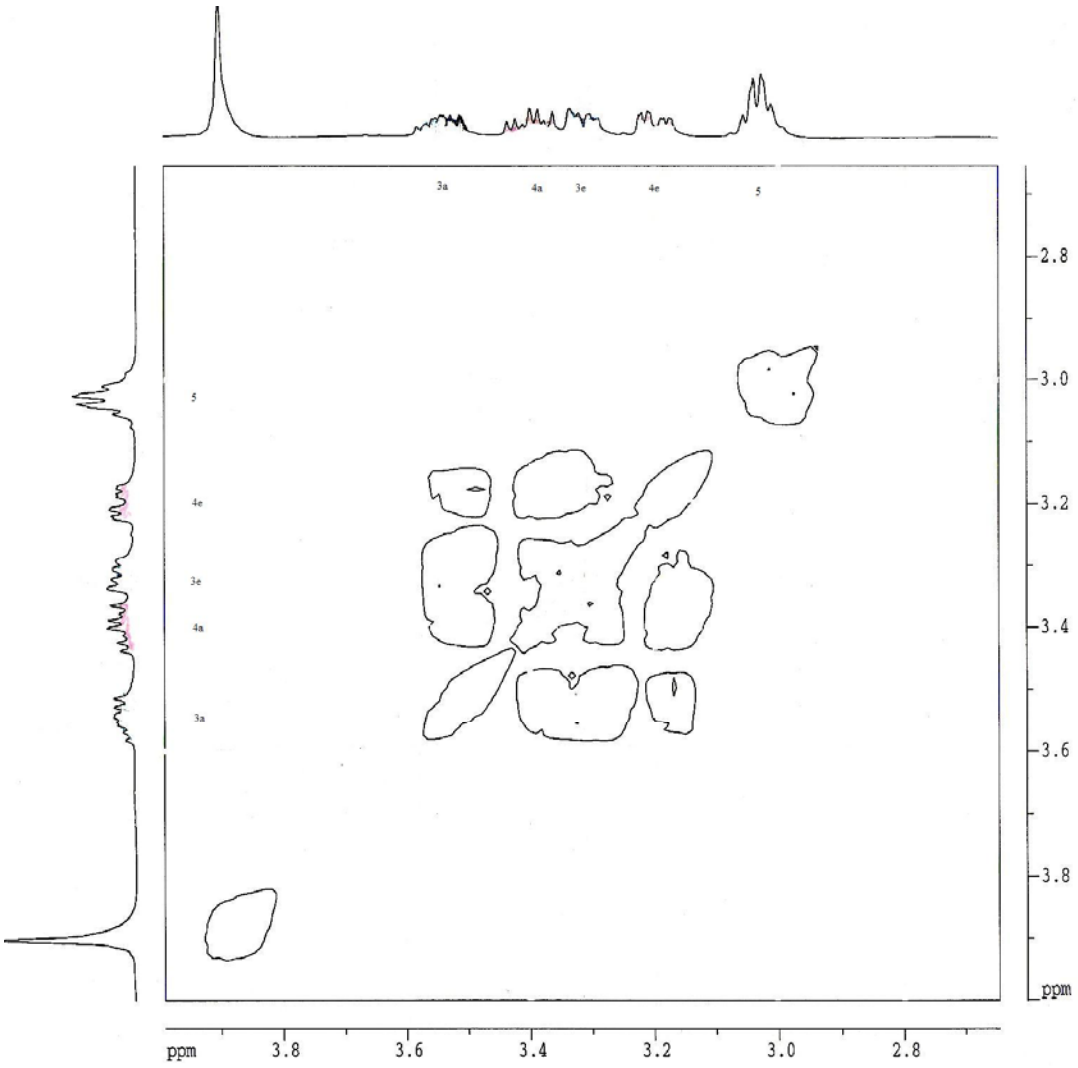


Figure 123: COSY NMR of 10^{+}.

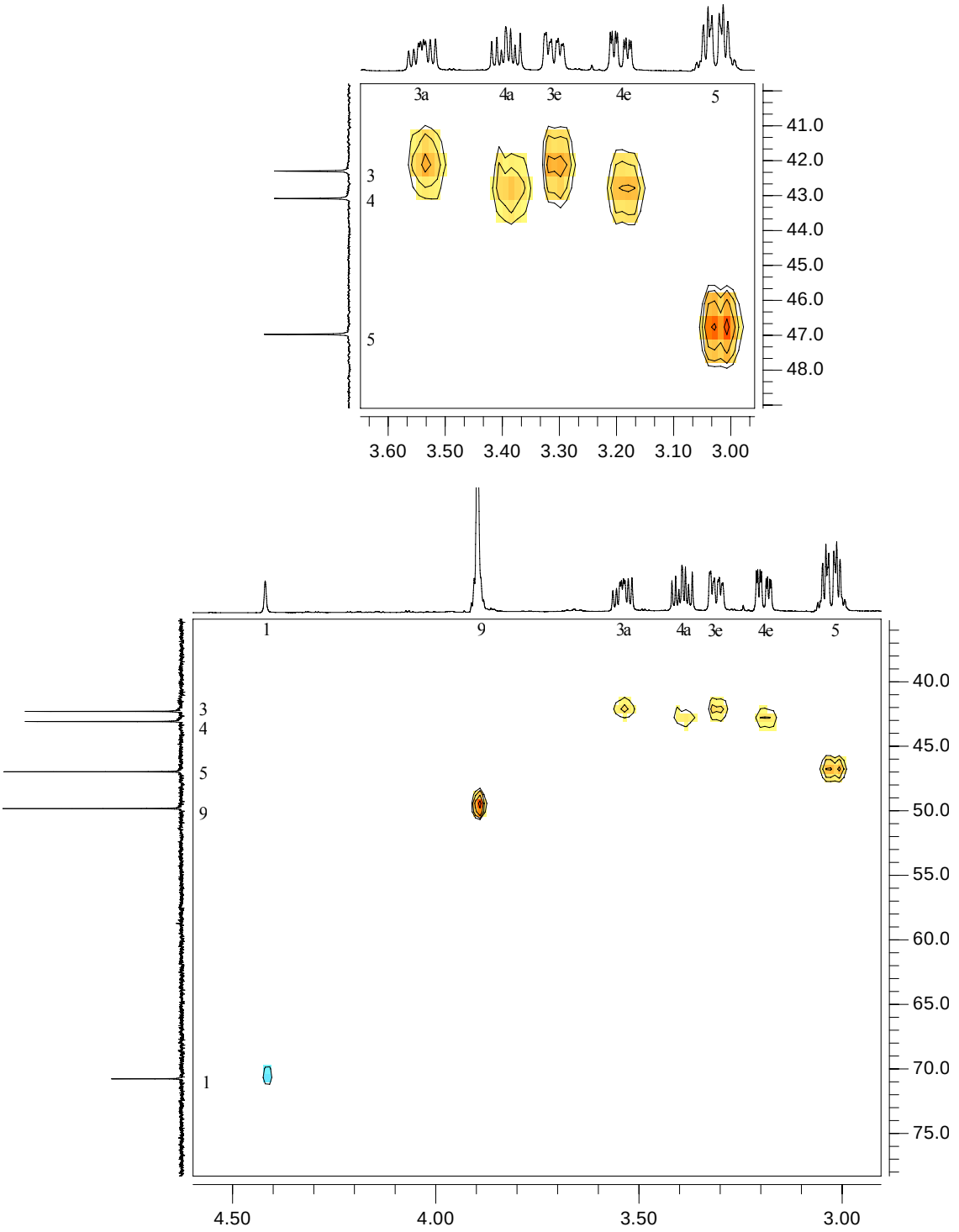


Figure 124: HSQC NMR of 10^{+}.

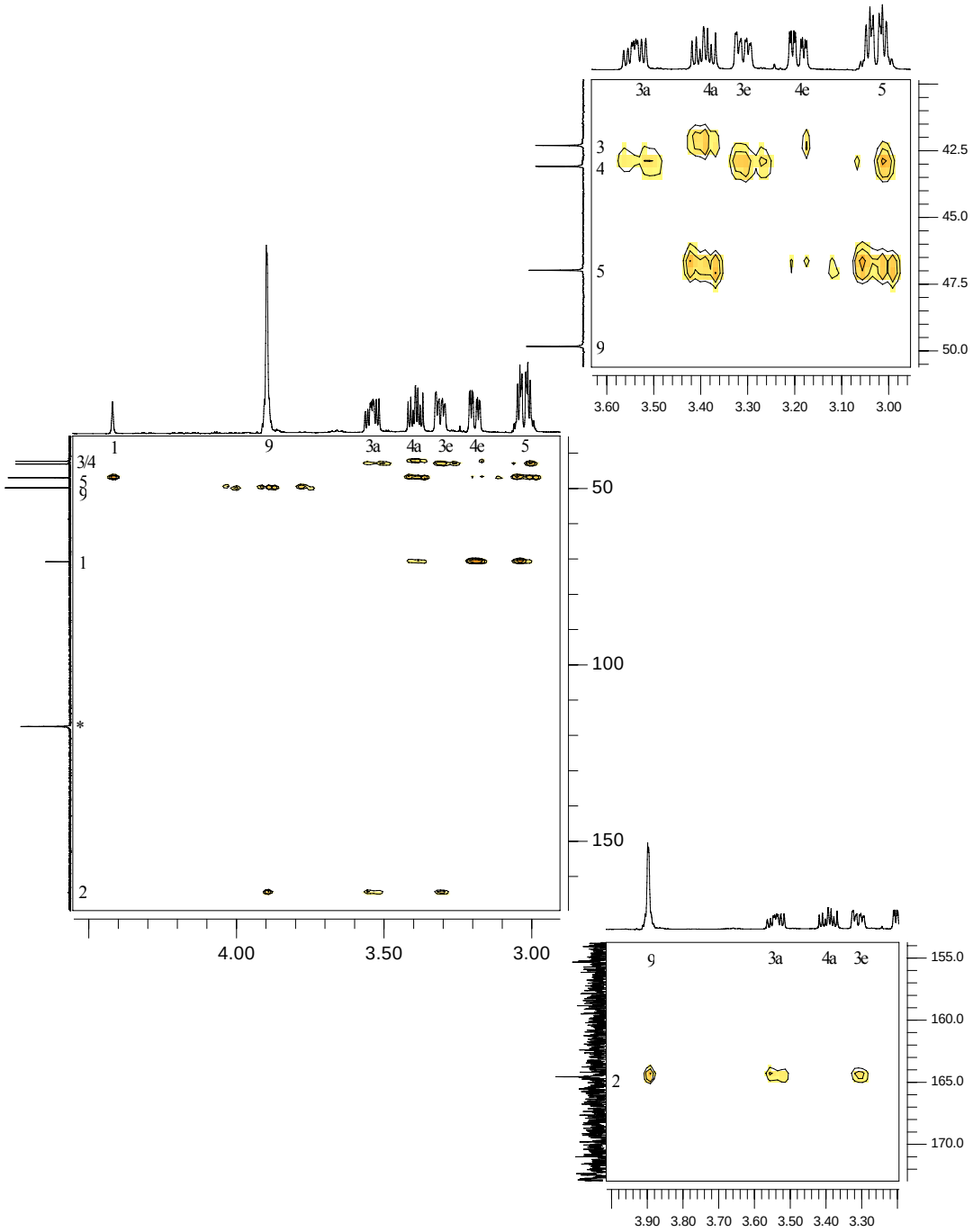


Figure 125: HMBC NMR of 10^{+}.

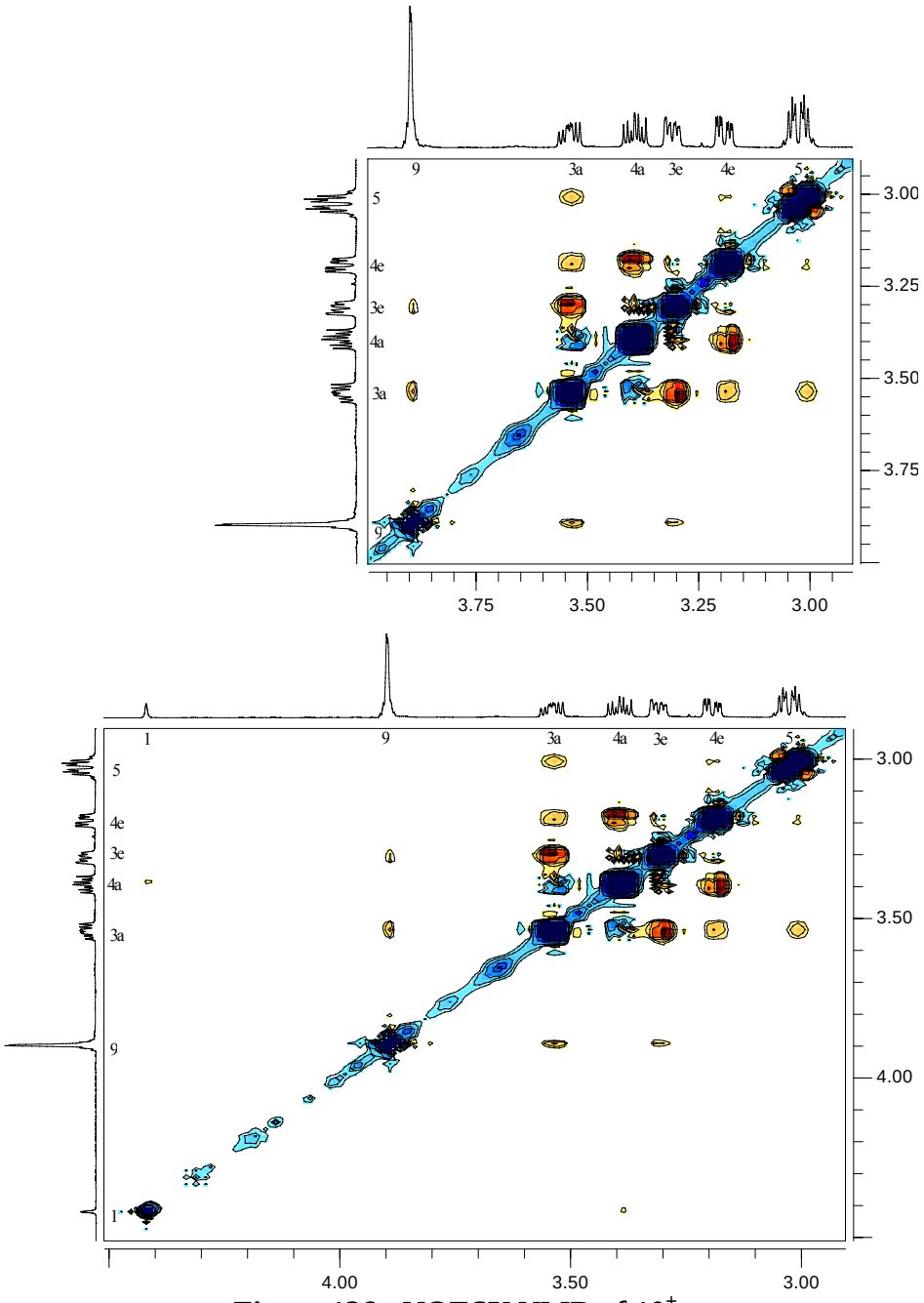


Figure 126: NOESY NMR of 10^{+}.
Mixing time used was 1.4 seconds.

3.4.1 Low temperature configuration

The molecular study will begin with the molecule in its low temperature configuration. The ^{13}C data contain five resonances and ^{1}H data contain nine resonances at low temperature; however, two of the previously mentioned nine ^{1}H resonances lie in the same position so that they appear to be nearly the same resonance. 2D spectra identify the difference between these protons clearly. When the 2D spectra are displaced on the same screen with the same margins, they can be compared directly which allows for comparison of overlapping multitplets and a better discernment of actual shift.

COSY spectra indicate the presence of two distinct and unrelated spin systems. One spin system exists between the protons on C3 and C4 and the other spin system exists between the protons on C5 and C6. TOCSY data further indicates that these spin systems do not show long range coupling values across the nitrogen atom.

Use of the information in the COSY in addition to the HMQC data allows assignment of all diastereotopic proton sets to carbon atoms. Protons designated as H_{3a} and H_{3b} are attached to C3 (δ/ppm 43.96). Protons designated as H_{4a} and H_{4b} are attached to C4 (δ/ppm 52.17). Protons designated as H_{5a} and H_{5b} are attached to C5 (δ/ppm 52.03). Protons designated as H_{6a} and H_{6b} are attached to C6 (δ/ppm 49.74). Additionally, the methine protons are also identified as H_1 and attached to C1 (δ/ppm 77.72). The protons that are most difficult to assign are H_{4a} and H_{5b} because they overlap in such a manner that use of only HMQC data would not have distinguished the peaks. It is beneficial though that these two protons are in different spin systems as previously identified from the COSY data. The proton to carbon designation for H_{4a} and H_{5b} is obvious when the rest of the peaks are assigned because one proton is missing from each system; therefore, one of the protons is attached to C4 while the other is attached to C5. Very close examination of TOCSY and COSY data at the overlap indicates that the proton in the C3, C4 spin system is slightly less deshielded than the proton in the C5, C6 spin system.

Once the diastereotopic sets are determined, coupling constants can be assigned so that dihedral angles can be calculated. Each proton signal would be expected to have three coupling constants: two due to dihedral coupling and one due to geminal coupling.

Coupling constants, which are approximately in the range of -8 to -18 Hz, most likely correspond to geminal coupling constants and in addition should be the only set of coupling constants that are in common within each diastereotopic set. The geminal coupling constant for: (H_{3a} and H_{3b}) is 10.9 Hz; (H_{4a} and H_{4b}) is 9.5 Hz; (H_{5a} and H_{5b}) is 11.5 Hz; and for (H_{6a} and H_{6b}) is 8.9 Hz. All the coupling constant values were determined from linear fitting the data using spinworks.

NOESY data indicate that the protons in the same coupling rings are close in proximity to one another which would be expected. Additionally, very important exchange information is obtained based on the strength and phase of certain crosspeaks. One proton in each group likely exchanges with the corresponding opposite proton. This means that H_{3a} would exchange with H_{4b}, H_{3b} would exchange with H_{4a}, H_{5b} would exchange with H_{6a}, H_{6a} would exchange with H_{4b}.

Using standard proton HMBC would not give further answers due to the fact that in either case, H4 protons would correspond to both C5 and C6 causing no further clarification. Instead, other information is needed to determine both which ring the protons lie in and which carbon atoms are nearer to each other outside of the spin system. Deuteration of one of the C1 hydrogen atoms would easily clarify the analysis of this species because the integration will be half of the original value for the protons in the ring system. Additionally, HMBC spectra of these deuterated compounds will show a correlation between the remaining H_5 protons and either H_3 or H_4 protons indicating which protons are closest to the ring.

The NOE difference that is available indicates *via* a pulse on H_1 that transfer occurs to: H_{4b}, H_{3a}, H_{6a}, and either H_{5b} or H_{4a}. It is likely that H_{5b} is the actual peak since it would be remaining peak with the same direction properties as H_{4b}, H_{3a}, and H_{6a}. If this were true, H_{3a}, H_{4b}, H_{6a}, and H_{5b} would be *up*. Their corresponding diastereotopic peaks would be *down*. Additionally, a pulse on H_{6a} indicates that it is close in proximity to H_1, verifying it is *up* as well as H_{6b} and H_{5a} which would be expected. A pulse on H_{4b}, shows some proximity to H_1, H_{3b}, and either H_{4a} or H_{5b}. The previous pulse is most likely an interaction with H_{4a} since it is in the same ring system. The protons are not *trans* due to the fact that there is a correlation between H_1 and H_{3a} and H_{4b} instead of H_{3a} and H_{4a}.

Based on the data obtained from room temperature NOESY data, which will be discussed shortly, the five membered rings should be less fluxional and thus finish chemical exchange at a lower temperature.

Finally, at low temperature, the T_1 relaxation of all these peaks is very fast ranging between 0.25 s and 0.75 s. H_1 has the longest relaxation of all the peaks.

Figure 127 shows eight possible structures of the molecule according to NMR. The proton and carbon NMR spectra are given in Figure 128. Relevant correlational data are given in Table 3.4. A Spinworks simulation of the low temperature data are shown in Figure 129. Figure 130 shows T_1 data. Relevant 2D spectra are shown in Figure 131 - Figure 134. VT data is given in Figure 135 - Figure 136. Figure 137 shows a Spinworks simulation of the spectra at a temperature slightly below coalescence. Intensity values selected peaks from NOESY experiments to be used for EXSYcalc are in Table 3.5 and Table 3.6.

3.4.2 VT data

VT data points were used to determine the correlational temperatures of the two processes in this molecule. One process coalesces at 243 K while the other process coalesces at 238K. The molecular motion at below 238 K, the molecular motion is on a time-scale that is slower than the NMR time-scale. This is evidenced by the fact that the spectrum changes dramatically as the temperature is decreased. New and unique correlations can be determined from low temperature correlations which are different but in accord with room temperature data.

Three types of programs were used to attempt to determine the exchange rate constants. In one case, Spinworks was used to simulate the spectrum at low temperature, then the MEXICO program was used to try to simulate the system at high temperature but the spin systems in **10** were too complicated for this program. Instead of MEXICO, DNMR was also used but it was not designed for eight exchanging protons. A close fitting room temperature simulation is given at the end of the section as determined by MEXICO.

A program offered in conjunction with the MestReC suite is EXSYcalc which uses actual NOESY intensity data to calculate exchange rates. The absolute intensities of the

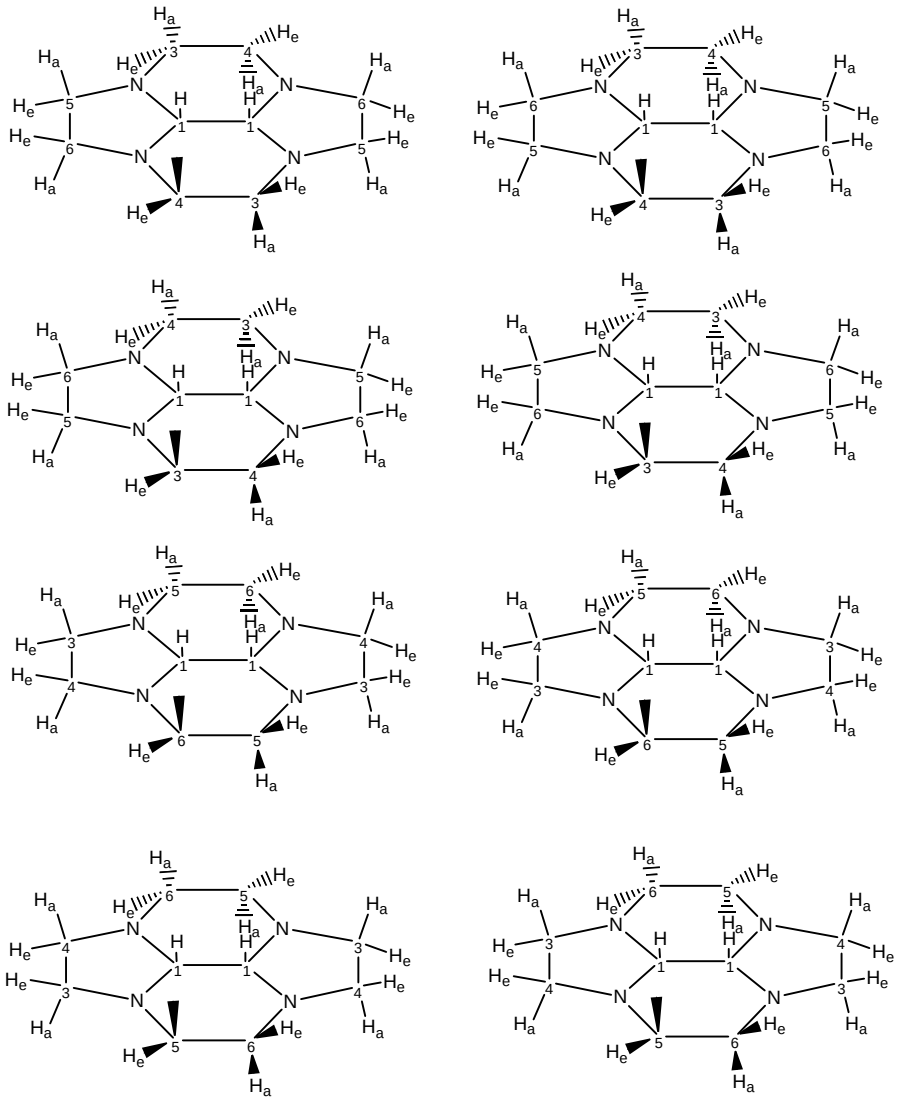


Figure 127: Eight possible structures for 10 at low temperature.

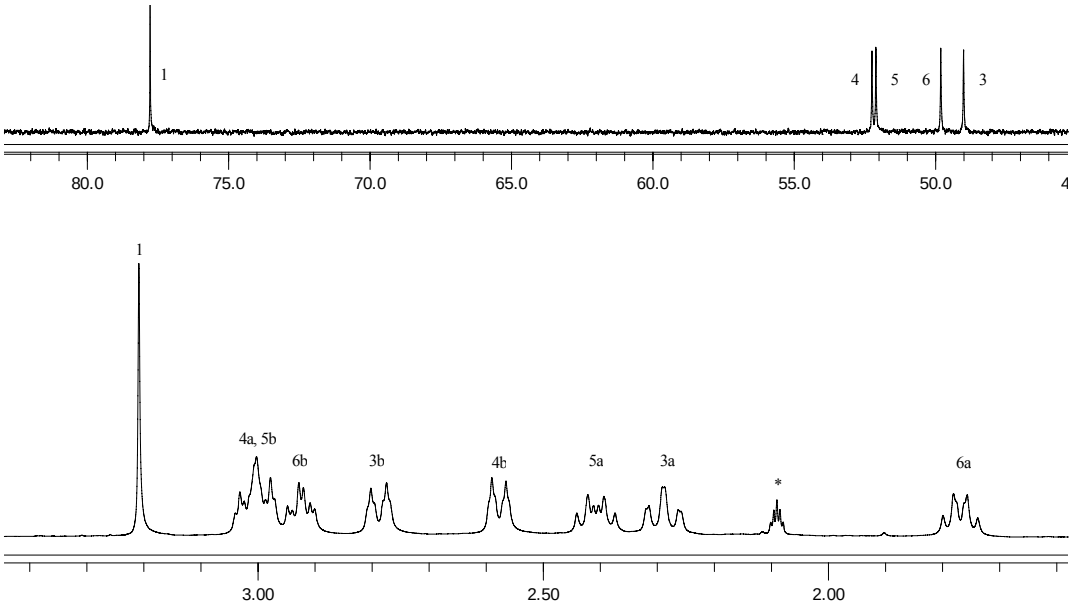


Figure 128: Proton and carbon spectra of 10 at low temperature.

^{1}H-NMR (400 MHz) 3.219 (s, 1H) 3.02 (tt, 1H, *J* = 2.9 Hz, *J* = 10.6 Hz) 2.92 (dt, 1H, *J* = 3.4 Hz, *J* = 7.9 Hz) 2.77 (td, 1H, *J* = 2.4 Hz, *J* = 10.7 Hz) 2.60 (td, 1H, *J* = 2.2 Hz, *J* = 10.9 Hz) 2.40 (td, 1H, *J* = 7.8 Hz, *J* = 12.4 Hz) 2.32 (dt, 1H, *J* = 2.5 Hz, *J* = 11.4 Hz) 1.76 (td, 1H, *J* = 7.1 Hz, *J* = 9.5 Hz). ^{13}C-NMR (400 MHz) 77.77\8 (CH), 52.25 (CH_2), 52.11 (CH_2), 49.82 (CH_2), 49.01 (CH_2)

Table 3.4: NMR correlations for 10 at low temperature.

^{1}H position	^{13}C (δ/ppm)	^{1}H (δ/ppm) HMQC	^{2}J (|J|/Hz)	^{3}J (|J|/Hz)	COSY & TOCSY	HMBC (*C*)	NOESY
1	77.72	-	-	-	-		-
3_a		2.29	^{2}J (11.1)	^{3}J (2.3,11.1)	3_b, 4_a, 4_b		3_b, 4_a, $^{a}4_b$
3_b	48.96	2.79	^{2}J (11.1)	^{3}J (2.3,3.1)	3_a, 4_a, 4_b		3_a, $^{a}4_a$, 4_b
4_a		3	^{2}J (9.8)	^{3}J (3.1, 11.1)	4_a, 3_a, 3_b		4_a, 3_a, $^{a}3_b$
4_b	52.17	2.58	^{2}J (9.8)	^{3}J (2.3,2.3)	4_b, 3_a, 3_b		4_b, $^{a}3_a$, 3_b
5_a		2.4	^{2}J (11.1)	^{3}J (7.9, 7.7)	5_b, 6_a, 6_b		5_b, 6_a, $^{a}6_b$
5_b	52.03	3'	^{2}J (11.1)	^{3}J (9.7, 3.4))	5_a, 6_a, 6_b		5_a, $^{a}6_a$, 6_b
6_a		1.77	^{2}J (7.7)	^{3}J (9.7, 7.7)	6_b, 5_a, 5_b		6_b, 5_a, $^{a}5_b$
6_b	49.74	2.92	^{2}J (7.7)	^{3}J (7.9, 3.4)	6_a, 5_a, 5_b		6_a, $^{a}5_a$, 5_b

^{a}Indicates exchange information rather than distance correlation.

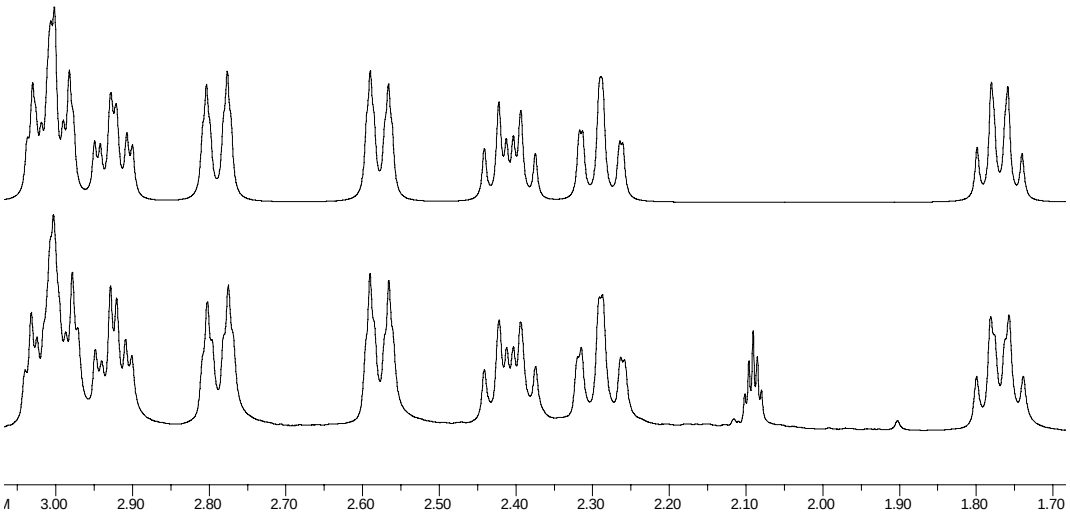


Figure 129: Spinworks simulation of 10 at low temperature.
Solvent peak is not included in simulation. Simulation is the higher spectrum and actual data are the lower spectrum.

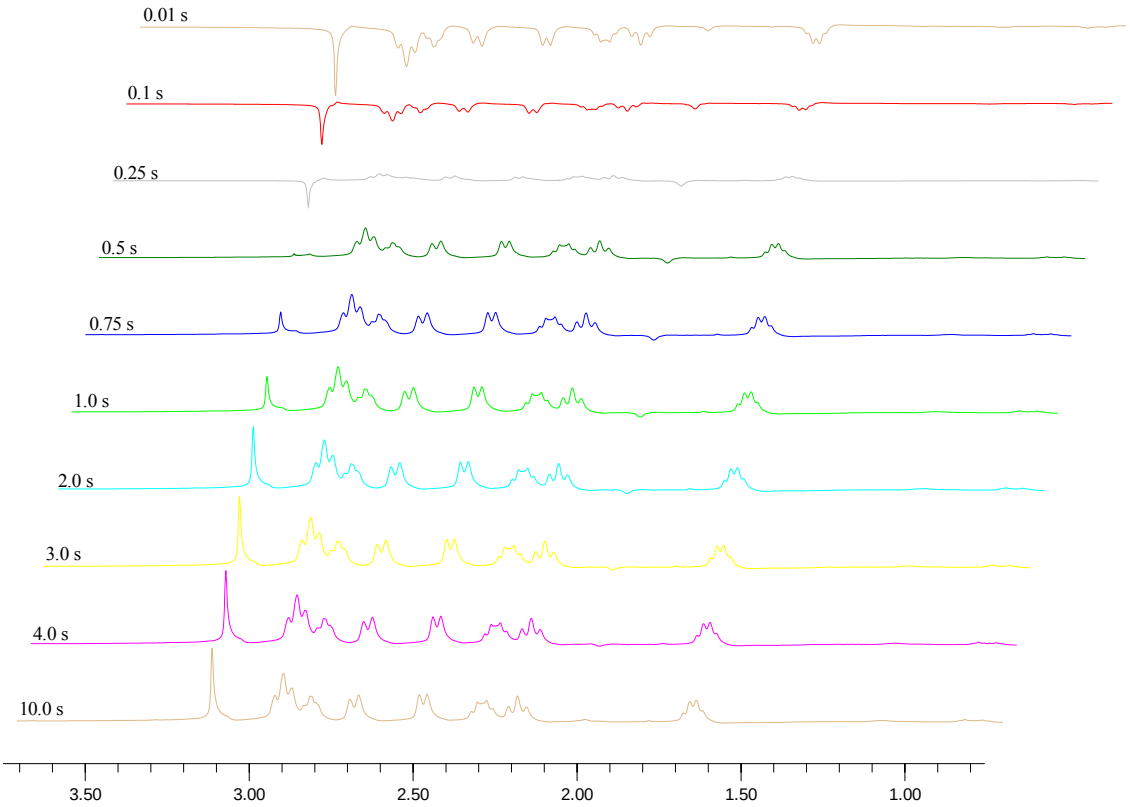


Figure 130: T_1 relaxation study of 10 at low temperature.

Time delays: 10.0 s, 4.0 s, 3.0 s, 2.0 s, 1.0 s, 0.5 s, 0.75 s, 0.25 s, 0.10 s, 0.01 s.^{1}H-NMR (400 MHz) 3.219 (0.66 s) 3.02 (0.29 s) 2.92 (0.29 s) 2.77 (0.28 s) 2.60 (0.28 s) 2.40 (0.25 s) 2.32 (0.25 s) 1.76 (0.26).

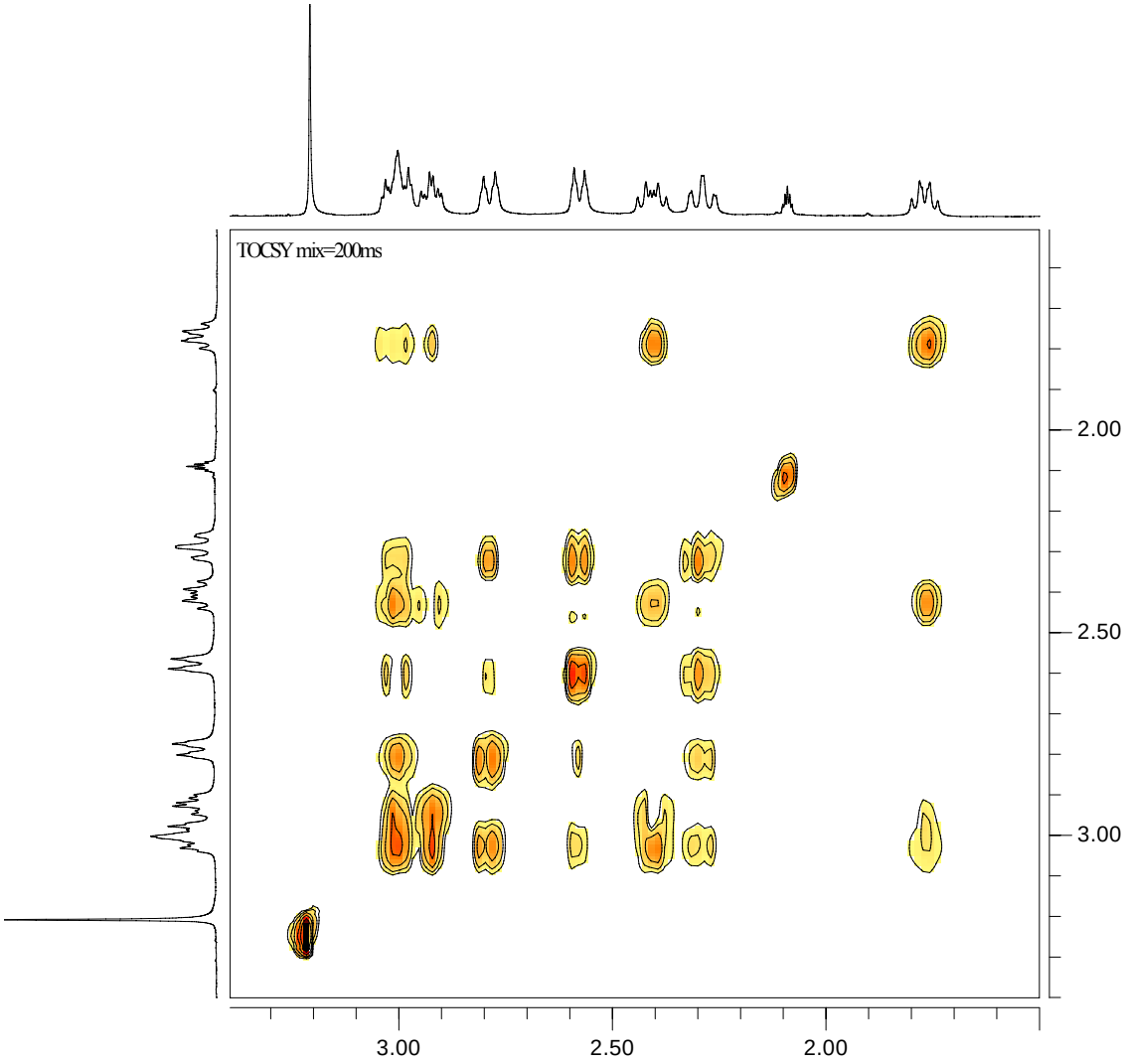


Figure 131: TOCSY NMR of 10 at low temperature.
The mixing time for this spectrum was 200 ms.

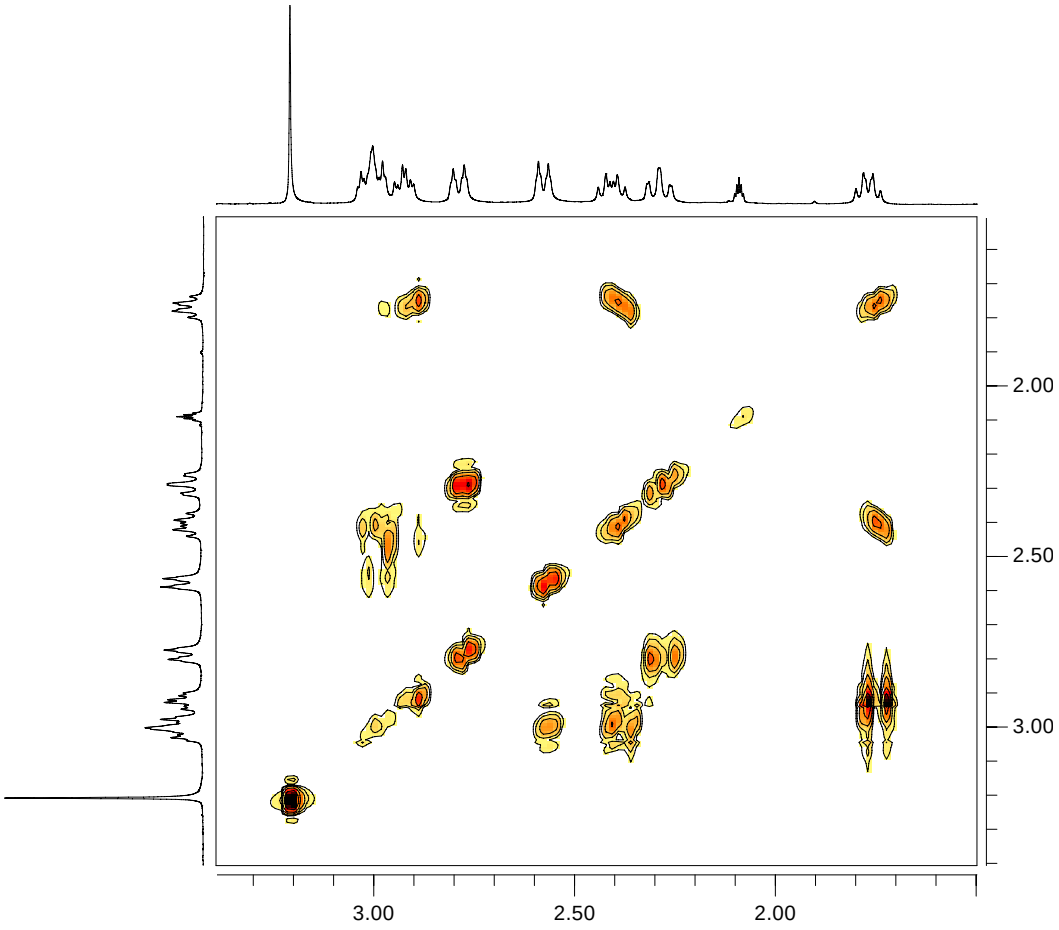


Figure 132: COSY NMR of 10 at low temperature.

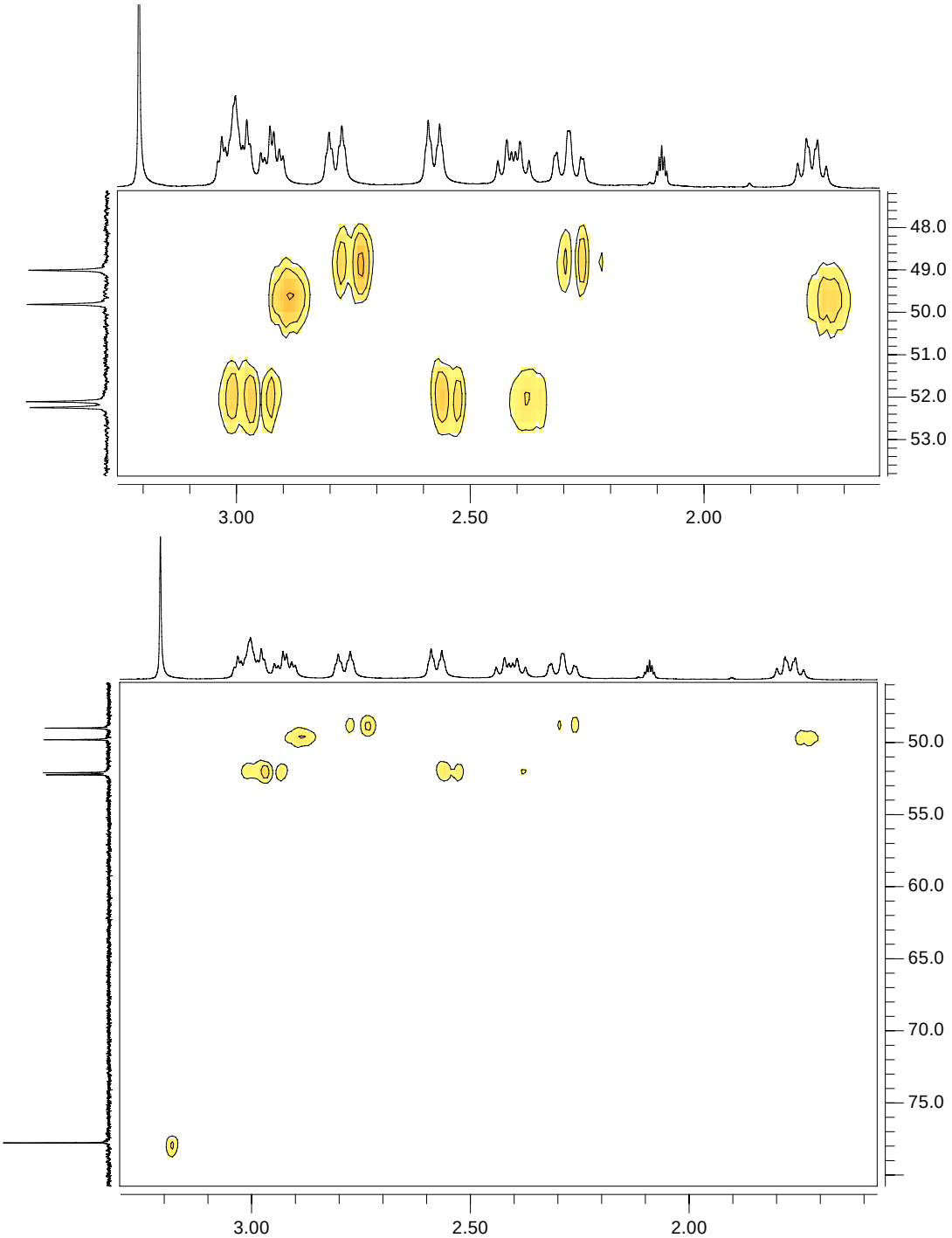


Figure 133: HMQC NMR of 10 at low temperature.

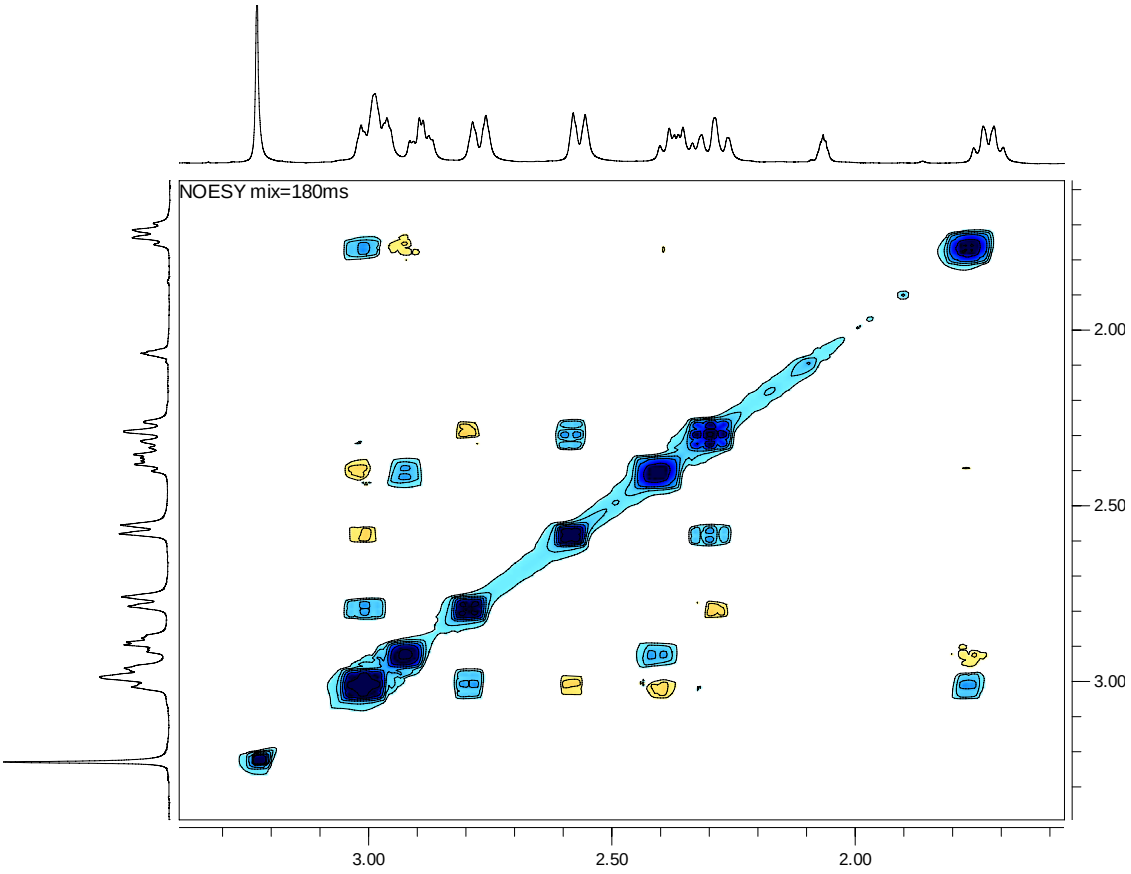


Figure 134: NOESY data of 10 at low temperature.

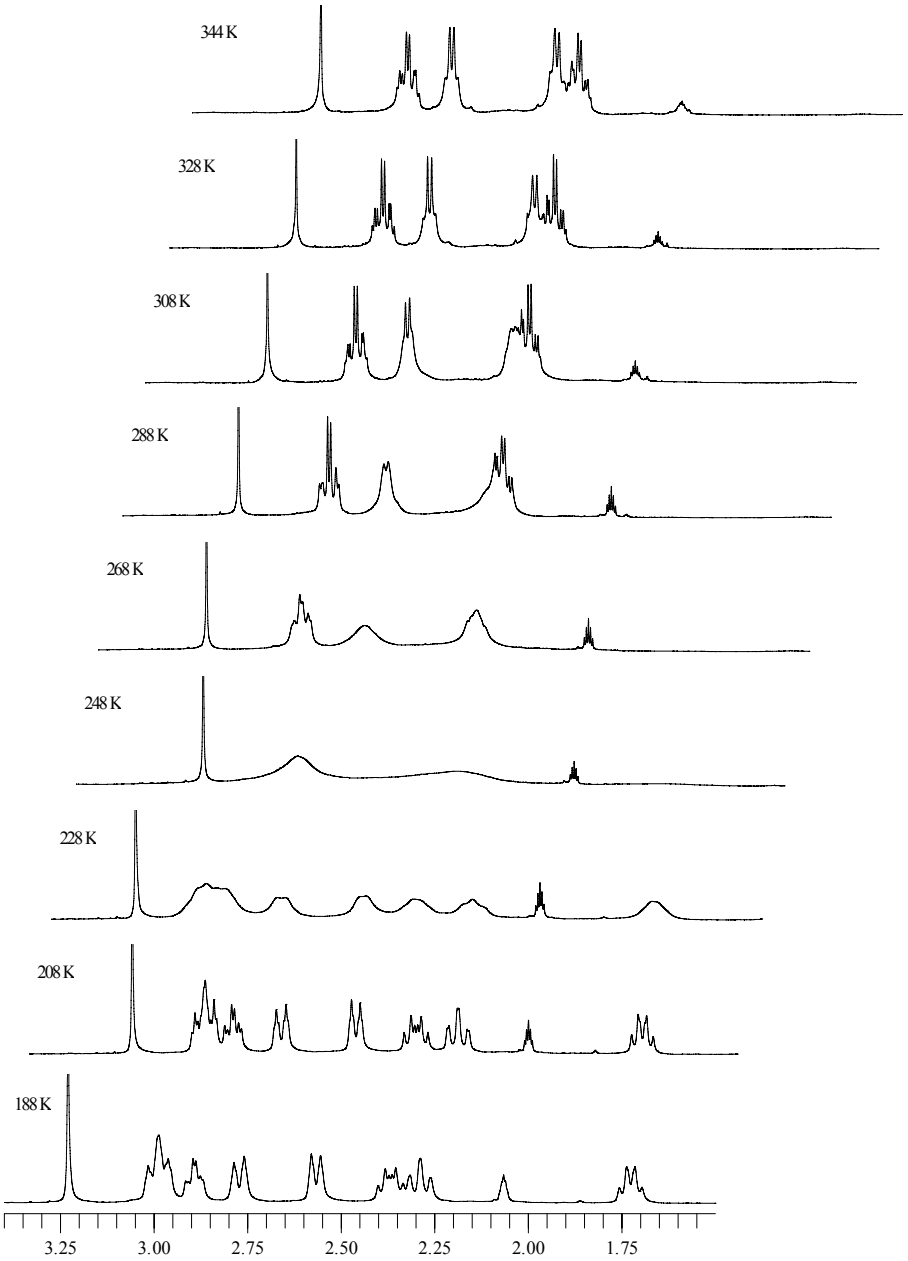


Figure 135: Stacked plot of proton VT NMR for 10.

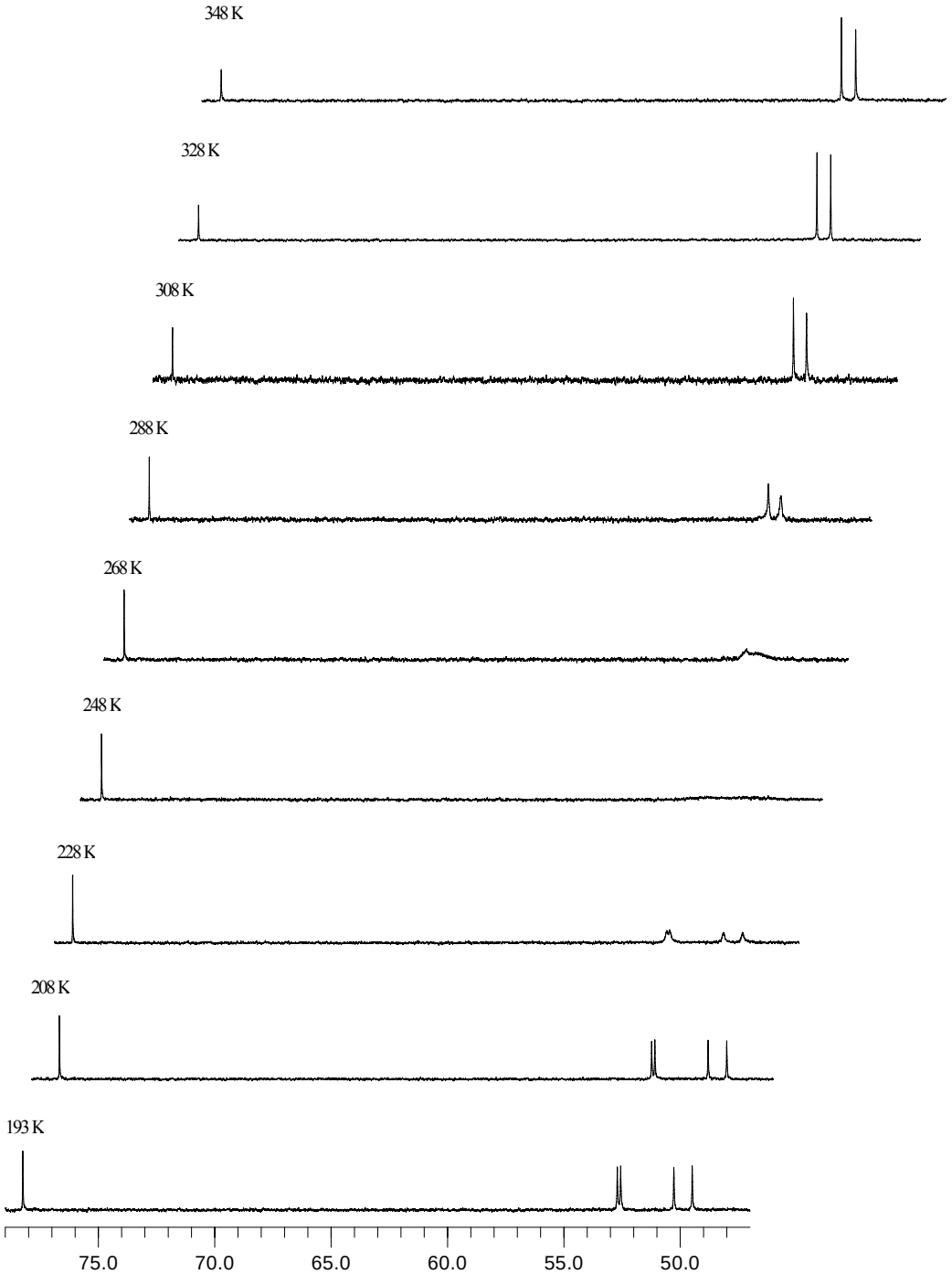


Figure 136: Stacked plot of carbon VT NMR for 10.

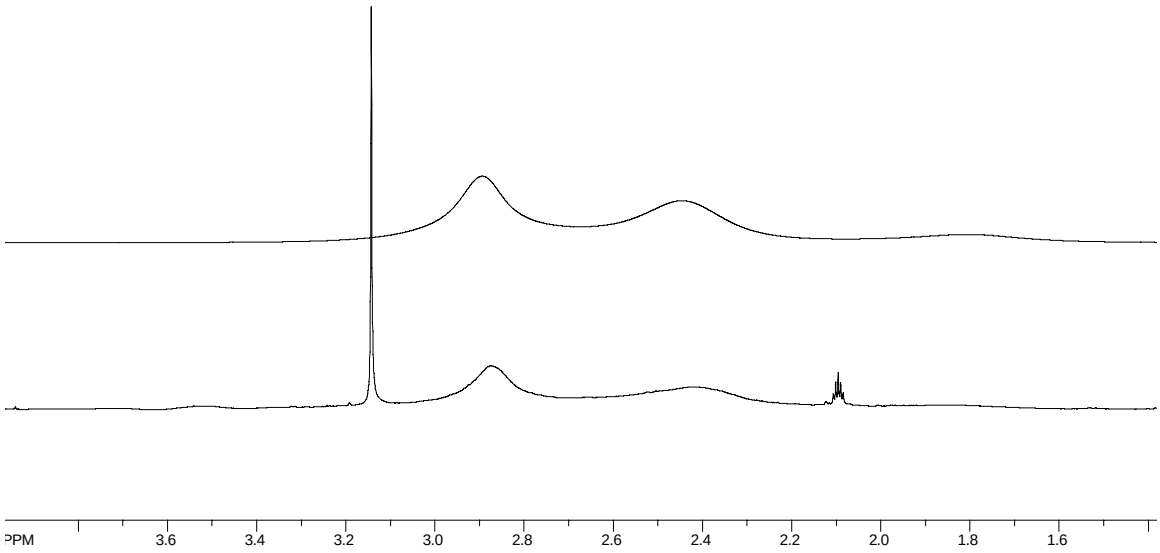


Figure 137: Spinworks 2.4 simulation of region above coalescence point for 10. The lower spectrum is the actual spectrum and the strong singlet not modeled was not shown to be involved in exchange *via* NOESY data. Solvent peak was also not modeled. Spinworks 2.4 uses the MEXICO dynamics modeling program.

Table 3.5: NOESY integral values for 10 at room temperature by EXSYcalc.

N	F1 ppm	F2 ppm	F1 Width (Hz)	F2 Width (Hz)	Integral +-	Norm. Int.	Label
1	2.664	2.6662	48.4258	34.4301	-20733.14	1.15	A
2	2.9399	2.9396	42.1774	29.735	-19510.21	1.08	B
3	2.9302	2.6662	26.5562	18.78	-1157.9	0.06	B-A
4	2.6562	2.9377	18.7455	15.65	-806.23	0.04	A-B
N	**F1 ppm**	**F2 ppm**	**F1 Width (Hz)**	**F2 Width (Hz)**	**Integral +-**	**Norm. Int.**	**Label**
1	2.9242	2.9379	32.8047	31.3	-18762.24	0.95	B
2	2.6463	2.6528	32.8046	28.17	-17719.07	0.9	A

Table 3.6: NOESY integral values for 10 at low temperature by EXSYcalc.

N	F1 ppm	F2 ppm	F1 Width (Hz)	F2 Width (Hz)	Integral +-	Norm. Int.	Label
1	1.748	1.7175	76.362	33.0814	-2509.27	0.92	A
2	2.2774	2.2571	83.0022	33.0814	-3085.29	1.13	E
3	2.385	2.3734	83.0022	33.0814	-2874.07	1.05	B
4	2.5711	2.556	96.2825	29.7733	-3915.4	1.43	F
5	2.7779	2.7677	73.042	29.7732	-3414.43	1.25	G
6	2.9103	2.8923	73.0419	29.7733	-2638.01	0.97	C
7	2.7738	2.9877	63.0817	33.0813	-2462.45	0.9	H-G
8	2.9888	2.7553	76.3621	33.0813	-2805.39	1.03	G-H
9	2.993	3.0002	86.3223	43.0059	-6761.81	2.47	D/H
10	2.9061	2.3734	76.362	33.0814	-2408.55	0.88	B-C
11	2.9971	1.7217	73.0419	33.0814	-2157.95	0.79	A-D
12	2.5628	2.2613	73.042	29.7732	-2683.41	0.98	E-F
13	2.3891	2.8881	56.4415	29.7733	-1280.17	0.47	C-B
14	2.2816	2.5602	66.4018	36.3895	-2289.93	0.84	F-E
15	1.7521	3.0168	59.7617	29.7732	-1515.63	0.55	D-A
N	**F1 ppm**	**F2 ppm**	**F1 Width (Hz)**	**F2 Width (Hz)**	**Integral +-**	**Norm. Int.**	**Label**
1	1.7218	1.7582	109.5629	49.6221	-116806.87	1	A
2	2.2512	2.2979	109.5629	43.0058	-124882.98	1.07	E
3	2.367	2.4017	112.883	49.6221	-133118.7	1.14	B
4	2.5325	2.576	106.2429	43.0058	-129207.88	1.11	F
5	2.7517	2.7877	116.2031	46.314	-129054.28	1.1	G
6	2.8758	2.9206	96.2825	39.6976	-123352.46	1.06	C
7	2.9709	3.0077	106.2428	56.2383	-247586.58	2.12	D/H

exchanging peaks are measured and put into the program and the exchange rate is calculated. The values calculated were much smaller than what would be expected for this type of system.

3.4.3 Room temperature configuration of 10

Due to fluxional behavior, this molecule has completely different spectra at room temperature. The low temperature helps to distinguish the room temperature spectra.

This molecule was characterized using 1D and 2D techniques at room and high temperature. 1D and 2D techniques were used to study the fluxionality of this molecule. All studies used a solution of **10** in d_8-toluene. Unless otherwise noted, all experiments were performed at room temperature. Acquisition parameters and other experimental details are given in Section 3.6. For reference purposes, relevant figures, spectra, and tables are placed at the end of this section.

The ^{13}C data contain three resonances and the ^{1}H data contain four resonances at room temperature. Two of the proton resonances overlap but are distinguishable especially when viewed with two-dimensional data. HMQC data distinguishes two diastereotopic protons correlated with C3 and C5. C3 has proton resonances at δ/ppm 2.37 and δ/ppm 2.82 while C5 has proton resonances at δ/ppm 2.71 and δ/ppm 2.42.

The COSY and TOCSY data indicate two distinct spin systems: one between protons H_{3up} and H_{3down} and another between protons H_{5up} and H_{5down}. This implies that C3 and C5 are in different rings. The protons at C3 have four coupling constants determined from the MestRe-C coupling constant analyzer. The dihedral angle can be calculated from these coupling constants. H_{3up} and H_{3down} have one coupling constant with a value of 3.5 Hz which corresponds to a dihedral angle of 55° when J^0 = 9.5 Hz is used. Additionally, it also contains a quartet with coupling constant values of 5.3 Hz, which corresponds to a dihedral angle of 42°. H_{4up} and H_{4down} have one coupling constant with a value of 4.9 Hz which corresponds to a dihedral angle of 55° when J^0 = 9.5 Hz is used. Additionally, it also contains a quartet with coupling constant values of J = 9.5 Hz which corresponds to a dihedral angle of 42°.

Room temperature NOESY data indicate that two peaks are still in exchange. These correlations are in phase with the diagonal instead of out of phase and are considered to be exchange rather than distance correlations. Based on general fact that a five membered ring will be more strained with respect to bond rotation, the six-membered ring is assumed to be the one in exchange. Additionally, the low temperature peaks that compose these room temperature peaks can be interpreted based on the coupling scheme, carbon data, and more. Because the low temperature peaks have been defined as *up* or *down* and axial or equatorial, the high temperature peaks no longer have the axial, equatorial orientation but they still have the *up* or *down* configuration due to the fact that an axial *up* proton will easily exchange with an equatorial *up* proton if the carbon bond is twisted. This allows the peak at δ/ppm 2.36 to be determined to be the combinations of $H_{3a/4b}$ and *up*. Likewise, δ/ppm 2.86 is made from the combinations of $H_{4a/3b}$ and *down*, δ/ppm 2.71 is from $H_{5a/6b}$ and *down*, δ/ppm 2.43 from $H_{6a/5b}$ and *up*.

These interpretations are also in accord with NOESY data which indicate a correlation between H_1 which is *up* and $H_{6a/5b}$ and *up*. Additionally, there is a proximity correlation between $H_{4a/3b}$ and $H_{5a/6b}$ which have both already been designated as *down*..

T_1 relaxation studies indication that the relaxation for the methine protons at room temperature is 7.335 seconds and at high temperature, 67° C, is 9.582 seconds. This is much a much longer time compared to the other protons which are close to 3.3 seconds and 4.3 seconds for room and high temperatures, respectively; however, they do relax more quickly for **10** than in $\mathbf{10}^+$ where the nearby carbocation affects the relaxation causing it to be longer on the order of 10 seconds. In both molecules, the relaxation is extraordinarily long.

Figure 138 shows the proposed structures of the molecule according to NMR. The proton and carbon NMR spectra is given in Figure 139. Relevant correlational data are given in Table 3.7. Figure 140 shows T_1 data. Relevant 2D spectra are shown in Figure 141 - Figure 143.

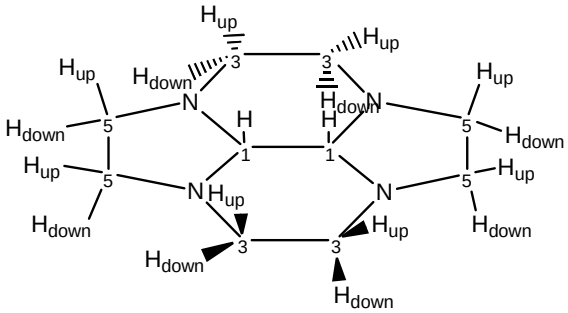


Figure 138: Structure of 10 that is consistent with NMR data at room temperature.

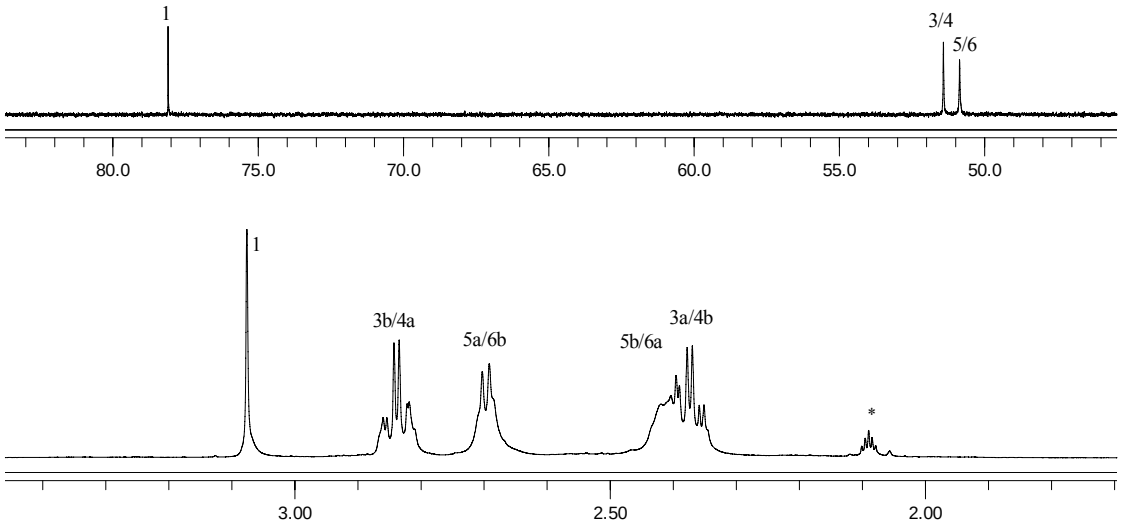


Figure 139: Proton and carbon spectra of 10 at room temperature.

^{1}H-NMR (400 MHz) 3.06 (s, 2H) 2.82 (dq, J = 3.1 Hz, J = 5.3 Hz, 4H) 2.71 (dd, 4H, J = 4.8 Hz, J = 9.4 Hz) 2.42 (dd, 4H, J = 5.0 Hz, J = 9.7 Hz) 2.36 (dq, 4H, J = 3.1 Hz, J = 5.4 Hz) ^{13}C-NMR (400 MHz) 78.098 (CH), 51.420 (CH_2), 50.863 (CH_2). (H coupling data based on HT values)

Table 3.7: NMR correlations for 10 at room temperature.

^{1}H position	^{13}C (δ/ppm)	^{1}H (δ/ppm) HSQC	^{2}J (|J|/Hz)	^{3}J (|J|/Hz)	COSY & TOCSY	HMBC *(C)*	NOESY
1	78.10	3.06	-	-	-		$6_{a}/5_{b\ up}$
$3_{a}/4_{b\ up}$	51.42	2.37	-	(3.1, 5.3, 5.3, 5.3)	$4_{a}/3_{b\ dn}$		$4_{a}/3_{b\ dn}$
$4_{a}/3_{b\ dn}$		2.82	-	(3.1, 5.3, 5.3, 5.3)	$3_{a}/4_{b\ up}$		$3_{a}/4_{b\ up}$, $5_{a}/6_{b\ dn}$
$5_{a}/6_{b\ dn}$	50.86	2.71	-	(4.9, 9.5)	$6_{a}/5_{b\ up}$		[a]$6_{a}/5_{b\ up}$, $4_{a}/3_{b\ dn}$
$6_{a}/5_{b\ up}$		2.42	-	(4.9, 9.5)	$5_{a}/6_{b\ dn}$		1, [a]$5_{a}/6_{b\ dn}$

[a]Exchange information indicated rather than distance correlation.

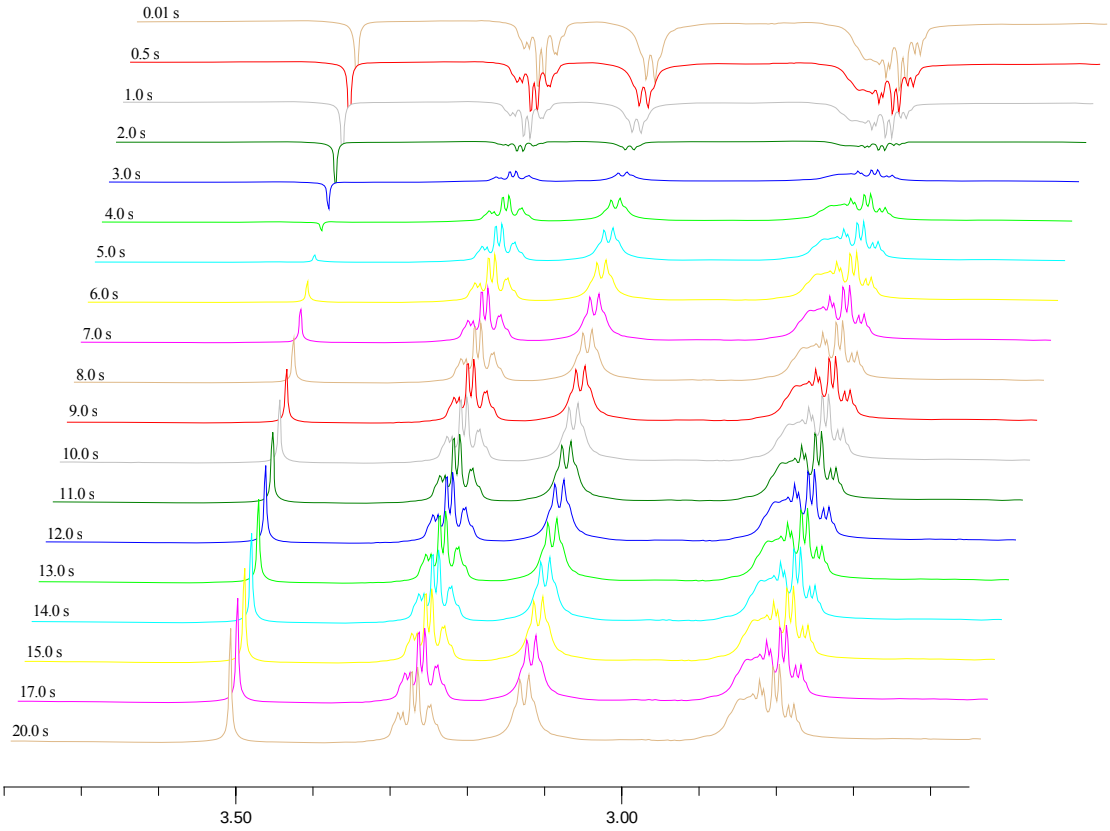


Figure 140: T_1 relaxation a room temperature of 10 at room temperature. The relaxation times were: 0.01 s, 0.1 s, 0.5 s, 1.0 s, 2.0 s, 3.0 s, 4.0 s, 5.0 s, 6 s,7.0 s, 8.0 s, 9.0 s, 10.0 s, 11.0 s, 12.0 s, 13.0 s, 14.0 s, 15.0 s, 17.0 s, 20.0 s. Calculated values are as follows: ^{1}H-NMR (400 MHz) δ/ppm 3.06 (6.28 s) 2.82 (3.45 s) 2.71 (3.38 s) 2.42 (3.27 s) and 2.36 (3.38 s).

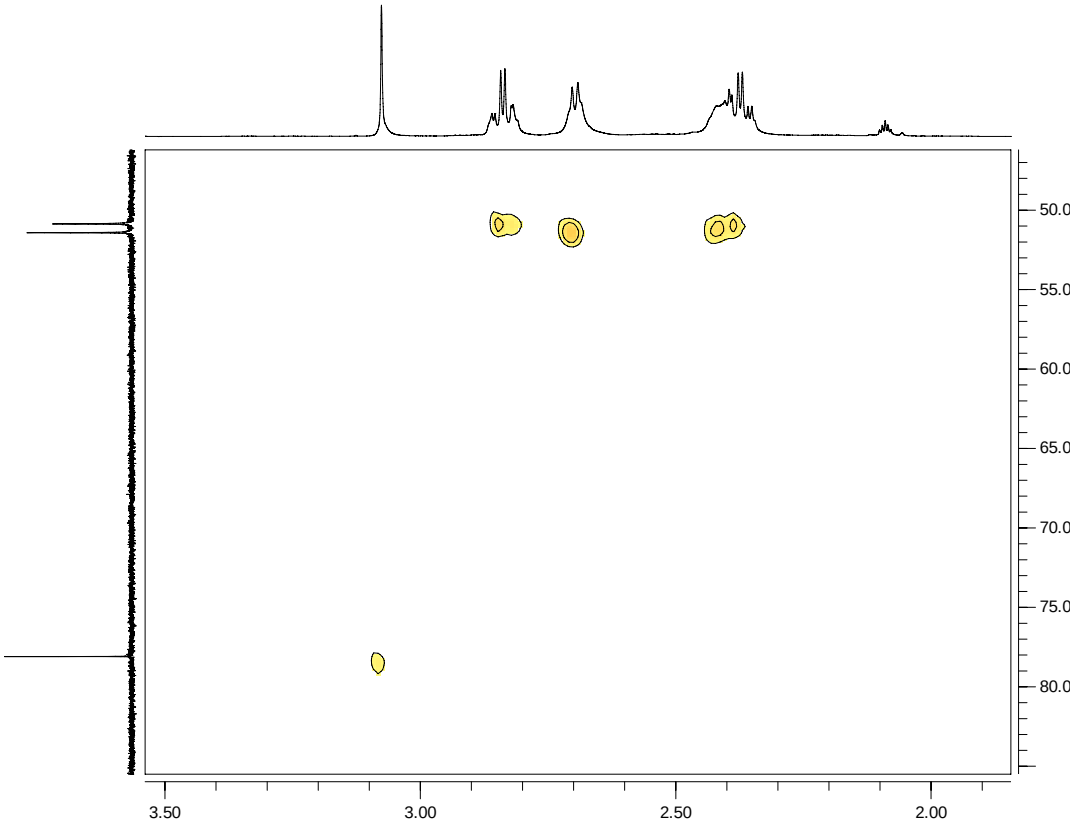


Figure 141: HMQC of 10 at room temperature.

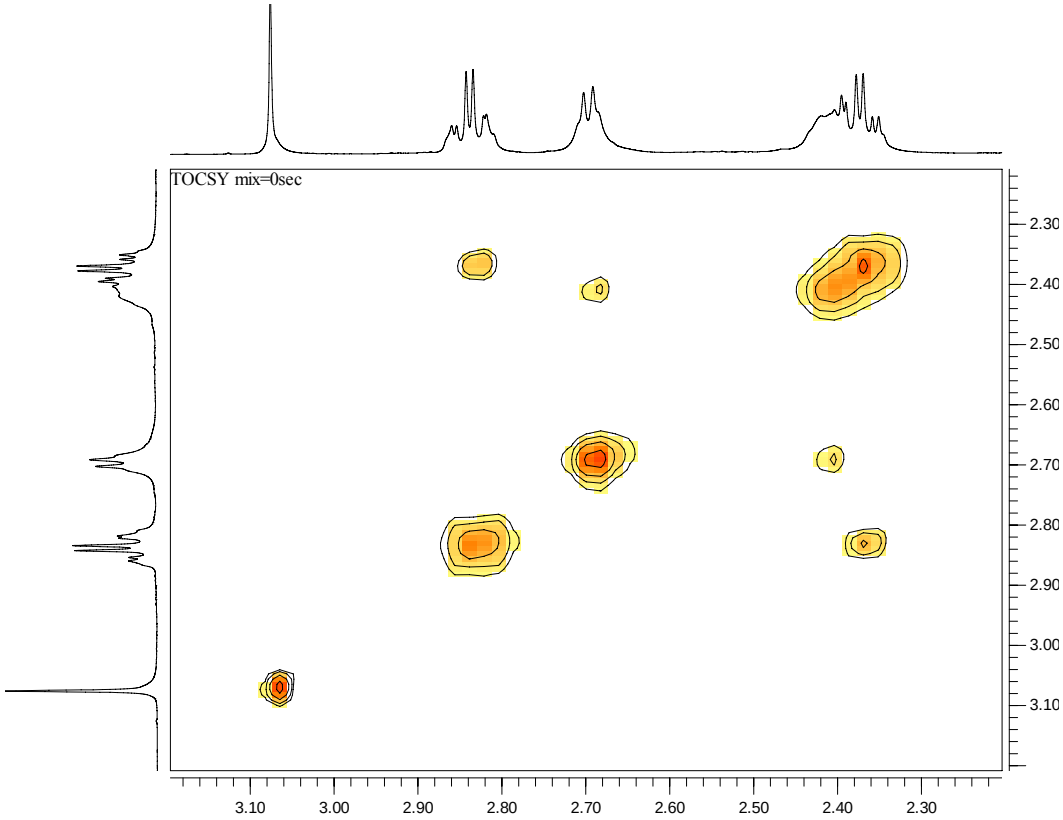


Figure 142: TOCSY of 10 at room temperature.

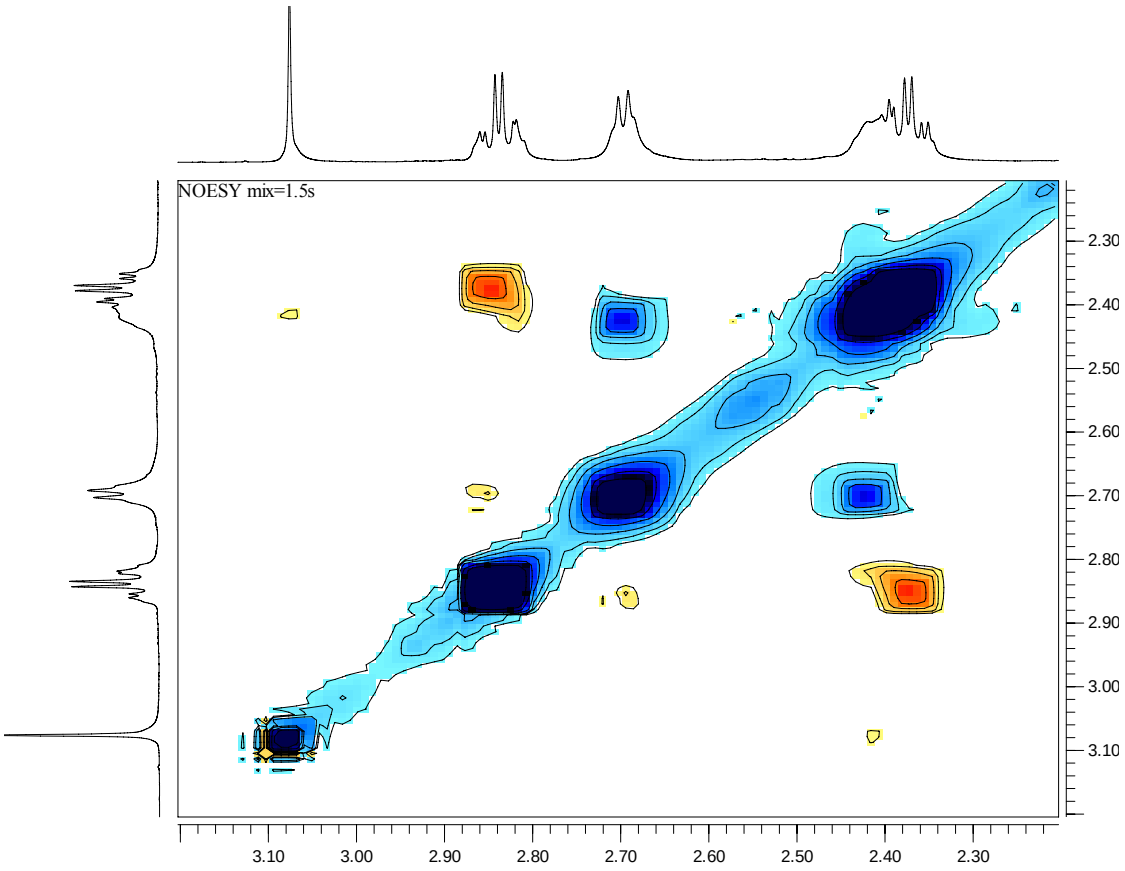


Figure 143: NOESY of 10 at room temperature.

3.5 Stereochemistry of $\mathbf{10}^{+2}$

This molecule was characterized using 1D and 2D NMR. All studies used solutions of $\mathbf{10}^{+2}$ in d_4-methanol. Acquisition parameters and other experimental details are given in Section 3.6. For reference purposes, relevant figures, spectra, and tables are placed at the end of this section.

The ^{13}C data contain fifteen resonances and ^{1}H data contain fourteen distinguishable resonances; however, two of the previously mentioned fourteen ^{1}H resonances lie in nearly the same position so that they appear to be the almost same resonance. 2D data identifies this information.

HMQC spectra indicates five diastereotopic proton sets. This information is given in accord with respective integration which is shown with the spectra. These appear on C3, C4, C5, C6, and C11. One set of these protons exists outside of the N_4 cage. Protons on C3 (δ/ppm 55.98) have resonances at δ/ppm 3.44 and δ/ppm 3.80. The protons on C4 (δ/ppm 44.06) have resonances at δ/ppm 3.344 and δ/ppm 3.59. The protons on C5 (δ/ppm 62.34) have resonances at δ/ppm 3.53 and δ/ppm 4.40. The value for the former proton is actually determined from line-fitting and simulation because it actually overlaps with another peak in the same spin system as well as slightly overlaps with a peak with a different spin system. Protons on C6 (δ/ppm 47.64) have resonances at δ/ppm 3.27 and δ/ppm 3.55. The protons on C11 (δ/ppm 62.15) are part of the benzyl group and have resonances at δ/ppm 4.94 and δ/ppm 5.19. Additionally, the aromatic ring as well as one aliphatic carbon peak only contains one proton. C1 (δ/ppm 79.40) has a proton resonance at δ/ppm 5.18. In the aromatic ring, C13 (δ/ppm 133.91) has a proton resonance at δ/ppm 7.68 and C14 (δ/ppm 130.97) and C15 (δ/ppm 132.45) proton resonances overlap at δ/ppm 7.51.

Based on HMQC spectra, the resonances can be clarified with respect to the degree of the carbon atom. There are no primary carbon atoms while C3, C4, C5, C6, and C11 are all secondary carbon atoms which would be expected from the HMQC data. The tertiary carbon atoms are C1, C13, C14, and C15. C12 is the remaining tertiary carbon atom.

COSY and TOCSY data indicate four unique spin systems. Two of these spin systems are due to the aliphatic rings, one of which contains: H_{3a}, H_{3e}, H_{4a}, and H_{4e} while the other contains H_{5a}, H_{5e}, H_{6e}, H_{6a}. In a manner similar to the previously discussed structures, these are the five- and six-membered rings contained in the N_4 heterocycle. Also in a unique spin system are in the aromatic region and belong to the aromatic rings: H_{13}, H_{14}, and H_{15}. The final unique spin system contains only one set of diastereotopic spin pairs, H_{11a} and H_{11b}. This final diastereotopic pair indicates this is the carbon atom near to the aromatic ring and outside of the N_4 heterocycle.

HMBC data further verifies the long range connectivity of these rings. Due to the deshielded chemical shift and integration, H_1 has already been determined as the single proton attached to each of the C1 atoms. Although their general positions can be determined *via* COSY connectivity, H_1 has long range connectivity with C3, C4, C6 ,and C11. This is logical and are all within 3 bonds of at least one of the H_1 atoms. Although there is no correlation between H_1 and the C5 protons, there is a correlation between H_{5e} and C1. Protons which have correlations with C1 include H_{3a}, H_{4e}, H_{5e}, and H_{6a}. It is interesting that the correlation is between the *down* axial or *down* equatorial protons and C1 except in the case of H_{4a}, which may or may not have a true correlation since this is actually an overlap of peaks.

Additionally, the protons on C11 show some significant correlations which help to determine aromatic structure. H_{11a} and H_{11b} both have long range correlations with C12 and C13. This is important and indicates that C13 is most likely the carbon atom next to the quaternary carbon, C12, which attaches the ring to C11. Alternatively, H_{14} and potentially H_{15} also have correlations with C11 over four bonds. It is difficult to distinguish these peaks and that is why the ambiguity is present. A very interesting point must be made with respect to correlations between C13 and C15 as opposed to C13 and C14 of which there is no peak. Without any other information, this would indicate that C15 is most likely next to C13. Inspection of the carbon spectra however indicates this must not be so. Although intensity and integration of carbon spectra is generally very inefficient, comparison of the intensity of two of the four carbon atoms indicates that two are much larger. This would result due to the overlap of two equivalent carbon atoms

which occurs only at C13 and C14, not at C15. Based on this reason alone, C14 is still designated as being next to C13. Lack of correlations does not necessarily indicate that there is not a relationship present. Additionally, it is very likely that the protons at H_{14} do have correlations with C13, this cannot be said with certainty however since these peaks overlap. It does appear from HMQC data that C14 may be slightly more deshielded than C15 and the HMBC data appears to have a correlation that is slightly more deshielded in this case. Both C14 and C15 appear to have correlations that extend to C12; these would be three to four bonds across which is reasonable for HMBC.

Typical expected correlations exist within each aliphatic ring *via* HMBC spectra. For example, H_{3a} and H_{3e} have correlations with C4; likewise, H_{4a} has a correlation with C3. Additionally, H_{5e} and H_{5a} have correlations with C6; likewise, H_{6e} has a correlation with C5. Some longer range interactions can also be seen between H_{3e}, H_{3a}, and H_{5a} with C11. Further supporting these correlations are the correlations between H_{11a} and C3,and C5 or H_{11b} and C5. These are all four bond correlations.

More important are the correlations that indicate which sides of the rings are near to each other. These interactions are all three bond correlations. H_{4a} has a correlation with C6, and H_{6e} has a correlation with C4. H_{5a} has a correlation with C3. These relationships indicate that C4 is the closest carbon to C6 in the adjacent ring and that C3 is the closet carbon to C5 in the adjacent ring. There is an overlap that should be addressed. C3 has a correlation with peaks that could belong to either H_{5e} or H_{6a}. To remain consistent with the previously mentioned data and to uphold symmetry in this molecule, it is much more likely that this interaction is between C3 and H_{5e} instead of H_{6a}. It is listed in the table because it is a possible overlap.

The HMBC spectral correlations of H_{11a} and H_{11b} to carbon atoms in the ring also give significant information about which sets of nitrogen atoms to which the C11 atom is attached. Long range correlations are evident between H_{11a} and C3 and C5 while H_{11b} and C5 also have correlations. This indicates that C11 is attached to the nitrogen atom between C3 and C5.

The use of NOESY is extremely beneficial in this case. Correlations associated with H_1, H_{11a}, and H_{11b} will be extremely useful considering that these protons are in

understood positions. It is consistent with the crystal structure to place both H_1 protons in the *up* position. If one were *up* and one were *down*, correlations would be seen between both the *down* protons on one side of the molecule as well as the *up* protons on the same carbon atoms on the other side of the molecule. As the data is, the NOESY data only includes correlations between H_1 and one of the two protons on the carbon atoms in the aliphatic rings. Other NOESY data will support this statement.

The aliphatic protons with NOESY correlations with H_1 will most likely be *up* regardless of axial or equatorial arrangements. H_1 has correlations with H_{4a}, H_{5a}, and H_{6e}; indicating that these must be *up* protons. At first, it seems unusual that there is no correlation with H_{3e}. In fact, this is very useful. If the H_1 protons have the stereochemistry shown in the figure, with one proton directed towards the back of the molecule and the other directed towards the front of the molecule, it would be logical that neither axial nor equatorial *up* H_3 protons would have a close distance correlation with H_1. Regardless of the side of the molecule, H_1 will always be pointing away from H_3. Further information can be obtained concerning the correlations with H_{4a}, H_{5a}, and H_{6e}, these protons indicate the protons that are in close proximity to H_1. It would be expected that the protons in the five-membered rings would be in close proximity to H_1 regardless of the forward or reverse tilt of H_1. The two protons in the same ring which do show correlations are H_{5a} and H_{6e} indicating that these protons are in the five-membered ring while the other protons are in the six-membered ring.

H_1 also has correlations with H_{11a} and H_{11b} which would be expected due to the close proximity of these protons. Finally, H_1 also has correlations with H_{13} which supports the fact that this is the proton next to the quaternary carbon on the aromatic ring. This indicates also that C11 must be at least perpendicular to the C1-C1 bond so that H_{13} is close enough to H_1 for a distance correlation.

Whether the *up* protons are axial or equatorial can be determined from H_{11a} and H_{11b} correlations. Notice that H_{11a} has a strong correlation with H_{5a} while H_{11b} has a strong correlation with H_{4a}. This indicates that H_{5a} and H_{4a} are axial to experience this kind of interaction. Additionally, there appears to be a weak correlation between H_{11b} and H_{3e}. Had this been as strong a correlation as the correlation between H_{11b} and H_{4a}, it

would have been difficult to determine the stereochemistry of H_{3e}; however, since the carbon atom, C3 obviously closer to these protons than C4, the interaction would have been a stronger interaction if these protons had been axial and H_{4a} had been equatorial. Since this is not the case, H_{3e} must be equatorial and farther away from H_{11b} and H_{13} than H_{4a}. This also leads to the assumption that H_{11b} and the aromatic ring is slightly tilted toward the ring a portion of the time so that H_{3e} can have an interaction with both of these atoms. There does not appear to be interactions between H_{6e} and either C11 proton. For this to be consistent with the data, H_{6e} must be equatorial, an axial proton would have been expected to have an interaction between these protons. In addition, if H_{5a} and H_{4a} were actually equatorial, there would be a very great distance between them and the C11 protons and very little correlation would be expected. For there to be no interaction with H_{6e} but interaction with H_{5a}, the H_{11b} atom and the ring are tilted away from this side of the molecule so that only axial interactions will be possible.

To allow for correlation between H_{4e} and H_{11b}, these atoms must be on the same side of the molecule and tilted closer to each other. H_{11a} is probably tilting away from the ring but H_{5a} still has proximity to this atom due to the fact H_{11a} is interacting with an axial proton in spite of the tilt away from the atom.

In accordance with the structure, a few other NOESY correlations reinforce this assignment. H_{6e} and H_{4a} have close proximity since they are both *up* as do H_{6a} and H_{4e} which are both *down*. Additionally, H_{5e} and H_{4e} have close proximity since they are both *down*. Finally, both protons on C3 have an interaction with H_{5e} which is *down*. These two interactions are logical since they are between two equatorial protons, H_{3e} and H_{5e}, and two *down* protons, H_{3a} and H_{5e}. Relevant spectra and expansions for comparative purposes are given at the end of this section.

2D data in this solvent did not reveal any significant changes in the compound. Ring verification can be identified *via* deuteration. At this point in time, the rings cannot be designated as they are labeled. It is unclear which ring is five-membered and which is six-membered.

A general comment can be made concerning the calculated coupling constants for one ring. These values are not completely consistent with the Karplus equation and may be a result of the strained nature of these rings.

Figure 144 shows the predicted structures of the molecule according to NMR. A portion of the crystal structures is shown in Figure 145 and Figure 146. The proton and carbon NMR spectra are given in Figure 147. Relevant correlational data are given in Table 3.8. Figure 148 shows T_1 data. Relevant 2D spectra are shown in Figure 149 - Figure 156.

3.5.1 Spectroscopic studies of 11

This molecule was characterized using 1D and two-dimensional NMR. All studies used solutions of **11** in d_8-toluene. For reference purposes, the final predicted structure for this species is given at the end of this section. Acquisition parameters and other experimental details are given in Section 3.6. For reference purposes, relevant figures, spectra, and tables are placed at the end of this section. Although VT studies were conducted on this molecule, the fluxional processes of this molecule are too fast at the viable low and high NMR temperature timescale.

The ^{13}C data contain three resonances and ^{1}H data contain two distinguishable resonances.; The most deshielded CH_2 carbon atom is assigned as C3 corresponding to the six-membered ring protons while the other CH_2 carbon atom is assigned as C5 corresponding to the five-membered ring protons. This assignment is only made for clarification purposes, as current NMR processes cannot definitely distinguish which carbon is in which ring. The assumption is based on the fact that for $\mathbf{10}^+$, C3 and C4 were more deshielded than C5. The author recognizes that this is not an adequate comparison due to the strained nature of the ring containing C5. The difficulty in assignment of the C3 and C5 resonances in **11** arises from the fact that the distances and number of possible coupling links between the carbon atom and protons is the same from the center of the molecule regardless of the ring. Additionally, the fact that the central atoms are quaternary carbon atoms, limits the total types of experiments that can be

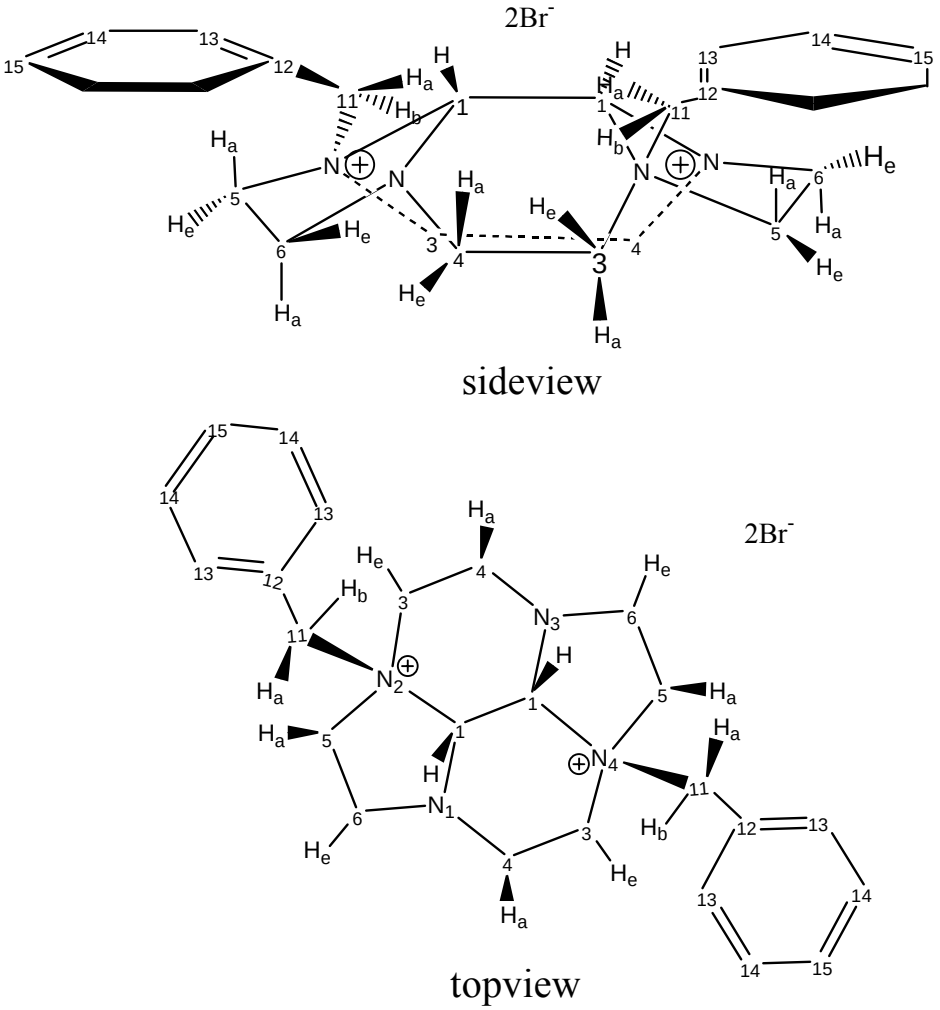


Figure 144: The structure of 10^{+2} that is consistent with the NMR data.

In the top view, only axial protons and the protons on C11 have been included so that the orientation of protons with respect to NOESY data are more noticeable. In the side view, the aromatic protons, one of the C3 protons, and one of the C4 protons have been omitted for clarity

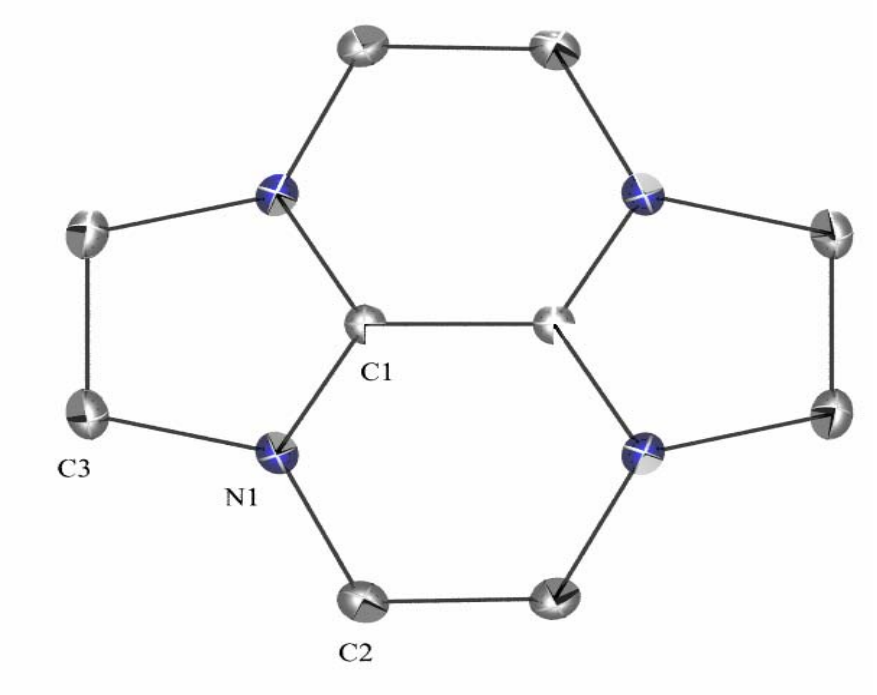


Figure 145: Crystal structure of 10^{+2}.
Phenyl rings and hydrogen atoms have been omitted for clarity.

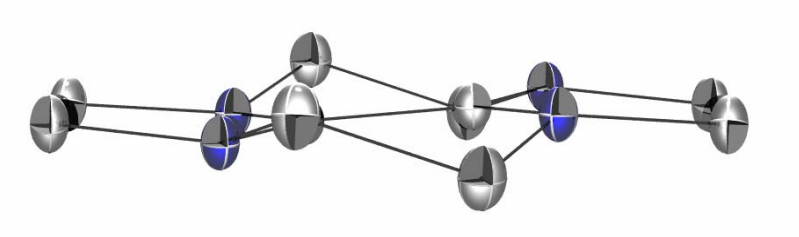


Figure 146: Side view of the crystal structure of 10^{+2}.
Phenyl rings and hydrogen atoms have been omitted for clarity.

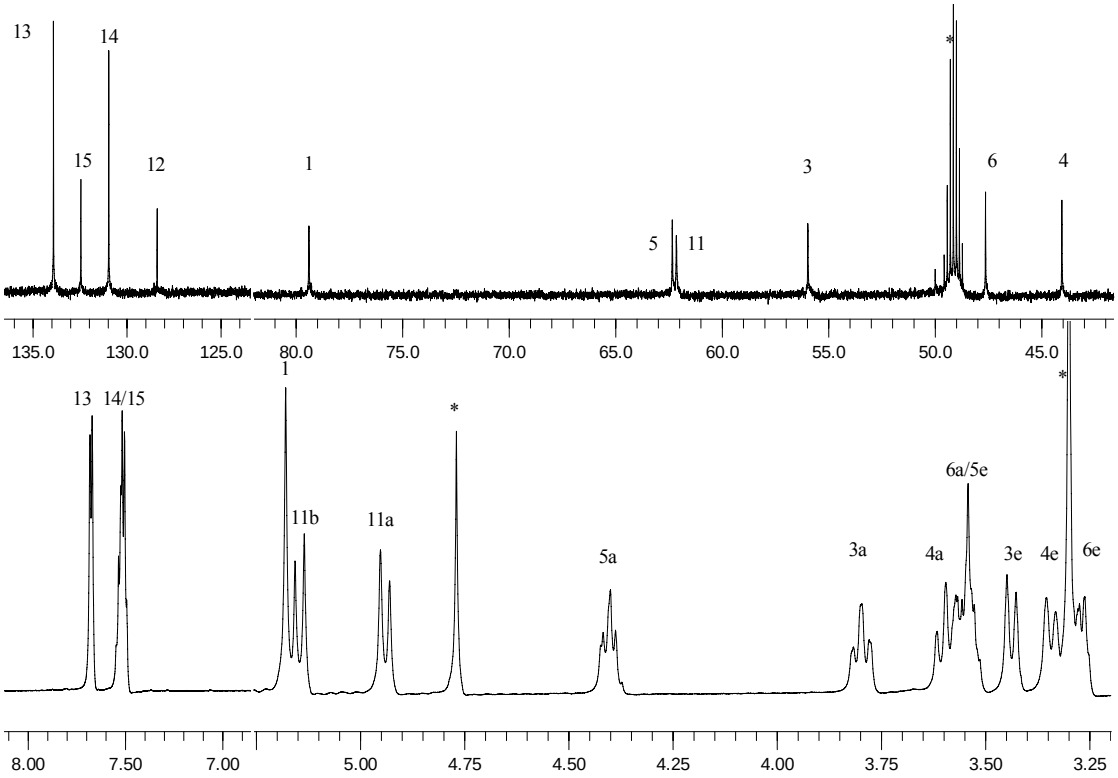


Figure 147: Carbon and proton spectra of 10^{+2}.

^{1}H-NMR (600 MHz) δ/ppm 7.68 (d, 4H, *J* = 7 Hz), 7.51 (m, 6H), 5.18 (s, 2H), 5.15 (d, 2H, *J* = 13.1 Hz), 4.94 (d, 2H, *J* = 13.1 Hz), 4.40 (ddd, 2H, *J* = 5.3 Hz, *J* = 7.4 Hz, *J* = 15 Hz), 3.80 (ddd, 2H, *J* = 3.0 Hz, *J* = 13.0 Hz, *J* = 13.2 Hz), 3.59 (ddd, 2H, ^{b}J = 2.0 Hz, *J* = 13.0 Hz, *J* = 13.1 Hz), ^{a}3.53 (m, 2H), ^{a}3.55 (m, 2H), 3.44 (ddd, 2H, *J* = 13.2 Hz, ^{b}J = 2.8 Hz, ^{b}J = 2.0 Hz) , 3.34 (ddd, 2H, *J* = 13.1 Hz, ^{b}J = 2.8 Hz, ^{b}J = 3.0 Hz), 3.27 (m, 2H)
^{13}C-NMR (600 MHz) 133.91 (CH), 132.45 (CH), 130.97 (CH), 128.40 (C), 79.40 (CH), 62.34 (CH_2), 62.15 (CH_2), 55.98 (CH_2), 47.64 (CH_2), 44.06 (CH_2)
^{a}Chemical shift differences simulated using Spinworks. ^{b}These coupling constants were determined using peak fitting and simulation.

Table 3.8: NMR correlations for 10^{+2}.

^{1}H position	^{13}C *(ppm)*	^{1}H *(ppm)*	m	^{2}J *(Hz)*	^{3}J *(Hz)*	COSY / TOCSY	^{j}HMBC *(C)*	NOESY
1	79.40	5.18	s	N/A	N/A	none	**3, 4, 6, 11**	**4_a**, **5_a**, **6_e**, **11_a**, **11_b**, ^{f}**13**
$3_{e\ up}$	55.98	3.44	ddd	13.2	^{a}2.8, ^{a}2.0	3_e, 4_a, 4_e	**1**, 4, **11**	3_a, $^{f}4_e$, $^{f}4_a$, ^{i}**5_e/6_a**, ^{f}**11_b**, **13**
$3_{a\ dn}$		3.80	ddd	13.2	3.0, 13	3_a, 4_a, 4_e	4, **11**	3_e, 4_e, $^{f}4_a$, ^{i}**5_e/6_a**
$4_{e\ dn}$	44.06	3.34	ddd	13.1	^{a}2.8, ^{a}3.0	4_a, 3_a, 3_e	**1**	$^{f}3_e$, 3_a, 4_e , ^{if}**6_a/5_e**
$4_{a\ up}$		3.59	ddd	13.1	13.0, ^{a}2.0	4_e, 3_a, 3_e	^{g}**1**, 3, ^{g}**6**	**1**, $^{f}3_a$, $^{f}3_e$, 4_e, ^{f}**6_e**, **11_b**, **13**
$5_{e\ dn}$	62.34	^{g}3.54	m	^{d}15	-	5_a, 6_a, 6_e	^{g}**1**, ^{g}**3**, ^{g}6	^{i}**3_a**, ^{i}**3_e**, ^{if}**4_e**, $^{i}5_a$, $^{i}6_e$
$5_{a\ up}$		4.40	ddd	15	5.3, 7.4	5_e, 6_a, 6_e	**3**, 6, **11**	**1**, $^{i}5_e$/6_a, 6_e, **11_a**, **13**
$6_{e\ up}$	47.64	3.27	m	-	-	6_a, 5_a, 5_e	**4**, 5	**1**, ^{f}**4_a**, $^{i}5_e$/6_a, 5_a
$6_{a\ dn}$		^{g}3.55	m	-	-	6_b, 5_a, 5_e	^{g}**1**, ^{h}**3**	^{i}**3_a**, ^{i}**3_e**, ^{if}**4_e**, $^{i}5_a$, $^{i}6_e$
11_a	62.15	4.94	d	13.1	N/A	11_a	**1, 3, 5, 12, 13**	**1**, **5_a**, 11_b, ^{f}**13**
11_b		5.15	d	13.1	N/A	11_b	**1, 5, 12, 13**	**1**, ^{f}**3_e**, **4_a**, 11_a, **13**
12	128.40	N/A	N/A	N/A	N/A	N/A	N/A	N/A
13	133.91	7.68	d	N/A	7	^{e}14, ^{e}15	**11,** 15	**1**, **3_e**, **4_a**, **5_a**, **11_a**, **11_b**, ^{e}14/15

Table 3.8. Continued.

^{1}H position	^{13}C *(ppm)*	^{1}H *(ppm)*	m	^{2}J *(Hz)*	^{3}J *(Hz)*	COSY / TOCSY	^{j}HMBC *(C)*	NOESY
14	130.97	7.51	m	N/A	-	^{e}13	^{e,f}**11**, ^{e}**12,** ^{e}13**,** ^{e}15	^{e}13
15	132.45	7.51	m	N/A	^{b}7	^{e}13	^{e,f}**11**, ^{e}**12,** ^{e}13**,** ^{e}14	^{e}13

In general, some multiplets cannot be accurately simulated with current software due to second order overlap between two peaks in the same spin system as well as 1st order overlap with a resonance in another spin system. Dashes are used to indicate that these datacould not be discerned. In addition, the use of bold values is used to indicate correlations between resonances in different spin systems. All spectra were obtained on a Varian 600 MHz instrument except for the HMQC spectrum which was obtained on a Bruker Avance 400 MHz spectrometer using a 5 mm broadband probe. Unless otherwise noted, all experiments were performed at room temperature. All other symbol explanations follow. ^{a}These values are calculated *via* line fitting and subsequent simulation. ^{b}One of the multiplets in this section is determined to be 7 Hz and is designated as an *ortho* coupling due to the value and thus given to C14 instead of C15 because C14 would have *ortho* coupling with C13. This does not mean that this coupling is not also possible between C14 and C15 but cannot be discerned from the data and is marked with a dash in the case of C15. ^{c}This peak difference results from a Spinworks simulated difference of: 2127 Hz and 2120 Hz on a 600 MHz spectrometer. ^{d}This assignment is placed as a *geminal* coupling constant instead of a dihedral coupling constant due to size. Other coupling constants cannot be discerned from the data due to the overlap of two different peaks. ^{e}Due to overlap between these peaks, cross coupling interactions are listed as belonging to both C14 and C15 some of these values may belong to only one of these peaks. ^{f}These peaks have very weak interaction. ^{g}On the HMBC spectra it is very difficult to discern between H_{4a}, H_{5a}, and H_{6b} coupling and C1, C3, and C4 in this particular case so the interaction is listed as belonging to all of them although this may not necessarily be true. ^{h}Due to overlap of peaks this value cannot be discerned as specifically belonging to this peak instead of H_{4a} and H_{5a} but it is extremely unlikely this peak is actually an interaction due to other information that can be obtained from other HMBC and NOESY data. It is still listed in this section. ^{i}Cannot discern between H_{5a} and H_{6b}; however, the most likely peak to which coupling given COSY, HMBC and other NOESY data are occurring is listed first. ^{j}HMQC breakthrough in HMBC not listed in this section.

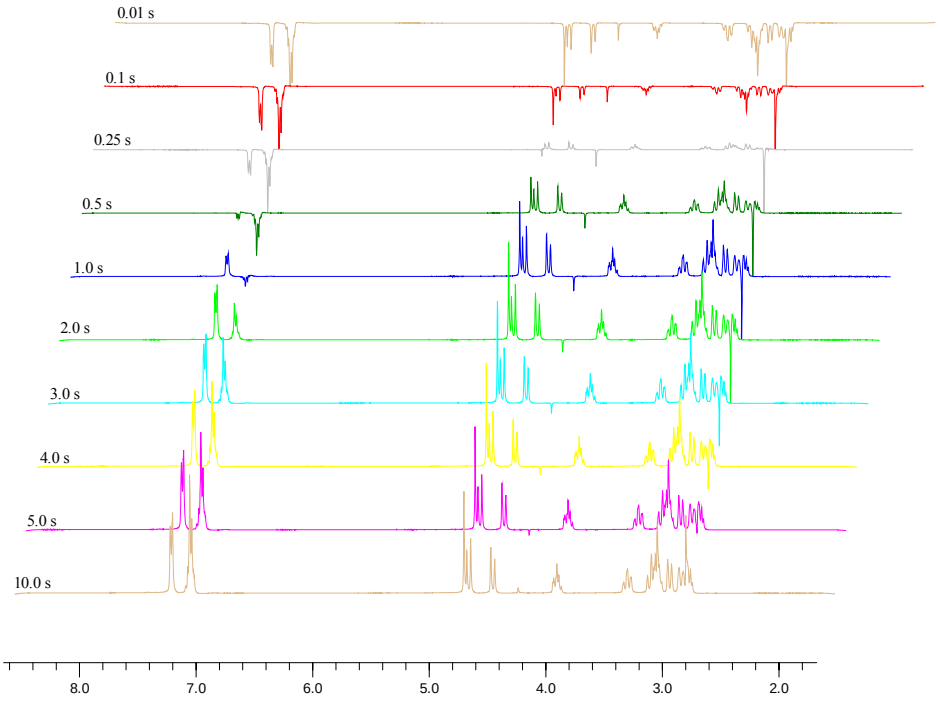


Figure 148: T_1 relaxation data of 10^{+2}.

Relaxation times: 10.0 s, 5.0 s, 4.0 s, 3.0 s, 2.0 s, 1.0 s, 0.5 s, 0.25 s, 0.1 s, 0.01 s.^{1}H-NMR (600 MHz) δ/ppm 7.68 (0.78 s), 7.51 (1.63 s), 5.18 (0.37 s), 5.15 (0.26 s), 4.94 (0.27 s), 4.40 (0.26 s), 3.80 (0.28 s), 3.59-3.55 (0.33 s) 3.44 (0.27) , 3.34 (0.31), 3.27 (0.33)

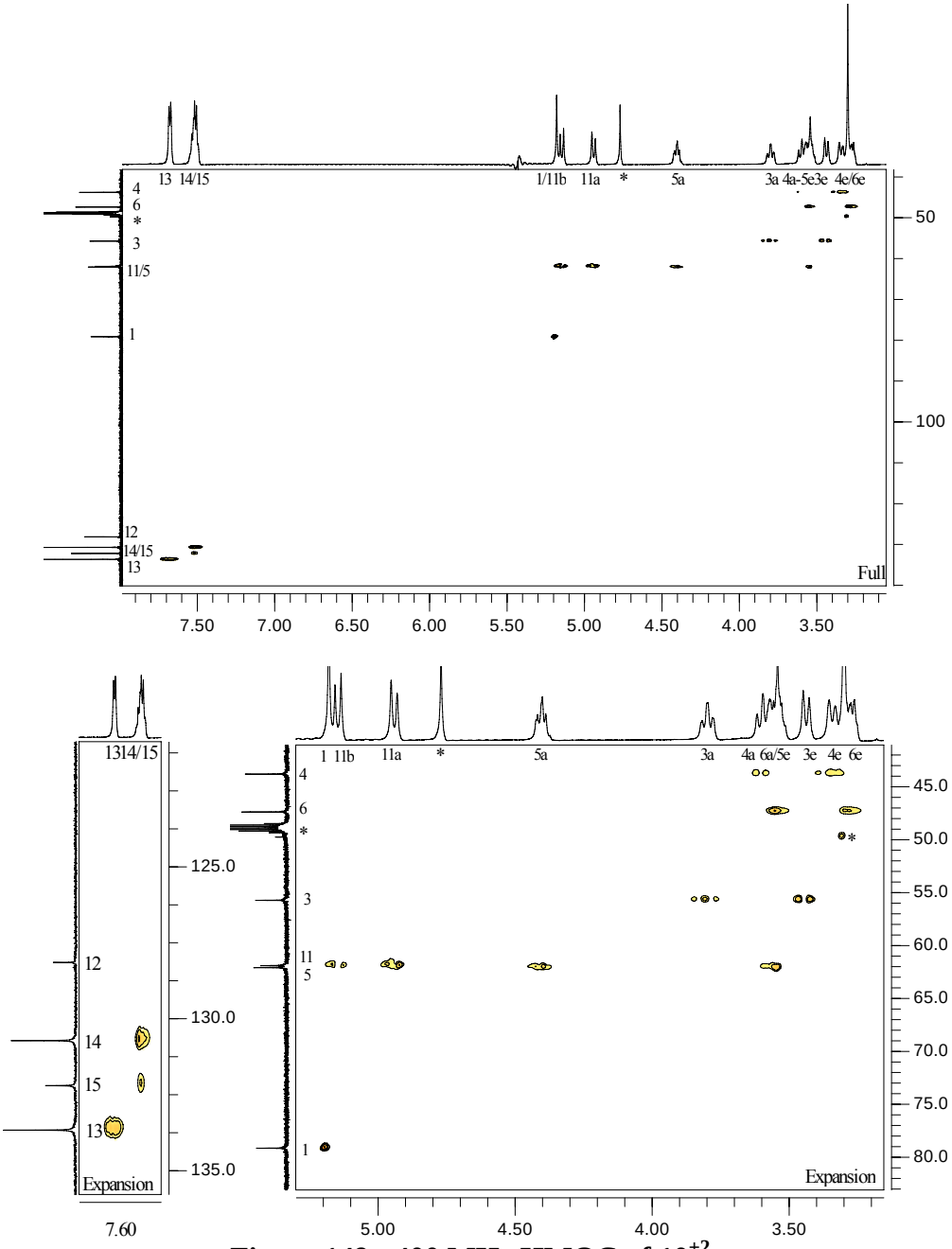


Figure 149: 400 MHz HMQC of 10^{+2}.

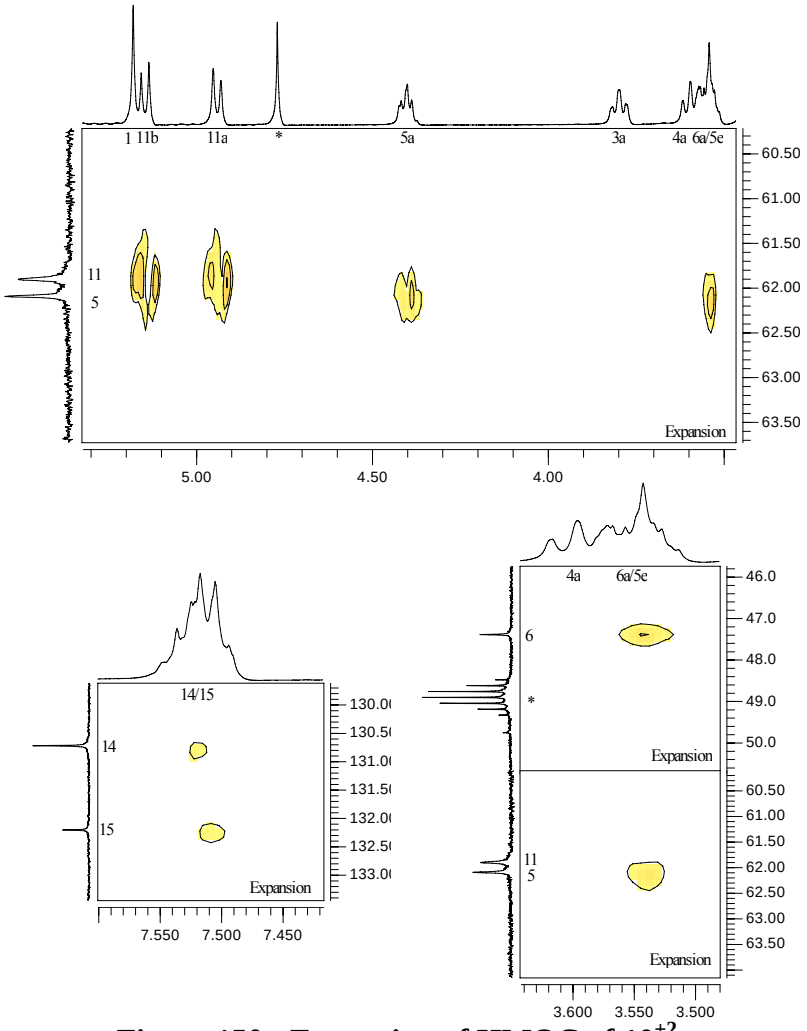


Figure 150: Expansion of HMQC of 10^{+2}.

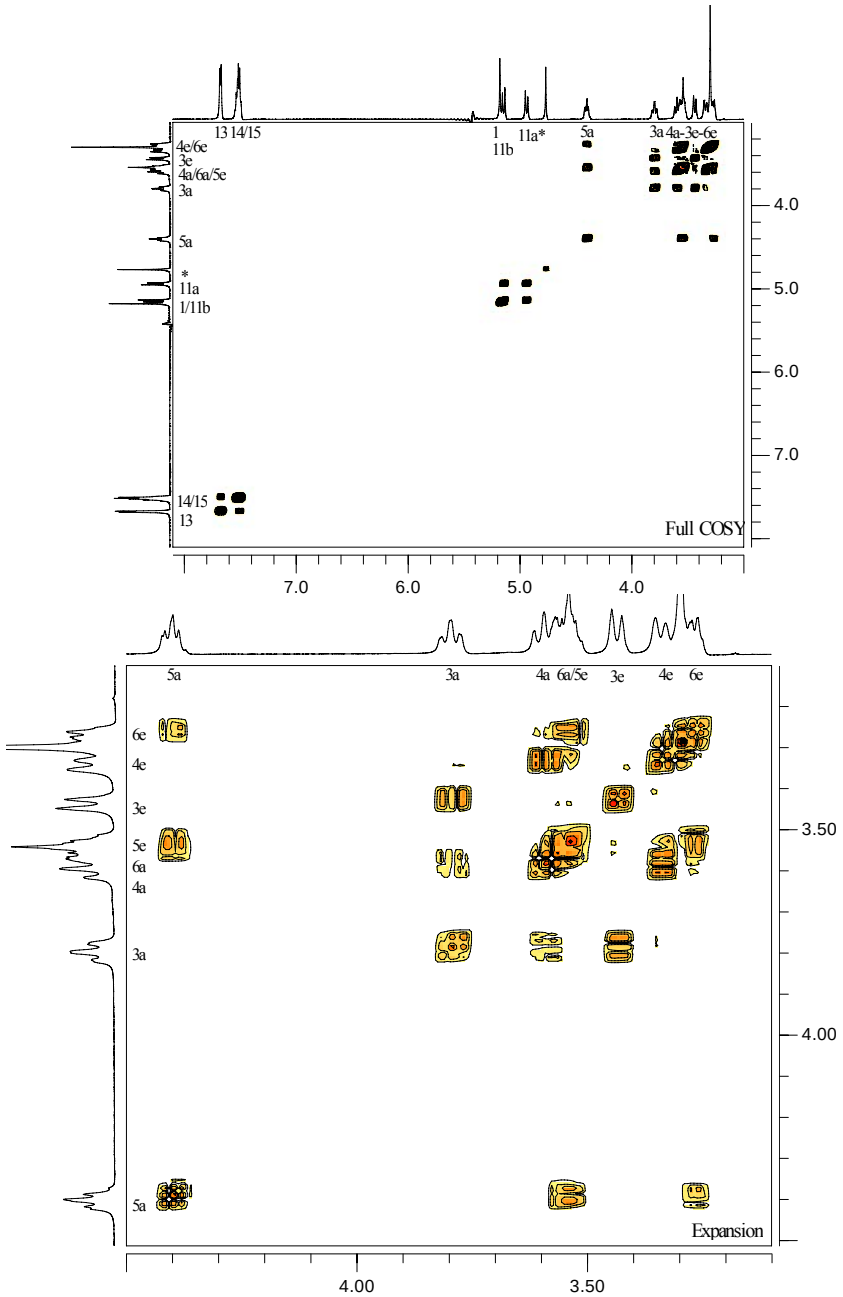


Figure 151: COSY NMR of 10^{+2}.

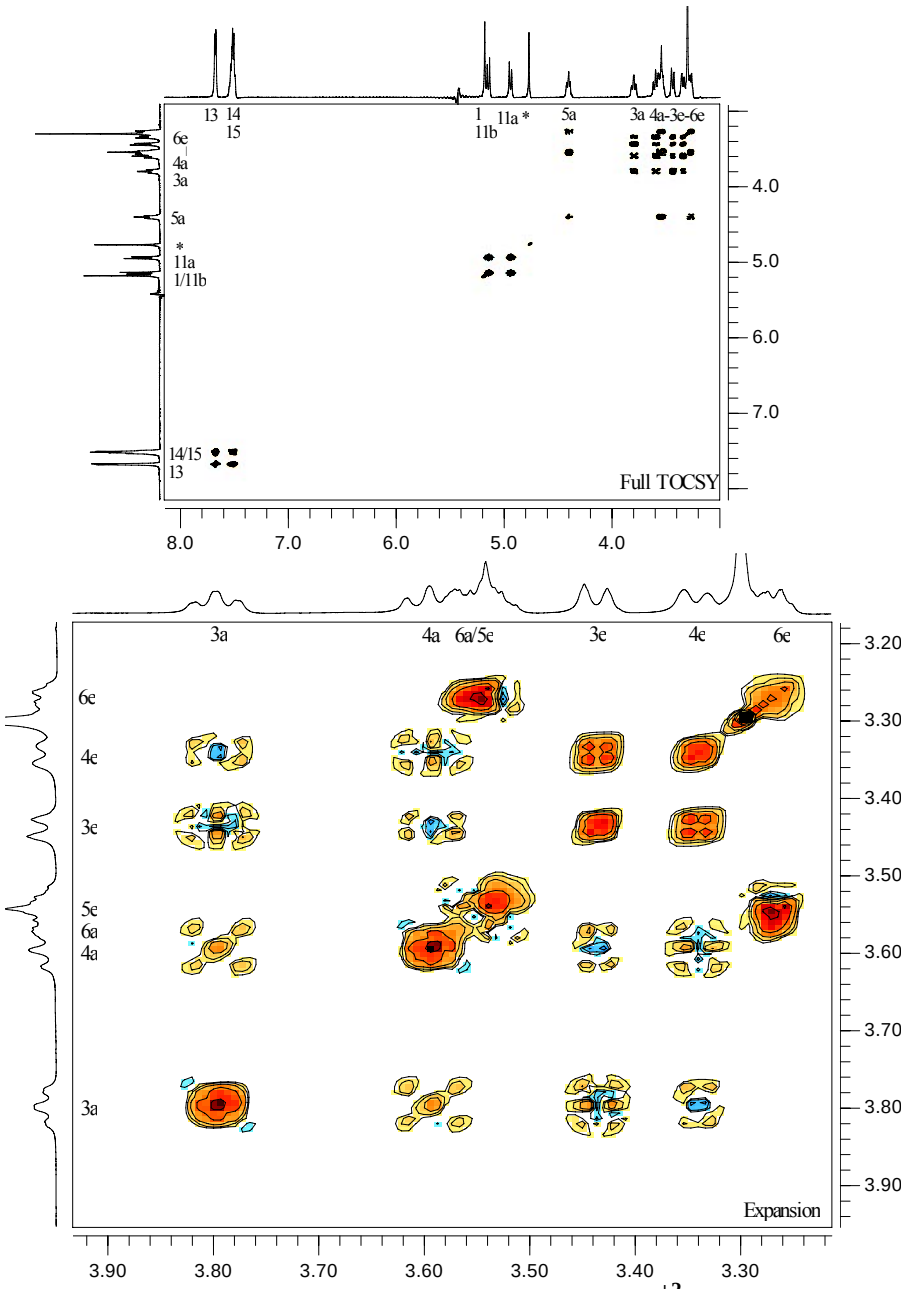


Figure 152: TOCSY NMR of 10^{+2}.
0.080s spin-lock mixing time was used.

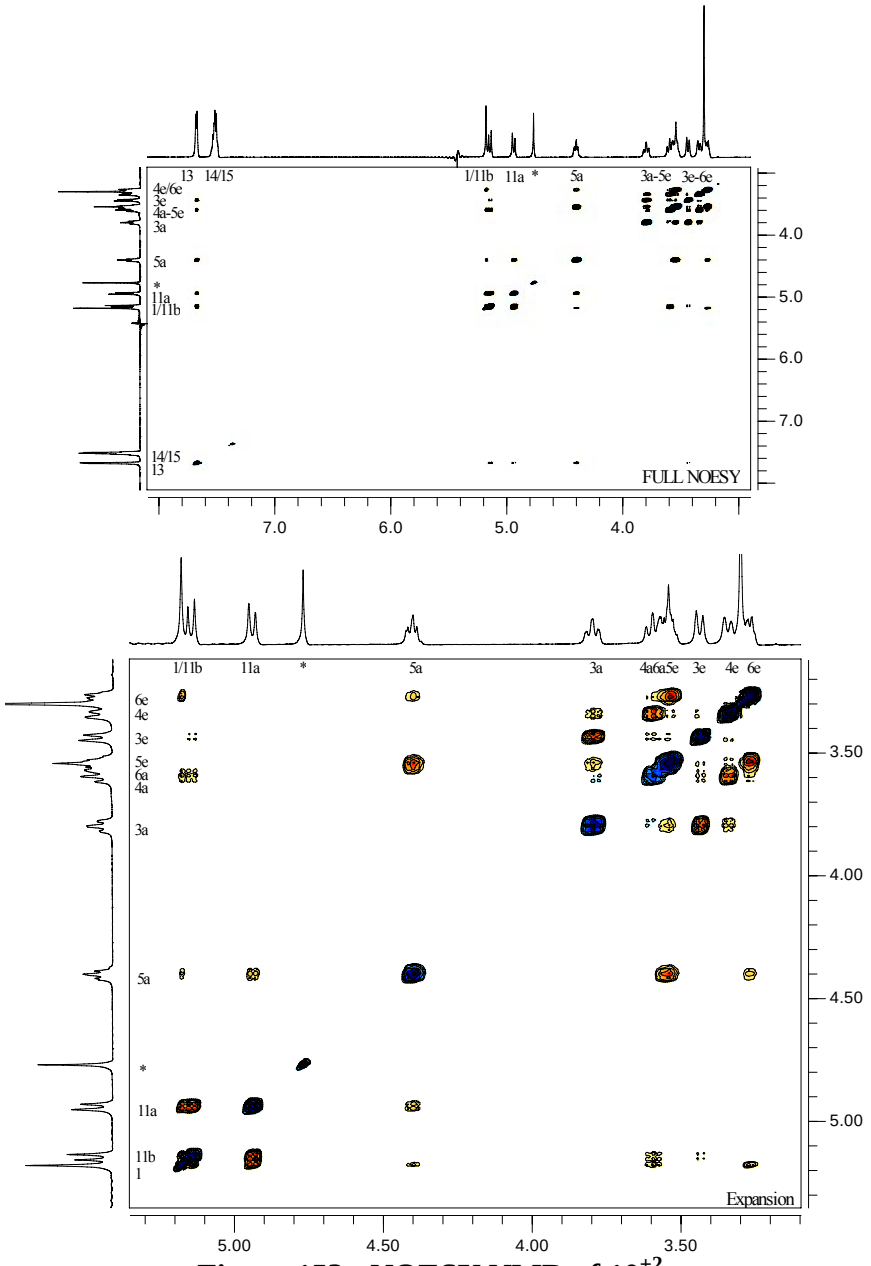


Figure 153: NOESY NMR of 10^{+2}.
1.0 s mixing time was used.

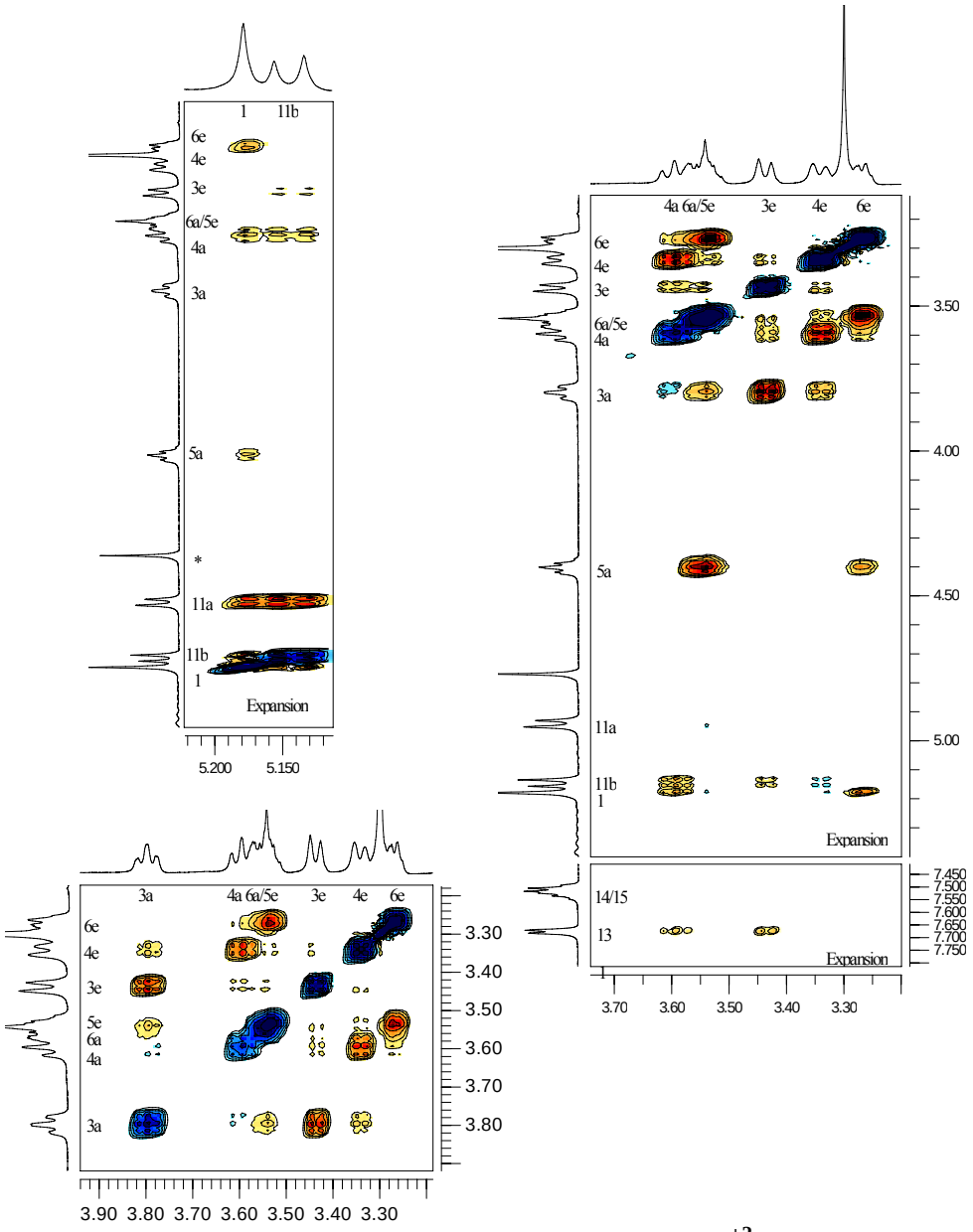


Figure 154: NOESY expansions of 10^{+2}.

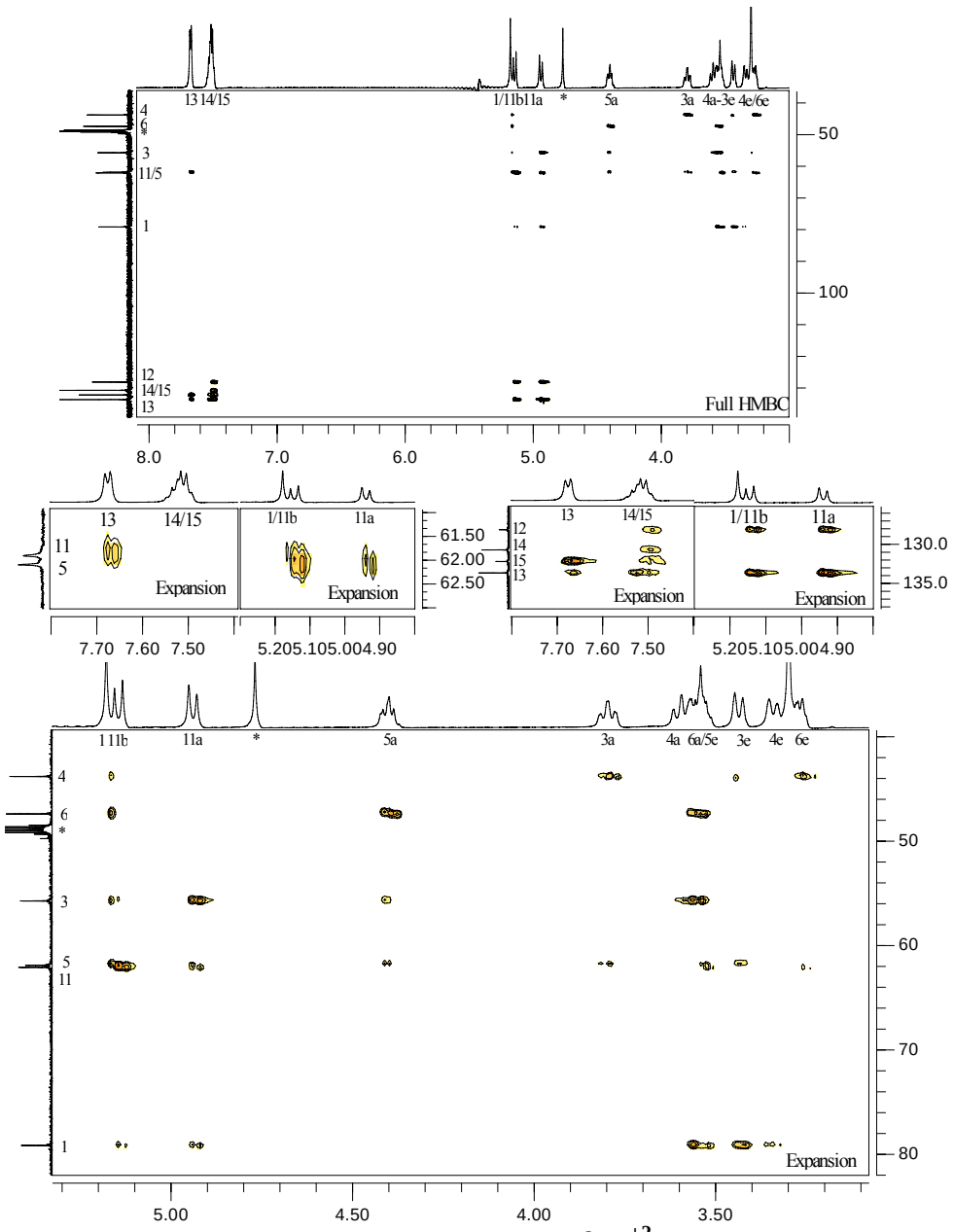


Figure 155: HMBC of 10^{+2}.

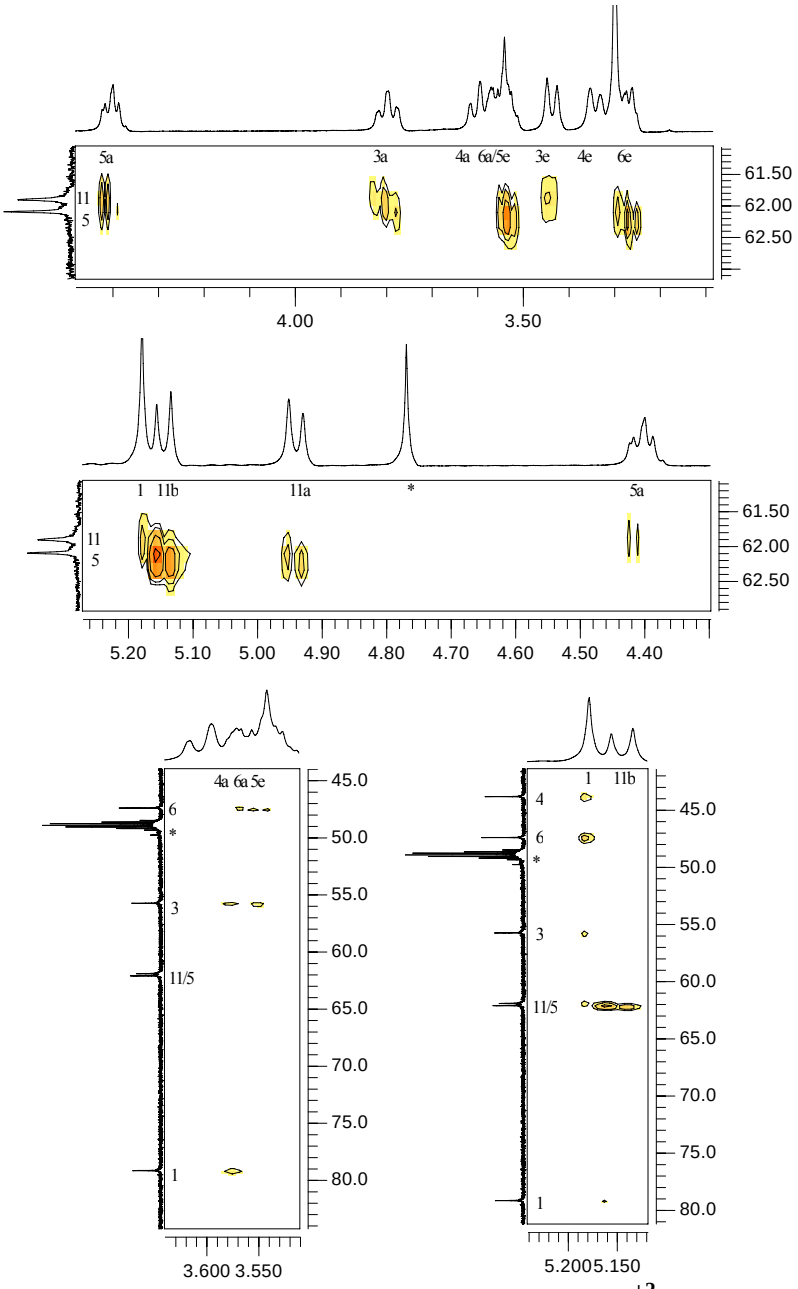


Figure 156: HMBC expansions of 10^{+2}.

performed to carbon-carbon or carbon-proton correlations because there are only two protons in the molecule. This assignment is not meant to make any implications concerning these rings and their spectroscopic properties rather it is for the purposes of clear discussion of this molecule. Having already assigned the carbon atoms, the proton connectivity is determined by HMQC and can be assigned based on the assumption of the carbon positions. Based on mirror symmetry arguments, one proton resonance must belong to the six membered ring whereas the other resonance belongs to the protons in the five membered rings.

HMQC spectra does not indicate diastereotopic proton sets. Instead, only one correlation for each CH_2 atom is present. C3 (δ/ppm 51.54) is connected to H_3 (δ/ppm 2.83) and C5 (δ/ppm 52.83) is connected to H_5 (δ/ppm 2.67).

Figure 157 shows the predicted structures of the molecule according to NMR. A portion of the crystal structures is shown in Figure 158 and Figure 159. The proton and carbon NMR spectra are given in Figure 160. . HMQC spectrum is shown in Figure 161.

3.6 Experimental

All samples were placed in NMR solvents which were previously dried by reflux over potassium, sodium, or calcium hydride for several days. The molecules were synthesized using Schlenk and vacuum line techniques. The NMR samples were handled in a glovebox and placed in a resealable Young's NMR tube or flame sealed before spectra were obtained. The solvent was transferred to the samples under reduced pressure.

3.6.1.1 Acquisition and processing parameters for 10^+

For the 2D data, longer mixing times were used to attempt to compensate for the long T_1 value of H_1.

Both of the 1D proton and carbon spectra for $\mathbf{10}^+$ were obtained on a Bruker Avance 400 MHz spectrometer at room temperature. The proton spectrum was obtained with the following parameters: pulse sequence, *zg30;* spectral width, 1812 Hz; number of scans, 16; relaxation time, 1.0 s; time domain points, 65536; pulse angle, 90°

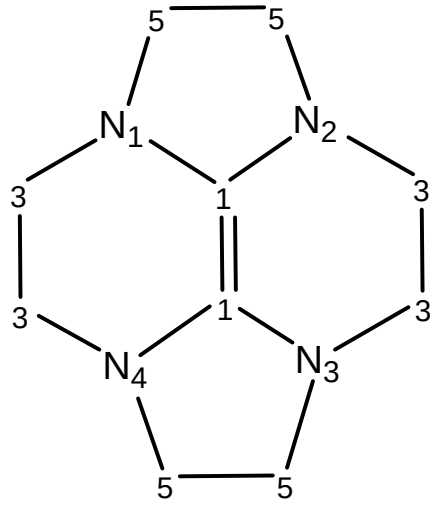


Figure 157: The structure of 11 that is consistent with the NMR data.

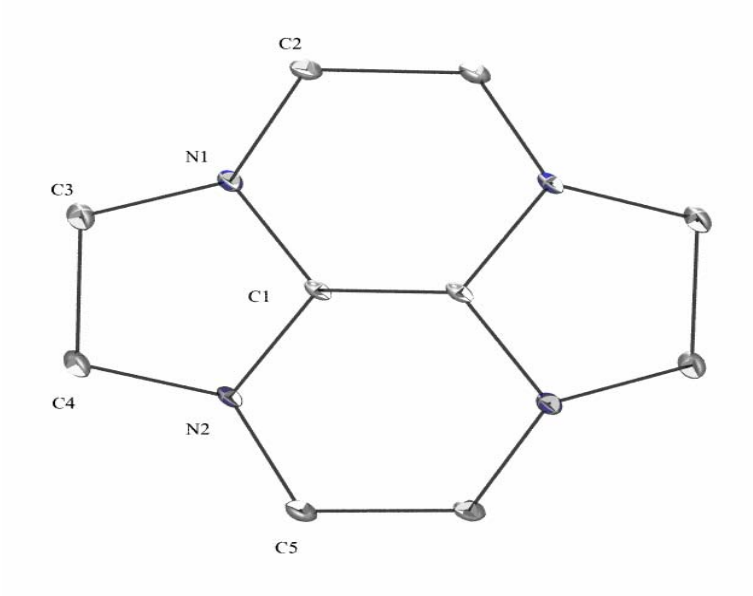


Figure 158: Crystal structure of 11.

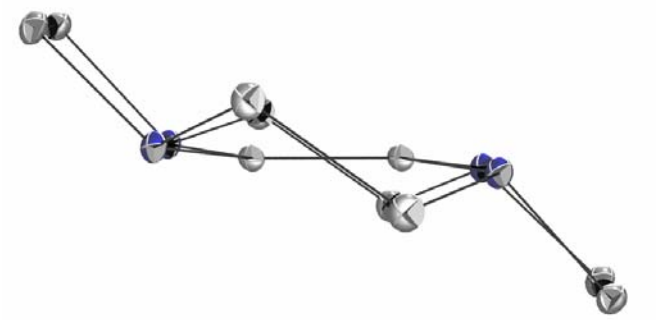


Figure 159: Sideview of the crystal structure of 11.

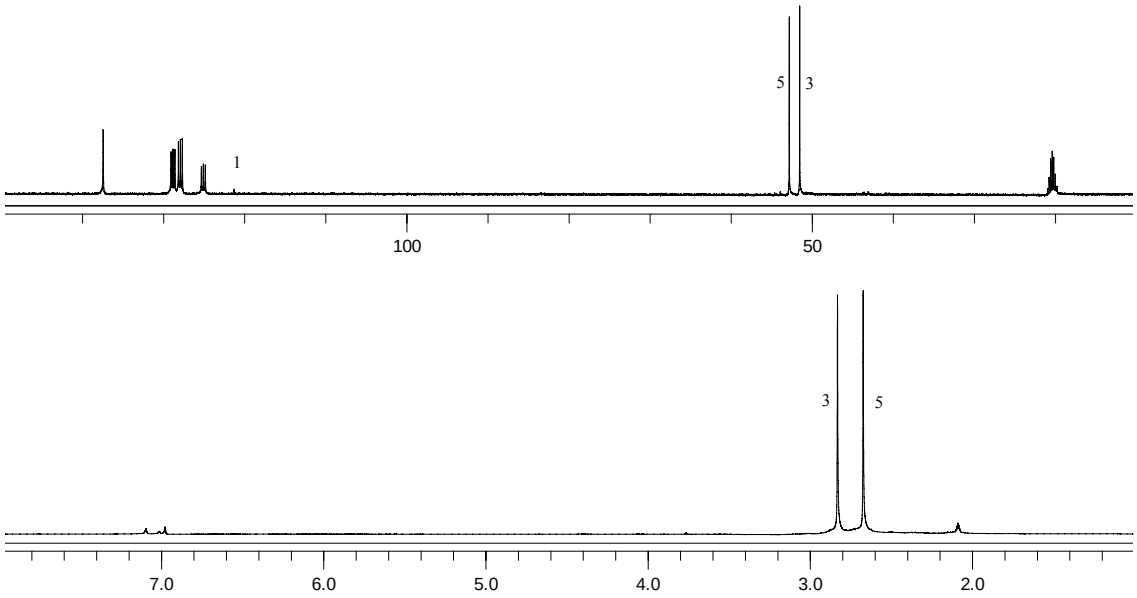


Figure 160 Carbon and proton spectra of 11.

^{1}H-NMR (400 MHz) δ/ppm 2.83 (s, 8H) δ/ppm 2.67 (s, 8H) ^{13}C-NMR (400 MHz) 121.30 (C), 52.83 (CH_2), 51.54 (CH_2)

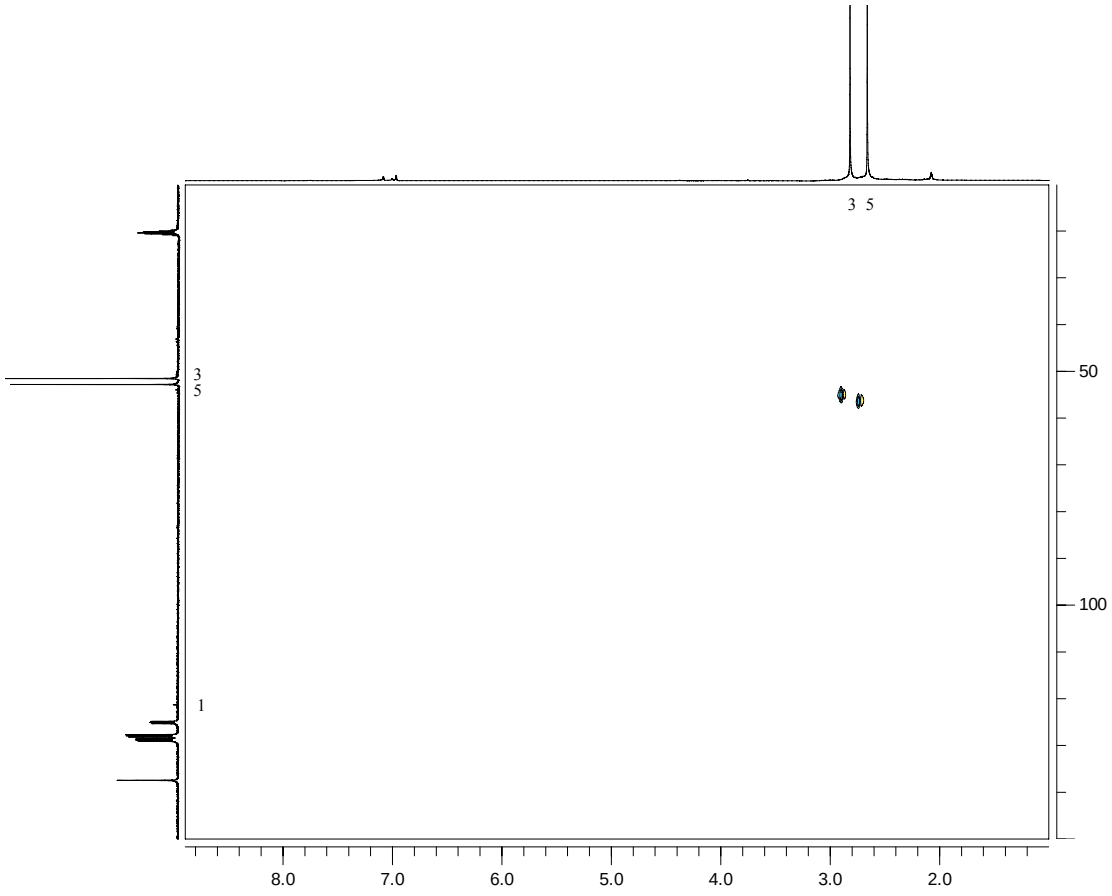


Figure 161: HMQC NMR of 11.

multiplied by the exponential function with line broadening 0.3 Hz; and Fourier transformed. The carbon spectrum was obtained with the following parameters: pulse sequence, *zgdc;* spectral width, 26,667 Hz; number of scans, pulse angle, 90°; with proton decoupling using the WALTZ-16 sequence; multiplied by the exponential function with line broadening 1.0 Hz; and Fourier transformed.

The T_1 relaxation study was obtained on a Bruker Avance 400 MHz spectrometer. The pulse sequence used was *tlir* with the following parameters: spectral width, 1812 Hz; number of scans, 8; relaxation times used were : 0.5 s, 1.0 s, 3.0 s, 5.0 s, 6.0 s, 7.0 s, 8.0 s, 9.0 s 10.0 s, 11.0 s, 12.0 s, 13.0 s, 14.0 s, 15.0 s, 17.0 s, 20.0 s; time domain points, 8192; pulse angle, 90°; multiplied by the exponential function with line broadening of 0.5 Hz; and Fourier transformed.

The VT 1D proton spectra were obtained on a Bruker Avance 400 MHz spectrometer. The pulse sequence used was *zg30* at specified temperature with the following parameters: spectral width, 1984 Hz; number of scans, 16; relaxation time, 1.0s; time domain points, 65536; pulse angle, 90°; multiplied by the exponential function with line broadening 0.3 Hz; and Fourier transformed.

The VT 1D carbon spectra were obtained on a Bruker Avance 400 MHz spectrometer at room temperature with the following parameters: following parameters: pulse sequence, *zgdc;* spectral width, 26,667 Hz; pulse angle, 90°; with proton decoupling using the WALTZ-16 sequence; multiplied by the exponential function with line broadening 1.0 Hz; and Fourier transformed.

The HMQC spectrum was obtained on a Varian Inova 600 MHz spectrometer at room temperature using the following parameters: pulse program, *gHSQC*, spectral widths of 3312 and 25,641 Hz in the ^{1}H and ^{13}C dimensions, respectively; 512 FIDS were collected. The resulting data points were zero-filled to 256 points in the t_1 dimension and multiplied by a sine squared window function shifted by $\pi/2$ along both dimensions and double Fourier transformed.

The HMBC spectrum was obtained on a Varian Inova 600 MHz spectrometer at room temperature using the following parameters: pulse program, *gHMBC*, spectral widths of 3311 and 36,199 Hz in the ^{1}H and ^{13}C dimensions, respectively; 512 FIDS

were collected with 400 t_1 increments; 24 transients; 2.0 s relaxation delay. Magnitude data points were obtained. The resulting data points were zero-filled to 512 points in the t_1 dimension and multiplied by an unshifted sinebell window function in both dimensions and double Fourier transformed.

The NOESY spectrum was obtained on a Varian Inova 600 MHz spectrometer at room temperature with the following parameters: pulse program, *NOESY*, spectral width in both dimensions of 3312 Hz; 512 FIDS collected with 256 t_1 increments;16 transients; 5.0 s relaxation delay, 1.4 second mixing time. Phase sensitive data points were obtained using TPPI methods. The resulting data points were multiplied by an exponential function in the t_2 dimensions with 2.0 Hz line broadening and then Fourier transformed. Then, the data points were linear predicted from points 256 to 511 points in the t_1 dimension and multiplied by a sine squared window function shifted by $\pi/2$; Fourier transformed; and symmetrized.

3.6.1.2 Acquisition and processing parameters for low temperature studies of 10

Very short delays and mixing times were used for the low temperature studies of this molecule due to the very short T_1 values at low temperature.

Both of the 1D proton and carbon spectra were obtained on a Bruker Avance 400 MHz spectrometer at 208 K. The proton spectrum was obtained with the following parameters: pulse sequence, *zg30;* spectral width, 3561 Hz; number of scans, 1; relaxation time, 1.0 s; time domain points, 65536; pulse angle, 90°; multiplied by the exponential function with line broadening 0.3 Hz; and Fourier transformed. The carbon spectrum was obtained with the following parameters: pulse sequence, *zgdc;* spectral width, 14,005 Hz; number of scans, 16; relaxation time, 2.0 s; pulse angle, 90°; with proton decoupling using the WALTZ-16 sequence; multiplied by the exponential function with line broadening 1.0 Hz; and Fourier transformed.

The T_1 study was obtained on a Bruker Avance 400 MHz spectrometer. The pulse sequence used was *tlir* with the following parameters: spectral width, 2403 Hz; number of scans, 8; relaxation times used were : 0.01 s, 0.1 s, 0.25 s, 0.5 s, 0.75 s, 1.0 s, 2.0 s, 3.0

s, 4.0 s, and 10.0 s; time domain points, 8192; pulse angle, 90°; multiplied by the exponential function with line broadening of 0.5 Hz; and Fourier transformed.

The TOCSY spectrum was obtained on a Bruker Avance 400 MHz spectrometer at 208 K with the following parameters: pulse program, *mlevtp*, spectral width in both dimensions of 1175 Hz; 512 FIDS collected with 128 t_1 increments; 4 transients; 2.0 s relaxation delay, 0.231 s spin-lock mixing time. Phase sensitive data points were obtained using hyper methods. The resulting data points were multiplied by a sinebell window function shifted by $\pi/2$ in the t_2 dimension and Fourier transformed. Then, the data points were linear predicted from points 128 to 255 points in the t_1 dimension and multiplied by a sine squared window function shifted by $\pi/2$ in the t_1 dimension; Fourier transformed; and symmetrized.

The COSY spectrum was obtained on a Bruker Avance 400 MHz spectrometer at 208 K with the following parameters: pulse program, *cosy45*, spectral width in both dimensions of 3180 Hz; 512 FIDS. Magnitude data points were obtained. A linear prediction was performed in the t_1 dimension from 128 to 255. The data points were multiplied by an unshifted sinebell window function in both dimension and double Fourier transformed. The data points were symmetrized.

The HMQC spectrum was obtained on a Bruker Avance 400 MHz spectrometer at 208 K with the following parameters: pulse program, *invbtp*, spectral widths of 3181 and 26,667 Hz in the ^{1}H and ^{13}C dimensions, respectively; 512 FIDS were collected with t1 increments of 256 points; 32 transients; 3.0 s relaxation delay. Phase sensitive data points were obtained. The data points were multiplied by a sinebell window function shifted by $\pi/2$ in the t_2 dimension. A linear prediction from 256 to 511 data points was applied in the t_1 dimension and multiplied by a sine squared window function shifted by $\pi/2$ along the t_1 dimension and Fourier transformed.

This NOESY spectrum was obtained on a Bruker Avance 400 MHz spectrometer at 208 K with the following parameters: pulse program, *noesytp*, spectral width in both dimensions of 2404 Hz; 512 FIDS collected with 256 t_1 increments; 32 transients; 2.0 s relaxation delay, 0.18 s mixing time. Phase sensitive data points were obtained using hyper method. The data points were predicted linearly predicted from 256 to 511 points

in the t_1 dimension; multiplied by a sinebell window function shifted by $\pi/2$; double Fourier transformed; and symmetrized.

3.6.1.3 Acquisition and processing parameters for VT studies of 10

Both of the 1D carbon and proton spectra were obtained on a Bruker Avance 400 MHz spectrometer at room temperature. The proton spectrum was obtained with the following parameters: pulse sequence, *zg30;* spectral width, 3561 Hz; number of scans, 16; relaxation time, 1.0s; time domain points, 65536; pulse angle, 90°; multiplied by the exponential function with line broadening 0.3 Hz; and Fourier transformed. The carbon spectrum was obtained with the following parameters: pulse sequence, *zgdc;* spectral width, 14,006 Hz; number of scans, 64; relaxation time, 2.0s; time domain points, 65536; pulse angle, 90°; with proton decoupling using the WALTZ-16 sequence; multiplied by the exponential function with line broadening 0.3 Hz; and Fourier transformed.

The relaxation study was obtained on a Bruker Avance 400 MHz spectrometer. The pulse sequence used was *tlir* with the following parameters: spectral width, 3205 Hz; number of scans, 8; relaxation times used were : 0.01 s, 0.1 s, 0.25 s, 0.5 s, 1.0 s, 2.0 s, 3.0 s, 4.0 s, and 10.0 s; time domain points, 8192; pulse angle, 90°; multiplied by the exponential function with line broadening of 0.5 Hz; and Fourier transformed.

The HMQC spectrum was obtained on a Bruker Avance 400 MHz spectrometer at room temperature with the following parameters: pulse program, *invbtp*, spectral widths of 3561 and 55,689 Hz in the ^{1}H and ^{13}C dimensions, respectively; 128 FIDS were collected with 8 transients; 3.0 s relaxation delay. Phase sensitive data points were obtained using hyper method. The data points were multiplied by a sinebell window function shifted by $\pi/2$ in the t_2 dimension. A linear prediction from 128 to 255 data points was applied in the t_1 dimension and multiplied by a sine squared window function shifted by $\pi/2$ along the t_1 dimension and Fourier transformed.

The TOCSY spectrum was obtained on a Bruker Avance 400 MHz spectrometer at room temperature with the following parameters: pulse program, *mlevtp*, spectral width in both dimensions of 3561 Hz; 256 FIDS collected with 8 transients; 4.0 s relaxation delay, and 0.15 s spin-lock mixing time. Phase sensitive data points were

obtained. The resulting data points were multiplied by a sinebell window function shifted by $\pi/2$ in the t_2 dimension and Fourier transformed. Then, the data points were linear predicted from points 256 to 511 points in the t_1 dimension and multiplied by a sine squared window function shifted by $\pi/2$ in the t_1 dimension; Fourier transformed; and symmetrized.

The NOESY spectrum was obtained on a Bruker Avance 400 MHz spectrometer at 208 K with the following parameters: pulse program, *noesytp*, spectral width in both dimensions of 3180 Hz; 256 FIDS collected with 16 transients; 3.0 s relaxation delay, and 1.0 s mixing time. Phase sensitive data points were obtained using hyper method. The data points were multiplied by a sinebell window function shifted by $\pi/2$ and Fourier transformed. The data points were predicted linearly from 128 to 255 points in the t_1 dimension; multiplied by a sine squared window function shifted by $\pi/2$; double Fourier transformed; and symmetrized.

3.6.1.4 Acquisition and processing parameters for 10^{+2}

Both of the 1D carbon and proton spectra were obtained on a Bruker Avance 400 MHz spectrometer at room temperature. The proton spectrum was obtained with the following parameters: pulse sequence, *zg30;* spectral width, 2790 Hz; number of scans, 16; relaxation time, 1.0s; time domain points, 65536; pulse angle, 90°; multiplied by the exponential function with line broadening 0.3 Hz; and Fourier transformed. The carbon spectrum was obtained with the following parameters: pulse sequence, *zgdc;* spectral width, 14,006 Hz; number of scans, 64; relaxation time, 2.0s; time domain points, 65536; pulse angle, 90°; with proton decoupling using the WALTZ-16 sequence; multiplied by the exponential function with line broadening 0.3 Hz; and Fourier transformed.

The HMQC was obtained on a Bruker Avance 400 MHz spectrometer at room temperature using the following parameters: pulse program, *inv4tp*, spectral widths of 2790 Hz and 43,599 Hz in the ^{1}H and ^{13}C dimensions, respectively; 256 FIDS were collected with t_1 increments of 1000 points; 8 transients; 1.5 s relaxation delay. Phase sensitive data points were obtained using TPPI. The resulting data points were multiplied by a sinebell window function shifted by $\pi/2$ along the t_2 dimension and Fourier

transformed. A linear prediction was applied in the t_1 dimension from 256 to 511. multiplied by a sine squared window function shifted by $\pi/2$ along the t_1 dimension and Fourier transformed.

This COSY spectrum was obtained on a Varian Inova 600 MHz spectrometer at room temperature with the following parameters: pulse program, *gCOSY*, spectral width in both dimensions of 4211 Hz; 128 FIDS collected with 1 transient; 1.0 s relaxation delay. Magnitude data points were obtained. The data points were zero filled to 1024 points in the t_1 dimension. The data points were multiplied by an unshifted sinebell window function in both dimension and double Fourier transformed. The data points were then symmetrized.

This TOCSY spectrum was obtained on a Varian Inova 600 MHz spectrometer at room temperature with the following parameters: pulse program, *TOCSY*, spectral width in both dimensions of 4211 Hz; 400 FIDS collected with 4 transients; 2.0s relaxation delay, 0.080s spin-lock mixing time. Phase sensitive data points were obtained using hyper methods. The resulting data points were multiplied by a sinebell window function shifted by $\pi/2$ in the t_2 dimension and Fourier transformed. Then, the data points were linear predicted from points 400 to 799 points in the t_1 dimension and multiplied by a sine squared window function shifted by $\pi/2$ in the t_1 dimension; Fourier transformed; and symmetrized.

This NOESY spectrum was obtained on a Varian Inova 600 MHz spectrometer at room temperature with the following parameters: pulse program, *NOESY*, spectral width in both dimensions of 4211 Hz; 400 FIDS collected; 8 transients; 1.0s relaxation delay, 1.0 s mixing time. Phase sensitive data points were obtained using hyper method. The data points were multiplied by a sinebell window function shifted by $\pi/2$ and Fourier transformed. The data points were predicted linearly predicted from 400 to 800 points in the t_1 dimension; multiplied by a sine squared window function shifted by $\pi/2$; Fourier transformed; and symmetrized.

The HMBC spectrum was obtained on a Varian Inova 600 MHz spectrometer at room temperature using the following parameters: pulse program, *gHMBC*, spectral widths of 4211 and 36,199 Hz in the ^{1}H and ^{13}C dimensions, respectively; 400 FIDS

were collected with 2048 t_1 increments; 8 transients; 1.0s relaxation delay. Magnitude data points were obtained. A linear prediction was applied in the t_1 dimension from 400 to 799 points and multiplied by an unshifted sinebell window function in both dimensions and double Fourier transformed.

3.6.1.5 Acquisition and processing parameters for 11

Both of the 1D carbon and proton spectra of **11** were obtained on a Bruker Avance 400 MHz spectrometer at room temperature. The proton spectrum was obtained with the following parameters: pulse sequence, *zg30;* spectral width, 2815 Hz; number of scans, 16; relaxation time, 1.0s; time domain points, 65536; pulse angle, 90°; multiplied by the exponential function with line broadening 0.3 Hz; and Fourier transformed. The carbon spectrum was obtained with the following parameters: pulse sequence, *zgdc;* spectral width, 26, 6667 Hz; number of scans, 64; relaxation time, 2.0s; time domain points, 65536; pulse angle, 90°; with proton decoupling using the WALTZ-16 sequence; multiplied by the exponential function with line broadening 1.0 Hz; and Fourier transformed.

The HMQC was obtained on a Bruker Avance 400 MHz spectrometer at room temperature using the following parameters: pulse program, *inv4tp*, spectral widths of 3592 Hz and 20120 Hz in the ^{1}H and ^{13}C dimensions, respectively; 256 FIDS were collected with t_1 increments of 1000 points; 8 transients; 1.5 s relaxation delay. Phase sensitive data points were obtained using TPPI. The resulting data points were multiplied by a sine bell window function shifted by $\pi/2$ along the t_2 dimension and Fourier transformed. The data points were zero filled applied in the t_1 dimension to 1024. It was then multiplied by a sine squared window function shifted by $\pi/2$ along the t_1 dimension and Fourier transformed.

4 SYNTHESIS AND SPECTROSCOPY OF ZIRCONIUM-AMIDO COMPLEXES AND CARBAZOYL DERIVATIVES

4.1 Forward

The study of innovative complexes, which display novel reactivity, is fundamental in the progression of chemical science. The molecules in this section are the precursors to a group of complexes potentially capable of small molecule activation. Carbazole was chosen because noninnocent ligands are able to tune reactivity at the metal center. Additionally, carbazole can be easily substituted thus allowing for fine-tuning of reactivity allowing catalytic properties to be manipulated. A series of coordination complexes were synthesized[132-134] for the purposes of determining catalytic reactivity and developing potentially new reactive catalysts. These catalysts are important as they have potential for high reactivity. Additionally, several simplified syntheses of carbazole derivatives, which were developed in the course of the work on this project, are also presented.

4.2 Carbazole

Carbazole was first discovered in coal tar in 1872.[135] The synthesis of carbazole was studied in the initial synthesis of indoles by Fischer. Derivatives of carbazole have important pharmacological uses; some of the better-known derivatives have been used in the past to treat a wide variety of illnesses. Carofen is used to treat arthritis in man and animals.[136] 9-Hydroxyx-2-methylellipticinium acetate was used to treat thyroid, kidney, and breast cancer[137] and carvedilol treated hypertension.[138] Carbazole derivatives also have several medicinal patents. Carbazole alkaloids has been shown to inhibit a cell cycle.[139]

Some of the ligands on highly reactive metal center include hindered imido species $[R_LN]^{2-}$ where R_L is a sterically hindered group *e.g.* ^{t}Bu, or 2,6 $R_2C_6H_3$, (R = Me, ^{i}Pr), $[(RNCH_2CH_2)_3N]^{3-}$ (R = $SiMe_3$, Me), $[((TMS)N(CH_2CH_2)_2\}N(TMS)^{2-}]$ and silox

$[(Me_3Si)_3Si\text{-}O]^-$. Based upon the steric similarities to some of these species as well as the tris-amido theme, carbazole was chosen as an appropriate yet underdeveloped ligand set.

4.3 Catalysts

Transition metal complexes with electron counts of 16 or 18 have been experimentally determined to be both stable and exhibit unusual activity. Complexes with 16 electrons are prevailing with metals in groups 4, 9, and 10. Conversely, 18 electron systems tend to be prevalent with metals in groups 6, 7, and 8. Metals with low coordination number bound to unusual *d* electron counts have shown interesting reactivity. Recent reports of this unusual reactivity include the cleavage of dinitrogen at a Mo(III) center and the activation of methane at Ti and Zr centers.[140-143]

4.4 Carbazole derivatives

As a ligand, carbazole should create a complex that has very interesting properties with respect to catalysis and small molecule activation. The ability to substitute on the carbazolyl rings makes the properties of these systems adjustable for enhancement of differing properties of the complex. Donor groups strategically synthesized can be used to tune electronic donation as well as ligand properties. These substituted carbazole molecules are easy to synthesize thus introducing carbazole as a favorable ligand. Additionally, carbazole has a potentially interesting bonding situation with respect to "L" donor capability. Extent of the balance would be between σ and π bonding is not necessarily clear. The donor groups tune the electronic donation capability as well as ligand properties.

Although unsubstituted carbazole is readily available and easily purified, carbazolyl complexes that were created containing the metals Ta, Zr, Hf, Cr, Fe, and V were insoluble and therefore difficult to purify. The reactivity of these species was subsequently difficult to study as the complexes are insoluble and not readily reactive in the solution phase. Crystal structures are also not easily obtained from insoluble

powders. Substituted carbazole ligands were then synthesized as ligands to improve the solubility limitation. Limited functional group size did indeed affect the solubility of the complexes.

Investigation of substituted carbazole atoms indicates that the solubility of the resultant metal complexes are strongly influenced by substitution. For these reasons and one more, substituted carbazolyl molecules were used. The final reason for use of substituted carbazole molecules is that substitution of "R" groups influences not only solubility and available aromaticity for electron donation but also constrains certain bonding configuration around the metal center. For example, an "R" group attached to the C3 position is electron withdrawing and reduces aromaticity potentially withdrawing nitrogen electron density from the metal donation. Figure 162 illustrates a constrained configuration.

4.4.1 Synthesized substituted carbazole molecules

A wide variety of methods have been used to synthesize both carbazole and its derivatives. Although there were many methods available, it was difficult to find a method that was inexpensive, fast, and high yielding. There are two general methodologies in the literature used to form substituted carbazole.

In one method, two starting materials which already contain the desired substituents, are joined usually *via* catalytic reaction. In the other method, substituents are added to certain carbazolyl positions after the nitrogen center has been protected. There are advantages and disadvantages to both methods and depending upon the desired product both methods were used for the synthesis of derivatives in this paper; however, the reagents and reaction conditions were unique in all but three cases.

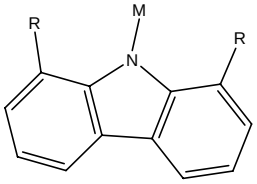


Figure 162: Steric hindrance generated on a disubstituted carbazole molecule.

4.4.1.1 Direct carbazole substitution

The advantage to adding substituents directly to carbazole is that in theory, it is very simple to predict the substitution pattern and the substitution should be possible in one step. Carbazole is also inexpensive; 500kg costs $30. The disadvantage is that unless protected, the most nucleophilic position in carbazole is the nitrogen atom; therefore, any functional group will add to this position first. Since this is the position that must add to a metal center, a more permanent addition to this position is undesirable.

The nitrogen center in carbazole can be protected with diethylaluminum chloride,[144] TMS,[145] as well as with a benzyl group as shown in this paper. The benzyl protecting group was used because it is relatively simple to cleave the benzyl bond after substitution *via* sodium/ammonia reaction. Another disadvantage of this type of reaction is the fact that carbazole is symmetrical which makes symmetric positions on both sides of the molecule equally favorable towards substitution. Synthesis of mono-substituted carbazole is therefore very difficult using this method.

In the literature, some of the substituents that have been added to carbazole alone or in combination include: isobutylene, phenylacetylene,[144] chlorine,[146] bromine,[146, 147] methyl,[146] and methoxy[146] groups. Nickel cross-coupling reactions of brominated carbazole compounds with substituents yields products in high yields.[148] The primary purpose of substitution will be discussed shortly but simple carbon chain substitution as postulated and shown will increase the solubility and therefore make purification more readily available.

Unsubstituted carbazole has been synthesized in a variety of ways which include from N-(N,N-diphenylamino)phthalimide and aluminum trichloride[146]; cyclohexanone and phenylhydrazones with phosphorous trichloride.[149] Carbazole was obtained from Acros as a yellow powder and purified in a hood from hot toluene.

4.4.1.2 Combination of substituted non-carbazole reagents

The advantage to substituted reagents is that multiple reactions needed to protect and deprotect the nitrogen center are not necessary. Additionally, it is possible to synthesize mono and multisubstituted carbazole molecules in potentially a single step.

The disadvantage is that many of these reactions require expensive catalysts or stringent reaction conditions. Another disadvantage is that these reactions can require an additional aromatization step if the reaction formed a tetrahydrocarbazole instead of carbazole.

Substituted reagents which have been combined to form carbazole and substituted carbazole include: free radical cyclisation *via* peroxide[150], iodine-catalyzed cyclisation of substituted diphenylamine,[151] brominated o-cyclohex-2-enylanilines followed with Pd/C.[152] Palladium/ dehydrogenation of tetrahydrocarbazole is a Wolff-Kishner-Huang-Minlon reduction and the primary method used in this research to convert tetrahydrocarbazole to carbazole.

One application of the Fisher indolization uses hydrazones and cyclohexanone as part of a two-step synthesis of substituted carbazole. Several references use variations of this.[153] In this work specifically, hydrazone hydrochloric salt is used in many cases instead of the hydrazone thus promoting the activity of the bond of the ring in shorter time periods than corresponding papers. It is theorized that the increased speed of the reaction is due to the fact that the hydrazone is already protonated making it a very good nucleophile.

4.4.1.3 Synthesized molecules

The compounds in Figure 163 have been synthesized. Of these four compounds, the second has the simplest NMR spectra containing three equivalent aromatic peaks, and subsequent focus has been directed towards this dimethyl derivative.

Other di- and tri- substituted compounds have also been investigated which are shown in Figure 164 and evidence has been obtained that indicates the tetrahydrocarbazolyl form of these species have been synthesized for the first time. The yields are low and the oily compounds are difficult to clean. Variations on the procedure given by Hopper[154]and reintroduced by Kuroki[155] were used to synthesize other species.

The aforementioned organic syntheses in section 4.4.1.2 are constrained by two factors. First, only certain substituted salts are available as shown in Figure 165. Second, there are limitations to cyclohexanone substitution shown in Figure 166.

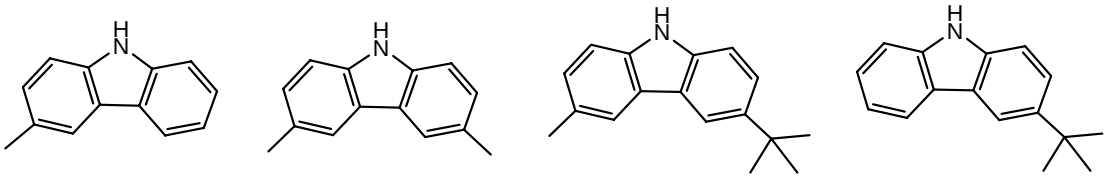


Figure 163: Mono and di-substituted carbazole.

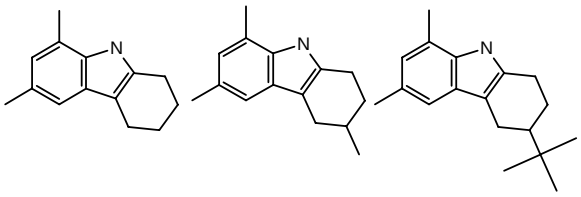


Figure 164: Di and tri-substituted tetrahydrocarbazole.

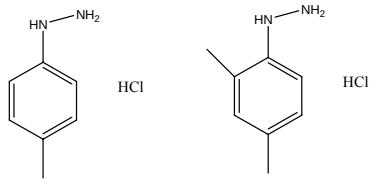


Figure 165: Available forms of the hydrochloric salt starting material 2005.

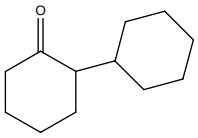


Figure 166: Sterically hindered cyclohexanone.

All of the other forms of the hydrazone hydrochloric salt are regulated and are extremely expensive such that 1g costs about $2000. The salts Figure 166 cost under $75 for 25g each. The second constraining factor on this synthesis is that very large substituents in the C1 position of the second reagent, cyclohexanone, hinder tetrahydrocarbazole formation. When this particular starting material is used, low yields result. In spite of these constraints, the organic synthesis for the substituted carbazole molecules shown in Figure 163 and Figure 164 is clean, easy to set-up, very quick, and only the last step is air sensitive. The workup is not difficult and all products are recrystallized from ethanol. In contrast, other methods to form these derivatives require reagents that are more sensitive.

4.5 Nitrogen complexes

Amido and Imido complexes are well-known for the rich reaction chemistry that they display. When complexed to transition metals, these ligands have been shown to promote new and unusual reactivity. This chemistry is often a result of both σ and π donation to the metal center.

Most amido and imido ligands are electronically innocent in that the electronics of the hydrocarbyl ligand frame are not generally strongly coupled to the electronics of the metal center. Other ligands such as pyrrole and indolyl are aromatic and not only have σ-donor abilities with respect to the metal center but also posses ligand-based interactions with the lone pair on the nitrogen atom. The extent of the balance between these two interactions is not immediately clear. These ligands are subsequently considered to be "non-innocent." Carbazole exemplifies this type of ligand. It is a noninnocent ligand in that the extent of electron density donation to and from a metal center is not immediately apparent. Once fully investigated, these carbazolyl organometallic species may be capable of acting as a polymerization catalyst or an organic reaction catalyst that for example, turns methane into methanol. The non-innocence of the carbazolyl ligand will strongly influence the properties of these catalysts.

4.5.1 Non-innocent complexes

There are two examples of noninnocent complexes given in Figure 167 and Figure 168. The first complex does not contain a carbon-metal bond and thus is considered a coordination complex. The number of electrons which can bond in this complex is variable partly due to the possibility that the lone pair of the sulfur atom can donate electron density to the metal bond. The second complex is an organometallic complex and is important in that the aromaticity of the ligands is dependent upon the donation to the metal center. It is possible however for these ligands to retain their aromaticity by either gaining or losing electron density. This allows for the possibility for the bonding to be ML_4X_4 or ML_5X_2. Figure 169 illustrates the noninnocent situation for carbazole specifically.

The non-innocent notation does not necessarily imply that in some cases the bonding can be determined *via* further measurements but rather that the bonding is not clear without these measurements.

4.5.2 Target carbazole ligands

Several derivatized forms of carbazole were added to zirconium (IV) chloride. The two target ligands with which the majority of the experiments were performed were carbazole and 3,6-dimethylcarbazole. This is due to the fact that these two derivatives provide a good contrast of properties but both have simplified spectra due to the symmetry of the ligand. As previously mentioned, unsubstituted carbazole has low solubility even when complexed to metal centers. It has no "R" groups to affect the electron bonding, and contains four aromatic peaks. In contrast, 3,6-dimethylcarbazole has much higher solubility when complexed to metal centers, the "R" groups in the *para* positions should be ring activating and improve the electric donor capacity of the nitrogen atom. The ligand contains only three aromatic peaks.

Protonated carbazole did not react with the metal center. To enhance the reactivity of the carbazole molecules, the proton was removed with various reagents. Trimethylsilane, lithium, and potassium were all used to remove the hydrogen. In the cases of the metals, metal hydrides were used. A large excess of metal hydride was

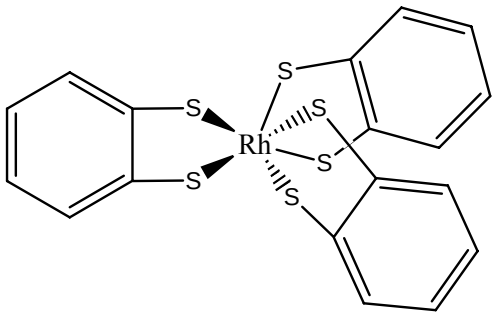


Figure 167: Classical noninnocent coordination.

The bonding in this complex can be described as any of the following and more: ML_6, MX_6, and ML_4X_2. Based on this notation, the total number of electrons in the species varies.

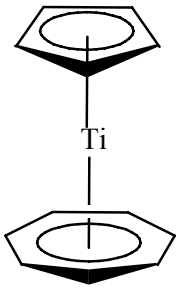


Figure 168: Classical noninnocent organometallic complex.

The bonding in this complex can be described as ML_4X_4 as well as ML_5X_2. In this case, the total number of bonding electrons has been conserved but the bonding is not clear.

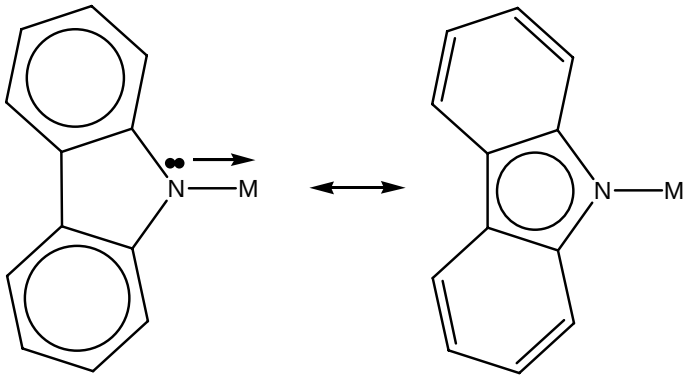


Figure 169: Illustrations of carbazole indicating two potential bonding schemes. The carbazole on the left is similar to ethylenediamine where the lone pair acts as a full *L* donor to the metal center. The right carbazole is similar to pyrrole where the electron pair participates in aromatic ring and has less density to donate to the metal center and has more *X* donor character. MLX naming was discussed in section 2.3.5.

required for complete deprotonation. This is likely due to the change in pH of the solution during deprotonation. The trimethylsilane reaction did react to form the protected carbazole but the complex was much less stable and light sensitive than the benzyl derivative. Additionally, the trimethylsilane complex did not react in a predictable manner so the metallated deprotonated forms of carbazole were used the majority of the time.

4.6 Experimental and NMR data

4.6.1 Zirconium connectivity

4.6.1.1 Correlations of 12a

This molecule was characterized using 1D and 2D NMR. All studies used solutions of the catalyst in d_2-dichloromethane. For reference purposes, the proton NMR, carbon NMR, and a proposed final structure of the molecule. A comparison of all spectroscopic data are given in the same section and correlational information follows in a table.

At room temperature, the ^{13}C data contain twelve (CH) resonances, two of which overlap as well as six quaternary resonances. The ^{1}H data contain eleven resonances, two of which overlap. The COSY data indicate three distinct spin system between four proton resonance sets, those designated as H_{1a}, H_{2a}, H_{3a}, and H_{4a}; H_{1b}, H_{2b}, H_{3b}, and $H_{4b;}$ and H_{1c}, H_{2c}, H_{3c}, and H_{4c}. It is reasonable to assume that these protons are contained in either the same ring system which correspond to three carbazole molecules or three rings which are symmetric.

HSQC data indicate that there are twelve separate CH resonances that correspond to twelve peaks. H_{1a} (δ/ppm 7.51) is connected to C_{1a} (δ/ppm 120.12), H_{2a} (δ/ppm 6.61) is connected to C_{2a} (δ/ppm 124.79). H_{3a} (δ/ppm 6.38) is connected to C_{3a} (δ/ppm 124.04). H_{4a} (δ/ppm 6.38) is connected to C_{4a} (δ/ppm 124.04). H_{1b}/H_{4b} (δ/ppm 7.69) is connected to C_{1b}/C_{4b} (δ/ppm 118.15). H_{2b} (δ/ppm 6.71) is connected to C_{2b} (δ/ppm 119.49). H_{3b} (δ/ppm 6.62) is connected to C_{3b} (δ/ppm 117.90). H_{1c} (δ/ppm 8.28) is connected to C_{1c} (δ/ppm 119.75). H_{2c} (δ/ppm 7.24) is connected to C_{2c} (δ/ppm 124.21). H_{3c} (δ/ppm 7.00) is connected to C_{3c} (δ/ppm 118.28). H_{4c} (δ/ppm 7.90) is connected to C_{4c} (δ/ppm 119.20).

The NOESY data are extremely interesting since all of the information obtained is in the same direction as the diagonal is phased. Distance correlations can be obtained from peaks which are oppositely phased form the diagonal but exchange information can also be obtained if the peaks are the same direction as the diagonal.

The overall effect is that protons in the “a” and “b” carbazole rings are in exchange or share an exchanging relationship. For these species, the interpretation of these data are that these carbazole species are twisting so that the rings are taking opposing orientations causing the exchange peaks. The protons in the “b” carbazole ring seem to have a different kind of exchange so this is likely the ring nearest the potassium atoms and slightly bound to potassium.

In addition to the ring “twisting,” it also appears as though each ring is also rocking so that one side of each carbazole can exchange with another side. In the NOESY spectrum, H_{1a} correlates in the same spin system with H_{4a} as well as outside of the spin system with H_{1c}. H_{2a} correlates in the same spin system with H_{3a} as well as outside of the

spin system with H_{2c}. H_{3a} correlates in the same spin system with H_{2a} as well as outside of the spin system with H_{2c}. H_{4a} correlates in the same spin system with H_{1a} as well as outside of the spin system with H_{1c}. Ring system "b" has a similar type of pattern with correlations: H_{1b}/H_{4b} correlates outside of the spin system with H_{4c}. H_{2b} correlates in the same spin system with H_{3b} as well as outside of the spin system with H_{3c}. H_{3b} correlates in the same spin system with H_{2b} as well as outside of the spin system with H_{3c}. H_{4a} correlates in the same spin system with H_{1a} as well as outside of the spin system with H_{1c}.

The most unique system is ring "c." H_{1c} only shows correlations outside of the spin system with H_{4a} and H_{1a}. H_{2c} only shows correlations outside of the spin system with H_{2a} and H_{3a}. H_{3c} only shows correlations outside of the spin system with H_{2b} and H_{3b}. H_{4c} only shows correlations outside of the spin system with H_{1b}/H_{4b}.

One of the difficulties with this system is the fact that the coalescence temperature is near to room temperature. For clear correlations, it is necessary to change the temperature. Additionally, from VT data, two processes are visible for this system.
Figure 170 shows the predicted structures of the molecule according to NMR. The proton and carbon NMR spectra are given in Figure 171. The crystal structure for **12**a, is given in Figure 172 and the crystal structure for **12b**, is given in Figure 173. Relevant correlational data are given in Table 4.1. Figure 174 and Figure 175 show VT studies. Relevant 2D spectra are given in Figure 176 - Figure 178.

4.6.1.2 Correlations of 13

This molecule was characterized using 1D and 2D NMR. All studies used solutions of the catalyst in d_2-dichloromethane. For reference purposes, the proton NMR, carbon NMR, and a proposed final structure of the molecule. A comparison of all spectroscopic data are given in the same section and correlational information follows in a table.

At room temperature, the ^{13}C data contain six (CH) resonances as well as six quaternary resonances. The ^{1}H data contain eight resonances. HSQC data indicate which protons are attached to which carbon atoms.

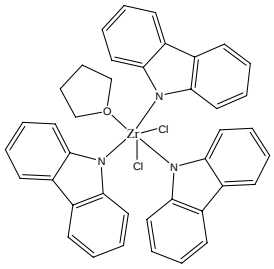


Figure 170: Structure of 12a according to NMR.

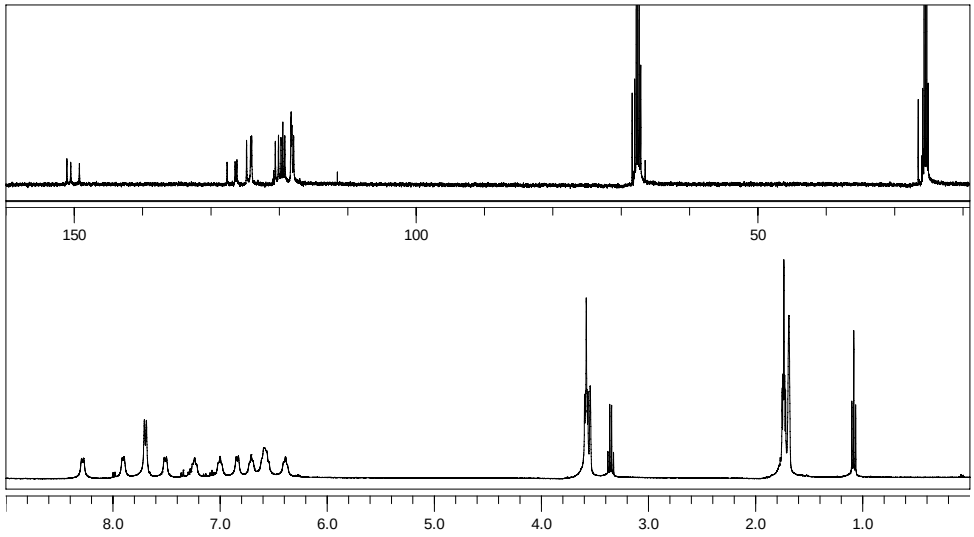


Figure 171: Carbon and proton spectra for 12a.

^{1}H-NMR (400 MHz) δ8.28 (d, *J* = 8.3 Hz, 1H) 7.90 (d, *J* = 7.4 Hz, 1H) 7.69 (d, *J* = 7.5 Hz, 2H) 7.51 (d, *J* = 8.2 Hz, 1H) 7.24 (t, *J* = 7.6 Hz, 1H) 7.00 (t, *J* = 7.1 Hz, 1H) 6.83 (d, *J* = 8.4 Hz, 1H) 6.71 (t, *J* = 7.3 Hz, 1H) 6.62 (m, 2H) 6.38 (t, *J* = 7.6 Hz, 1H) ^{13}C-NMR (400 MHz) 151.069 (C), 150.504 (C), 149.245 (C), 127.641 (C), 126.467 (C), 126.199 (C), 124.788 (CH), 124.209 (CH), 124.037 (CH), 120.589 (CH), 120.117 (CH), 119.750 (CH), 119.488 (CH), 119.197 (CH), 118.277 (CH), 118.151 (CH), 117.901 (CH)

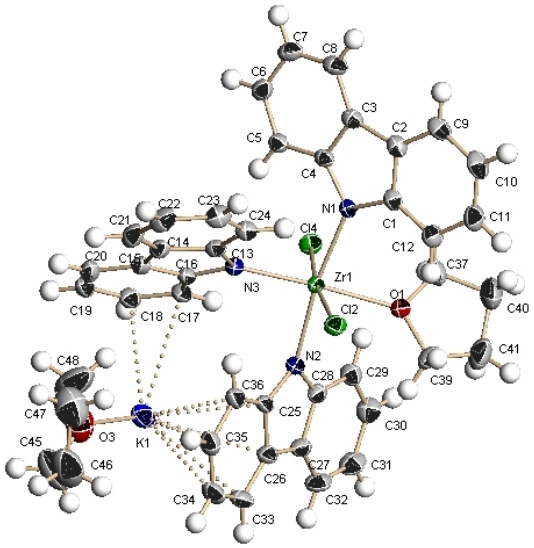


Figure 172: Crystal structure of $ZrCl_2Cb_3THF{\cdot}KTHF$, 12a

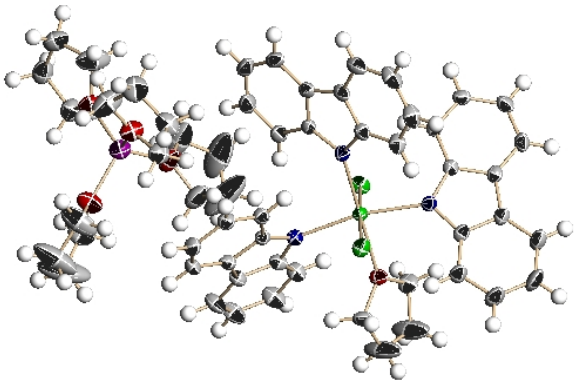


Figure 173: Crystal structure of $ZrCl_2Cb_3THF{\cdot}Li(THF)_4$, 12b

Table 4.1: Correlation NMR data for 12a.

^{1}H position	^{13}C *(ppm)*	^{1}H *(ppm)*	M	^{2}J *(*Hz*)*	^{3}J *(*Hz*)*	COSY / TOCSY	NOESY (exchange)
1a	120.12	7.51	d	8.2	N/A	2a	4a, **1c**
2a	124.79	6.61	m	-	-	1a, 3a	3a, **2c**
3a	124.04	6.38	t	7.6	7.6	2a, 4a	2a, **2c**
4a	120.59	6.83	d	8.4	N/A	3a	1a, **1c**
1b/4b	118.15	7.69	d	7.5	N/A	4b, 1b, 3b, 2b	**4c**
2b	119.49	6.71	t	7.3	7.3	3b, 1b/4b	3b, **3c**
3b	117.90	6.62	m	-	-	2b, 1b/4b	2b, **3c**
1c	119.75	8.28	d	8.38	N/A	2c	**1a**, **4a**
2c	124.21	7.24	t	7.6	7.60	1c, 3c	**2a**, **3a**
3c	118.28	7.00	t	7.1	7.10	2c, 4c	**2b**, **3b**
4c	119.20	7.90	d	7.40	N/A	3c	**1b/4b**

Bold numbers indicate peaks outside of the spin system of the carbazole molecule.

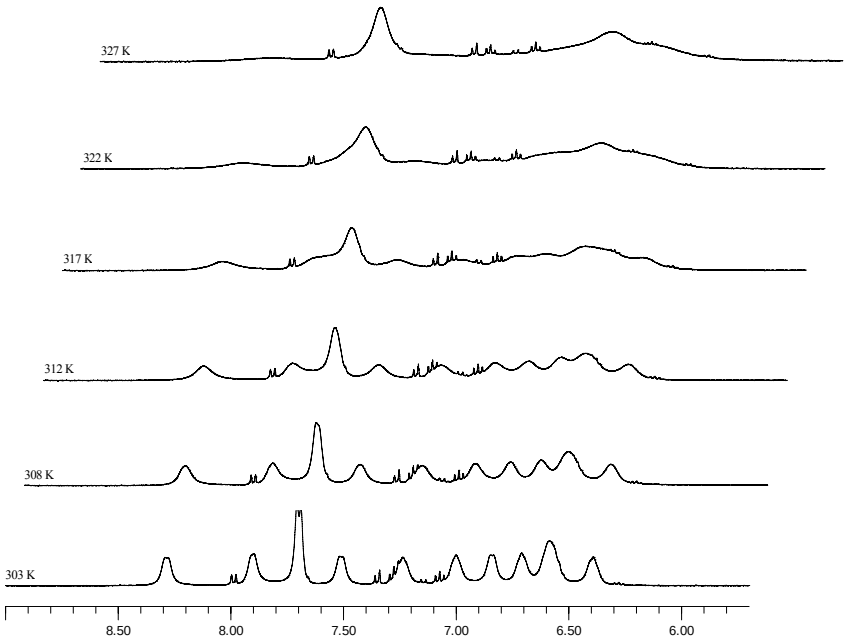


Figure 174: High VT NMR of 12a.

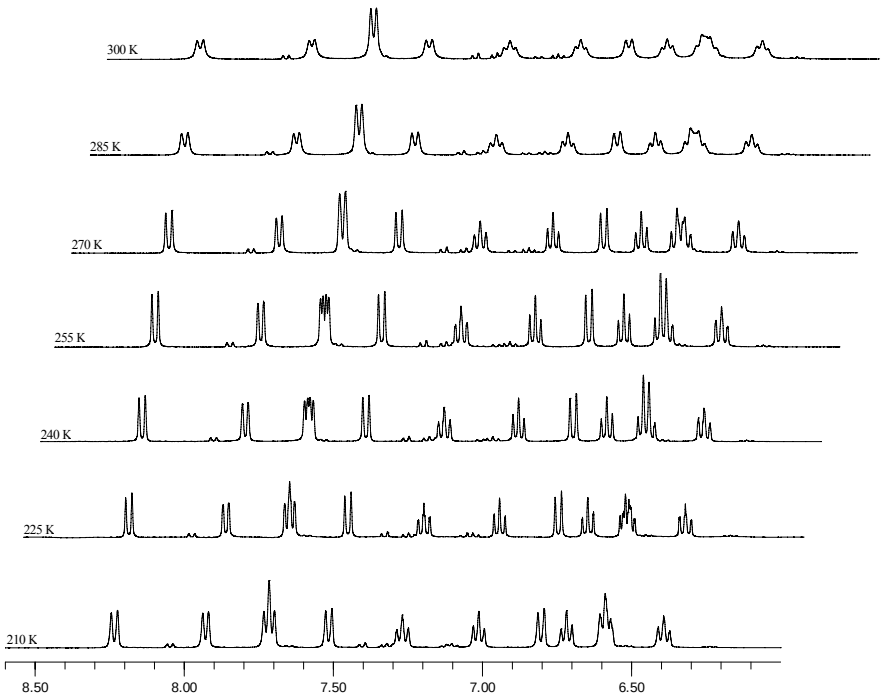


Figure 175: Low VT NMR of 12a.

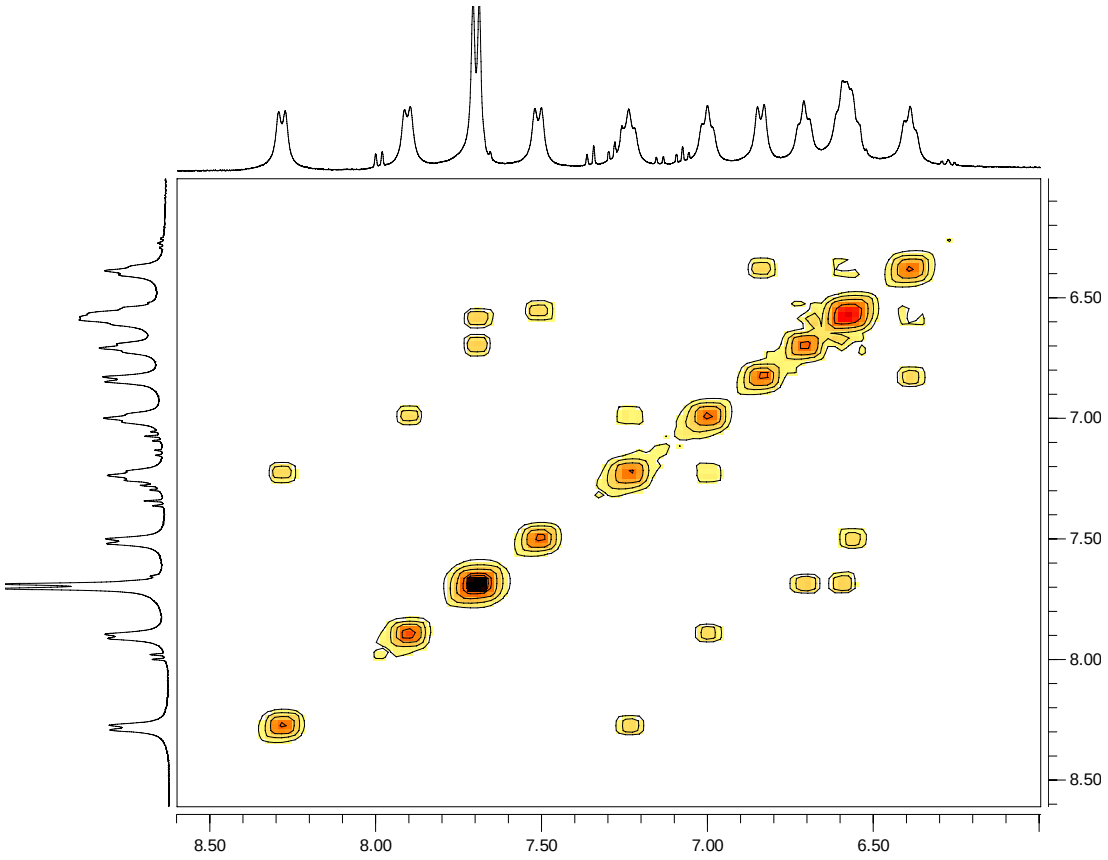


Figure 176: COSY of 12a.

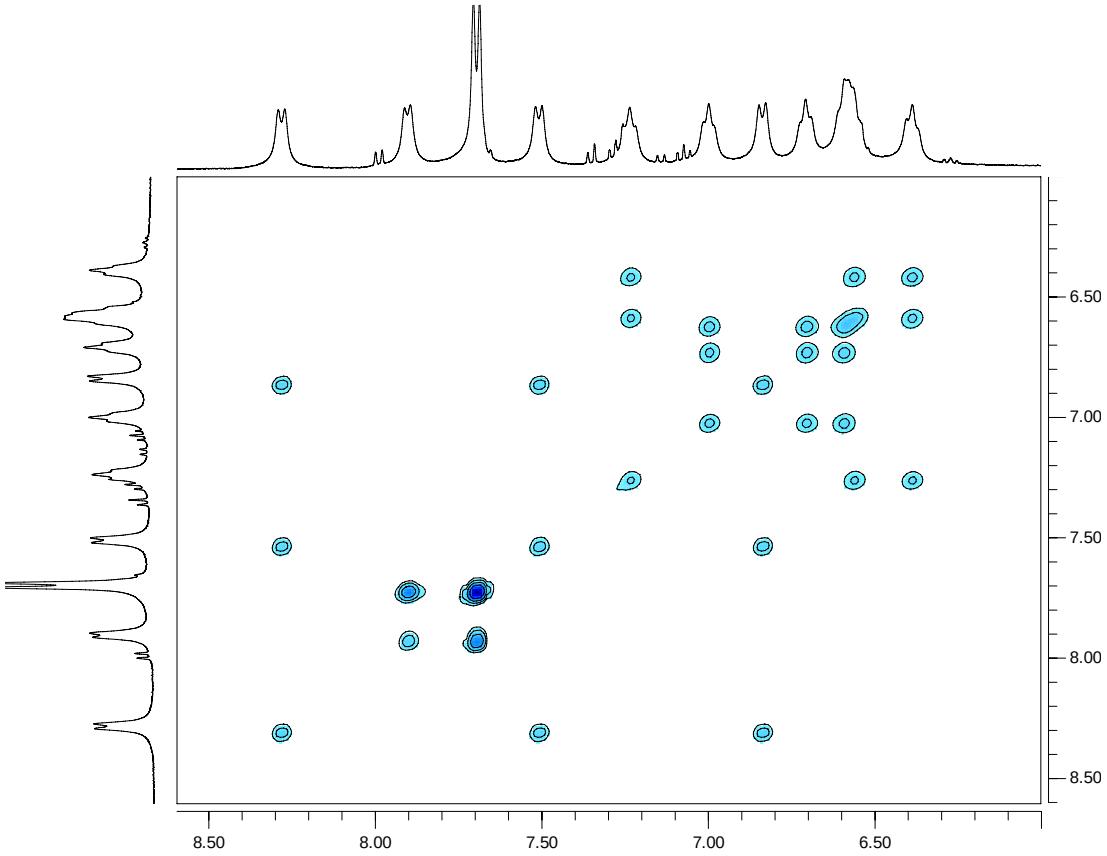


Figure 177: NOESY of 12a.
Mixing Time is 0.7sec

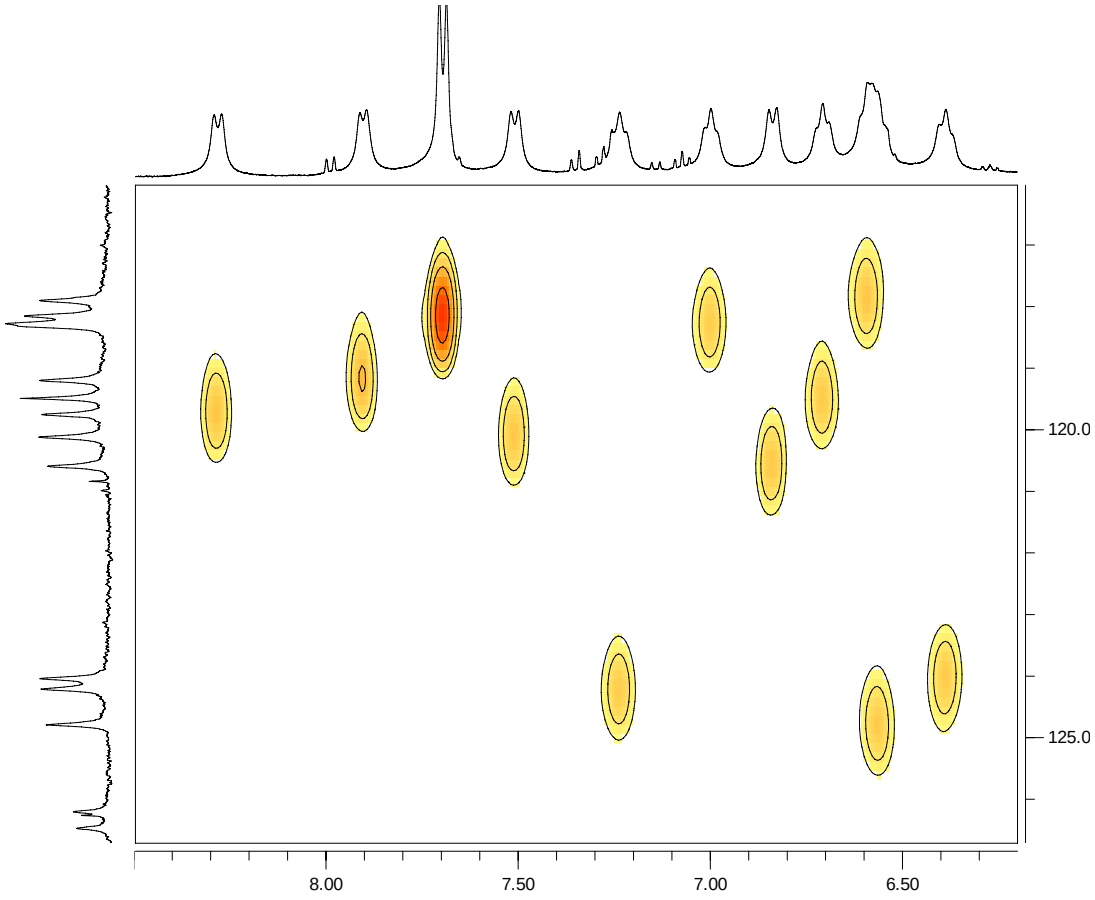


Figure 178: HMQC of 12a.

These VT studies show that two processes seem to be occurring at the high temperature limit. The most deshielded process appears to have a correlation temperature at 33°C and the other process appears to have a correlations temperature at 45°C. This indicates hindered rotation and isomerization at low temperature but ligand dissociation and pseudo-rotation at high temperature.

Figure 179 shows the predicted structures of the molecule according to NMR. The proton and carbon NMR spectra are given in Figure 180. The crystal structure is given in Figure 181. Relevant correlational data are given in Table 4.2. Figure 182 shows the T_1 relaxation study. Figure 183 and Figure 184 show the VT studies. The HMQC is given in Figure 185. A diagram showing the nature of the fluxionality of the molecule at two different temperatures is shown in Figure 186.

4.6.2 Carbazole NMR spectroscopy of various derivatives

4.6.3 Experimental

4.6.3.1 3-Methyl-2, 3, 4, 4a, 9, 9a-hexahydro-1H-carbazole, 14

In a 500 mL round bottom flask, 21.6 g (0.19 mol) of 4-methylcyclohexanone was weighed and a minimum amount of acetic acid (100 mL) was added. Then, 22.43 g (0.20 mol) of phenyl hydrazine were weighed and added. A distillation column was added and the acetic acid was refluxed at 100 °C for three hours during which time the reaction mixture turned bright red. As the mixture cooled, the entire mixture solidified. The product was removed and placed on a filter funnel and washed with water and a small amount of cold ethanol. The product was recrystallized in ethanol.

*4.6.3.2 3-*Tert*-butyl-1,2,3,4-tetrahydrocarbazole, 16*

In a 500 mL round bottom flask, 34 g (0.22 mol) of 4-*tert*-butylcyclohexanone was placed and a minimum amount of acetic acid (80 mL) was added. Then, 24 g (0.22 mol) of phenylhydrazine were weighed and added. A distillation column was added and the acetic acid was refluxed at 100 °C for three hours during which time the reaction mixture turned bright red. As the mixture cooled, the entire mixture solidified. The

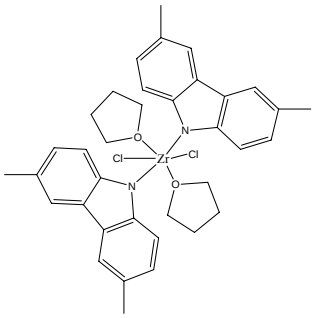


Figure 179: Structure of 13a according to NMR.

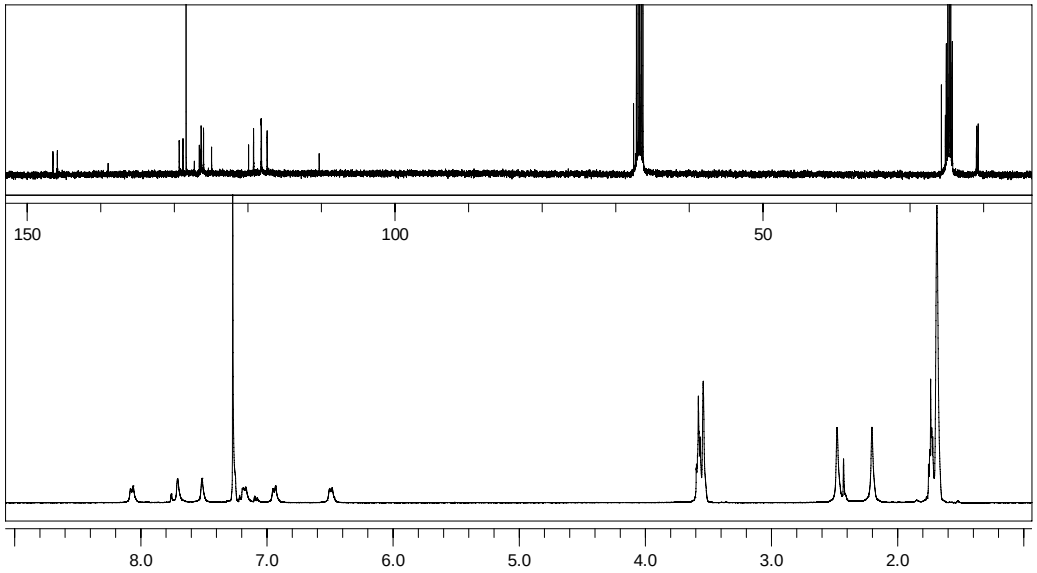


Figure 180: Carbon and proton spectra of 13a.

^{1}H-NMR (400 MHz) δ 8.06 (d, *J* = 8.3 Hz, 1H) 7.71 (s, 1H) 7.52 (s, 1H) 7.18 (d, *J* = 8.3 Hz, 1H) 6.94 (d, *J* = 8.5 Hz, 1H) 6.49 (d, *J* = 8.5 Hz, 1H) 3.54 (s, 8H) 2.48 (s, 3H) 2.21 (s, 3H) 1.69 (s, 8H) ^{13}C-NMR (400 MHz) δ 146.49 (C), 145.90 (C), 129.33 (C), 128.82 (C), 126.51 (C), 126.35 (CH), 126.01 (CH), 124.92 (C), 119.22 (CH), 118.19 (CH), 118.16 (CH), 117.38 (CH), 67.56 (CH_2), 25.73 (CH_2), 20.95 (CH_3), 20.74 (CH_3)

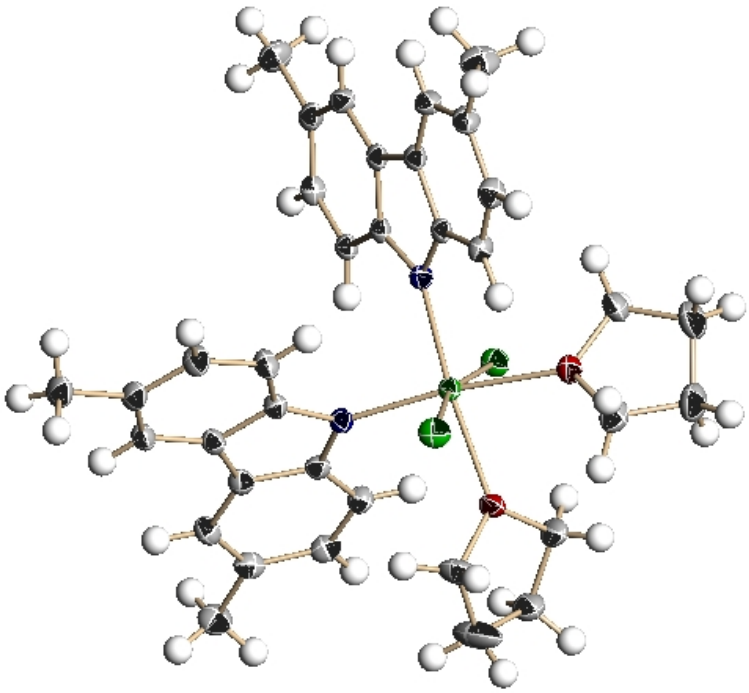


Figure 181: Crystal structure of 13a.

Table 4.2: Correlations for 13a.

^{1}H position	^{13}C *(ppm)*	^{1}H *(ppm)*	m	^{2}J *(Hz)*
1a	117.38	8.06	d	8.3
2a	126.03	7.18	d	8.3
4a	119.22	7.71	s	-
1b	118.16	6.94	d	8.5
2b	126.35	6.49	d	8.5
4b	118.19	7.52	s	-
5	20.95	2.48	s	-
5’	20.74	2.21	s	-

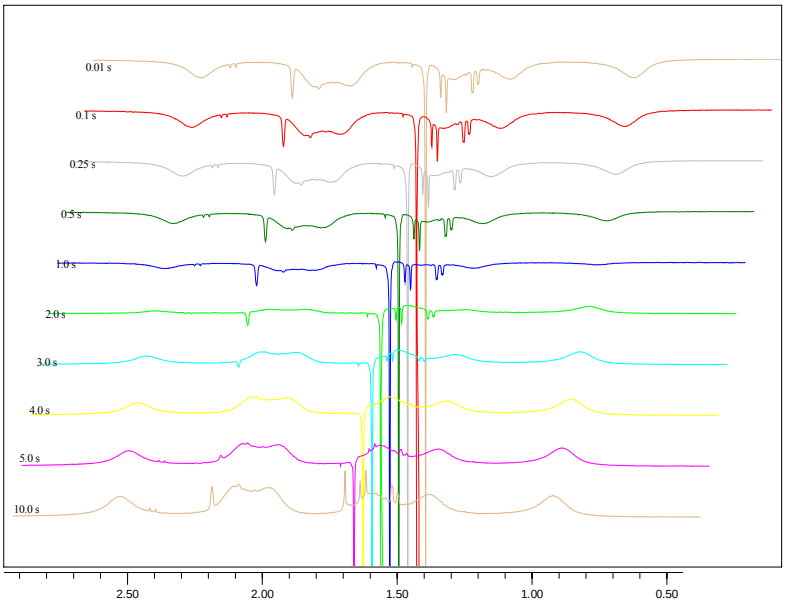


Figure 182: T_1.study of 13a.

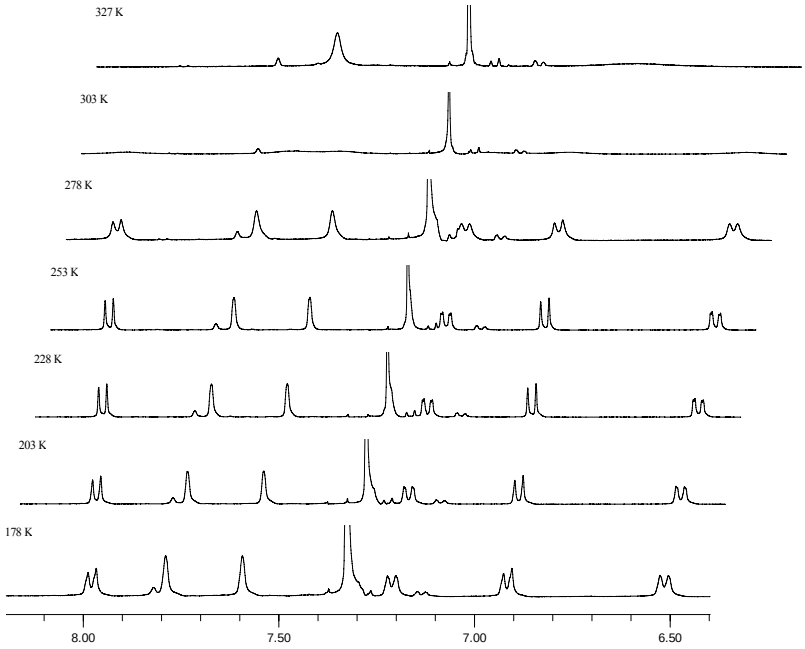


Figure 183: Expansion VT NMR of 13a.

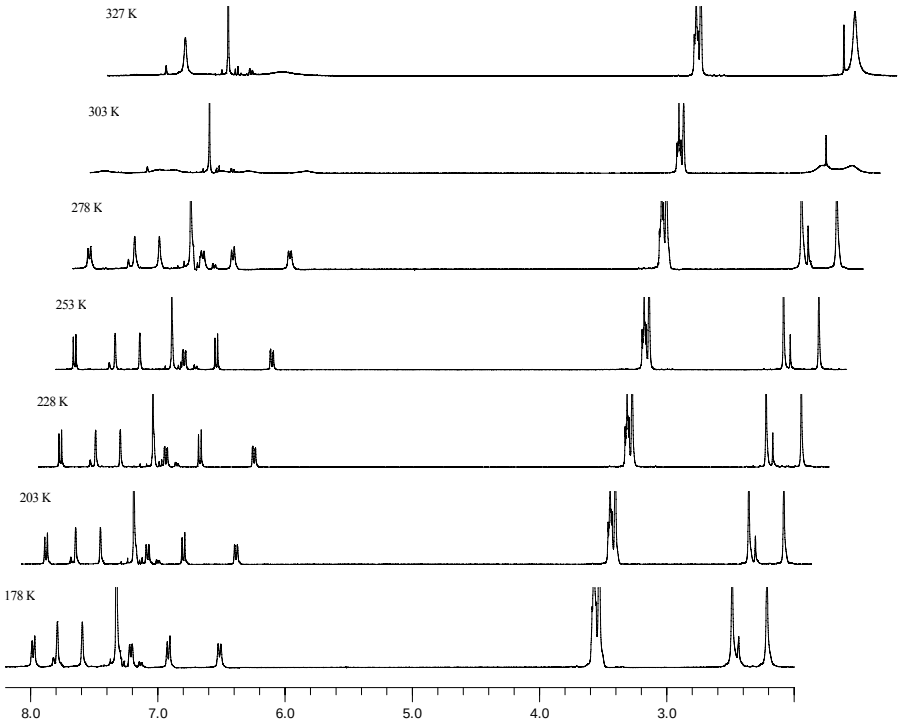


Figure 184: VT of 13a.

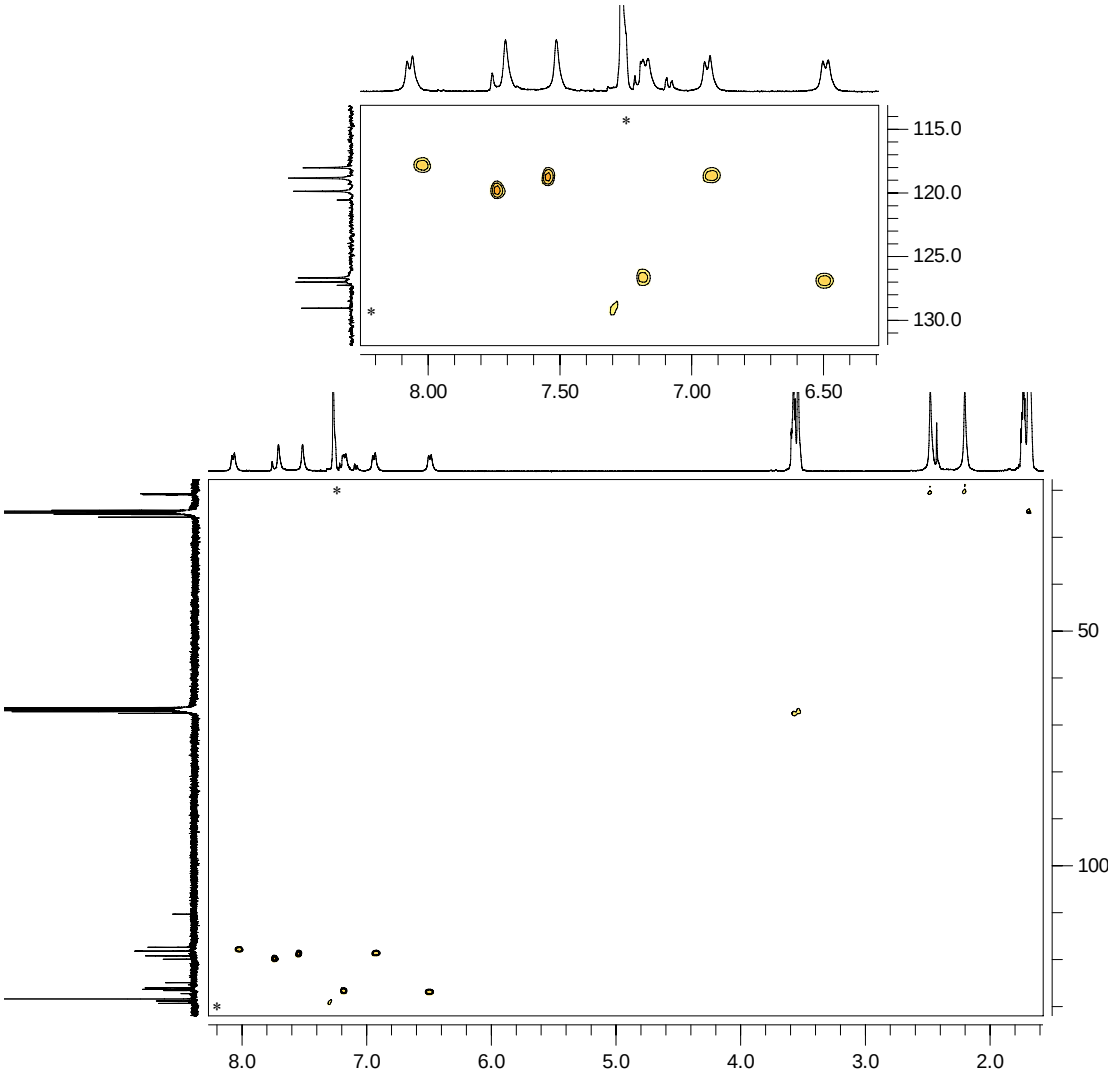


Figure 185: HMQC of 13a.

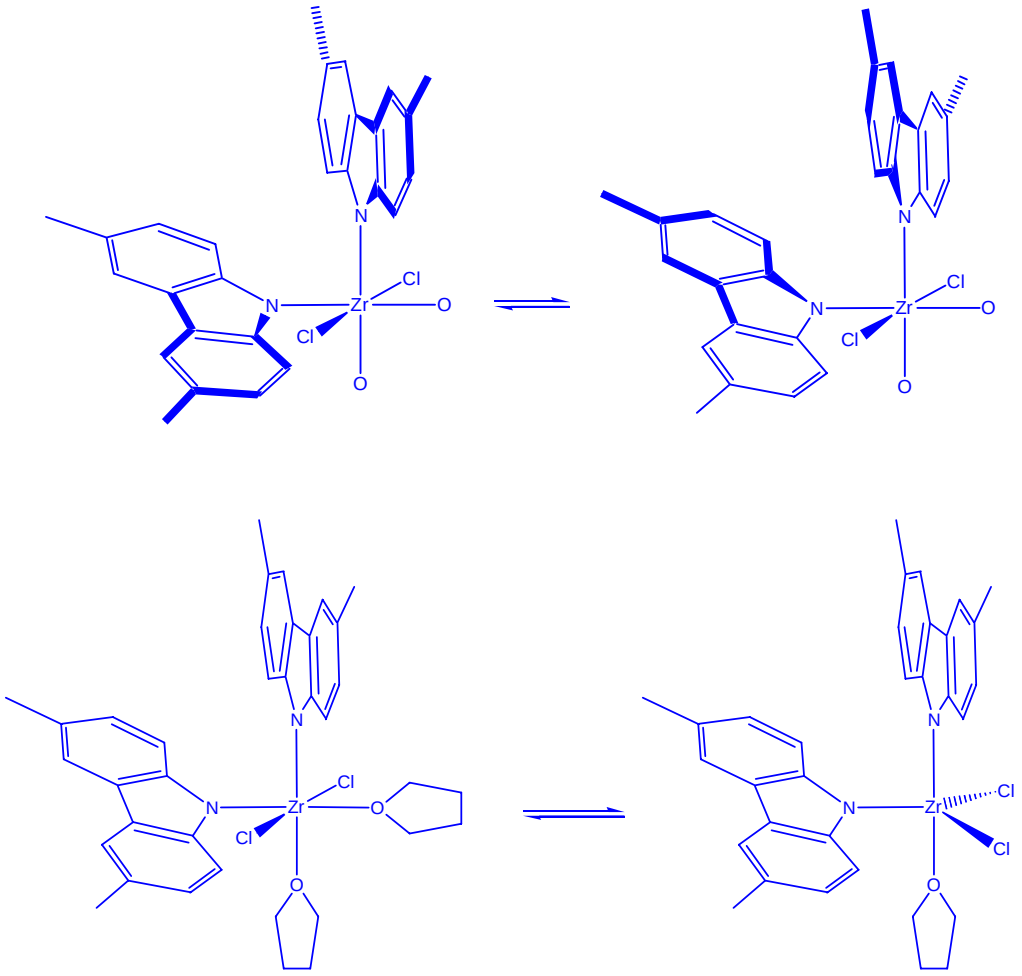


Figure 186: Fluxionality of dimethyl species.

product was removed and placed on the filter funnel and washed with water and a small amount of cold ethanol. The product was recrystallized in ethanol.

4.6.3.3 3,6-Dimethyl-1,2,3,4-tetrahydrocarbazole, 18

In a 50 mL round bottom flask, 0.9 g (0.007 mol) of 4-methylcyclohexanone was weighed and 1 g (0.006 mol) of tolylhydrazinium hydrochloride and 4 mL of methanol was added. This mixture was heated until the reaction mixture began to emit gas (about 30 seconds). Then, the flask was immediately placed in an ice bath as the reaction continued during which time the reaction turned dark red. The methanol was removed by vacuum and the reaction mixture was washed with water to remove all salt. The product was then recrystallized from ethanol.

4.6.3.4 3-Methyl-6-tert-butyl-1,2,3,4-tetrahydrocarbazole, 20

This procedure was the same as given in section 4.6.3.4 except that 4-*tert*-butylcyclohexanone was used instead of 4-methylcyclohexanone.

4.6.3.5 6,8-Dimethyl-1,2,3,4-tetrahydrocarbazole, 22

This procedure was the same as given in section 4.6.3.4 except that cyclohexanone was used instead of 4-methylcyclohexanone and 2,4-dimethylphenylhydrazinium hydrochloride was used instead of tolylhydrazinium hydrochloride. An oil resulted from this reaction.

4.6.3.6 3,6,8-Trimethyl-1,2,3,4-tetrahydrocarbazole, 23

This procedure was the same as given in section 4.6.3.4 except that 2,4-dimethylphenylhydrazinium hydrochloride was used instead of tolylhydrazinium hydrochloride. An oil resulted from this reaction.

*4.6.3.7 3-*Tert*-butyl-6,8-dimethyl-1,2,3,4-tetrahydrocarbazole, 24*

This procedure was the same as given in section 4.6.3.6 except that 4-*tert*-butylcyclohexanone was used instead of 4-methylcyclohexanone. An oil resulted from this reaction.

4.6.3.8 Tetrahydrocarbazole to carbazole conversion

A Schlenk flask was charged with 0.1 mmol of carbazole and 0.11 mmol of Pd/C. The flask was then heated under argon on a Schlenk line for 3-12 hours at the minimum melting temperature of the tetrahydrocarbazole. Because carbazole derivatives typically have a lower melting point in many cases than the tetrahydrocarbazole derivatives, the product carbazole began to sublime up the side of the container. When no further product appeared to be subliming, the reaction was stopped and product was collected from the sides of the flask. Because the reaction occurred with carbon, these were very pure but contained small quantities of carbon. The solid was dissolved in ethyl acetate and then filtered over silica. This last step was repeated two times. Additionally, the remaining Pd/C and product was stirred with ethyl acetate and also filtered over a silica filter. The ethyl acetate was evaporated and the product was recrystallized from ethyl acetate/hexanes.

4.6.3.9 Generic carbazole deprotonation

A Schlenk flask was charged with 0.1 mmol of carbazole or carbazole derivative and a large excess (usually on the order of 0.4 mmol) of potassium hydride. Both the flask and THF, which had been dried over potassium metal, were cooled to -78 °C using a carbon dioxide/acetone bath. The THF was transferred *via* canula slowly at -78 °C. The reaction was allowed to warm to room temperature and stirred overnight. Hydrogen gas was initially evolved at a high rate from the reaction and the reaction became slightly fluorescent and yellow as the reaction proceeded. The product was filtered using glass filter paper attached to a filter canula. The solid was washed three times and the mother liquor was retained. The THF was removed by vacuum and the product was washed with pre-dried hexanes. The hexanes were evaporated and resultant powder was stored in a glovebox. The NMR NH peak was removed as a result of this procedure.

4.6.3.10 Synthesis of 12

A Schlenk flask was charged with a 1:3 ratio of zirconium(IV) chloride to deprotonated carbazole. Both the flask and THF which had been dried over potassium metal were cooled to -78 °C using a carbon dioxide/acetone bath. The THF was

transferred *via* canula slowly at -78 °C. The reaction was allowed to warm to room temperature and stirred for an hour. At close to 0 °C, a vibrant yellow solution had quickly resulted. The product was filtered using glass filter paper attached to a filter canula. The solid was washed three times and the mother liquor was retained. The THF was removed by vacuum and the product was washed with pre-dried hexanes. If more solid salt resulted from the addition of hexanes, the product was filtered again, evaporated, and hexanes were added again and the product was filtered again. After removing the solvent by vacuum, the yellow powder was pumped on overnight and stored in a dry glovebox. The crystals were grown in benzene over a period of weeks. Coordinated THF was in the structure and instead of forming the expected neutral product, a zirconium anion resulted with potassium as the counterion. The potassium chloride was obviously not generated as the additional chloride appears to be attached to the zirconium metal center. The product was *trans*-Dichloro-*cis*-*bis*(3,6-dimethyl-carbazolyl)-*cis*-*bis*(tetrahydrofuran)-zirconium(IV) benzene sesquisolvate.

4.6.3.11 Acquisition and processing parameters for 12a

Both of the 1D proton and carbon spectra for **12a** were obtained on a Bruker Avance 400 MHz spectrometer at room temperature. The proton spectrum was obtained with the following parameters: pulse sequence, *zg30;* spectral width, 4167 Hz; number of scans, 16; relaxation time, 1.0 s; time domain points, 84,960; pulse angle, 90°; multiplied by the exponential function with line broadening 0.3 Hz; and Fourier transformed. The carbon spectrum was obtained with the following parameters: pulse sequence, *zgdc;* spectral width, 26,667 Hz; number of scans, 1024; relaxation time, 2.0 s; time domain points, 65536; pulse angle, 90°; with proton decoupling using the WALTZ-16 sequence; multiplied by the exponential function with line broadening 1.0 Hz; and Fourier transformed.

The T_1 relaxation study was obtained on a Bruker Avance 400 MHz spectrometer. The pulse sequence used was *tlir* with the following parameters: spectral width, 4167 Hz; number of scans, 8; relaxation times used were : 10.0 s, 5.0 s, 4.0 s, 3.0 s, 2.0 s, 1.0 s, 0.5 s, 0.25 s, 0.10 s, 0.05 s, 0.01 s; time domain points, 8192; pulse angle, 90°;

multiplied by the exponential function with line broadening of 0.5 Hz; and Fourier transformed.

The HMQC spectrum was obtained on a Bruker Avance 400 MHz spectrometer at room temperature using the following parameters: pulse program, *invist*, spectral widths of 4167 and 84,960 Hz in the ^{1}H and ^{13}C dimensions, respectively; relaxation time, 3.0 s; time domain points, 1000; number of scans, 16; 256 FIDS were collected. The resulting data points were multiplied by a sine squared window function shifted by $\pi/2$ along both dimensions and double Fourier transformed.

The COSY spectrum was obtained on a Bruker Avance 400 MHz spectrometer at room temperature with the following parameters: pulse program, cosy45, spectral width in both dimensions of 4167 Hz; 128 FIDS collected; number of transients 8; 3.0 s relaxation delay. The resulting data points were multiplied by an exponential function in the t_2 dimensions with 2.0 Hz line broadening and then Fourier transformed. Then, the data points were linear predicted from points 256 to 511 points in the t_1 dimension and multiplied by a sine squared window function shifted by $\pi/2$; Fourier transformed; and symmetrized.

The NOESY spectrum was obtained on a Bruker Avance 400 MHz spectrometer at room temperature with the following parameters: pulse program, noesytp, spectral width in both dimensions of 4167 Hz; 256 FIDS collected; number of scans 32; 3.0 s relaxation delay, 0.70 second mixing time. Phase sensitive data points were obtained. The resulting data points were multiplied by an exponential function in the t_2 dimensions with 2.0 Hz line broadening and then Fourier transformed. Then, the data points were multiplied by a sine squared window function shifted by $\pi/2$; Fourier transformed; and symmetrized.

4.6.3.12 Synthesis of 13

A procedure identical to that described in section 4.6.3.10 was used except that deprotonated dimethylcarbazole was one starting material instead of unsubstituted carbazole. A ratio of 1:3 zirconium(IV) chloride and substituted carbazole was used. Unlike the previous product, a neutral species resulted with one less substituted carbazole than was added. Analysis of the mother liquor after crystallization indicated that

protonated carbazole was present. It may be that due to the steric strain of the methyl groups, there was not room for all three ligands to remain on the metal center. The product was (Tetrahydrofuran)potassium *mer*-*trans*-tris(carbazolyl)dichloro-(tetrahydrofuran)zirconate.

4.6.3.13 Acquisition and processing parameters for 13a

Both of the 1D proton and carbon spectra for **13a** were obtained on a Bruker Avance 400 MHz spectrometer at room temperature. The proton spectrum was obtained with the following parameters: pulse sequence, *zg30;* spectral width, 4401 Hz; number of scans, 16; relaxation time, 1.0 s; time domain points, 65536; pulse angle, 90°; multiplied by the exponential function with line broadening 0.3 Hz; and Fourier transformed. The carbon spectrum was obtained with the following parameters: pulse sequence, *zgdc;* spectral width, 84,960 Hz; number of scans, 1024; relaxation time, 2.0 s; time domain points, 65536; pulse angle, 90°; with proton decoupling using the WALTZ-16 sequence; multiplied by the exponential function with line broadening 1.0 Hz; and Fourier transformed.

The T_1 relaxation study was obtained on a Bruker Avance 400 MHz spectrometer. The pulse sequence used was *tlir* with the following parameters: spectral width, 4401 Hz; number of scans, 8; relaxation times used were : 10.0 s, 5.0 s, 4.0 s, 3.0 s, 2.0 s, 1.0 s, 0.5 s, 0.25 s, 0.10 s, 0.05 s, 0.01 s; time domain points, 8192; pulse angle, 90°; multiplied by the exponential function with line broadening of 0.5 Hz; and Fourier transformed.

The HMQC spectrum was obtained on a Bruker Avance 400 MHz spectrometer at room temperature using the following parameters: pulse program, *inv4tp*, spectral widths of 4401 and 84,960 Hz in the ^{1}H and ^{13}C dimensions, respectively; relaxation time, 1.5 s; time domain points, 1000; number of scans, 16; 256 FIDS were collected. The resulting data points were multiplied by a sine squared window function shifted by $\pi/2$ along both dimensions and double Fourier transformed.

4.6.3.14 Carbazole spectroscopy

A series of carbazole derivatives were synthesized. The proton and carbon spectra for these different species is shown in Figure 187 - Figure 207. Synthetic schemes follow in Figure 208 - Figure 217.

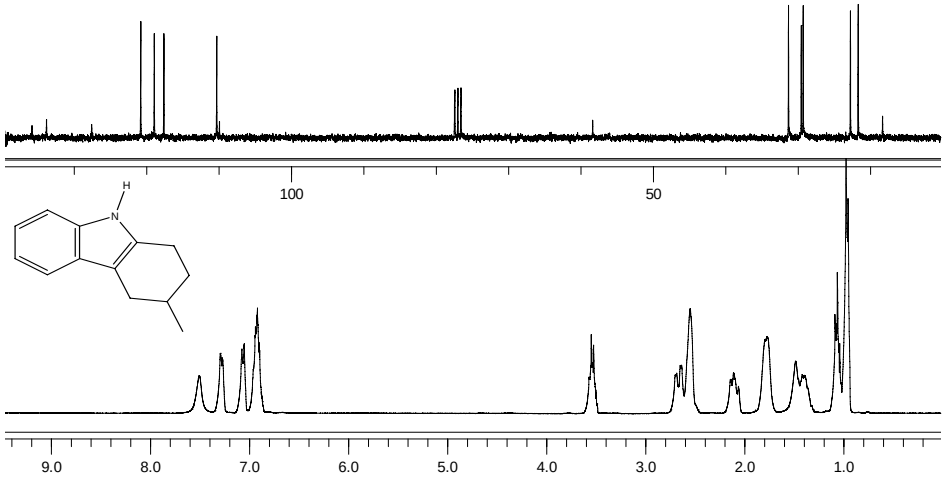


Figure 187: Proton and carbon spectra of 14 in $CDCl_3$.

^{1}H NMR (300 MHz, $CDCl_3$, 25 °C) δ7.506 (b, 1H), 7.284 (d, *J* = 6 Hz, 1H), 7.053-7.082 (m, 1H), 6.898-6.944 (m, 2H), 2.669 (dd, *J* = 4.5 Hz, 15.3 Hz, 1H), 2.551 (b, 2H), 2.063-2.1145 (m, 1H), 1.780 (m, 2H), 1.360-1.420 (m, 1H), 0.968 (d, *J* = 6.3 Hz, 3H) ^{13}C NMR (300 MHz, $CDCl_3$, 25 °C) δ135.865 (C), 133.842 (C), 127.601 (C), 120.818 (CH), 118.951 (CH), 117.619 (CH), 110.323 (CH), 109.944 (C), 31.331 (CH_2), 29.567 (CH), 29.301 (CH_2), 22.779 (CH_2), 21.702 (CH_3)

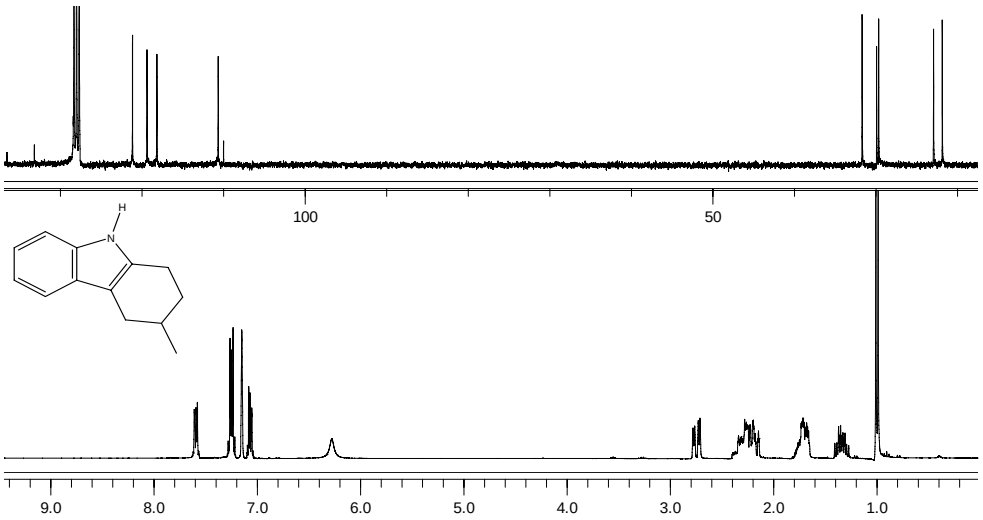


Figure 188: Proton and carbon spectra of 14 in C_6D_6.

^{1}H NMR (300 MHz, C_6D_6, 25 °C) δ7.595 (m, 1H), 7.250 (m, *J* = 1.8 Hz, *J* = 3.6 Hz, 2H), 7.072 (m, *J* = 2.8 Hz, *J* = 5.7 Hz, 1H), 6.278 (b, 1H), 2.740 (dd, *J* = 5.4 Hz, *J* = 15.6 Hz, 1H), 2.141-2.347(m, 3H), 1.661-1.765 (m, 2H), 1.34 (dddd, *J* = 2.1 Hz, 6.3 Hz, 11.1 Hz, 13.2 Hz, 1H), 1.005 (d, *J* = 6.6 Hz, 3H) ^{13}C NMR (300 MHz, C_6D_6, 25 °C) δ136.57, 133.195, 121.162, 119.384, 118.165, 110.653, 109.992, 31.695, 29.919, 29.670, 22.939, 21.867

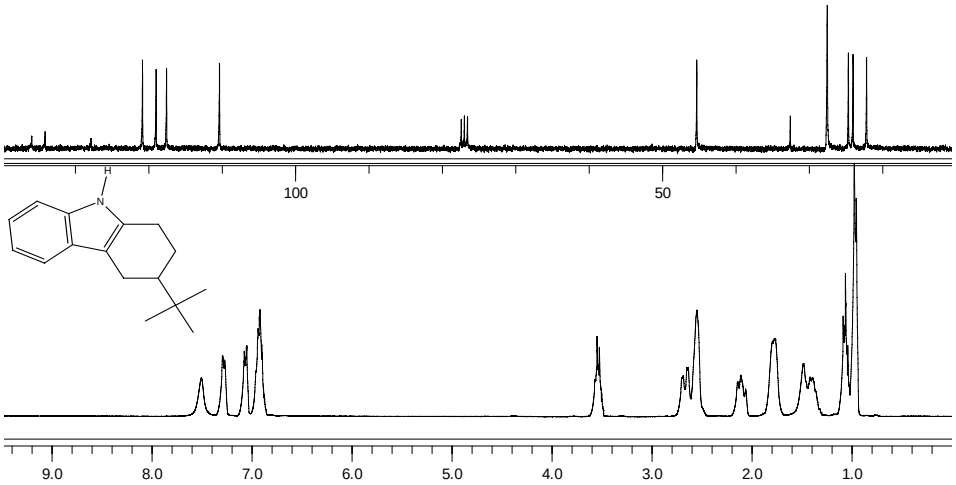


Figure 189: Proton and carbon spectra of 16 in $CDCl_3$.

^{1}H NMR (300 MHz, $CDCl_3$, 25 °C) δ7.534 (b, 2H), 7.260 (m, 1H), 7.144 (m, 2H), 2.756-2.886 (m, 3H), 2.463 (d, J = 6.3 Hz, 1H), 2.145 (m, 1H), 1.574 (m, 2H), 1.047 (s, 9H) ^{13}C NMR (300 MHz, $CDCl_3$, 25 °C) 135.960 (C), 134.135 (C), 127.871 (C), 120.867 (CH), 119.012 (CH), 117.593 (CH), 110.372 (CH), 45.342 (CH), 32.583 (C), 27.548 (CH_3), 24.680 (CH_2), 24.039 (CH_2), 22.195 (CH_2)

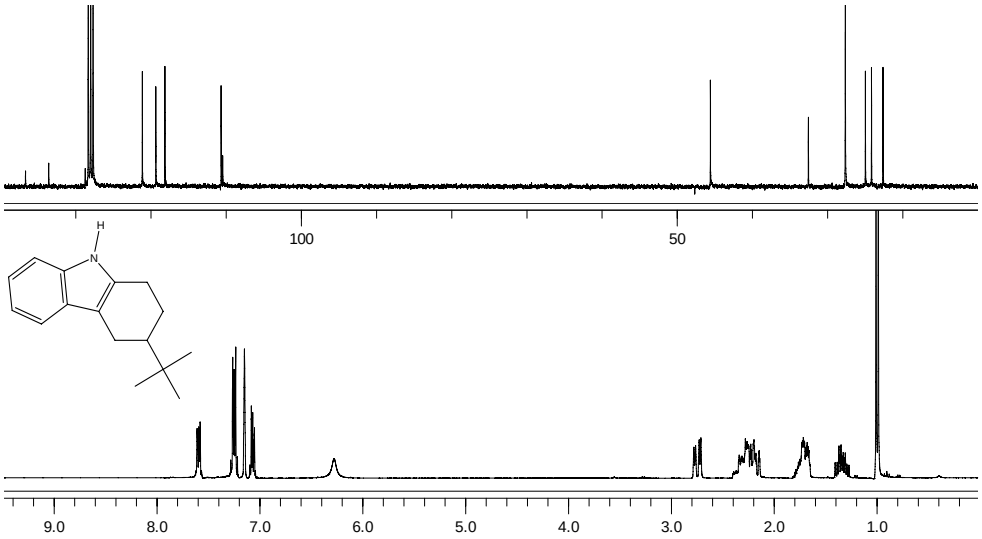


Figure 190: Proton and carbon spectra of 16 in C_6D_6.

^{1}H NMR (300 MHz, C_6D_6, 25 °C) δ7.601 (m, 1H), 7.259 (m, J = 5.1 Hz, J = 2.1 Hz, J = 3.3 Hz, 2H), 7.092 (m, 1H), 6.311 (b, 1H), 2.793 (dd, J = 3 Hz, J = 13.8 Hz, 1H), 2.272-2.382 (m, 3H), 1.823-1.877 (m, 1H), 1.361-1.243 (m, 2H), 0.912 (s, 9H) ^{13}C NMR (300MHz, C_6D_6, 25°C) δ136.685, 133.602, 128.746, 121.147, 119.355, 118.143, 110.669, 110.464, 45.587, 32.549, 27.641, 24.968, 24.155, 22.628

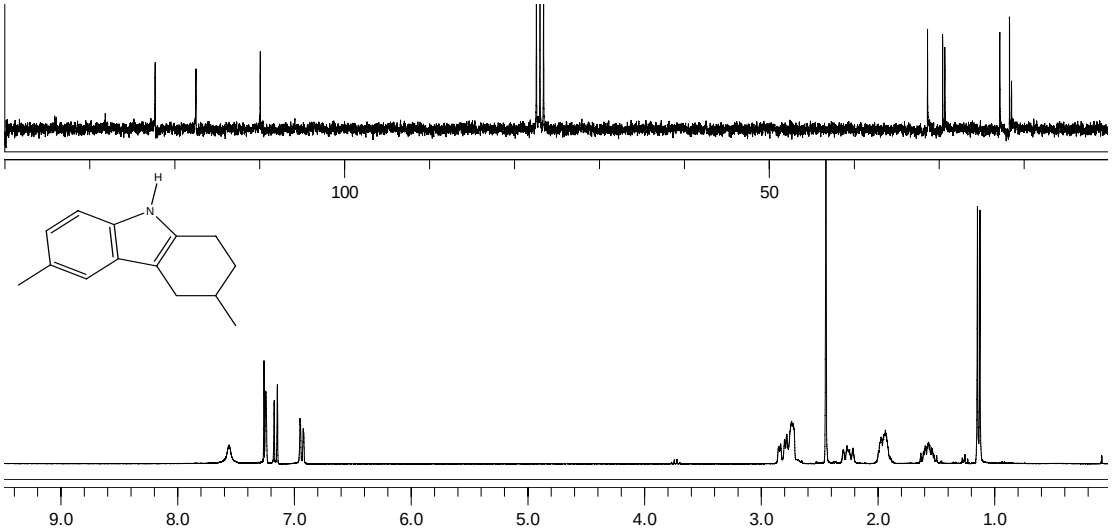


Figure 191: Proton and carbon spectra of 18 in $CDCl_3$.

^{1}H NMR (300 MHz, $CDCl_3$, 25 °C) δ7.559 (b, 1H), 7.224 (b, 1H), 7.160 (d, *J* = 8.4 Hz, 1H), 6.938 (d, *J* = 8.1 Hz, 1H), 2.817 (dd, *J* = 5.1 Hz, 1H), 2.740 (m, 2H), 2.446 (s, 3H), 2.214-2.297 (m, 1H), 1.915-1.995 (m, 2H), 1.497-1.633 (m, 1H), 1.147 (d, *J* = 6.3 Hz, 3H) ^{13}C NMR (300 MHz, $CDCl_3$, 25 °C) δ134.135, 133.945, 128.174, 122.299 (CH), 117.498 (CH), 109.928 (CH), 109.642 (C), 31.376(CH_2), 29.594(CH), 29.343(CH_2), 22.869 (CH_2), 21.726 (CH_3), 21.480 (CH_3)

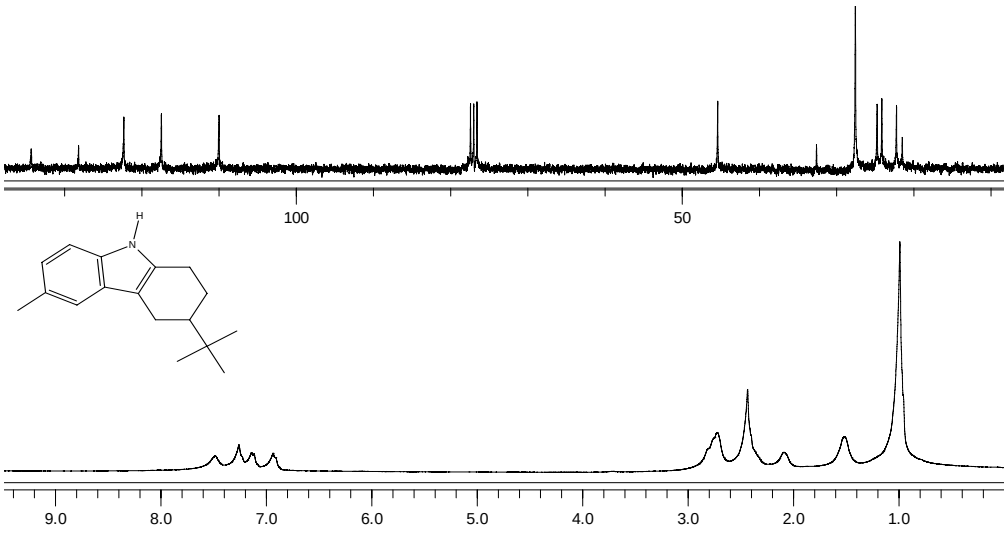


Figure 192: Proton and carbon spectra of 20 in $CDCl_3$.

^{1}H NMR (300 MHz, $CDCl_3$, 25 °C) δ7.486 (b, 1H), 7.260 (b, 1H), 7.129 (d, 7.5 Hz, 1H), 6.325 (d, *J* = 6.9 Hz, 1H), 2.722 (m, 3H), 2.435 (s, 3H), 2.091 (m, 1H), 1.519 (m, 3H), 0.991 (s, 9H) ^{13}C NMR (300 MHz, $CDCl_3$, 25 °C) δ134.324 (C), 134.284 (C), 128.186 (C), 122.327 (CH), 117.462 (CH), 109.987 (CH), 45.404 (CH), 32.601 (C), 27.563 (CH_3), 24.749 (CH_2), 24.140 (CH_2), 22.240 (CH_2), 21.491 (C)

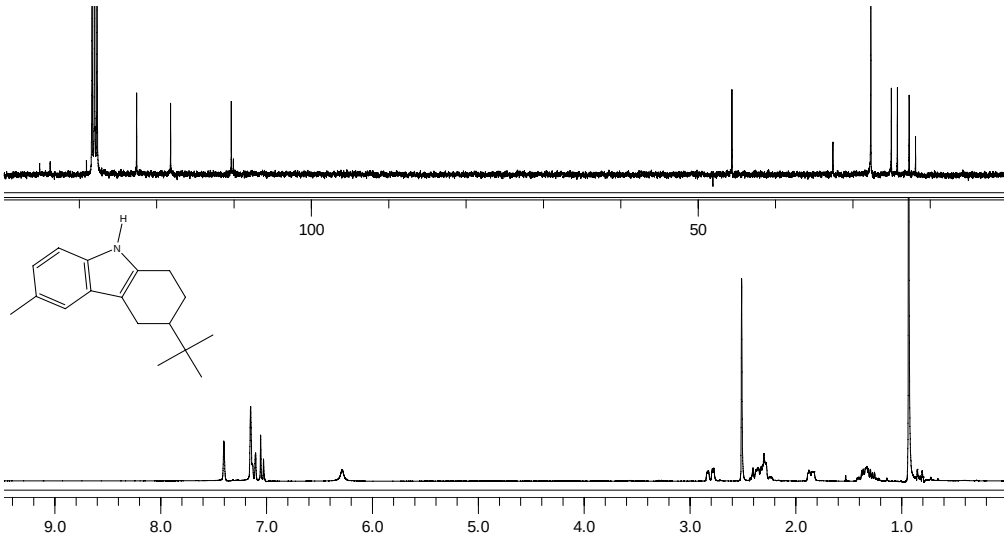


Figure 193: Proton and carbon spectra of 20 in C_6D_6.

^{1}H NMR (300 MHz, C_6D_6, 25 °C) δ7.403 (b, 1H), 7.119 (d, *J* = 9.6 Hz, 1H), 7.042 (d, *J* = 8.4 Hz, 1H), 6.285 (b, 1H), 2.806 (dd, *J* = 4.2 Hz, *J* = 14.7 Hz, 1H), 2.512 (s, 3H), 2.229-2.430 (m, 3H), 1.828-1.876 (m, 1H), 1.217-1.419 (m, 2H), 0.934 (s, 9H) ^{13}C NMR (300 MHz, C_6D_6, 25 °C) δ135.188, 133.753, 129.069, 122.583, 118.189, 110.342, 110.076, 45.627, 32.580, 27.670, 25.022, 24.240, 22.718, 21.892

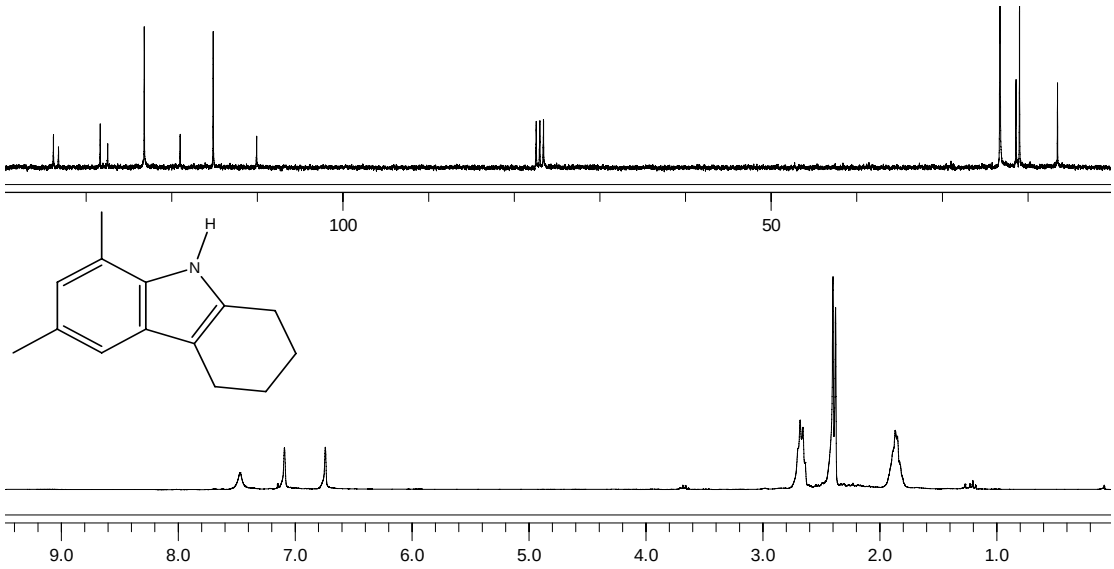


Figure 194: Proton and carbon spectra of 22 in $CDCl_3$.

^{1}H NMR (300 MHz, $CDCl_3$, 25 °C) δ7.470 (b, 1H), 7.091 (s, 1H), 6.741 (s, 1H), 2.670 (m, *J* = 7.2 Hz, 4H), 2.389 (d, *J* = 6.9 Hz, 6H), 1.858 (m, *J* = 5.7 Hz, 4H) ^{13}C NMR (300 MHz, $CDCl_3$, 25 °C) δ133.808, 133.219, 128.348, 127.472, 123.199, 119.006, 115.153, 110.081, 23.244, 23.300, 21.399, 20.986, 16.551

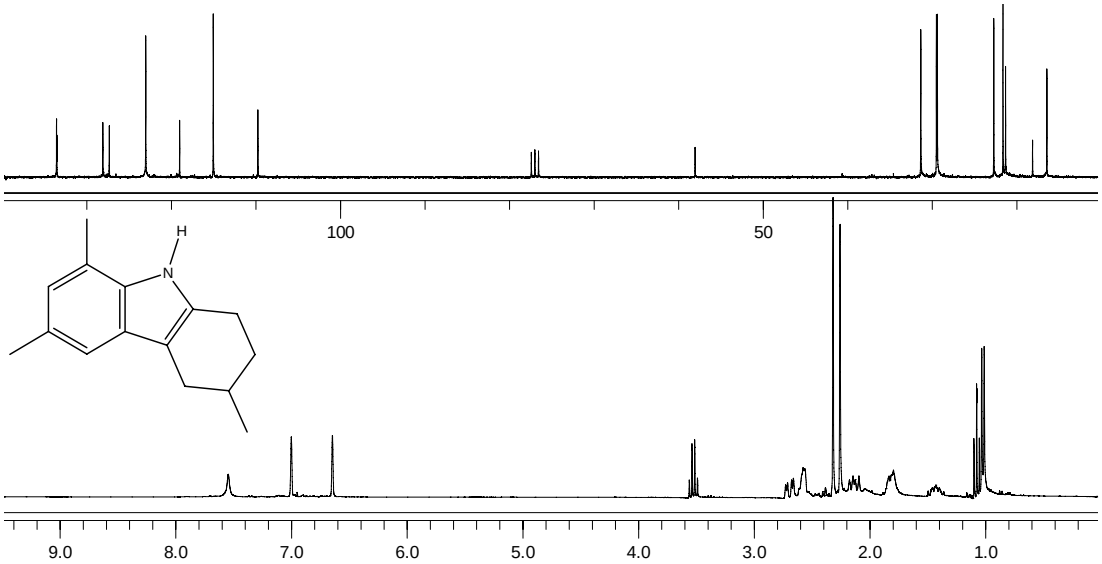


Figure 195: Proton and carbon spectra of 23 in $CDCl_3$.

^{1}H NMR (300 MHz, $CDCl_3$, 25 °C) δ7.547 (b, 1H), 7.002 (s, 1H), 6.646 (s, 1H), 2.695 (dd, J = 5.1 Hz, J = 15.3 Hz, 1H), 2.566 (m, 2H), 2.319 (s, 3H), 2.259 (s, 3H), 2.137 (dd, J = 5.7 Hz, J = 15.3 Hz, 1H), 1.814 (m, 2H), 1.430 (m, 1H), 1.023 (d, J = 6.6 Hz, 3H) ^{13}C NMR (300 MHz, $CDCl_3$, 25 °C) δ133.584 (C), 133.535 (C), 128.098 (C), 127.336 (C), 123.033 (CH), 119.015 (C), 115.043 (CH), 109.769 (C), 31.350 (CH_2), 29.510 (CH), 29.396 (CH_2), 22.722 (CH_2), 21.630 (CH_3), 21.330 (CH_3), 16.436 (CH_3)

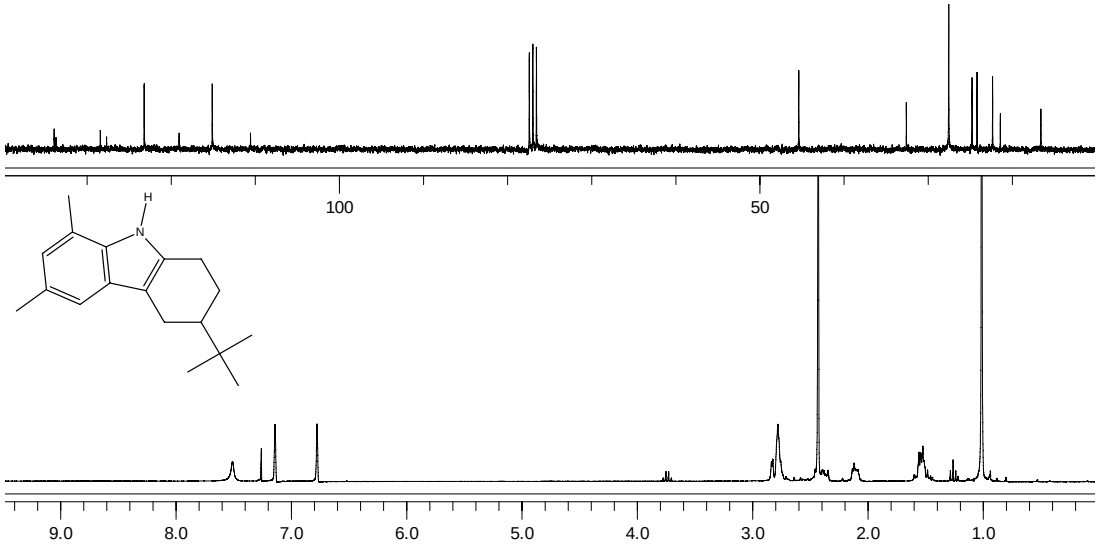


Figure 196: Proton and carbon spectra of 24 in $CDCl_3$.

^{1}H NMR (300 MHz, $CDCl_3$, 25 °C) δ7.510 (b, 1H), 7.141 (s, 1H), 6.777 (s, 1H), 2.831 (d, J = 3.6 Hz, 1H), 2.781 (b, 2H), 2.431 (s, 6H), 2.079-2.135 (m, 1H), 1.483-1.599 (m, 3H) 1.013 (s, 9H) ^{13}C NMR (300 MHz, $CDCl_3$, 25 °C) δ133.908 (C), 133.700 (C), 128.419 (C), 127.677 (C), 123.209 (CH), 119.052 (C), 115.116 (CH), 110.571 (C), 45.388 (CH), 32.594 (C), 27.551 (CH_3), 24.783 (CH_2), 24.188 (CH_2), 22.343 (CH_2), 21.416 (CH_3), 16.600 (CH_3)

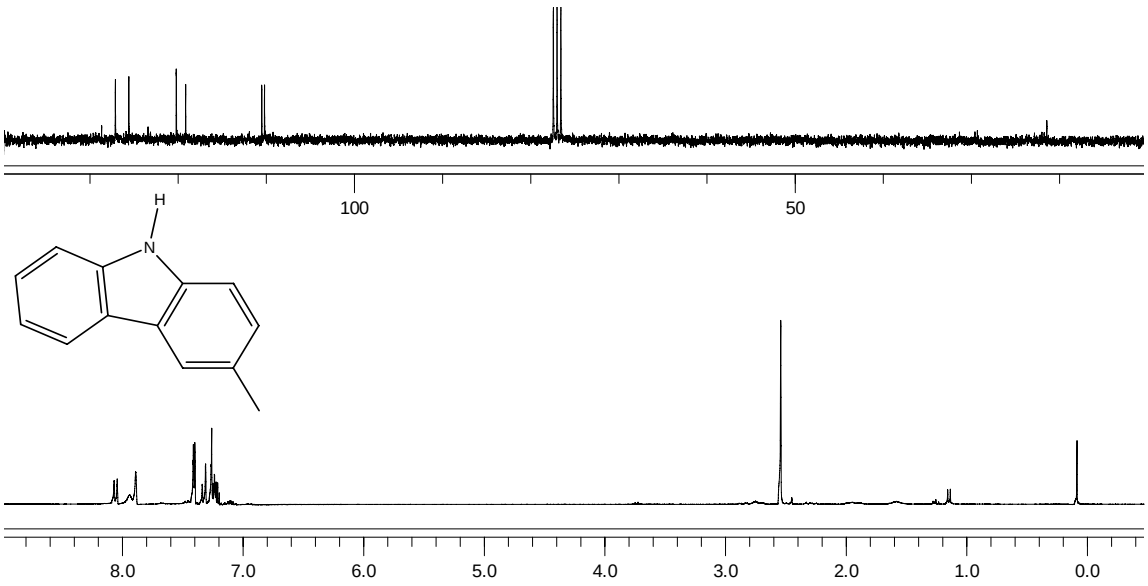


Figure 197: Proton and carbon spectra of 15 in C_6D_6.

^{1}H NMR (300 MHz, 25 °C) δ8.056 (d, *J* = 7.8 Hz, 1H), 7.940 (b, 1H), 7.891 (s, 1H), 7.405 (d, *J* = 3.6 Hz, 2H), 7.324 (d, *J* = 8.4 Hz, 1H), 7.197-7.260 (m, 2H), 2.542 (s, 3H)
^{13}C NMR (300 MHz, $CDCl_3$, 25 °C) δ128.676 (C), 127.118 (CH), 125.592 (CH), 123.411 (C), 120.207 (CH), 119.145 (CH), 110.507 (CH), 110.193 (CH) 21.435 (CH_3)
^{1}H NMR (300 MHz, C_6D_6, 25 °C) δ7.999-8.027 (d, *J* = 7.5 Hz, 1H), 7.788 (b, 1H), 7.325-7.380 (m, 1H), 7.177-7.231 (m, 2H), 6.973-7.053 (m, 2H), 6.488 (b, 1H), 2.402 (s, 3H)

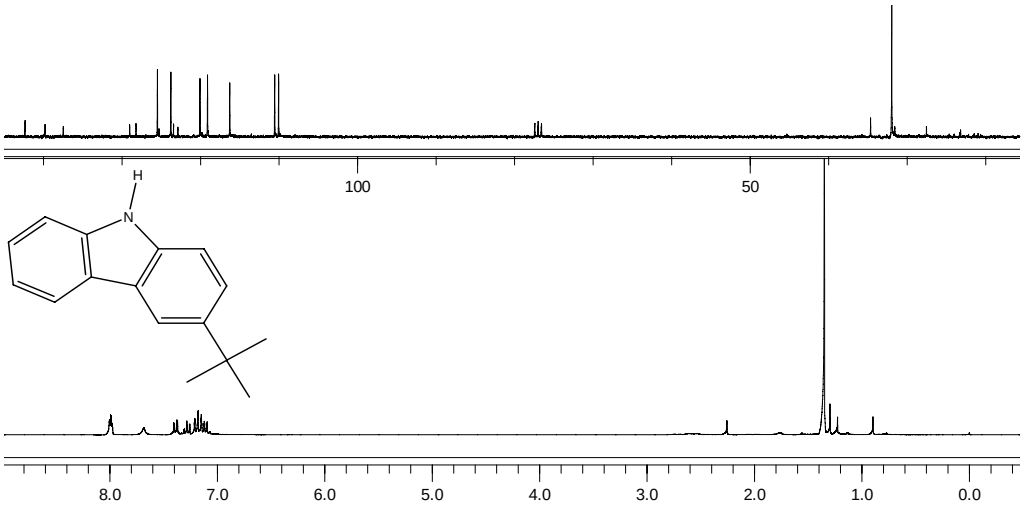


Figure 198: Proton and carbon spectra of 17 in $CDCl_3$.

^{1}H NMR (300 MHz, $CDCl_3$, 25 °C) δ7.973-8.008 (m, 2H), 7.682 (b, 1H), 7.389 (dd, *J* = 2.1 Hz, *J* = 8.7 Hz, 1H), 7.213 (td, *J* = 1.2 Hz, *J* = 7.5 Hz, 1H), 7.094-7.213 (m, 3H), 1.350 (s, 9H) ^{13}C NMR (300 MHz, $CDCl_3$, 25 °C) δ142.349 (C), 139.799 (C), 137.471 (C), 125.483 (CH), 123.776 (CH), 123.434 (C), 122.881 (C), 120.067 (CH), 119.103 (CH), 116.274 (CH), 110.549 (CH), 110.055 (CH), 34.653 (C), 31.966 (CH_3)

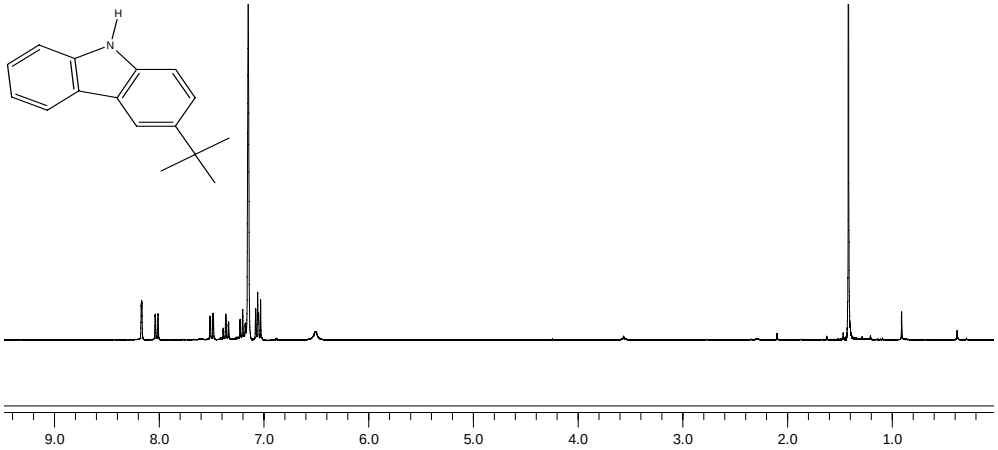


Figure 199: Proton and carbon spectra of 17 in C_6D_6.

^{1}H NMR (300 MHz, C_6D_6, 25 °C) δ8.168 (d, *J* = 1.2 Hz, 1H), 8.024 (d, *J* = 7.8 Hz, 1H), 7.5025 (d, *J* = 8.7 Hz, 1H), 7.364 (t, *J* = 7.2 Hz, 1H), 7.202 (t, *J* = 7.6 Hz, 1H), 7.055 (dd, *J* = 5.7 Hz, 8.2 Hz, 2H), 6.507 (b, 1H), 1.418 (s, 9H)

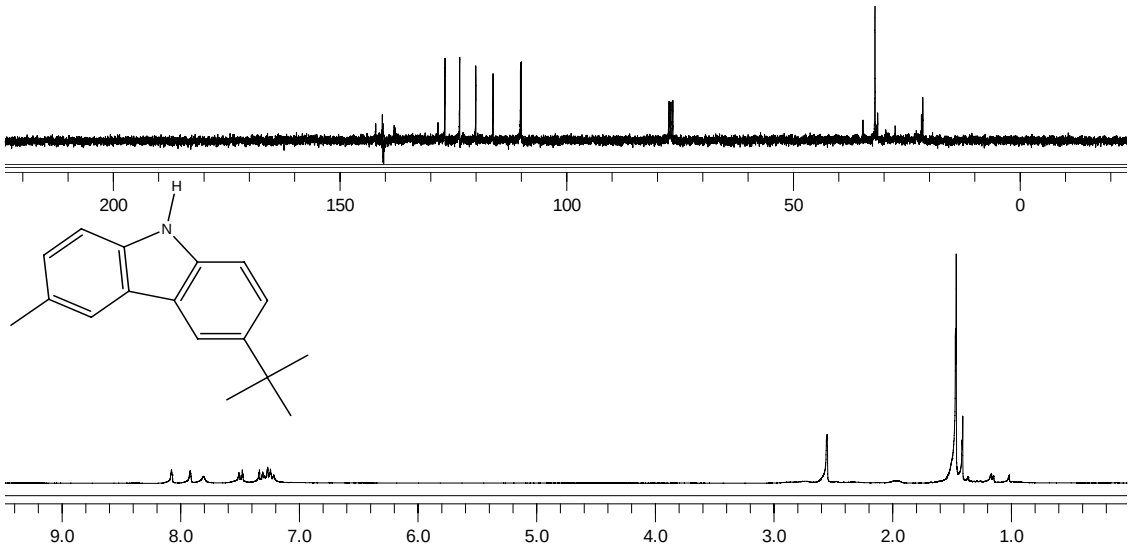


Figure 200: Proton and carbon spectra of 21 in $CDCl_3$.

^{1}H NMR (300 MHz, $CDCl_3$, 25 °C) δ8.076 (s, 1H), 7.917 (s, 1H), 7.806 (b, 1H), 7.497 (d, *J* = 8.7 Hz, 1H), 7.215-7.336 (m, 3H), 2.553 (s, 3H), 1.470 (s, 9H) ^{13}C NMR (300 MHz, $CDCl_3$, 25 °C) δ142.114 (C), 138.059 (C), 127.838 (C), 128.384 (C), 126.837 (CH), 123.589 (CH), 120.048 (CH), 116.237 (CH), 110.181 (CH), 109.998 (C), 31.977 (CH_3), 21.449 (CH_3)

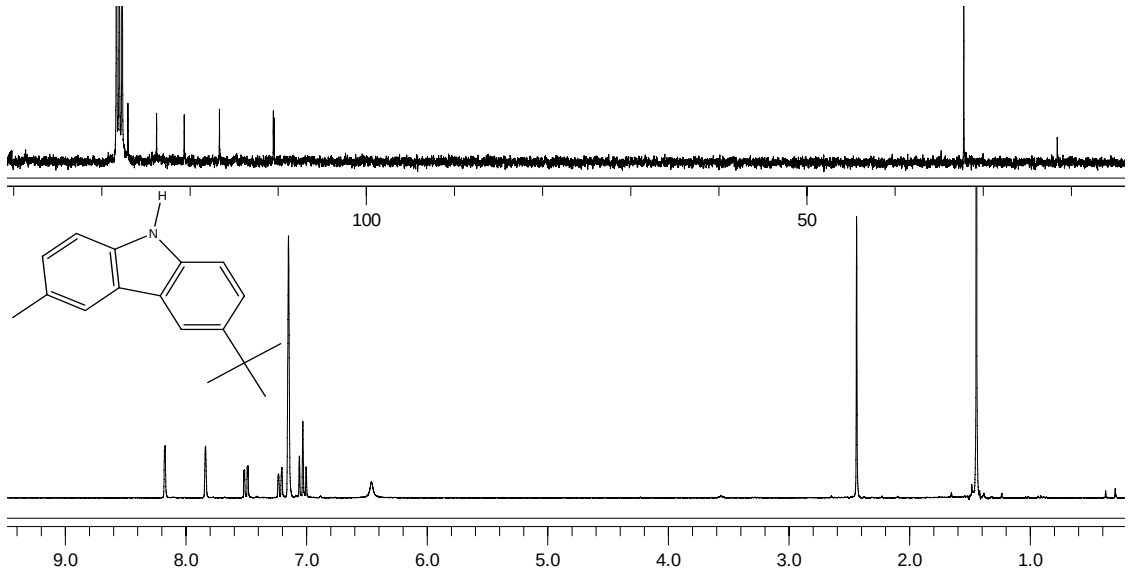


Figure 201: Proton and carbon spectra of 21 in C_6D_6.

^{1}H NMR (300 MHz, C_6D_6, 25 °C) δ8.174 (d, *J* = 1.5 Hz, 1H), 7.837 (s, 1H), 7.502 (dd, *J* = 1.5 Hz, *J* = 8.4 Hz, 1H) , 7.219 (d, *J* = 8.1 Hz, 7.031 (t, *J* = 8.4 Hz, 2H), 6.462 (m, 1H), 2.439 (s, 3H), 1.447 (s, 9H) ^{13}C NMR (300 MHz, C_6D_6, 25 °C) δ127.033 (CH), 123.785 (CH), 120.652 (CH), 116.658 (CH), 110.539 (CH), 110.464 (CH), 32.204 (CH_3), 21.599 (CH_3)

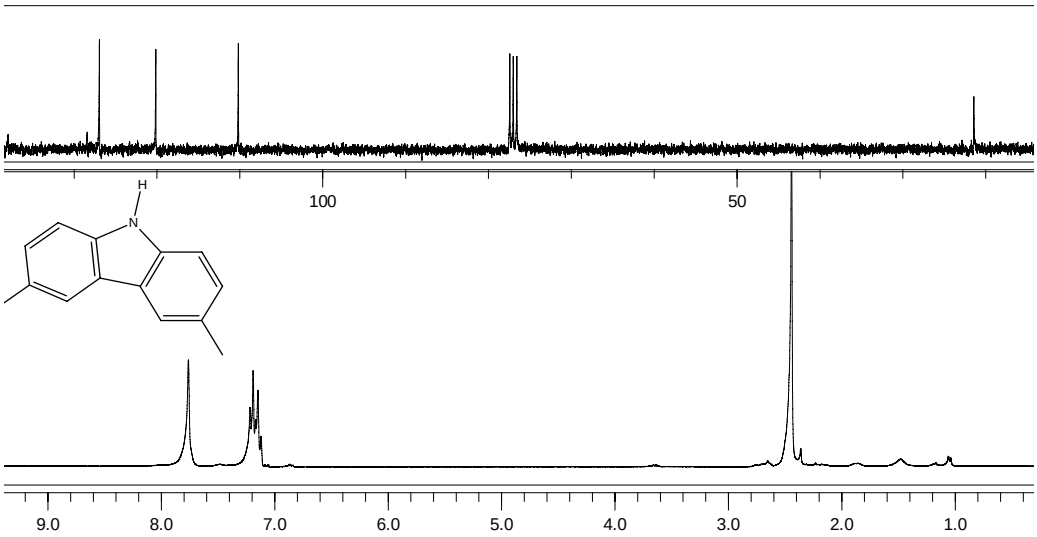


Figure 202: Proton and carbon spectra of 19 in $CDCl_3$.

^{1}H NMR (300 MHz, $CDCl_3$, 25 °C) δ7.759 (b, 3H), 7.119-7.215 (m, 4H), 2.443 (s, 6H)
^{13}C NMR (300 MHz, $CDCl_3$, 25 °C) δ137.957 (C), 128.411 (C), 126.933 (CH), 120.135 (CH), 110.174 (CH), 21.431 (CH_3)

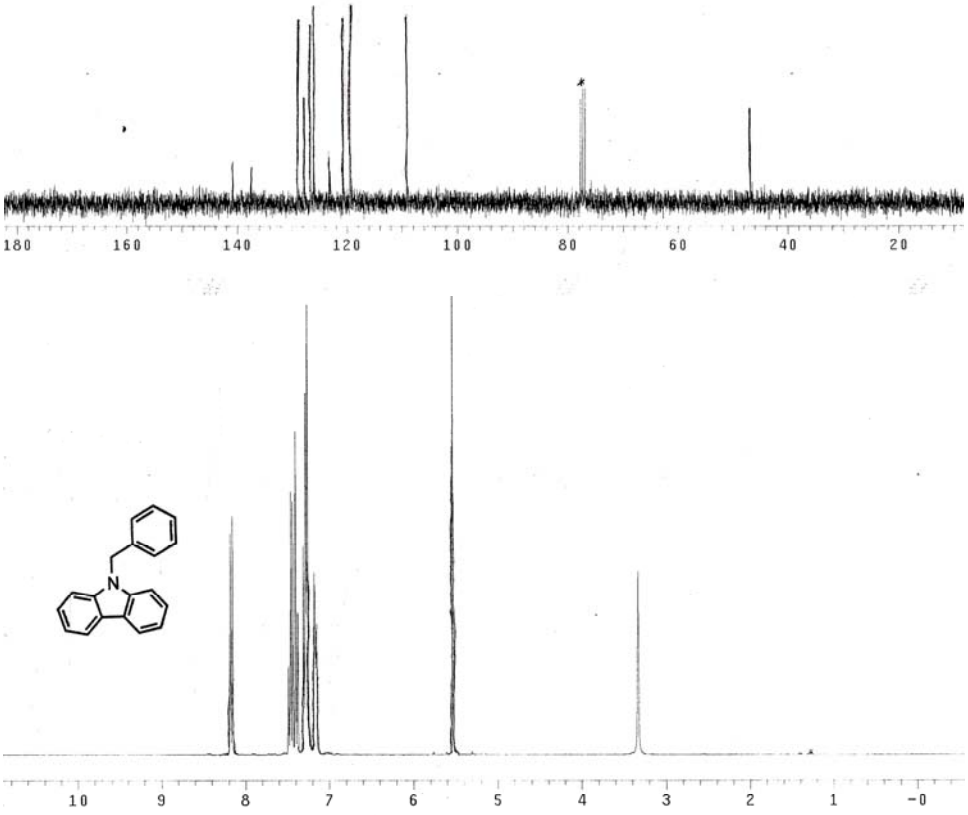


Figure 203: Proton and carbon spectra of 25 in $CDCl_3$.

^{1}H NMR (300 MHz, $CDCl_3$, 25 °C) δ8.17 (d, *J* = 7.8 Hz, 2H), 7.37 (m, 4H), 7.287 (m, 5H), 7.166 (m, 2H), 5.49 (s, 2H) ^{13}C NMR (300 MHz, $CDCl_3$, 25 °C) δ140.6 (C), 137.12 (C), 128.732 (CH), 127.4 (CH), 126.6 (CH), 125.8 (CH), 122.95 (C), 120.4 (CH), 119.16 (CH), 108.9 (CH), 46.5 (CH_2)

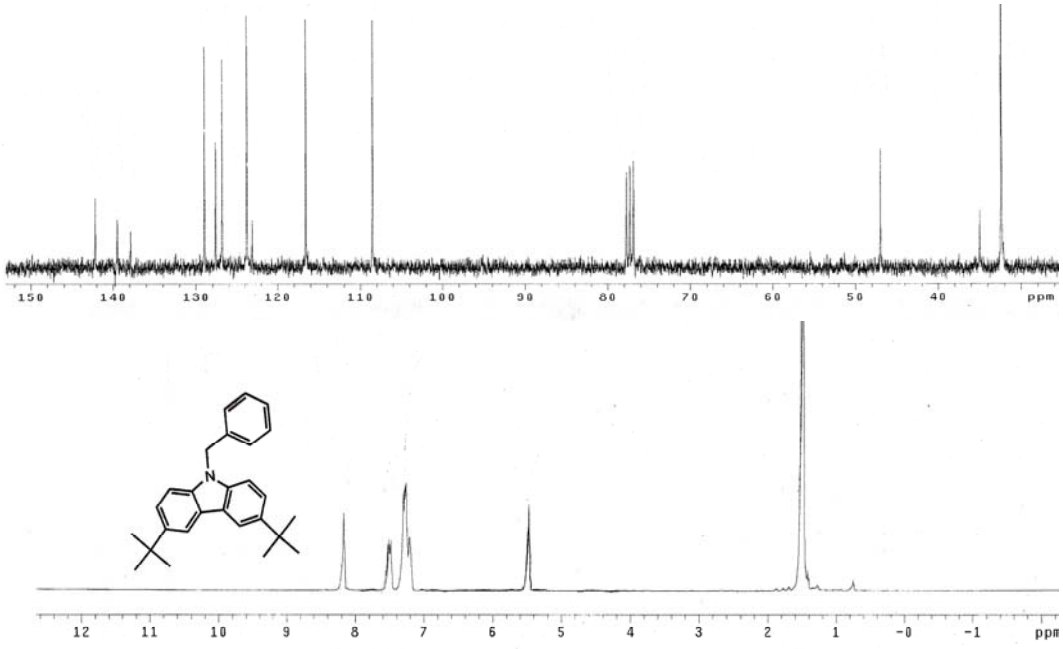


Figure 204: Proton and carbon spectra of 28 in $CDCl_3$.

^{1}H NMR (300 MHz, $CDCl_3$, 25 °C) δ8.16 (s, 2H), 7.48 (m, 2H), 7.286 (m, 7H), 5.47 (s, 2H), 1.49 (s, 18H) ^{13}C NMR (300 MHz, $CDCl_3$, 25 °C) δ141.9 (C), 139.2 (C), 137.6 (C), 128.7 (CH), 127.3 (CH), 126.5 (CH), 123.5 (CH), 116.3 (CH), 108.2 (CH), 46.7 (CH_2), 34.7 (C), 32.0 (CH_3)

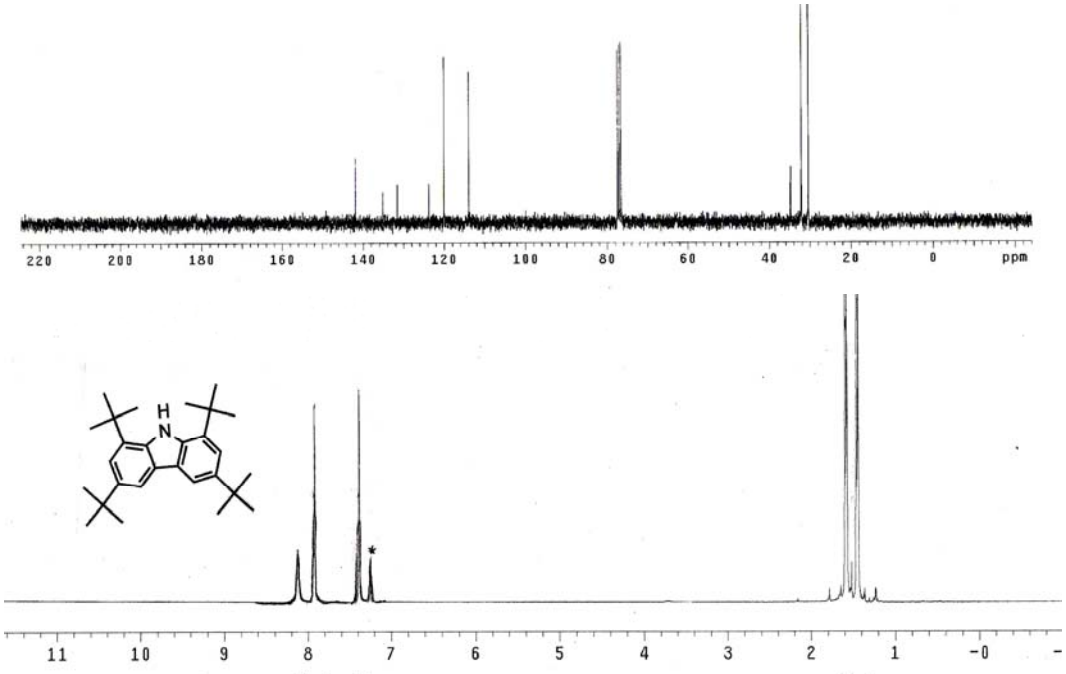


Figure 205: Proton and carbon spectra of 29 in $CDCl_3$.

^{1}H NMR (300 MHz, $CDCl_3$, 25 °C) δ8.121 (s, 1H), 7.921 (d, *J* = 2.4 Hz, 2H), 7.382 (d, *J* = 1.8 Hz, 2H), 1.573 (s, 18H), 1.439 (s, 18H) ^{13}C NMR (300 MHz, $CDCl_3$, 25 °C) δ141.9 (C), 135.1 (C), 131.5 (C), 123.7 (C), 120.0 (CH), 113.9 (CH), 34.8 (C), 34.7 (C), 32.1 (CH_3), 30.4 (CH_3)

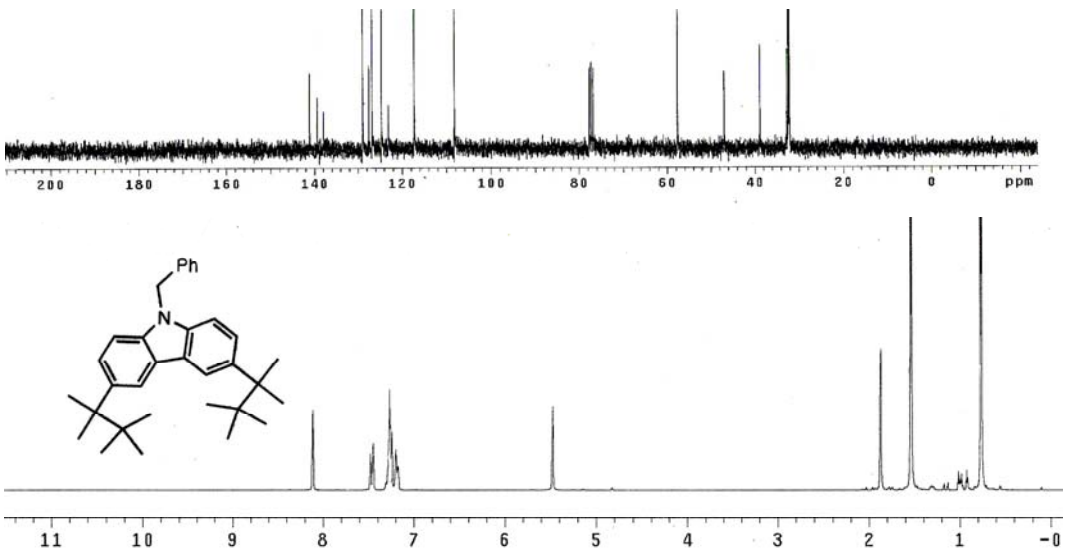


Figure 206: Proton and carbon spectra of 26 in $CDCl_3$.

^{1}H NMR (300 MHz, $CDCl_3$, 25 °C) δ/ppm (s, 2H), (d, *J* = , 2H), (m, 5H), 1.573 (m, 2H), (s, 2H), (s, 4H), (s, 12H), (s, 18H) ^{13}C NMR (300 MHz, $CDCl_3$, 25 °C) δ140.9 (C), 139.1 (C), 138.5 (C), 128.7 (CH), 127.3 (CH), 126.3 (CH), 124.4 (CH), 122.8 (C), 117.0 (CH), 108.0 (CH), 57.4 (CH_2), 46.7 (CH_2), 38.6 (C), 32.5 (C), 32.1 (CH_3), 31.9 (CH_3)

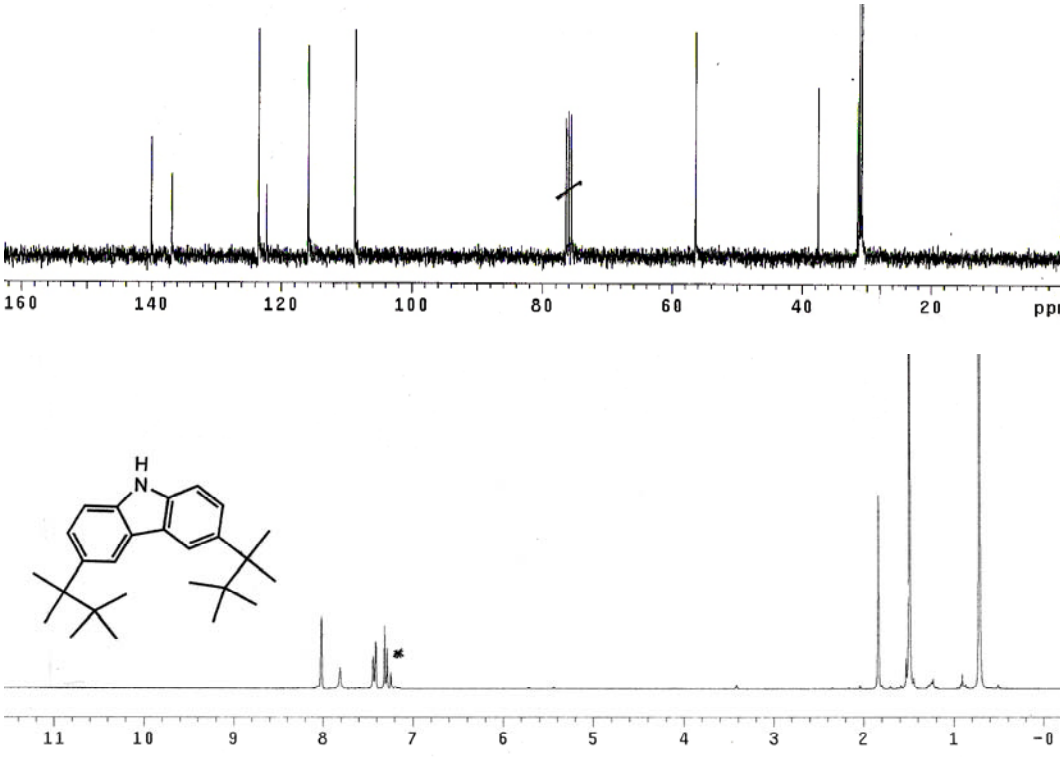


Figure 207: Proton and carbon spectra of 27 in $CDCl_3$.

^{1}H NMR (300 MHz, $CDCl_3$, 25 °C) δ7.963 (s, 2H), 7.75 (s, 1H), 7.361 (d, *J* = 8.4 Hz, 2H), 7.217 (d, *J* = 8.4 Hz, 2H) 1.774 (s, 4H), 1.433 (s, 12H), 0.659 (s, 16H) ^{13}C NMR (300 MHz, $CDCl_3$, 25 °C) δ (C), (C), (CH), (C), (CH), (CH), (CH_2), (C), (C), (CH_3), (CH_3)

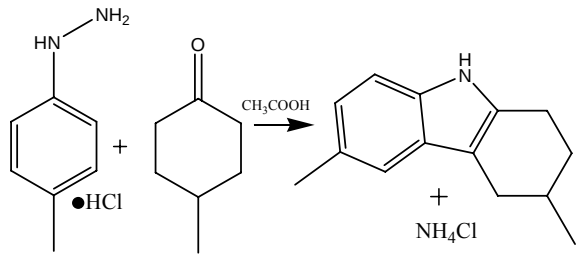


Figure 208: Synthesis of 3,6-dimethyl-1,2,3,4-tetrahydrocarbazole, 18.

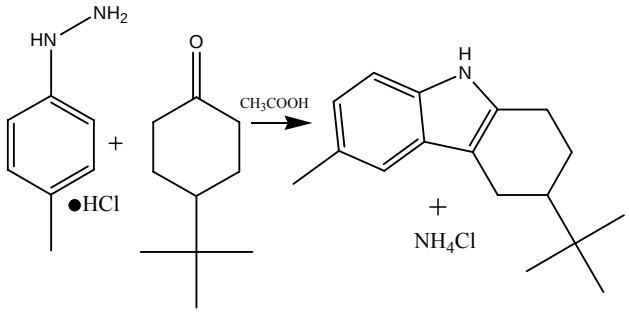


Figure 209: Synthesis of 3-methyl-5-tert-butyl-1,2,3,4-tetrahydrocarbazole, 20.

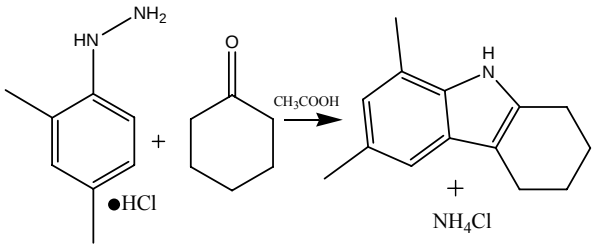


Figure 210: Synthesis of 6,8-dimethyl-1,2,3,4-tetrahydrocarbazole, 22.

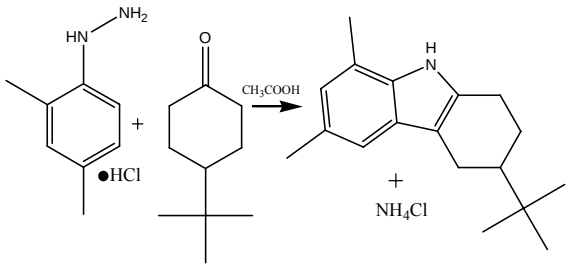


Figure 211: Synthesis of 3-tert-6,8-dimethyl-1,2,3,4-tetrahydrocarbazole, 24.

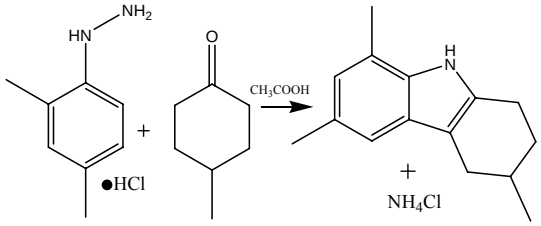


Figure 212: Synthesis of 3,6, 8 – trimethyl-1,2,3,4 tetrahydrocarbazole, 23.

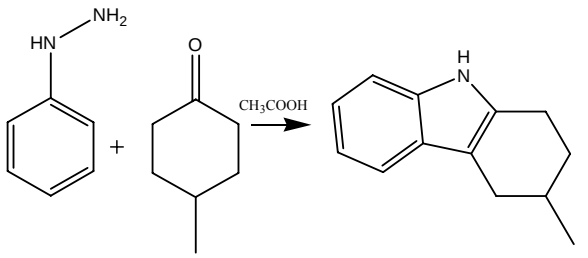


Figure 213: Synthesis of 3-methyl-2,3,4, 4a, 9, 9a-hexahydro-1*H*-carbazole, 14.

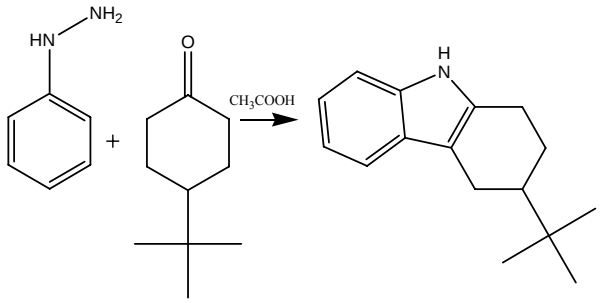


Figure 214: Synthesis of Synthesis of 3-*tert*-butyl-1,2,3,4-tetrahydrocarbazole, 16.

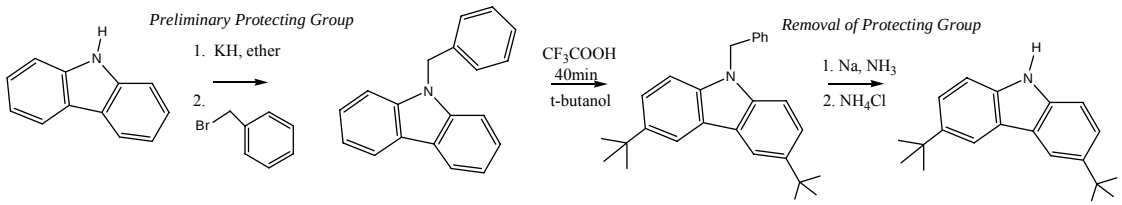


Figure 215: Alternative synthesis I of disubstituted carbazole.

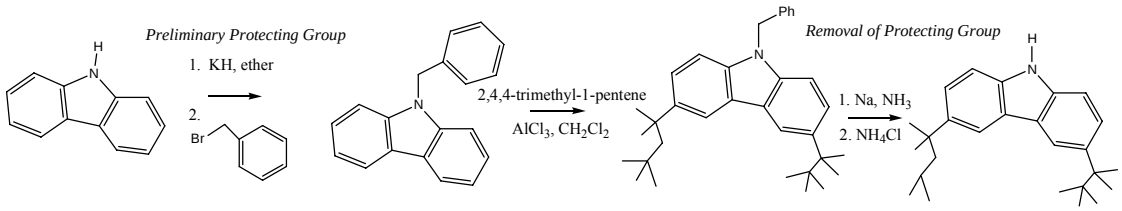
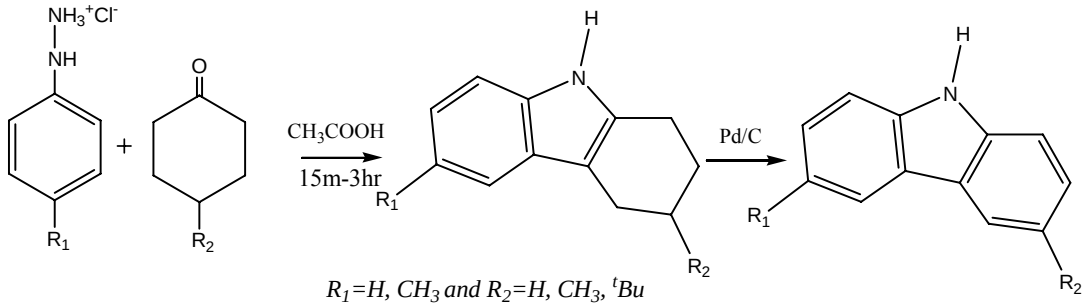


Figure 216: Alternative synthesis II of disubstituted carbazole, 27**.**



R_1=H, CH_3 and R_2=H, CH_3, ^tBu

Figure 217: Fisher-Indole type synthesis.

5 SUGAR CATALYST PREPARATION AND SPECTROSCOPY

The advancement of chemistry in catalysis is an important area of research due to the massive number of organic reactions which depend upon organometallic molecules. Because of the availability of chiral sugar molecules, a system was designed for the purposes of developing reactivity on in this underdeveloped field in September 2000. A proposed synthetic scheme for the sugar is given in Figure 218. A proposed synthetic scheme for the ligand is given in Figure 219 - Figure 221.

5.1.1 Conclusions on the sugar project

In February 2002, it came to the attention of the researcher that other work had been recently published on this topic. This publication as well as some of the future publications have been included in the references.[156-159] Several articles were published almost simultaneously by Dieguez *et al*. Their results proved that the sugars of the type that Turner *et al* were synthesizing showed high catalytic reactivity.

5.1.2 Synthesis of 30b[160]

1,2:5,6-di-*O*-isopropylidine-α-D-allofuranose, **30b**, was synthesized from 1,2:5,6-di-*O*-isopropylidine-α-D-ribo-hexofuranos-3-ulos Hydrate which was synthesized from 1,2:5,6-di-*O*-isopropylidine-α-D-glucofuranose, **30a**.

Before synthesis reaction was attempted, RuO_2 was activated[161] so that it would form RuO4 in solution. In a platinum reaction vessel, 3.006 g (0.02 mol) ruthenium dioxide and 8.042 g (0.2 mol) sodium hydroxide and 7.991 g (0.08 mol) sodium chlorate were heated until they melted and fused together. This mixture was molten for 5 minutes and allowed to cool. The activated ruthenium dioxide was dissolved in an excess of a 25% ethanol water mixture and allowed to form a suspension, which was gravity filtered using glass filter paper. The product was washed with water.

1,2:5,6-di-*O*-isopropylidine-α-D-glucofuranose was initially prepared from D-glucofuranose. Approximately 4 L of acetone was cooled, then 80 mL of concentrated sulfuric acid was added to the acetone. When the solution was at room temperature, 225

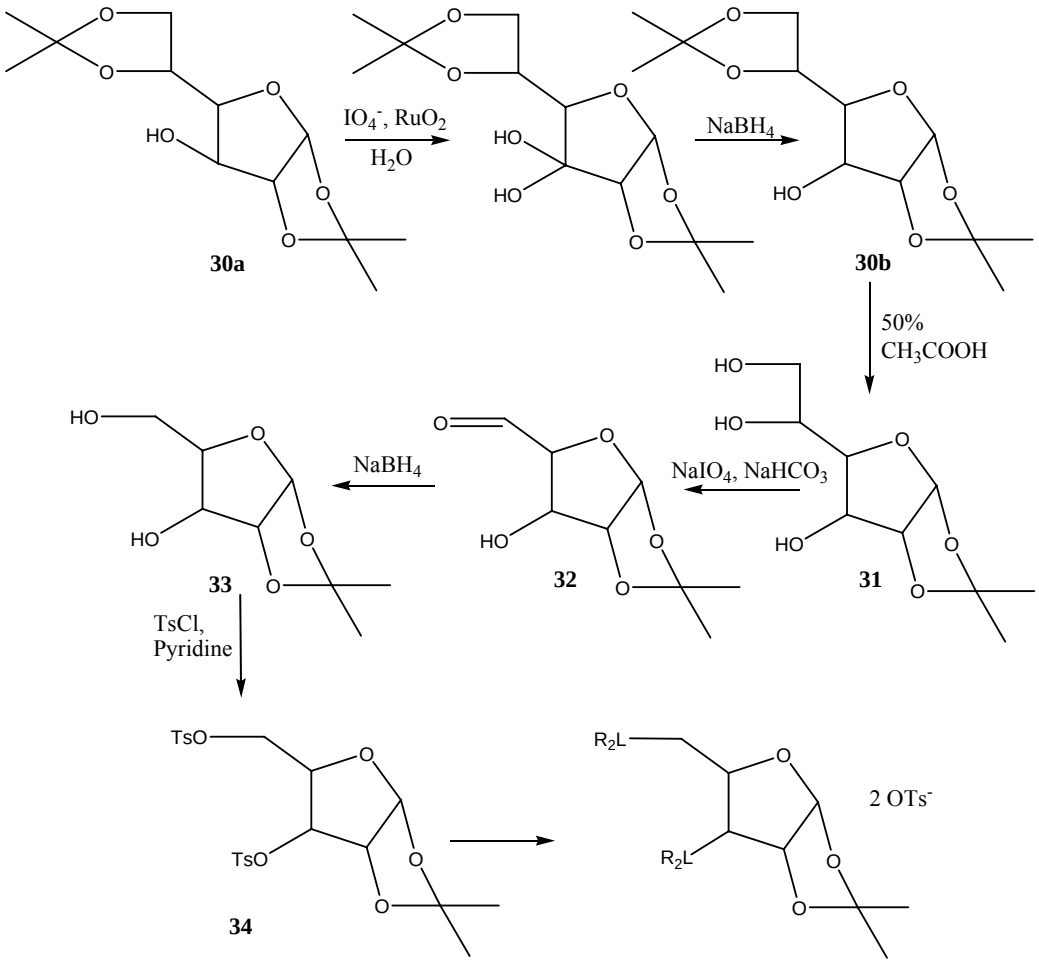


Figure 218: Sugar catalyst synthetic scheme.

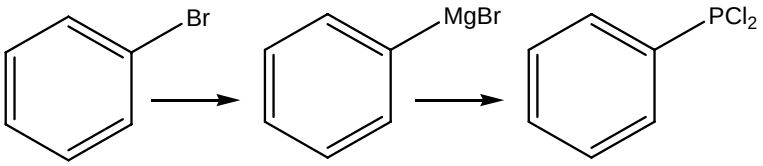


Figure 219: Scheme for synthesis of 35.

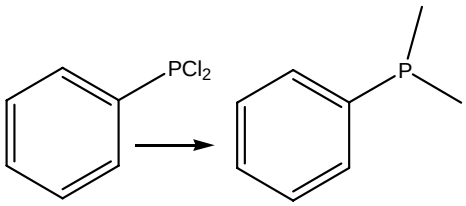


Figure 220: Scheme for synthesis of 36.

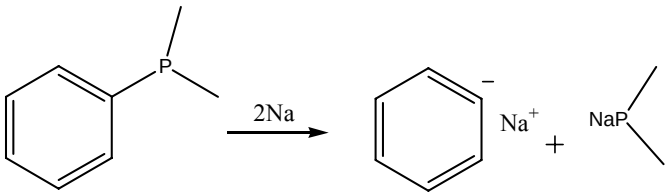


Figure 221: Scheme for synthesis of 37.

g (1.25 mol) of D-glucofuranose was added and the reaction was stirred for 5 minutes and followed by TLC with solvent composition 1:10 CH_2Cl_2:ether. Then, 250 g (6.25 mol) NaOH dissolved in 350 mL deionized water was added until solution was basic and allowed to sit overnight. The solution was filtered by vacuum and the acetone was removed by evaporation under vacuum. The product was dissolved in methylene chloride, extracted with water, and then dried with sodium sulfate. The methylene chloride was then filtered by vacuum and evaporated under vacuum. Product was recrystallized from cyclohexanone.

Into a 5L Morton flask equipped with a heavy-duty stirrer, 125.05 g (0.48 mol) of 1,2:5,6-di-*O*-isopropylidine-α-D-glucofuranose was placed. Alcohol free chloroform was prepared using an alumina column and 550 mL were added to the flask. To this solution, 500 mL of water as well as 153.55 g (0.72 mol) of sodium periodate were added. Previously, potassium periodate had been used but the reaction did not proceed as expected. Sodium periodate is more soluble and therefore used in this synthesis. Also added to the solution were 2.010 g (0.02 mol) ruthenium oxide and 18.4616 g (0.13 mol) of potassium carbonate[160]. So that the solution was further basic, portions of potassium carbonate was added dissolved in water. These portions were: 5.03 g in 100 mL of water, 5.03 g in 100 mL of water, 6.13 g in 75 mL of water, 10 g in 200 mL of water, 5 g in 50 mL of water, and finally 25 g in 200 mL of water so that the total amount of potassium carbonate in solution was 74.65 g (0.54 mol). This mixture was stirred rapidly and monitored by TLC for 48 hours. The developing solvent for TLC was 1:1 ether:chloroform. Two spots were still visible after this period of time. It was determined that complete conversion did not occur. The reaction was quenched with 50 mL of isopropyl alcohol and stirred for 10 minutes. To remove active ruthenium(IV) tetraoxide, the reaction mixture was filtered using a pad of Celite and then filtered again using glass filter paper. The filter paper was washed with chloroform. The mixture was then extracted with three 200 mL portions of chloroform. The extracts were combined and washed with magnesium sulfate and then evaporated under reduced pressure.

For 1 hour, 16.08 g (0.06 mol) of the recovered 1,2:5,6-di-*O*-isopropylidine-a-D-ribo-hexofuranos-3-ulos Hydrate was added to a solution of 50 mL ethanol and 117 mL water. Slowly, fresh sodium borohydride, 2.8647 g (0.08 mol), was added. The solvent mixture was partially removed by vacuum under reduced pressure. Water was added and the mixture was again concentrated as a result of vacuum under reduced pressure. The solution was extracted with methylene chloride and dried with magnesium sulfate. The methylene chloride was removed by vacuum under reduced pressure and the remaining product was recrystallized from hot hexane.

High performance liquid chromatography was used to separate the initial starting material, 1,2:5,6-di-O-isopropylidine-α-D-glucofuranose (R_f 0.31), from the final product, 1,2:5,6-di-O-isopropylidine-α-D-allofuranose (R_f 0.25). Several other mixtures such as ethyl acetate and methanol as well as methylene chloride and ether were tested but the aforementioned mixture resulted in R_f values that were close to 0.3. The solvent mixture used in this separation was 1:30 isopropanol:methylene chloride. Syrup formed when this product was evaporated at 50 °C under reduced pressure. After ether was added and removed by evaporation, the product was crystalline.

5.1.3 Synthesis of 31[162]

1,2-*O*-isopropylidine-α-D-allofuranose, **31** was synthesized from 1,2:5,6-di-*O*-isopropylidine-α-D-allofuranose, **30b**. Initially, this synthesis was attempted using Amberlite CG-50 resin. To regenerate this resin, it was soaked overnight in 50% methanol and then vacuum filtered. The resin was suspended in 80% hydrochloric acid. The suspension was then filtered by vacuum, suspended in deionized water, and filtered by vacuum. The resin was washed with deionized water until neutral to litmus paper and stored in water.

A 40% ethanol:water solution was used as solvent to which 1.02 g of 1,2:5,6-di-*O*-isopropylidine-α-D-allofuranose was added. The solution was stirred at 45 °C while 3 mL of wet Amberlite CG-50 were added. The reaction was followed by TLC using a solvent composition of 1:1 methylene chloride:ethyl acetate for 96 hours and no reaction change was observed so the following procedure was used:

At room temperature, 2.0 g (0.008 mol) of 1,2:5,6-di-*O*-isopropylidine-α-D-allofuranose was added to 53 mL of 50% acetic acid in methanol. This mixture was stirred overnight. The solvent was evaporated under reduced pressure. The residue was dissolved in absolute ethanol several times as well as ether, and all solvents were evaporated. The percent yield of this product was 96%. Some degradation of product was visible *via* TLC. Other solvent mixtures of 75%, and 25% acetic acid in methanol were also tried and although the 25% mixture did not indicate degraded product, the reaction did not go to completion after 48 hours.

5.1.4 Synthesis of 32[163]

1,2-*O*-isopropylidine-α-D-ribo-pentadialdo-1,4-furanose, **32** was synthesized from 1,2-*O*-isopropylidine-α-D-allofuranose, **31**. In a round-bottom flask, 2.0 g (9.1 mmol) of 1,2-*O*-isopropylidine-α-D-allofuranose and 0.909 g (11 mmol) sodium bicarbonate were added to 40 mL 50% ethanol:water. To this mixture, 4.545 g (21 mmol) of sodium periodate was added. This reaction mixture bubbled and was stirred for 3.5 hours. The solvent was concentrated at reduced pressure using an acetone/carbon dioxide bath. The reaction mixture was extracted four times with ethyl acetate. The ethyl acetate was removed under vacuum and yielded the product in a syrup form. The product was used without purification in the next reaction. The NMR spectrum was not clean, but a very sharp peak in a region indicative of an aldehyde was observed at δ/ppm 9.706 on a 300 MHz instrument.

5.1.5 Synthesis of 33[164]

1,2-*O*-isopropylidine-α-D-ribofuranose, **33**, was synthesized from 1,2-*O*-isopropylidine-α-D-ribo-pentodialdo-1,4-furanose, **32**. Ethanol was added to 1,2-*O*-isopropylidine-α-D-ribo-pentodialdo-1,4-furanose from the previous reaction. To the mixture, 0.378 g (10 mmol) of $NaBH_4$ was added. The solvent was partially removed by vacuum under reduced pressure. Water was added, and the mixture was again concentrated as a result of vacuum under reduced pressure. The solution was extracted with ethyl acetate and dried with magnesium sulfate. The ethyl acetate was removed by

vacuum under reduced pressure. This product was purified by column chromatography with a solvent composition of 4:1 methanol: ethyl acetate.

5.1.6 Synthesis of 34a[165]

1,2-*O*-isopropylidine-3,5-di-*O*-*p*-toluenesulfonyl-β-D-ribofuranose, **34a**, was synthesized from 1,2-*O*-isopropylidine-α-D-ribofuranose, **33**. A solution of 3 mL pyridine and 0.5 g (2.6 mmol) of 1,2-*O*-isopropylidine-α-D-ribofuranose was added dropwise over 30 minutes to a mixture of 1 mL of chloroform containing 1.15 g (6 mmol) of toluenesulfonyl chloride. The reaction was followed by TLC as it was stirred at 0 °C for 1 hour, then allowed to warm to room temperature and stir for 20 h. Deionized water was added to the solution, and the aqueous phase was extracted twice with chloroform. The organic layers were combined and washed twice with 3 N sulfuric acid and then washed again with 2% sodium bicarbonate solution. The organic layer was dried over sodium sulfate and evaporated under reduced pressure. A mixture of mono- and di-tosylated products were visible by NMR spectroscopy. For further purification, a silica gel column was used with a solvent composition of 4:5 ethyl acetate:hexanes.

5.1.7 Synthesis of 34b

1,2-*O*-isopropylidine-5-*O*-*p*-toluenesulfonyl-β-D-ribofuranose, **34b**, was a byproduct from the reaction in Section 5.1.6. This product was analyzed *via* NMR and is included in the spectroscopy section.

5.1.8 Synthesis of metal L donor

It is necessary to add a substituent to sugar molecules that have metal-donor capacity so that the sugar will attach to the metal. In this project, both imidazole and dimethylphenylphosphine were considered as possibilities with electron density for metal binding.

5.1.9 Synthesis of 35

In a Schlenk flask, 2.19 g (0.09 mol) magnesium was stirred dry overnight. Diethyl ether was added to the flask and a catalytic quantity of iodine was added to

oxidize the magnesium surface. Then, 8.83 mL (0.084 mol) of bromobenzene was added. The resultant Grignard was added to 11 mL (0.13 mol) trichlorophosphine *via* a large canula. The product, dichlorophenylphosphine, **35**, was filtered and then distilled. ^{31}P NMR (300 MHz, $CDCl_3$, 25 °C) δ 81 ^{13}C NMR (300 MHz, $CDCl_3$, 25 °C) δ 126 (CH), 128 (CH), 130 (CH), 138 (C)

5.1.10 Synthesis of 36

In a Schlenk flask, 1.8 g (0.12 mol) magnesium was stirred dry overnight. Diethyl ether was added to the flask and a catalytic quantity of iodine was added to oxidize the magnesium surface. Then, 4.5 mL (0.075 mol) of iodomethane was added and stirred for 4 hours. The resultant Grignard was added to 5 mL (0.037 mol) of dichlorophenylphosphine, **35**, diluted with ether at –78 °C. The precipitate from this reaction mixture changed from gray to yellow to finally white. The liquid is difficult to separate from the solid so degassed water saturated with ammonium chloride was added dropwise at 0 °C. Additional degassed water and ether were added to the reaction mixture until all products were dissolved. The organic layer was separated from the aqueous layer. Degassed brine was added to the organic layer and the organic layer was separated *via* canula. The organic layer was dried with sodium sulfate. Ether was removed under vacuum while the organic flask was immersed in a carbon dioxide and acetone bath. The product was dimethylphenylphosphine, **36**, and it was purified by flash distillation. The percent yield was 45.3%. ^{31}P NMR (300 MHz, $CDCl_3$, 25 °C) δ -44.822 ^{13}C NMR (300 MHz, $CDCl_3$, 25 °C) δ 130.259 (d, J = 70 Hz, CH), 128.042 (d, J = 48 Hz, CH), 127.764 (s, CH), 14.148 (d, J = 50 Hz, CH_3) ^{1}H NMR (300 MHz, $CDCl_3$, 25 °C) δ 7.495–7.444 (m, 2H), 7.359-7.352 (m, 3H), 1.322 (d, J = 3.6 Hz, 6H)

5.1.11 Synthesis of 37

As shown in Figure 222, freshly cut sodium metal was placed in a Schlenk flask and ammonia was added to the Schlenk at –78 °C over a period of two hours. A condenser was used. Then, dimethlyphenylphosphine was diluted with ether and added to the sodium/ammonia mixture dropwise. The reaction product was a sticky yellow

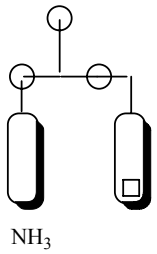


Figure 222: Sodium/ammonia reaction set-up.

solid. Analysis did not yield a clean product but major peaks are listed as follows: ^{31}P NMR (300 MHz, $CDCl_3$, 25 °C) δ -15.409 ^{13}C NMR (300 MHz, $CDCl_3$, 25° C) δ 29.988 (d, J = 90 Hz)

5.1.12 Related spectroscopy and schemes

Both NMR data and schemes are given for the compounds in this chapter in Figure 223 - Figure 233.

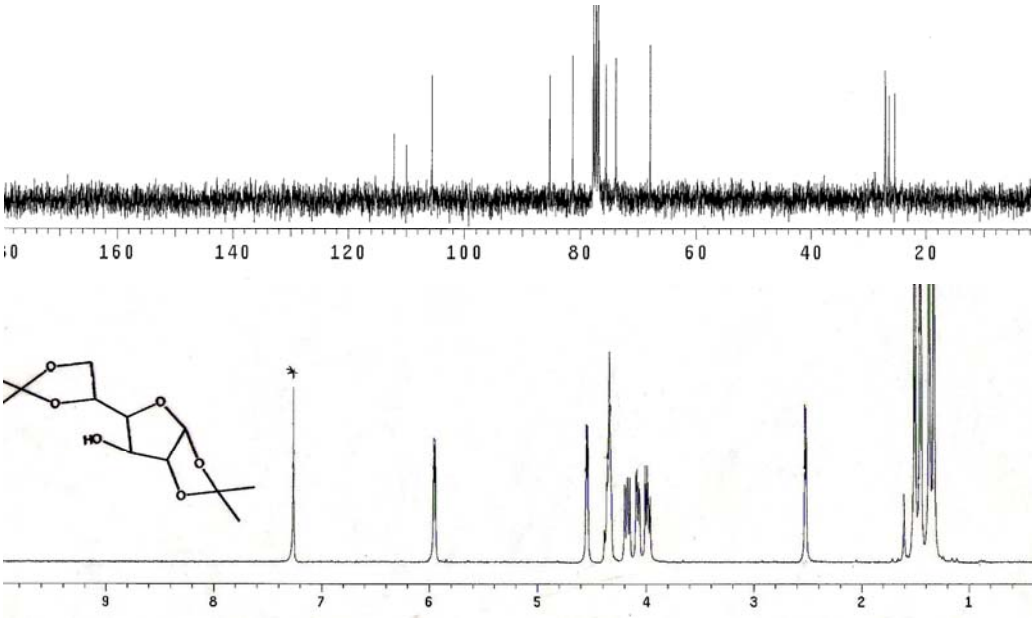


Figure 223: Carbon and proton spectra of 30a in $CDCl_3$.
1,2:5,6-di-*O*-isopropylidine-α-D-glucofuranose

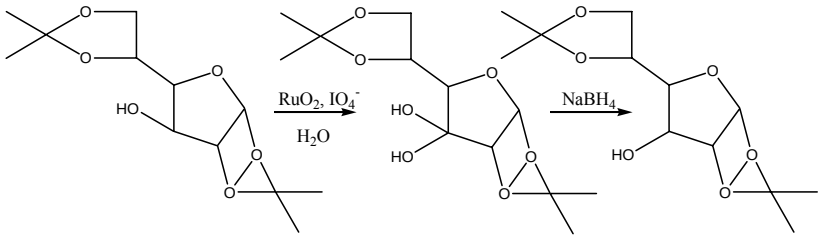


Figure 224: Synthesis of 30b.
1,2:5,6-di-*O*-isopropylidine-α-D-allofuranose

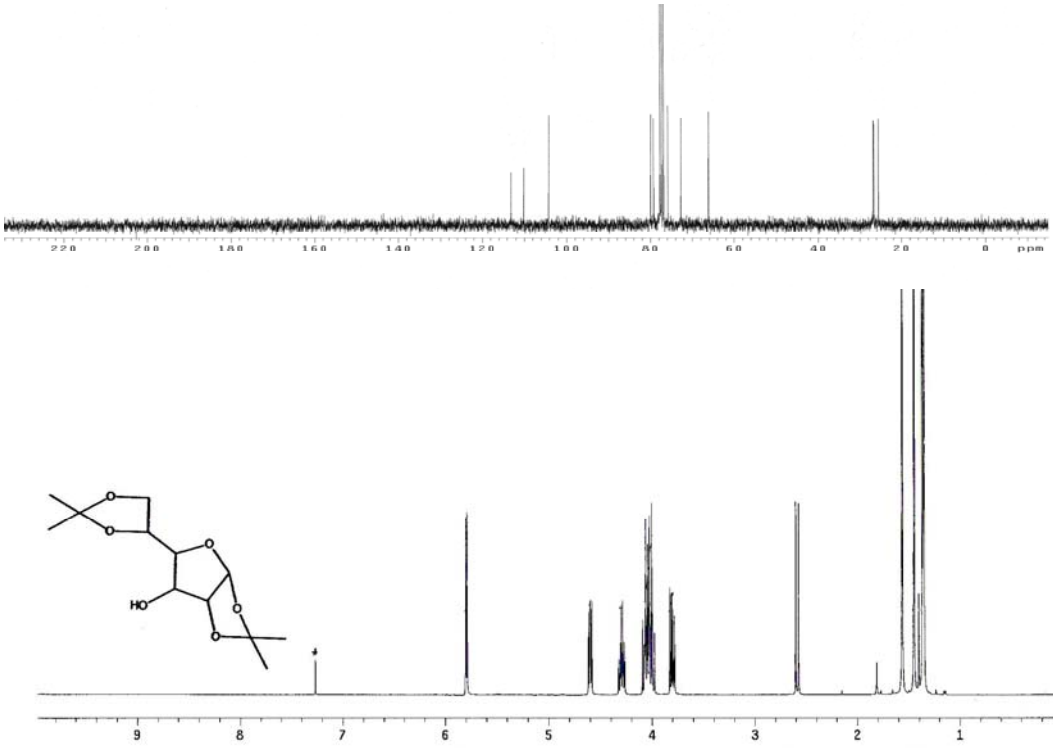


Figure 225: Carbon and proton spectra NMR of 30b in $CDCl_3$.
^{13}C NMR (300 MHz, $CDCl_3$, 25 °C) δ112.84 (C), 109.85 (C), 103.90 (CH), 79.66 (CH), 78.92 (CH), 75.55 (CH), 72.45 (CH), 65.85 (CH_2), 26.56 (CH_3), 26.49 (CH_3), 26.30 (CH_3), 25.26 (CH_3)

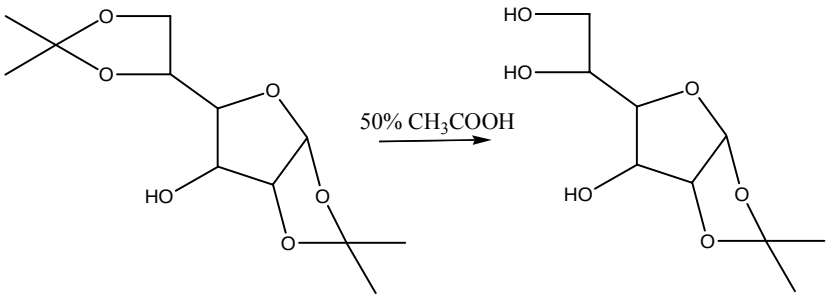


Figure 226: Synthesis of 31.

1,2-*O*-isopropylidine-α-D-allofuranose

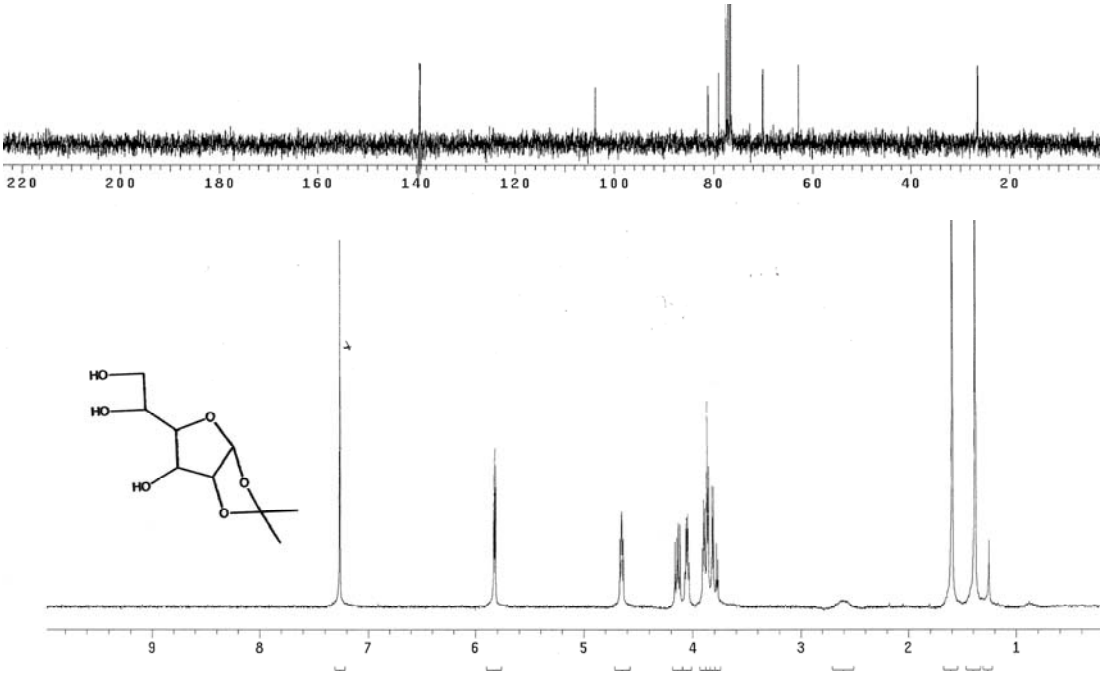


Figure 227: Carbon and proton of 31 in $CDCl_3$.

^{1}H NMR (300 MHz, $CDCl_3$, 25 °C) δ 5.80 (d, 1H), 4.65 (t, 1H), 4.14 (m, 1H), 4.05 (m, 1H), 3.90 (m, 1H), 3.86 (d, *J* = 4.5 Hz, 1H), 3.82 (d, *J* = 4 Hz, 1H), 1.4 (s, 3H), 1.60 (s, 3H)

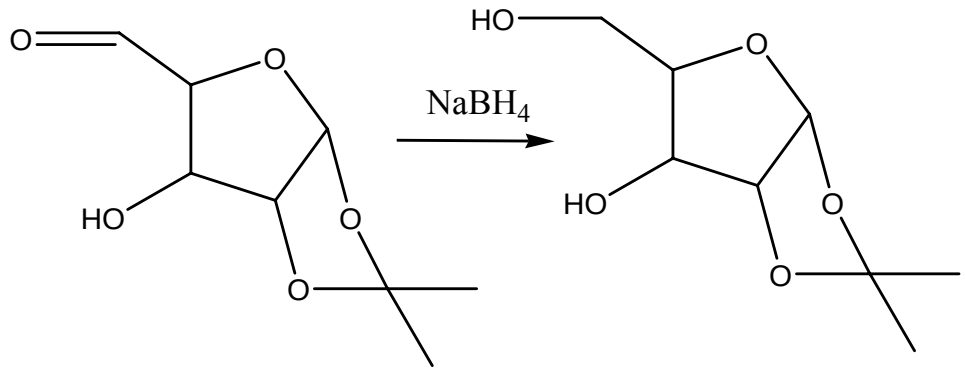


Figure 228: Synthesis of 33.
1,2-*O*-isopropylidine-α-D-ribofuranose

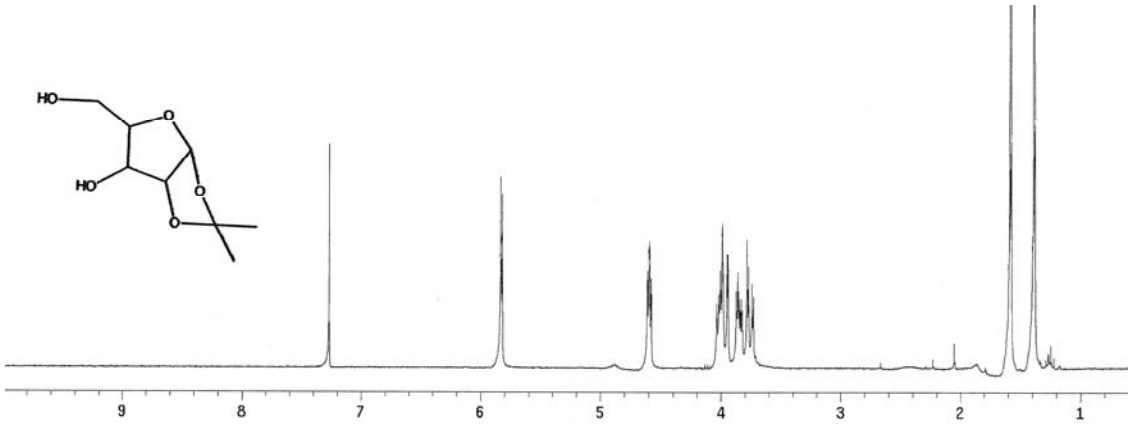


Figure 229: Carbon and proton spectra of 33 in $CDCl_3$.
^{1}H NMR (300 MHz, $CDCl_3$, 25 °C) δ 5.749 (d, *J* = 3.6 Hz, 1H), 4.537 (d, *J* = 3.6 Hz, 1H), 3.825-4.00 (m, 3H), 3.651 (d, *J* = 2.1 Hz, 1H), 3.2 (b, 2H), 1.519 (s, 3H), 1.316 (s, 3H)

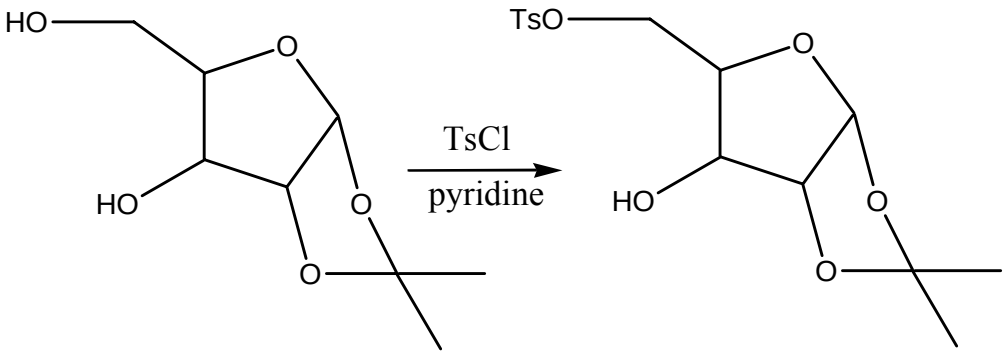


Figure 230: Synthesis of 34b.
1,2-*O*-isopropylidine-5-*O*-*p*-toluenesulfonyl-β-D-ribofuranose

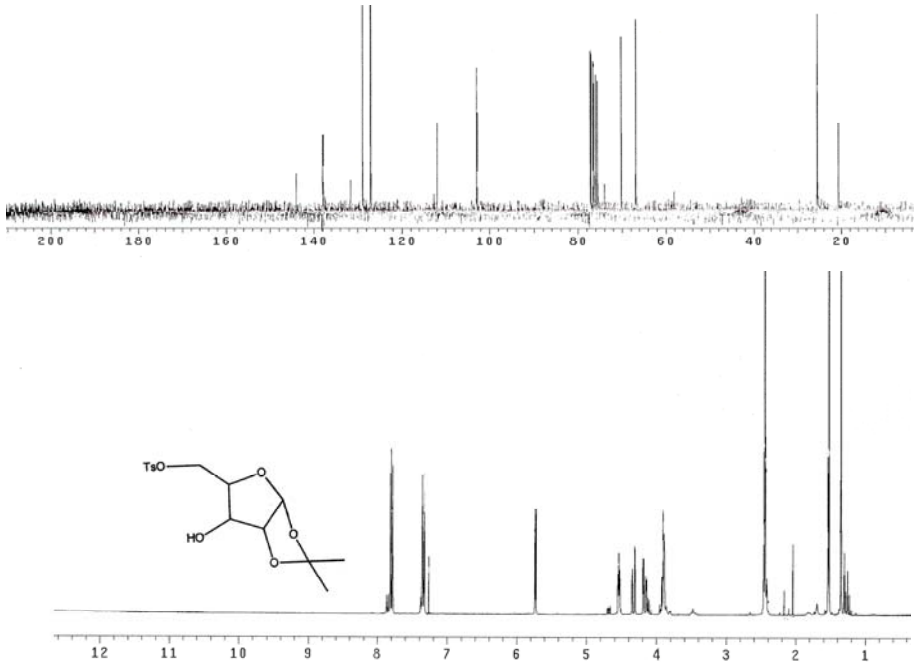


Figure 231: Carbon and proton spectra of 34b in $CDCl_3$.
^{1}H NMR (, $CDCl_3$, 25 °C) δ 7.797 (dd, *J* = 1.8 Hz, 6.6 Hz, 2H), 7.343 (dd, *J* = 1 Hz, 8.4 Hz, 2H), 5.73 (d, *J* = 3.9 Hz, 1H), 4.541 (m, 1H), 4.331 (dd, *J* = 1.8, 11.4 Hz, 1H), 4.169 (dd, *J* = 4.2 Hz, 11.4 Hz, 1H), 4.901 (m, 2H), 2.442 (s, 3H), 2.041 (s, 1H), 1.523 (s, 3H), 1.349 (s, 3H).

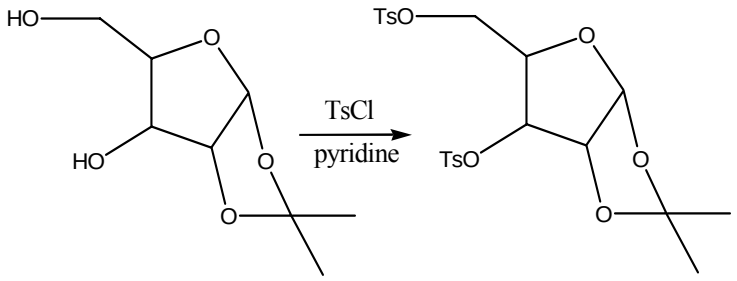


Figure 232: Synthesis of 34a.
1,2-*O*-isopropylidine-3,5-di-*O*-*p*-toluenesulfonyl-β-D-ribofuranose

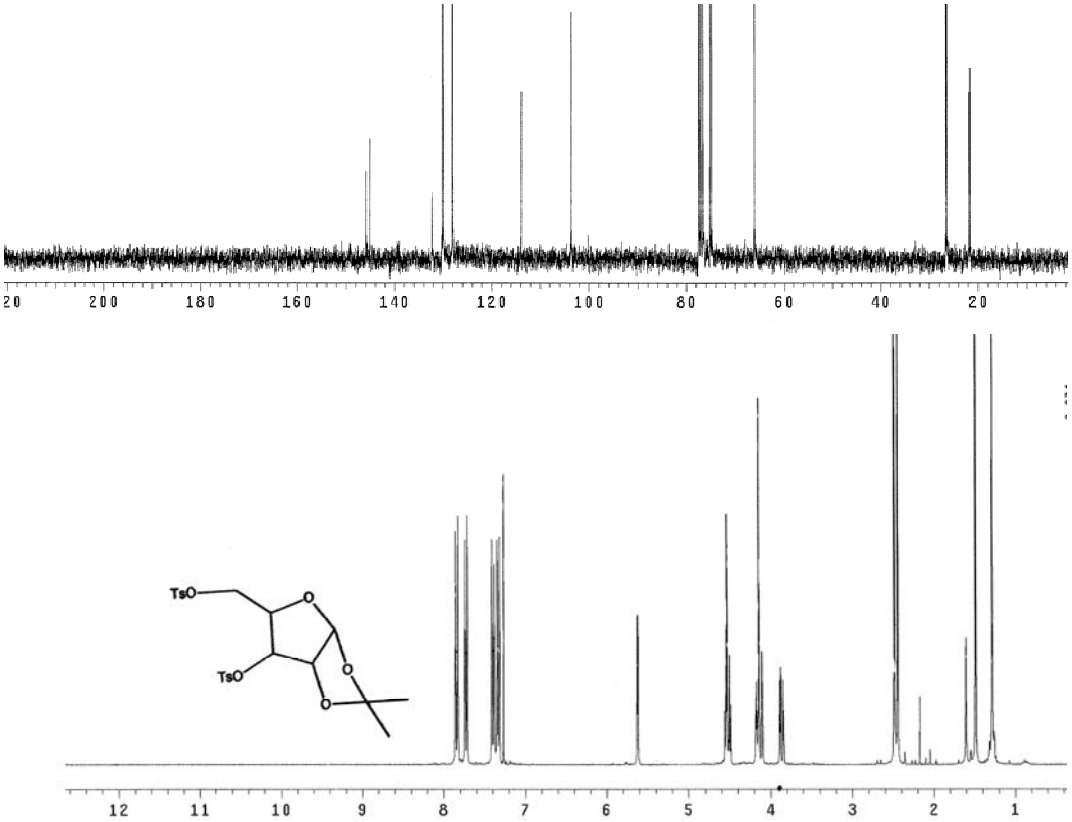


Figure 233: Carbon and proton spectra of 34a in $CDCl_3$.
^{1}H NMR (300 MHz, $CDCl_3$, 25 °C) δ 7.841 (d, *J* = 8.7 Hz, 2H), 7.725 (d, *J* = 8.1 Hz, 2H), 7.394 (d, *J* = 8.4 Hz, 2H), 7.331 (d, *J* = 8.4 Hz, 2H), 5.620 (d, *J* = 3Hz, 1H), 4.524 (m, 2H), 4.124 (m, 2H), 3.868 (d, *J* = 8.4 Hz, 1H), 2.483 (s, 1H), 2.441 (s, 1H), 1.485 (s, 3H), 1.284 (s, 3H). ^{13}C NMR (300 MHz, $CDCl_3$, 25 °C) 145.90 (C), 145.08 (C), 132.29 (C), 132.18 (C), 130.17 (CH), 129.89 (CH), 128.12 (CH), 128.04 (CH), 113.91, 103.70, 77.46, 75.13, 74.78, 66.09, 26.63 (CH_3), 26.41 (CH_3), 21.77 (CH_3), 21.68 (CH_3)

LIST OF REFERENCES

List of References

1. Nygren, C. L.; Bragg, M. E. T.; Turner, J. F. C., (Tetrahydrofuran)potassium mer-trans-tris(carbazolyl)dichloro(tetrahydrofuran)zirconate. *Acta Crystallographica, Section C: Crystal Structure Communications* **2003,** C59, (7), m275-m276.
2. Nygren, C. L.; Bragg, M. E. T.; Turner, J. F. C., Tetrakis(tetrahydrofuran-κO)lithium mer-tris(carbazolyl-κN)-trans-dichloro(tetrahydrofuran-κO)zirconate. *Acta Crystallographica, Section C: Crystal Structure Communications* **2004,** C60, (2), m94-m96.
3. Nygren, C. L.; Bragg, M. E. T.; Turner, J. F. C., trans-Dichloro-cis-bis(3,6-dimethylcarbazolyl)-cis-bis(tetrahydrofuran)zirconium(IV) benzene sesquisolvate. *Acta Crystallographica, Section C: Crystal Structure Communications* **2004,** C60, (1), m4-m6.
4. Lonsdale, R. Electronic structure of alkenes, carbenes and complexes. University of Oxford, 2005.
5. Pauli, W., Naturwisschaften. *12* **1924**, 741.
6. Rabi, I. I.; Zacharias, J. R.; Millman, S.; Kusch, P., A new method of measuring nuclear magnetic moment. *Physical Review* **1938,** 53, 318.
7. Rabi, I. I.; Millman, S.; Kusch, P.; Zacharias, J. R., Molecular beam resonance method for measuring nuclear magnetic moments. The magnetic moments of Li-6, Li-7 and F-19. *Physical Review* **1939,** 55, 526-35.
8. Lindburg, A. A., The Nobel Foundation. In The Nobel Foundation: 2005.
9. Purcell, E. M.; Torrey, H. C.; Pound, R. V., Resonance absorption by nuclear magnetic moments in a solid. *Physical Review* **1946,** 69, 37-8.
10. Bloch, F.; Hansen, W. W.; Packard, M., Nuclear Induction. *Physical Review* **1946,** 69, 127.
11. Bloembergen, N.; Purcell, E. M.; Pound, R. V., Relaxation effects in nuclear magnetic resonance absorption. *Physical Review* **1948,** 73, 679-712.
12. Proctor, W. G.; Yu, F. C., The dependence of a nuclear magnetic resonance frequency upon chemical compound. *Physical Review* **1950,** 77, 717.

13. Dickinson, W. C., Dependence of the fluorine-19 nuclear resonance position on chemical compound. *Physical Review* **1950,** 77, 736-7.

14. Knight, W. D., Nuclear magnetic resonance shift in metals. *Physical Review* **1949,** 76, 1259-60.

15. Proctor, W. G.; Yu, F. C., On the Nuclear Magnetic Moments of Several Stable Isotopes. *Physical Review* **1951,** 81, (1), 20.

16. Gutowsky, H. S.; McCall, D. W., Nuclear magnetic resonance fine structure in liquids. *Physical Review* **1951,** 82, 748-9.

17. Hahn, E. L.; Maxwell, D. E., Chemical shift and field-independent frequency modulation of the spin echo envelope. *Physical Review* **1952,** 84, 1246-7.

18. Purcell, E. M.; Ramsey, N. F., Interactions between Nuclear Spins in Molecules. *Physical Review* **1952,** 85, 143.

19. Hahn, E. L., Spin Echoes. *Physical Review* **1950,** 80, (4), 580-601.

20. Overhauser, A. W., Polarization of nuclei in metals. *Physical Review* **1953,** 92, 411-15.

21. Gutowsky, H. S.; McCall, D. W.; Slichter, C. P., Nuclear Magnetic Resonance Multiplets in Liquids. *The Journal of Chemical Physics* **1953,** 21, (2), 279.

22. Bloom, A. L.; Shoolery, J. N., Effects of Perturbing Radiofrequency Fields on Nuclear Spin Coupling. *Physical Review* **1954,** 97, (5), 1261.

23. Bloch, F., Line-narrowing by macroscopic motion. *Physical Review* **1954,** 94, 496-7.

24. Anderson, W. A.; Arnold, J. T., A line-narrowing experiment. *Physical Review* **1954,** 94, 496.

25. Golay, M. J. E., Field Homogenizing Coils for Nuclear Spin Resonance Instrumentation. *Review of Scientific Instruments* **1958,** 29, (4), 313.

26. Ernst, R. R.; Anderson, W. A., Application of Fourier transform spectroscopy to magnetic resonance. *Review of Scientific Instruments* **1966,** 37, (1), 93-102.

27. Aue, W. P.; Bartholdi, E.; Ernst, R. R., Two-dimensional spectroscopy. Application to nuclear magnetic resonance. *The Journal of Chemical Physics* **1976,** 64, (5), 2229.

28. Andrew, E. R.; Szczesniak, E., A historical account of NMR in the solid state. *Progress in Nuclear Magnetic Resonance Spectroscopy* **1995,** 28, (1), 11.

29. Andrew, E. R., *Nature* **1958,** 182, 1659.

30. Akitt, J. W., *NMR and Chemistry: An Introduction to Modern NMR Spectroscopy*. 4th ed.; 2000; p 296.

31. Claridge, T. D. W., *High-Resolution NMR Techniques in Organic Chemistry*. Pergamon: Oxford, 1999; Vol. 19, p 384.

32. Lowe, I. J., Free Induction Decays of Rotating Solids. *Physical Review Letters* **1959,** 2, (7), 285-287.

33. Saunders, M.; Wishnia, A., Nuclear magnetic resonance spectra of proteins. *Annals of the New York Academy of Sciences* **1958,** 70, 870-4.

34. McDonald, C. C.; Phillips, W. D., Manifestations of the tertiary structures of proteins in high-frequency nuclear magnetic resonance. *Journal of the American Chemical Society* **1967,** 89, (24), 6332-41.

35. Moon, R. B.; Richards, J. H., Determination of Intracellular pH by 31P Magnetic Resonance. *Journal of Biological Chemistry* **1973,** 248, (20), 7276.

36. Ugurbil, K.; Guernsey, D. L.; Brown, T. R.; Glynn, P.; Tobkes, N.; Edelman, I. S., 31P NMR Studies of Intact Anchorage-Dependent Mouse Embryo Fibroblasts. *PNAS* **1981,** 78, (8), 4843-4847.

37. Foxall, D. L.; Cohen, J. S., NMR studies of perfused cells. *Journal of Magnetic Resonance (1969)* **1983,** 52, (2), 346.

38. Pykett, I. L.; Rosen, B. R., Nuclear magnetic resonance: in vivo proton chemical shift imaging. Work in progress. *Radiology* **1983,** 149, (1), 197-201.

39. Hare, D. R.; Wemmer, D. E.; Chou, S.-H.; Drobny, G.; Reid, B. R., Assignment of the non-exchangeable proton resonances of *d*(C-G-C-G-A-A-T-T-C-G-C-G) using two-dimensional nuclear magnetic resonance methods. *Journal of Molecular Biology* **1983,** 171, (3), 319.

40. Wagner, G.; Wuthrich, K., Sequential resonance assignments in protein 1H nuclear magnetic resonance spectra. Basic pancreatic trypsin inhibitor. *Journal of molecular biology* **1982,** 155, (3), 347-66.

41. Lauterbur, P. C., Image formation by induced local interactions. Examples employing nuclear magnetic resonance. *Nature* **1973,** 242, (5394), 190-1.

42. Mansfield, P.; Grannell, P. K., NMR 'difraction' in solids? *Journal of Physics C: Solid State Physics* **1973,** 6, L422.

43. Prichard, J.; Rothman, D.; Novotny, E.; Petroff, O.; Kuwabara, T.; Avison, M.; Howseman, A.; Hanstock, C.; Shulman, R., Lactate rise detected by proton NMR in human visual cortex during physiologic stimulation. *Proceedings of the National Academy of Sciences of the United States of America* **1991,** 88, (13), 5829-31.

44. Atkins, P. W., *Quanta, A Handbook of Concepts*. 2nd ed.; Oxford University Press: Oxford, 1991; p 434.

45. Gerlach, W.; Stern, O., Experimental demonstration of directional quantization in a magnetic field. *Zeitschrift fuer Physik* **1922,** 9, 349-52.

46. Gerlach, W.; Stern, O., Experimental demonstration of the magnetic moment of the silver atom. *Zeitschrift fuer Physik* **1921,** 8, 110-1.

47. Gerlach, W.; Stern, O., The magnetic moment of the silver atom. *Zeitschrift fuer Physik* **1922,** 9, 353-5.

48. Dirac, P. A. M., *The Principles of Quantum Mechanics.* 4 ed.; 1958; p 311.

49. Jammer, M., *The Conceptual Development of Quantum Mechanics*. 1967; p 399.

50. Lide, D. R., *Handbook of Chemistry and Physics*. 75 ed.; CRC Press: Ann Arbor, 1995.

51. Atkins, P. W., *Physical Chemistry*. 5th ed.; W. H. Freeman and Company: New York, 1994; p 1014.

52. T.Saito; K.Hayamizu; M.Yanagisawa; O.Yamamoto, Spectral Database for Organic Compounds SDBS. In 2005.

53. Karplus, M., Contact electron-spin coupling of nuclear magnetic moments. *Journal of Chemical Physics* **1959,** 30, 11-15.

54. Pretsch, E.; Buehlmann, P.; Affolter, C., *Structure Determination of Organic Compounds: Tables of Spectral Data, 3rd Completely Revised and Enlarged Edition*. 2000; p 421.

55. Levitt, M., *Spin Dynamics: Basic Principles of NMR Spectroscopy*. John Wiley & Sons, LTD: Chichester, 2001; p 672.

56. Roberts, J. D., *ABCs of FT-NMR*. University Science Books: Sausalito, 2000; p 322.

57. Abdur-Rashid, K.; Clapham, S. E.; Hadzovic, A.; Harvey, J. N.; Lough, A. J.; Morris, R. H., Mechanism of the hydrogenation of ketones catalyzed by trans-dihydrido(diamine)ruthenium(II) complexes. *Journal of the American Chemical Society* **2002,** 124, (50), 15104-15118.

58. Knoevenagel, E.; Heckel, W., Behavior of benzohydrol during its heating and in the presence of palladium black. *Berichte der Deutschen Chemischen Gesellschaft* **1903,** 36, 2816-2822.

59. Linstead, R. P.; Braude, E. A.; Mitchell, P. W. D.; Wooldridge, K. R. H.; Jackman, L. M., Transfer of hydrogen in organic systems. *Nature* **1952,** 169, 100-3.

60. Braude, E. A.; Brook, A. G.; Linstead, R. P., Hydrogen transfer. IV. The use of quinones of high potential as dehydrogenation reagents. *Journal of the Chemical Society, Abstracts* **1954**, 3569-74.

61. Braude, E. A.; Brook, A. G.; Linstead, R. P., Hydrogen transfer. V. Dehydrogenation reactions with diphenylpicrylhydrazyl. *Journal of the Chemical Society, Abstracts* **1954**, 3574-8.

62. Braude, E. A.; Jackman, L. M.; Linstead, R. P., Hydrogen transfer. II. The dehydrogenation of 1,4-dihydronaphthalene by quinones. Kinetics and mechanism. *Journal of the Chemical Society, Abstracts* **1954**, 3548-63.

63. Braude, E. A.; Jackman, L. M.; Linstead, R. P., Hydrogen transfer. III. The dehydrogenation of hydroaromatic hydrocarbons by quinones. Quantitative comparison of donors. *Journal of the Chemical Society, Abstracts* **1954**, 3564-8.

64. Braude, E. A.; Linstead, R. P., Hydrogen transfer. I. Introductory survey. *Journal of the Chemical Society, Abstracts* **1954**, 3544-7.

65. Braude, E. A.; Linstead, R. P.; Mitchell, P. W. D., Hydrogen transfer. VI. Metal catalyzed transfer-hydrogenation of ethylenic compounds. *Journal of the Chemical Society, Abstracts* **1954**, 3578-85.

66. Braude, E. A.; Linstead, R. P.; Mitchell, P. W. D.; Wooldridge, K. R. H., Hydrogen transfer. VIII. Metal catalyzed transfer hydrogenation of miscellaneous acceptors. *Journal of the Chemical Society, Abstracts* **1954**, 3595-8.

67. Braude, E. A.; Linstead, R. P.; Wooldridge, K. R. H., Hydrogen transfer. VII. Metal catalyzed transfer hydrogenation of nitro compounds. *Journal of the Chemical Society, Abstracts* **1954**, 3586-95.

68. Young, J. F.; Osborn, J. A.; Jardine, F. H.; Wilkinson, G., Hydride intermediates in homogeneous hydrogenation reactions of olefins and acetylenes using rhodium catalysts. *Chemical Communications (London)* **1965**, 131-132.

69. Schrock, R. R.; Osborn, J. A., Catalytic hydrogenation using cationic rhodium complexes. I. Evolution of the catalytic system and the hydrogenation of olefins. *Journal of the American Chemical Society* **1976,** 98, (8), 2134-43.

70. Schrock, R. R.; Osborn, J. A., Catalytic hydrogenation using cationic rhodium complexes. II. The selective hydrogenation of alkynes to cis olefins. *Journal of the American Chemical Society* **1976,** 98, (8), 2143-7.

71. Schrock, R. R.; Osborn, J. A., Catalytic hydrogenation using cationic rhodium complexes. III. The selective hydrogenation of dienes to monoenes. *Journal of the American Chemical Society* **1976,** 98, (15), 4450-5.

72. Wade, L. G., Jr., *Organic Chemistry*. 3 ed.; Prentice Hall: New Jersey, 1995; p 1, 269.

73. Crabtree, R. H., *The Organometallic Chemistry of the Transition Metals*. 3 ed.; John Wiley & Sons, Inc.: New York, 2001; p 534.

74. Mao, J.; Baker, D. C., A Chiral Rhodium Complex for Rapid Asymmetric Transfer Hydrogenation of Imines with High Enantioselectivity. *Organic Letters* **1999,** 1, (6), 841-843.

75. Mao, J.; Baker, D. C. Preparation of arylsultams as HIV reverse transcriptase inhibitors. 2000056332, 2000.

76. Osborn, J. A.; Jardine, F. H.; Young, J. F.; Wilkinson, G., Preparation and properties of tris(triphenylphosphine)halorhodium(I) and some reactions thereof including catalytic homogeneous hydrogenation of olefins and acetylenes and their derivatives. *Journal of the Chemical Society [Section] A: Inorganic, Physical, Theoretical* **1966**, 1711-1732.

77. Jardine, F. H.; Osborn, J. A.; Wilkinson, G., Further studies on the homogeneous hydrogenation of olefins using tris(triphenylphosphine)halorhodium(I) catalysts. *Journal of the Chemical Society [Section] A: Inorganic, Physical, Theoretical* **1967**.

78. Yamamoto, A., *Organotransition Metal Chemistry: Fundamental Concepts and Applications*. John Wiley and Sons: New York, 1985; p 455.

79. Bowers, C. R.; Weitekamp, D. P., Para hydrogen and synthesis allow dramatically enhanced nuclear alignment. *Journal of the American Chemical Society* **1987,** 109, 5541-5542.

80. Eisenschmid, T. C.; Kirss, R. U.; Deutsch, P. P.; Hommeltoft, S. I.; Eisenberg, R.; Bargon, J.; Lawler, R. G.; Balch, A. L., *Para*-hydrogen induced polarization in hydrogenation reactions. *Journal of the American Chemical Society* **1987,** 109, (26), 8089-91.

81. Eisenberg, R.; Eisenschmid, T. C.; Chinn, M. S.; Kirss, R. U., Para-hydrogen-induced polarization and polarization transfer in hydrogenation and oxidative addition reactions. A mechanistic probe. *Advances in Chemistry Series* **1992,** 230, (Homogeneous Transition Met. Catal. React.), 47-74.

82. Landis, C. R.; Brauch, T. W., Probing the nature of H_2 activation in catalytic asymmetric hydrogenation. *Inorganica Chimica Acta* **1998,** 270, (1,2), 285-297.

83. Duckett, S. B.; Sleigh, C. J., Applications of the para hydrogen phenomenon: a chemical perspective. *Progress in Nuclear Magnetic Resonance Spectroscopy* **1999,** 34, (1), 71-92.

84. Song, J. S.; Szalda, D. J.; Bullock, R. M.; Lawrie, C. J. C.; Rodkin, M. A.; Norton, J. R., Hydride transfer via transition metal hydrido complexes, ionic

hydrogenation of aldehydes and ketones, and the structure of an alcohol complex. *Angewandte Chemie* **1992,** 104, (9), 1280-2.

85. Papish, E. T.; Magee, M. P.; Norton, J. R., Protonation of transition metal hydrides to give dihydrogen complexes. Mechanistic implications and catalytic applications. *Recent Advances in Hydride Chemistry* **2001**, 39-74.
86. Bullock, R. M., Catalytic ionic hydrogenations. *Chemistry--A European Journal* **2004,** 10, (10), 2366-2374.
87. Magee, M. P.; Norton, J. R., Stoichiometric, Catalytic, and Enantioface-Selective Hydrogenation of C:N Bonds by an Ionic Mechanism. *Journal of the American Chemical Society* **2001,** 123, (8), 1778-1779.
88. Guan, H.; Saddoughi, S. A.; Shaw, A. P.; Norton, J. R., Ruthenium-Catalyzed Ionic Hydrogenation of Aziridinium Cations. *Organometallics* **2005**, ACS ASAP.
89. Mao, J.; Baker, D. C., Pentamethylcyclopentadienyl-rhodium complex catalyzed transfer hydrogenation of imines by triethylammonium formate. *Book of Abstracts, 217th ACS National Meeting, Anaheim, Calif., March 21-25* **1999**, ORGN-279.
90. Murata, K.; Ikariya, T.; Noyori, R., New Chiral Rhodium and Iridium Complexes with Chiral Diamine Ligands for Asymmetric Transfer Hydrogenation of Aromatic Ketones. *Journal of Organic Chemistry* **1999,** 64, (7), 2186-2187.
91. Torii, T.; Hamada, T.; Onishi, T.; Izawa, K.; Ikariya, T.; Noyori, R. Process for producing optically active halohydrin compound by asymmetric hydrogen transfer reduction of a-halo ketones. 2002051781, 2002.
92. Hamada, T.; Torii, T.; Izawa, K.; Ikariya, T., A practical synthesis of optically active aromatic epoxides via asymmetric transfer hydrogenation of a-chlorinated ketones with chiral rhodium-diamine catalyst. *Tetrahedron* **2004,** 60, (34), 7411-7417.
93. Hamada, T.; Torii, T.; Onishi, T.; Izawa, K.; Ikariya, T., Asymmetric Transfer Hydrogenation of α-Aminoalkyl α'-Chloromethyl Ketones with Chiral Rh Complexes. *Journal of Organic Chemistry* **2004,** 69, (21), 7391-7394.

94. Bragg, M. E. T.; Kafri, R.; Baker, D. C.; Turner, J. F. C., Spectroscopic investigation of several key reaction intermediates in the catalytic asymmetric ionic hydrogenation with medicinal application using Cp*Rh(TsDPEN)Cl. *Abstracts of Papers, 229th ACS National Meeting, San Diego, CA, United States, March 13-17, 2005* **2005**, INOR-030.

95. Arnold, D. P.; Bennett, M. A., Hydrido(phenyl) and hydrido(methyl)platinum(II) complexes via thermally unstable methoxo and formato complexes. *Journal of Organometallic Chemistry* **1980,** 199, (1), C17-C20.

96. Crespo, M.; Sales, J., Organometallic formate complexes of platinum(II). *Journal of Organometallic Chemistry* **1987,** 322, (3), 405-11.

97. Darensbourg, D. J.; Darensbourg, M. Y.; Goh, L. Y.; Ludvig, M.; Wiegreffe, P., Reaction of $(Cy_3P)_2Ni(H)(CH_3)$ with carbon dioxide. Formation of an hydridonickel formate complex, $HNi(O_2CH)(Cy_3P)_2$. *Journal of the American Chemical Society* **1987,** 109, (24), 7539-40.

98. Grushin, V. V.; Bensimon, C.; Alper, H., The First Isolable Organopalladium Formato Complexes: Synthesis, Characterization, and X-ray Structure. Facile and Convenient Thermal Generation of Coordinatively Unsaturated Palladium(0) Species. *Organometallics* **1995,** 14, (7), 3259-63.

99. Mashima, K.; Abe, T.; Tani, K., Asymmetric transfer hydrogenation of ketonic substrates catalyzed by $(h_5\text{-}C_5Me_5)MCl$ complexes (M = Rh and Ir) of (1S,2S)-N-(*p*-toluenesulfonyl)-1,2-diphenylethylenediamine. *Chemistry Letters* **1998**, (12), 1199-1200.

100. Mashima, K.; Abe, T.; Tani, K., The half-sandwich hydride and 16-electron complexes of rhodium and iridium containing (1S,2S)-N-(*p*-toluenesulfonyl)-1,2-diphenylethylenediamine: relevant to asymmetric transfer hydrogenation. *Chemistry Letters* **1998**, (12), 1201-1202.

101. Puckner, W. A.; Hilpert, W. S., Detection and Estimation of Hexamethylenamine in Pharmaceutical Mixtures. *Journal of the American Chemical Society* **1908,** 30, 1471-4.

102. Dickinson, R. G.; Raymond, A. L., The crystal structure of hexamethylenetetramine. *Journal of the American Chemical Society* **1923,** 45, 22-9.

103. Schmidtchen, F. P., Synthesis of macrotricyclic amines. *Chemische Berichte* **1980,** 113, (3), 864-74.

104. Weisman, G. R.; Rogers, M. E.; Wong, E. H.; Jasinski, J. P.; Paight, E. S., Cross-bridged cyclam. Protonation and lithium cation (Li^+) complexation in a diamond-lattice cleft. *Journal of the American Chemical Society* **1990,** 112, (23), 8604-5.

105. Springborg, J.; Olsen, C. E.; Soetofte, I., An inert proton coordinated inside a nearly tetrahedral tetraamine cavity. Synthesis and X-ray crystal structure of the aquatrichlorozincate(II) salt of the inside monoprotonated amine 1,4,8,11-tetraazatricyclo[6.6.2.24,1]octadecane. *Acta Chemica Scandinavica* **1995,** 49, (8), 555-63.

106. Zwier, J. M.; Brouwer, A. M.; Keszthelyi, T.; Balakrishnan, G.; Offersgaard, J. F.; Wilbrandt, R.; Barbosa, F.; Buser, U.; Amaudrut, J.; Gescheidt, G.; Nelsen, S. F.; Little, C. D., Electron Delocalization in the Radical Cation of 1,3,6,8-Tetraazatricyclo[4.4.1.13,8]dodecane, a 4-Nitrogen-7-Electron System. *Journal of the American Chemical Society* **2002,** 124, (1), 159-167.

107. Galasso, V., On the structure and spectroscopic properties of free and protonated adamanzanes. *Chemical Physics* **2001,** 270, (1), 79-91.

108. Howard, S. T., Relationship between Basicity, Strain, and Intramolecular Hydrogen-Bond Energy in Proton Sponges. *Journal of the American Chemical Society* **2000,** 122, (34), 8238-8244.

109. Howard, S. T.; Fallis, I. A., Ab Initio Studies of Proton Sponges (V): 1,4,7,10-Tetraazatricyclo[5,5,2,24,10]hexadecane, a Tricyclic Proton Sponge. *Journal of Organic Chemistry* **1998,** 63, (20), 7117-7119.

110. Llamas-Saiz, A. L.; Foces-Foces, C.; Elguero, J., Proton sponges. *Journal of Molecular Structure* **1994,** 328, 297-323.

111. Staab, H. A.; Saupe, T., New proton-sponge compounds. Part 5. Proton sponges and the geometry of hydrogen bridges. Aromatic nitrogen bases with unusual basicity. *Angewandte Chemie* **1988,** 100, (7), 895-909.

112. Miyahara, Y.; Tanaka, Y.; Amimoto, K.; Akazawa, T.; Sakuragi, T.; Kobayashi, H.; Kubota, K.; Suenaga, M.; Koyama, H.; Inazu, T., The proton cryptate of hexaethylenetetramine. *Angewandte Chemie, International Edition* **1999,** 38, (7), 956-959.

113. Colvin, A. J.; Glover IV, L. C.; Schell, F. M.; Turner, J. F. C., Unpublished results. **2005**.

114. Weisman, G. R., Unpublished results. **2005**.

115. Springborg, J., Adamanzanes bi- and tricyclic tetraamines and their coordination compounds. *Dalton Transactions* **2003,** 9, 1653-1665.

116. Jahn, H. A.; Teller, E., Stability of polyatomic molecules in degenerate electronic states. I. Orbital degeneracy. *Proc. Roy. Soc. (London)* **1937,** A161, 220-35.

117. Jahn, H. A., Stability of polyatomic molecules in degenerate electronic states. II. Spin degeneracy. *Proc. Roy. Soc. (London)* **1938,** A164, 117-31.

118. Pearson, R. G., Jahn-Teller effects. *Proceedings of the National Academy of Sciences of the United States of America* **1975,** 72, (6), 2104-6.

119. Pearson, R. G., The second-order Jahn-Teller effect. *Theochem* **1983,** 12, 25-34.

120. Pearson, R. G., Symmetry rule for predicting molecular structure and reactivity. *Journal of the American Chemical Society* **1969,** 91, (5), 1252-4.

121. Pearson, R. G., Symmetry rule for predicting molecular structures. *Journal of the American Chemical Society* **1969,** 91, (18), 4947-55.

122. Bersuker, I. B., Modern Aspects of the Jahn-Teller Effect Theory and Applications To Molecular Problems. *Chemical Reviews (Washington, D. C.)* **2001,** 101, (4), 1067-1114.

123. Albright, T. A.; Burdett, J. K.; Whangbo, M. H., *Orbital Interactions in Chemistry*. John Wiley & Sons: New York, 1985; p 447

124. Niu, W.; Wong, E. H.; Weisman, G. R.; Sommer, R. D.; Rheingold, A. L., Gallium(III) and indium(III) complexes of cross-bridged tetraamine ligands. *Inorganic Chemistry Communications* **2002,** 5, (1), 1-4.

125. Niu, W.; Wong, E. H.; Weisman, G. R.; Zakharov, L. N.; Incarvito, C. D.; Rheingold, A. L., Copper(II) and zinc(II) complexes of amide pendant-armed cross-bridged tetraamine ligands. *Polyhedron* **2004,** 23, (6), 1019-1025.

126. Niu, W.; Wong, E. H.; Weisman, G. R.; Peng, Y.; Anderson, C. J.; Zakharov, L. N.; Golen, J. A.; Rheingold, A. L., Structural and dynamic studies of zinc, gallium, and cadmium complexes of a dicarboxylate pendant-armed cross-bridged cyclen. *European Journal of Inorganic Chemistry* **2004**, (16), 3310-3315.

127. Anderson, C. J.; Dehdashti, F.; Cutler, P. D.; Schwarz, S. W.; Laforest, R.; Bass, L. A.; Lewis, J. S.; McCarthy, D. W., ^{64}Cu-TETA-octreotide^{64}Cu-TETA-octreotide as a PET imaging agent for patients with neuroendocrine tumors. *Journal of Nuclear Medicine* **2001,** 42, (2), 213-221.

128. Edwards, W. B.; Anderson, C. J.; Fields, G. B.; Welch, M. J., Evaluation of Radiolabeled Type IV Collagen Fragments as Potential Tumor Imaging Agents. *Bioconjugate Chemistry* **2001,** 12, (6), 1057-1065.

129. Aoki, S.; Kawatani, H.; Goto, T.; Kimura, E.; Shiro, M., A Double-Functionalized Cyclen with Carbamoyl and Dansyl Groups (Cyclen = 1,4,7,10-Tetraazacyclododecane): A Selective Fluorescent Probe for Y^{3+} and La^{3+}. *Journal of the American Chemical Society* **2001,** 123, (6), 1123-1132.

130. Becka, L. N.; Cruickshank, D. W. J., The crystal structure of hexamethylenetetramine. I. X-ray studies at 298, 100, and 34 K. *Proc. Roy. Soc. (London)* **1963,** 273, (Ser. A), 435-54.

131. Nygren, C. L.; Colvin, A. J.; Turner, J. F. C., Unpublished results. **2005**.

132. Bragg, M. E. T.; Hedge, M.; Nygren, C. L.; Turner, J. F. C., Synthesis and spectroscopy of amido zirconium complexes. *Abstracts of Papers, 227th ACS National Meeting, Anaheim, CA, United States, March 28-April 1, 2004* **2004**, INOR-442.

133. Bragg, M. E. T.; Hedge, M.; Nygren, C. L.; Turner, J. F. C., Synthesis, reactivity, and structural characterization of a series of carbazoyl complexes. *Abstracts of Papers, 226th ACS National Meeting, New York, NY, United States, September 7-11, 2003* **2003**, INOR-428.

134. Bragg, M. E. T.; Hedge, M.; Turner, J. F. C., Synthesis and characterization of a series of novel carbazole complexes. *Abstracts of Papers, 225th ACS National Meeting, New Orleans, LA, United States, March 23-27, 2003* **2003**, INOR-682.

135. Graebe, C.; Glaser, C., *Berichte der Deutschen Chemischen Gesellschaft* **1872,** 5, 12.

136. Manchand, P. S.; Coffen, D. L.; Belica, P. S.; Wong, F.; Wong, H. S.; Berger, L., Syntheses of carprofen, a carbazole-based nonsteroidal antiinflammatory agent. *Heterocycles* **1994,** 39, (2), 833-45.

137. Juret, P.; Tanguy, A.; Girard, A.; Le Talaer, J. Y.; Abbatucci, J. S.; Dat-Xuong, N.; Le Pecq, J. B.; Paoletti, C., Preliminary trial of 9-hydroxy-2-methyl ellipticinium (NSC 264--137) in advanced human cancers. *European journal of cancer* **1978,** 14, (2), 205-6.

138. Von Moellendorff, E.; Abshagen, U.; Akpan, W.; Neugebauer, G.; Schroeter, E., Clinical pharmacologic investigations with carvedilol, a new beta-blocker with direct vasodilator activity. *Clinical Pharmacology & Therapeutics (St. Louis, MO, United States)* **1986,** 39, (6), 677-82.

139. Cui, C.-B.; Yan, S.-Y.; Cai, B.; Yao, X.-S., Carbazole alkaloids as new cell cycle inhibitor and apoptosis inducers from Clausena dunniana Levl. *Journal of Asian Natural Products Research* **2002,** 4, (4), 233-241.

140. Schaller, C. P.; Bonanno, J. B.; Wolczanski, P. T., Does Methane Bind to d_0 (tBu$_3$SiNH)$_2$Zr:NSitBu$_3$ Prior to C-H Bond Activation? An Inter vs Intramolecular Isotope Effect Study. *Journal of the American Chemical Society* **1994,** 116, (9), 4133-4.

141. Schaller, C. P.; Cummins, C. C.; Wolczanski, P. T., Hydrocarbon Activation via Reversible 1,2-RH-Elimination from (tBu$_3$SiNH)$_3$ZrR: Synthetic, Structural, and

Mechanistic Investigations. *Journal of the American Chemical Society* **1996,** 118, (3), 591-611.

142. Cummins, C. C.; Baxter, S. M.; Wolczanski, P. T., Methane and benzene activation via transient (*tert*-$Bu_3SiNH)_2Zr$:NSi-*tert*-Bu_3. *Journal of the American Chemical Society* **1988,** 110, (26), 8731-3.

143. Bennett, J. L.; Wolczanski, P. T., Energetics of C-H Bond Activation and Ethylene Binding to d_0 Transient (silox)2Ti:NSi*t*Bu_3. *Journal of the American Chemical Society* **1994,** 116, (5), 2179-80.

144. Kuznetsov, V. L.; Lopatinskii, V. P.; Filimonov, V. D., Alkylation and alkenylation of carbazole with isobutene and phenylacetylene in the presence of chlorodiethylaluminum. *Zhurnal Organicheskoi Khimii* **1986,** 22, (10), 2214-17.

145. Appler, H., Preparation of carbazolylsilanes. *Journal of Organometallic Chemistry* **1988,** 350, (2), 217-26.

146. Kikugawa, Y.; Aoki, Y.; Sakamoto, T., Synthesis of Carbazoles from N-(Diarylamino)phthalimides with Aluminum Chloride via Diarylnitrenium Ions. *Journal of Organic Chemistry* **2001,** 66, (25), 8612-8615.

147. Smith, K.; James, D. M.; Mistry, A. G.; Bye, M. R.; Faulkner, D. J., A new method for bromination of carbazoles, b-carbolines and iminodibenzyls by use of N-bromosuccinimide and silica gel. *Tetrahedron* **1992,** 48, (36), 7479-88.

148. Park, M.; Buck, J. R.; Rizzo, C. J., A convenient synthesis of 3,6-substituted carbazoles via nickel catalyzed cross-coupling. *Tetrahedron* **1998,** 54, (42), 12707-12714.

149. Chakrabarty, M.; Batabyal, A.; Patra, A., Indolization of cyclohexanone phenylhydrazones using phosphorous trichloride. *Indian Journal of Chemistry, Section B: Organic Chemistry Including Medicinal Chemistry* **1992,** 31B, (3), 199-201.

150. Bhattacharyya, P.; Jash, S. S.; Dey, A. K., Free radical cyclization of diphenylamine: a convenient synthesis of carbazole and 3-methylcarbazole. *Journal of the Chemical Society, Chemical Communications* **1984**, (24), 1668-9.

151. Islam, A.; Bhattacharyya, P.; Chakraborty, D. P., Thermal cyclization of diphenylamine to carbazole. Synthesis of the natural product glycozolidine. *Journal of the Chemical Society, Chemical Communications* **1972**, (9), 537.

152. Majumdar, K. C.; Das, U.; Kundu, A. K., Synthesis of carbazoles from O-cyclohex-2-enylanilines. *Synthetic Communications* **1998,** 28, (9), 1593-1600.

153. Murakami, Y.; Yokooa, H.; Watanabe, T., New syntheses of murrayafoline-A and murrayaquinone-A via Fischer indolization of 2-sulfonyloxyphenylhydrazone (Fischer indolization and its related compounds. Part 29). *Heterocycles* **1998,** 49, 127-132.

154. Berlin, K. D.; Clark, P. E.; Schroeder, J. T.; Hopper, D. G., Synthesis of 1,2,3,4-tetrahydrocarbazoles with large groups. Aromatization to carbazoles. *Proceedings of the Oklahoma Academy of Science* **1968,** 47, 215-20.

155. Kuroki, M.; Tsunashima, Y., The chemistry of carbazoles. VII. Syntheses of methylcarbazoles. *Journal of Heterocyclic Chemistry* **1981,** 18, (4), 709-14.

156. Dieguez, M.; Pamies, O.; Ruiz, A.; Claver, C.; Castillon, S., Novel diphosphite derived from D-gluco-furanose provides high regio- and enantioselectivity in Rh-catalyzed hydroformylation of vinyl arenes. *Chemical Communications (Cambridge)* **2000**, (17), 1607-1608.

157. Dieguez, M.; Pamies, O.; Ruiz, A.; Castillon, S.; Claver, C., Chiral diphosphites derived from D-glucose: new ligands for the asymmetric catalytic hydroformylation of vinyl arenes. *Chemistry--A European Journal* **2001,** 7, (14), 3086-3094.

158. Dieguez, M.; Ruiz, A.; Claver, C., Chiral diphosphites derived from D-glucose: new highly modular ligands for the asymmetric catalytic hydrogenation. *Journal of Organic Chemistry* **2002,** 67, (11), 3796-801.

159. Dieguez, M.; Pamies, O.; Claver, C., Ligands derived from carbohydrates for asymmetric catalysis. *Chemical reviews* **2004,** 104, (6), 3189-216.

160. Baker, D. C.; Horton, D.; Tindall, C. G., Jr., Large-scale preparation of D-allose: observations on the stereoselectivity of the reduction of 1,2:5,6-di-*O*-

isopropylidene-D-ribo-hexofuranos-3-ulose hydrate. *Carbohydrate research* **1972,** 24, (1), 192-7.

161. Whistler, R. L.; BeMiller, J. N.; Editors, *Methods in Carbohydrate Chemistry, Vol. 7: General Methods, Glycosaminoglycans, and Glycoproteins*. 1976; p 293.

162. Paulsen, H.; Guenther, C., Monosaccharides containing nitrogen in the ring. XXXV. Investigations into the synthesis of 5-amino-5-deoxyhexuronic acids. *Chemische Berichte* **1977,** 110, (6), 2150-7.

163. Miculka, C., Synthesis of racemic ribose from D-glucose. *Synlett* **1999,** S1, 948-950.

164. Trifonova, A.; Foldesi, A.; Dinya, Z.; Chattopadhyaya, J., Diastereospecific chemical synthesis of ribonucleosides-3',4',5',5'-d_4. *Tetrahedron* **1999,** 55, (15), 4747-4762.

165. Kiss, J.; D'Souza, R.; Van Koeveringe, J. A.; Arnold, W., Stereospecific synthesis of the anticancer agent 5'-deoxy-5-fluorouridine (5-DFUR) and its 5'-deuterated derivatives. *Helvetica Chimica Acta* **1982,** 65, (5), 1522-37.

VITA

Megan Taliaferro Bragg was born in Austin, Texas and moved to Hendersonville, Tennessee at the age of seven. Though already developed at this time, her interest in music grew as she began playing French horn at Hawkins Middle school. She attended Hendersonville High school and discovered that she really enjoyed the subject of chemistry. She graduated from high school in 1996.

Megan attended Tennessee Technological University and received the freshman and sophomore outstanding chemistry student awards, chemistry departmental scholarships, and music scholarships. While at TTU, she developed an interest in NMR spectroscopy which was encouraged in her second year of graduate school. She graduated from TTU in 2000 with a Bachelor's degree in Chemistry, ACS accredited. She started research at University of Tennessee, Knoxville in June, 2000 as part of the summer REU program and entered graduate school in August, 2000. She is a Zeigler Buehler fellow and has received both the Chemistry department graduate teaching award and the C. W. Keenen outstanding graduate teaching award. She will graduate from UTK with her PhD in December, 2005.